Interfacial Analysis on Lithium-ion Batteries with Solid Polymer Electrolytes

Dem Fachbereich Biologie und Chemie
der Justus-Liebig-Universität Gießen
vorgelegte Dissertation zur Erlangung
des akademischen Grades
Doktor der Naturwissenschaften
– Dr. rer. nat. –

Yuriy Yusim

November 2023

Dekan / Dean	Prof. Dr. Thomas Wilke
1. Gutachter / 1st Reviewer	Prof. Dr. Dr. h.c. Jürgen Janek (Justus-Liebig-Universität Gießen)
2. Gutachter / 2nd Reviewer	Prof. Dr. Stefano Passerini (Sapienza Università di Roma)
Zusätzliche Betreuerin / Additional Supervisor	Dr. Anja Henss (Justus-Liebig-Universität Gießen)
Eingereicht / Submitted	29.11.2023

Eidesstattliche Erklärung

Die vorliegende Arbeit wurde im Zeitraum vom 01.07.2020 bis 29.11.2023 am Physikalisch-Chemischen Institut der Justus-Liebig-Universität Gießen unter Betreuung von Prof. Dr. Dr. h.c. Jürgen Janek angefertigt. Ich erkläre: Ich habe die vorgelegte Dissertation selbstständig und ohne unerlaubte fremde Hilfe und nur mit den Hilfen angefertigt, die ich in der Dissertation angegeben habe. Alle Textstellen, die wörtlich oder sinngemäß aus veröffentlichten Schriften entnommen sind, und alle Angaben, die auf mündlichen Auskünften beruhen, sind als solche kenntlich gemacht. Ich stimme einer evtl. Überprüfung meiner Dissertation durch eine Antiplagiat-Software zu. Bei den von mir durchgeführten und in der Dissertation erwähnten Untersuchungen habe ich die Grundsätze guter wissenschaftlicher Praxis, wie sie in der „Satzung der Justus-Liebig-Universität Gießen zur Sicherung guter wissenschaftlicher Praxis“ niedergelegt sind, eingehalten.

Gießen, 29.11.2023

_____

Yuriy Yusim

Для моїх батьків

For my parents

Abstract

State-of-the-art lithium-ion batteries (LIBs) with a liquid electrolyte will soon reach their physicochemical limits in terms of energy density. To overcome these limitations, solid-state batteries (SSBs) are currently one of the most promising concepts. At the same time, safety aspects could be improved by replacing flammable liquid electrolyte by a solid electrolyte (SE). Among all classes of SEs, only solid polymer electrolytes (SPEs) based on poly(ethylene oxide) (PEO) with lithium bis(trifluoromethanesulfonyl)imide (LiTFSI) as conducting salt were successfully commercialized so far. However, remaining challenges on the way to higher performances must be addressed such as substituting the currently utilized low-voltage $LiFePO_4$ (LFP) by high-voltage $LiNi_{1-x-y}Co_xMn_yO_2$ (NCM) cathode active material (CAM). In this context, the literature presents a very contradictory understanding of the compatibility and reactivity of PEO-based SPEs with high-voltage cathodes.

Therefore, the properties of the PEO/NCM interface were systemically investigated in this dissertation. It was shown that the "noisy voltage" phenomenon associated with cell failure is due to the penetration of lithium dendrites through the SPE and not due to the oxidation of the SPE. Therefore, reaction products of lithium dendrites were visualized. This issue can be overcome by a simple modification of the SPE using PEO with higher molecular weight, resulting in an improved cycling stability compared to lower molecular weight PEO. However, since the cells still experience a significant capacity fading, electrochemical impedance spectroscopy (EIS) measurements in a three-electrode setup were applied. These confirmed that the NCM/PEO interface is indeed the Achilles' heel in PEO-based SSBs at high voltages. In this context, the interfacial stability depends not only on the applied potential but also on the molecular weight of PEO, which is related to the number of terminal groups per volume. Furthermore, X-ray photoelectron spectroscopy (XPS) analysis confirmed an oxidative degradation of the SPE at high voltages. This is supported by scanning electron microscopy (SEM) images of the cathodes after cycling, suggesting that the interfacial degradation at high voltages leads to a fragmentation of the polymer backbone and to a decrease in viscosity of the SPE.

In addition, this work also addresses potential pitfalls during XPS analysis of PEO-based SPEs. In particular, the photodecomposition of conducting salts can be easily overlooked and misinterpreted as interfacial degradation. It has been shown that the photodecomposition of LiTFSI is more pronounced, when it is dissolved in a PEO matrix compared to pure material. Further, this decomposition can be mitigated by shortening the measurement time or by measuring under cryogenic conditions.

Overall, the results of this dissertation expand the understanding of interfacial degradation in PEO-based SPEs with high-voltage cathodes. Such knowledge is crucial for developing effective protection strategies and improving the cycle stability of SSBs. The analytical approach presented in this work provides a workflow for further research to analyze not only PEO-based SPEs with NCM, but also other difficult-to-access interfaces in SSBs.

Zusammenfassung

State-of-the-art Lithium-Ionen-Batterien (LIBs) mit flüssigen Elektrolyten werden in Bezug auf die Energiedichte bald an ihre physikalisch-chemischen Grenzen stoßen. Um diese zu überwinden, sind Festkörperbatterien (SSBs) derzeit eines der vielversprechendsten Konzepte. Gleichzeitig könnten die Sicherheitsaspekte verbessert werden, indem der entflammbare flüssige Elektrolyt durch einen festen Elektrolyten (SE) ersetzt wird. Von allen SE-Klassen wurden bisher nur feste Polymerelektrolyte (SPEs) auf der Basis von Polyethylenoxid (PEO) mit Lithium bis(trifluormethylsulfonyl)imid (LiTFSI) als Leitsalz erfolgreich kommerzialisiert. Auf dem Weg zu höheren Leistungen müssen jedoch noch einige Herausforderungen bewältigt werden, wie z.B. die Substitution des derzeit verwendeten Niedigvolt-$LiFePO_4$ (LFP) durch das Hochvolt-$LiNi_{1-x-y}Co_xMn_yO_2$ (NCM)-Kathodenaktivmaterial. In diesem Zusammenhang gibt es in der Literatur ein sehr widersprüchliches Verständnis über die Kompatibilität und Reaktivität von PEO-basierten SPEs mit Hochvoltkathoden.

Daher wurden in dieser Dissertation die Eigenschaften der PEO/NCM-Grenzfläche systematisch untersucht. Es konnte gezeigt werden, dass das Phänomen des "Spannungsrauschens", das mit einem Zellversagen verbunden ist, auf das Eindringen von Lithiumdendriten durch den SPE und nicht auf dessen Oxidation zurückzuführen ist. Dazu wurden Reaktionsprodukte der Lithiumdendriten sichtbar gemacht. Dieses Problem konnte durch eine einfache Modifikation unter Verwendung des PEOs mit einem höheren Molekulargewicht behoben werden, was zu einer verbesserten Zyklenstabilität im Vergleich zum PEO mit einem niedrigeren Molekulargewicht führte. Da die Zellen jedoch immer noch einen erheblichen Kapazitätsabfall aufwiesen, wurden elektrochemische Impedanzspektroskopie-Messungen (EIS) in einem Drei-Elektroden-Setup durchgeführt. Diese bestätigten, dass die NCM/PEO-Grenzfläche die Achillesferse in PEO-basierten SSBs bei hohen Spannungen ist. Dabei hing die Grenzflächenstabilität nicht nur vom angelegten Potential ab, sondern auch vom Molekulargewicht des PEOs, das mit der Anzahl der Endgruppen pro Volumen zusammenhängt. Darüber hinaus bestätigten die Röntgen-Photoelektronenspektroskopie (XPS)-Messungen eine oxidative Zersetzung des SPEs bei hohen Spannungen. Dies wurde durch elektronenmikroskopische (SEM) Bilder der Kathoden nach dem Zyklisieren unterstützt. Diese legten nahe, dass die Grenzflächendegradation bei hohen Spannungen zu einer Fragmentierung des Polymerrückgrats und zu einer Abnahme der Viskosität des SPEs führt.

Darüber hinaus wurde in dieser Arbeit auch potentielle Fallstricke bei der XPS-Analyse von PEO-basierten SPEs untersucht. Insbesondere die Photozersetzung von Leitsalzen kann leicht übersehen und als eine Grenzflächendegradation fehlinterpretiert werden. Die durchgeführten Untersuchungen zeigten, dass die Photozersetzung von LiTFSI ausgeprägter ist, wenn es in einer PEO-Matrix gelöst ist als in einem reinen Material. Des Weiteren konnte diese Zersetzung kann durch eine Verkürzung der Messzeit oder durch das Messen unter kryogenen Bedingungen abgeschwächt werden.

Insgesamt vertiefen die Ergebnisse dieser Dissertation das Verständnis der Grenzflächendegradation von PEO-basierten SSBs mit Hochvoltkathoden. Dieses Wissen ist entscheidend für die Entwicklung wirksamer Schutzstrategien und die Verbesserung der Zyklenstabilität von SSBs. Der präsentierte analytische Ansatz bietet zudem einen Workflow für weitere Untersuchungen, nicht nur bei PEO-basierten SPEs mit NCM, sondern auch bei anderen schwer zugänglichen Grenzflächen in SSBs.

List of Abbreviations

CAM	Cathode active material
CEI	Cathode electrolyte interphase
CT	Charge transfer
DFT	Density function theory
DEMS	Differential electrochemical mass spectrometry
EIS	Electrochemical impedance spectroscopy
FIB	Focused ion beam
FTIR	Fourier transform infrared spectroscopy
IR	Infrared spectroscopy
LATP	$Li_{1.5}Al_{0.5}Ti_{1.5}(PO_4)_3$
LCO	$LiCoO_2$
LFP	$LiFePO_4$
LIB	Lithium-ion battery
LiTFSI	$LiC_2NO_4F_6S_2$
LLZO	$Li_{6.25}Al_{0.25}La_3Zr_2O_{12}$
LPSCl	Li_6PS_5Cl
NCM	$LiNi_{1-x-y}Co_xMn_yO_2$
NMR	Nuclear magnetic resonance
PEO	Poly(ethylene oxide)
PVDF	Polyvinylidene fluoride
RE	Reference electrode
RT	Room temperature
SE	Solid electrolyte
SEI	Solid electrolyte interphase
SEM	Scanning electron microscopy
SOC	State of charge
SPE	Solid polymer electrolyte
SSB	Solid-state battery
TEM	Transmission electron microscopy
ToF-SIMS	Time-of-flight secondary ion mass spectrometry
XPS	X-ray photoelectron spectroscopy
XRD	X-ray diffraction

Table of Contents

1 Introduction

Since their market introduction by Sony in 1991, lithium-ion batteries (LIBs) have been established themselves as efficient energy storage devices due to their excellent cycle stability and high energy density.[1],[2] Nowadays, LIBs are widely applied in consumer products, stationary applications and electric vehicles (EVs). According to a recent market research report by Grand View Research Inc.[3], the global market size for LIBs was valued at USD 48.19 billion in 2022. The report predicts that the market will grow with a compound annual growth rate (CAGR) of 18.1% to reach USD 182.53 billion by 2030. This large increase is mainly due to the electrification of transport, which will represent the largest share of battery demand in 2030 in terms of total energy storage capacity. One notable example is the German government's ambitious target of introducing at least 15 million electric vehicles by 2030 to reduce the carbon emissions.[4] There is no doubt that the LIB has played a crucial role to create a wireless society that is increasingly less dependent on fossil fuels. For this reason, the scientific efforts of J. Goodenough, A Yoshino and M. Whittingham in the development of the lithium-ion battery were awarded with the Nobel prize in Chemistry in 2019.[5]

However, current state-of-the-art LIBs with an organic liquid electrolyte will soon approach a physicochemical limit in terms of energy density.[6],[7] Their theoretical gravimetric energy density (~300 Wh kg^{-1}) is too low to overcome the current issues of electric vehicles such as limited ranges compared to fossil fuel vehicles.[8] Therefore, alternative follow-up energy storage solutions are currently under intensive research, including solid-state batteries (SSBs). In SSBs, the liquid electrolyte of conventional LIBs is replaced by a lithium-ion conducting solid electrolyte (SE), which can offer numerous advantages. Compared to LIBs, SEs may enable the use of lithium metal as anode material, offering higher energy density due to lithium's low redox potential (-3.04 V *vs*. SHE) and its lightweight. For instance, SSB cells with $LiNi_{0.8}Co_{0.15}Al_{0.05}O_2$ (NCA) and lithium may theoretically reach energy densities of 393 Wh kg^{-1} and 1,143 Wh L^{-1}, while LIBs with NCA and graphite electrodes can only achieve 265 Wh kg^{-1} and 635 Wh L^{-1}, respectively.[6],[9] Furthermore, utilizing SEs can prevent electrode cross talk, a well-known undesirable chemical interaction of dissolved active materials that contributes to the gradual decline in long-term performance of LIBs.[6],[10] Further, the use of SEs can potentially improve the safety of cell through the mitigation of various hazards such as electrolyte flammability, cell leakage and the formation of lithium dendrites that can lead to a short circuit failure.[11],[12] Overall, the potential of the SSB technology is highly promising, as demonstrated by the significant progress made by leading companies such as Bolloré, Samsung, Solid Power, QuantumScape and Toyota.

Several classes of solid electrolytes (SEs) have been identified as potential candidates for use in SSBs. These include oxide-[13],[14], halide-[15],[16], thiophosphate-[17],[18], and polymer-based SEs[19],[20], each exhibiting distinct material-specific advantages and drawbacks that are relevant for practical applications. Among all SEs, solid polymer electrolytes (SPEs) using poly(ethylene oxide) PEO with lithium bis(trifluoromethanesulfonyl)imide (LiTFSI) as conducting salt have emerged as one of the most successful SEs to date. This technology

has already been commercialized by Bolloré and is currently being utilized by Daimler in their electric "eCitaro" buses with $LiFePO_4$ (LFP) as cathode active material (CAM). The concept of polymer electrolytes was developed already in 1973, when Fenton *et al.*[21] reported that alkali metal salts could be dissolved in PEO to form conductive complexes. Armand *et al.*[22] then proposed the use of such polymer electrolyte in SSBs, in which lithium may be used as the anode. This approach is particularly attractive due to numerous benefits offered by PEO-based SPEs including low cost, high solvation ability of lithium salts and moderate ionic conductivity at elevated temperatures ($\sim$1 mS cm^{-1} at 80 °C). Further, PEO-based SPEs exhibit high flexibility that allows good interfacial contact to the electrode active materials in contrast to inorganic SEs.[19] An important key advantage of utilizing a PEO-based electrolyte is its acceptable interface stability against lithium metal[19],[23]-[26], which can lead to higher energy densities compared to conventional LIBs, as previously mentioned.

Despite its potential, the widespread use of PEO-based SPEs in SSBs is hindered by several challenges, including: (1) limited ionic conductivity at room temperature,[27] (2) susceptibility to lithium dendrites,[28] and (3) instability against high voltage cathodes such as $LiCoO_2$ (LCO) and $LiNi_{1-x-y}Co_xMn_yO_2$ (NCM).[29] In recent years, enormous research efforts have been made to overcome the challenges (1) and (2). For instance, the group of S. Passerini[30] increased the ionic conductivity of the PEO-based SPE from $\sim 10^{-3}$ mS cm^{-1} to 0.1 mS cm^{-1} at 20 °C by adding *N*-alkyl-*N*-methylpyrrolidinium TFSI as ionic liquid to the PEO-based SPE. Further, numerous studies[27],[28] suggested to introduce inorganic fillers into the PEO matrix to increase not only the ionic conductivity of the PEO-based SPE at RT but also to mitigate the dendrite formation issues.

However, only limited research attentions have been dedicated to address the issue of the interfacial instability of PEO-based SPE with high-voltage cathodes (challenge (3)).[29] Although PEO-based SPEs exhibit reasonable cycle performance with LFP within a limited voltage window (typically < 3.8 V *vs.* Li^+/Li)[31], it is necessary to introduce high-voltage CAMs into PEO-based SSBs to substantially enhance their energy density for large-scale EV applications. As a side note, all potentials in this dissertation are given relative to Li^+/Li, unless specified otherwise. The oxidation onset of the PEO-based SPE has been widely discussed in literature with strongly inconsistent results, as some authors assign it to 3.2 V[32], 4.0 V[33] or even 4.6 V[34]. Furthermore, in some reports PEO-based SSBs with high-voltage CAMs experience a sudden cell failure caused by "voltages noise". This phenomenon is believed to be caused by either lithium dendrites[34] or oxidative processes[35],[36] at the cathode side.

In this dissertation, the interfacial stability of PEO-based SSBs with high-voltage cathodes is reinvestigated. The aim is to gain a deeper understanding into the interfacial degradation phenomena, to explain and to overcome the observed "voltage noise" failure. Further, various techniques such as impedance spectroscopy, electron microscopy and X-ray photoelectron spectroscopy (XPS), just to name few, are applied to evaluate the stability of PEO-based SPE with NCM. Additionally, the lithium salt degradation in the PEO matrix during XPS analysis is explored to ensure a reliable interfacial analysis.

In the first publication of this dissertation, titled "*Evaluation and Improvement of the Stability of Poly(ethylene oxide)-based Solid-state Batteries with High-Voltage Cathodes*", the stability of PEO-based SSBs with high-voltage cathodes was critically evaluated and improved (see chapter 3.1)[37]. In this study, the penetration of lithium dendrites through the SPE was verified as the cause for "voltage noise" cell failure. This issue was overcome by a simple modification of the SPE by using a higher molecular weight PEO, which resulted in an improved cycling stability compared to lower molecular weight PEO. Furthermore, the oxidative degradation of the SPE was confirmed by XPS after cycling with NCM, which was not possible by Fourier transform infrared spectroscopy due to its limited surface sensitivity.

In the second publication of this dissertation, titled "*Investigation of the Stability of the Poly(ethylene oxide)|$LiNi_{1-x-y}Co_xMn_yO_2$ Interface in Solid-State Batteries*", the stability of PEO-based SSBs with NCM was further investigated (see chapter 3.2)[38]. In this study, electrochemical impedance spectroscopy (EIS) measurements in a three-electrode setup were performed to investigate the resistive processes at the NCM/PEO interface as indication for SPE degradation. The results confirm that the interfacial stability on the cathode side depends not only on the upper cut-off voltage, but also on the molecular weight of PEO, strongly affecting the capacity fading over the time. Furthermore, scanning electron microscopy (SEM) images of the cathodes after cycling indicate that at high voltages interfacial degradation leads to fragmentation of the polymer backbone and to a decrease in viscosity of the SPE.

In the third publication of this dissertation (in preparation), titled "*Challenges in XPS Analysis of PEO-LiTFSI Batteries (Electrolytes): Interpreting X-ray Photodecomposition*", the X-ray photodecomposition of conducting salts during XPS analysis was examined (see chapter 3.3). The study demonstrates that X-ray photodecomposition can easily be overlooked and misinterpreted, especially when analyzing PEO-LiTFSI-based systems. Moreover, the data suggest that the photodecomposition process is more pronounced, when LiTFSI is dissolved in materials such as PEO compared to its pure form. The decomposition can be significantly reduced if measuring under cryogenic conditions or if the measurement time is kept to a minimum.

The fourth and fifth publication (shared first authorship) are not main focus of this dissertation, as they deal with interfaces in thiophosphate-based SSBs. In the fourth publication, titled "*A Dry-Processed $Al_2O_3/LiAlO_2$ Coating for Stabilizing the Cathode/Electrolyte Interface in High-Ni NCM-Based All-Solid-State Batteries*", $Al_2O_3/LiAlO_2$ surface coating for Ni-rich NCM in thiophosphate-based SSBs was developed (see chapter 3.4.1)[39]. Therefore, the coating was achieved by a high-energy mixing process followed by a high-temperature annealing step. Consequently, the coating significantly improves the electrochemical performance, since it reduces the charge transfer resistance on the cathode side. In the fifth publication (submitted), titled "*State of Charge Dependent Impedance Spectroscopy as a Helpful Tool to Identify Reasons for Fast Capacity Fading in All-Solid-State Batteries*", the electrochemical performance of thiophosphate-based SSBs was investigated with electrochemical impedance spectroscopy (see chapter 3.4.2). The results suggest that a high charge transfer resistance on the cathode side is not necessarily responsible for poor

electrochemical performance. To better understand the reasons for capacity fading in SSBs, state of charge (SOC) dependent impedance measurements are required.

Overall, the results of this work expand the understanding of degradation and failure mechanisms in PEO-based SSBs with high-voltage cathodes. The obtained picture of degradation processes, in particular dendrite growth and the oxidation of the PEO-based SPE, is important to develop improvement strategies on the one hand and to avoid misleading interpretations of electrochemical and analytical data on the other hand. Additionally, this dissertation highlights the fact that in SSB with a SPE, chemical degradation is accompanied by mechanical degradation, leading to very complex degradation phenomena.

2 Fundamentals

In the following, the fundamental knowledge, which is essential for understanding this dissertation, is briefly summarized. This includes a detailed description of materials employed in PEO-based SSBs and their inherent properties. Special attention is given to the topic of the interfacial degradation occurring between PEO-based SPE and high-voltage cathodes and the associated analytical challenges, which is only shortly summarized in the publications and not evaluated in detail. However, the subject is vital to understand the motivation as well as the results of this dissertation.

2.1 Solid-State Batteries

In general, solid-state batteries (SSBs) refer to a category of batteries where all components are in a solid state. The roots of solid-state batteries (SSBs) can be traced back to the early 1800s, when Michael Faraday discovered mass transport in Ag_2S and PbF_2.[40] Nowadays, lithium-ion SSBs are a rapidly developing technology that promises to revolutionize current energy storage devices. The main drivers for the application of SSBs are the potentially higher energy density, superior safety, and the possibility to achieve fast charging, compared to conventional lithium-ion batteries (LIBs). The defining difference between SSBs and conventional LIBs is the choice of the electrolyte used to transfer lithium ions between anode and cathode: While LIBs use a liquid electrolyte, SSBs rely on a solid electrolyte (SE) that additionally acts as a separator (see Figure 1).

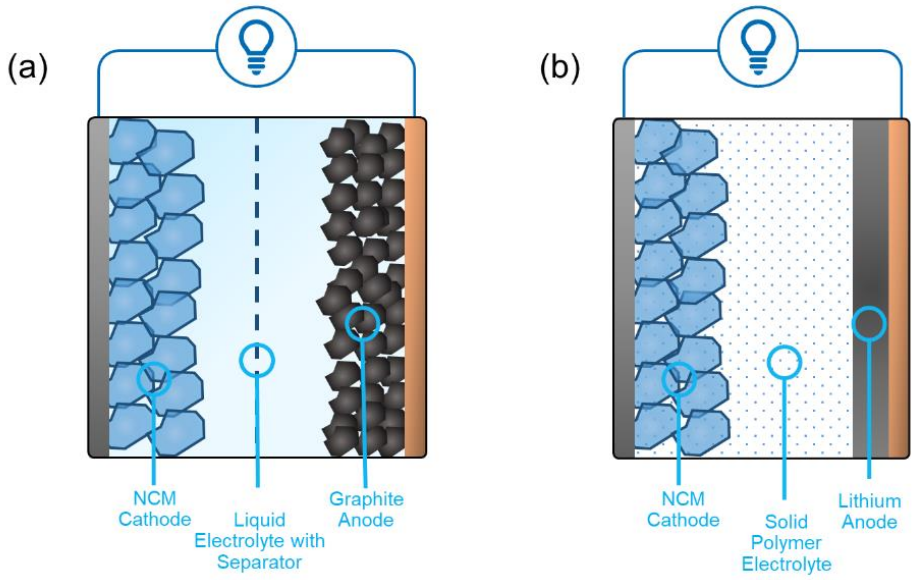

Figure 1: (a) Conventional LIB cell with a liquid electrolyte, NCM cathode, graphite anode and a polyolefin separator. (b) SSB cell with an SPE, NCM cathode and a lithium metal anode. Herein, the SPE also functions as a separator.

An SSB cell consists basically of three main components: a lithium metal anode, an SE separator layer, and a cathode composite, which is a mixture of the SE, carbon and CAM (e.g. LCO, NCM). During the discharge process, lithium ions are extracted from CAM and

migrate through the electrolyte to the anode, where they are deposited as lithium metal. Since the SE is ideally electron blocking (ideal case), electrons migrate from the cathode to the anode through an external circuit, thereby powering the electronic device. During the charging, the reverse process takes place.

Unquestionably, the SE represents the critical component in an SSB, and must fulfil several crucial requirements, including high ionic conductivity, chemical and electrochemical stability towards electrode materials, mechanical robustness, processability, and cost-effectiveness. Numerous types of SEs have been recognized as promising options for applications in SSBs, including oxide-[13],[14], halide-[15],[16], thiophosphate-[17],[18] and polymer-based SEs[19],[20]. Oxide based-SEs including garnet ceramics (e.g., $Li_7La_3Zr_2O_{12}$) and perovskites (e.g., $Li_{1+x}Al_xTi_{2-x}(PO_4)_3$) require high-temperature sintering processes (>700 °C) to achieve sufficient interfacial contact between CAM and SE due to their rigid and non-flexible nature. However, the thermal treatment causes irreversible degradation reactions at the electrode/electrolyte interfaces, which leads to an increase in cell resistances.[41],[42] Halide-based SEs such as Li_3InCl_6 and Li_3ErI_6 have gained recently renewed interest, since they offer high RT ionic conductivity (>10^{-3} S cm^{-1}, theoretically possible 10^{-2} S cm^{-1}), wide electrochemical stability window (up to 6 V) and even water-based synthesis approaches.[15] However, while halides seem to provide good stability against cathode oxide materials, they are highly unstable against lithium metal.[43] Lithium thiophosphates such as $Li_{10}GeP_2S_{12}$ or Li_6PS_5Cl exhibit by far the highest conductivities, some of which reach values above 20 mS cm^{-1} at RT, and are noteworthy for their malleable nature.[44] However, the remaining challenges are interfacial stability issues in contact with cathode oxide materials[18] as well as with lithium metal[45]. Furthermore, chemo-mechanical contraction of the cathode active material upon delithiation results in a loss of contact between SE and CAM particles which increases the interfacial resistance.[46] Polymer-based SEs such as PEO offer high flexibility allowing good interfacial contact, moderate ionic conductivities at elevated temperatures (~1 mS cm^{-1} at 80 °C) and acceptable interface stability against lithium.[19],[23]-[26] Compared to inorganic SEs, solid polymer electrolytes (SPEs) based on PEO exhibit a significantly lower concentration of lithium ions, leading to decreased reliance on lithium reserves and a reduction in production costs. However, they suffer from limited ionic conductivity at room temperature,[27] susceptibility to lithium dendrites,[28] and instability with high-voltage cathodes such as $LiCoO_2$ (LCO) and $LiNi_{1-x-y}Co_xMn_yO_2$ (NCM).[29] Since SPEs and their interfaces with electrodes are the major topic of this dissertation, a thorough overview of SPE-based electrolytes and electrodes utilized in SSBs is given in the following chapter.

2.1.1 Solid Polymer Electrolytes

Solid polymer electrolytes (SPEs) typically consist of a polymer host serving as the solid matrix, with a lithium salt dissolved within, and without the presence of any liquid components. An ideal polymer matrix should meet several crucial criteria to be considered suitable for its application as SPE. These include[47] (1) the cation solvation nature that promotes salt dissociation, (2) the utilization of a high dielectric constant for efficient charge separation,

(3) the requirement of backbone flexibility to facilitate segmental motion, and (4) the incorporation of a high molecular weight polymer matrix to enhance the mechanical strength. Preferably, the polymer repeating units contain donor atoms, particularly O and N, which coordinate cations to form polymer-salt complexes.[48] The first ion conducting polymer, poly(ethylene oxide) PEO (see Figure 2a), complexed with alkali metal salts, was discovered by Fenton *et al.*[21], which opened a new era of research. Building upon this foundation, Armand *et al.*[22] proposed the application of such lithium conducting polymers in SSBs with lithium metal as anode. The PEO polymer is a linear polyether compound with terminal hydroxy groups as demonstrated in Figure 2a. It is worth mentioning that materials with a molecular weight below 20,000 g mol^{-1} are commonly referred to as poly(ethylene glycol) (PEG), while those with a molecular weight above 20,000 g mol^{-1} are typically known as PEO. The groundwork for PEG-based polymers was established by Wurtz in 1859, who introduced ethylene oxide into water.[49] In industry, PEG or PEO are nowadays obtained from an anionic polymerization of ethylene oxide (EO) monomers using catalysts or initiators, allowing good control over molecular weight M_W.

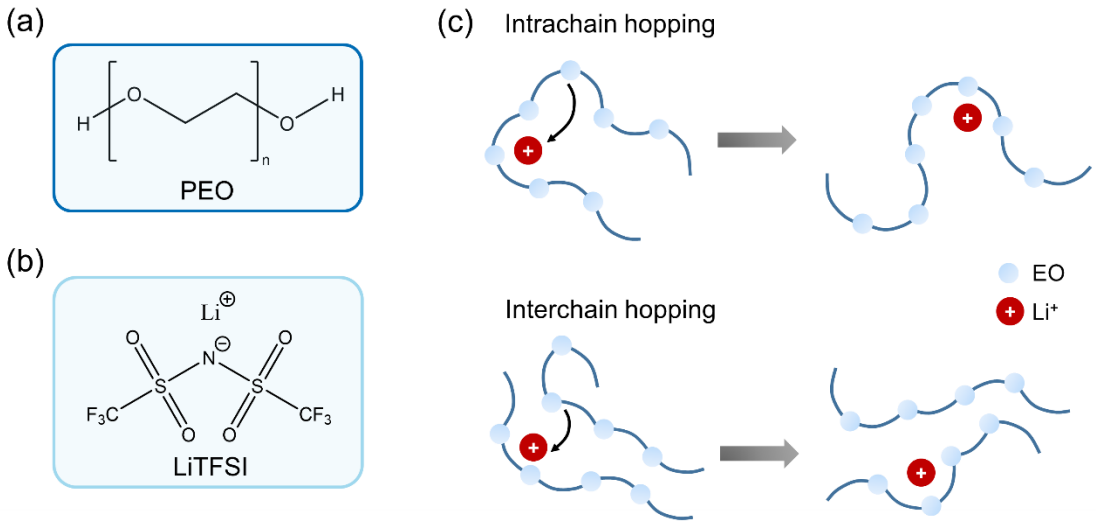

Figure 2: Chemical structure of (a) linear PEO polymer and (b) LiTFSI conducting salt comprising the SPE. (c) Schematic conduction mechanism within the SPE which is based on intrachain and interchain hopping processes.

The conductive mechanism of lithium ions within the PEO matrix is the result of a combination of intrachain and interchain ion hopping (see Figure 2c), accompanied by the formation and breaking of EO-Li bonds. Initially, the electron-donating EO groups form complexes with the Li^+ charge carriers, with approximately five EO units matching one Li^+ ion (not shown in Figure 2c for reasons of simplification).[50] Subsequently, the conduction of Li^+ is facilitated by the segmental motion of the PEO main chains. This enables the ion transport along a single chain or between the chains. However, since the movement of the molecular chain is attributed to the amorphous regions, the ion transport occurs primarily in these regions, while crystalline phases are usually considered as poorly conductive. Consequently, the ionic conductivity of PEO is strongly determined by the volume fraction of the amorphous regions.[50],[48] In this regard, the glass-transition temperature (T_g) characterizes the temperature, at which the polymer transitions from a rigid, glassy state to a more

flexible, rubbery state. In other words, it represents the threshold, when segmental motions begin.[50] Accordingly, the ionic conductivity of PEO is directly influenced by its T_g, with lower values associated with higher conductivity. A low T_g and a high conductivity can be achieved with a very low molecular weight PEO, which however, has poor mechanical strength and cannot act as a solid separator in SSBs. By increasing the M_W, the mechanical strength can be improved at the expense of conductivity. However, for M_W higher than 9,000 g mol^{-1} the conductivity reaches a plateau value, independent of the terminal groups.[51] The influence of the molecular weight on the mechanism of ion transport, viscosity, and glass transition temperature is described in detail by Devaux *et al.*[51] In this regard, the use of PEO with higher molecular weight, which results in increased mechanical strength without significant loss of conductivity, was employed in publication I.

Besides the polymer matrix, the choice of the lithium salt plays a significant role for the ionic conductivity of SPEs.[50] Among the commonly used lithium salts such as $LiBF_4$, $LiAsF_6$, $LiClO_4$ and LiTFSI, the latter (see Figure 2b) is particularly favored due to its outstanding solubility and plasticizing effects[48],[52]. The charge delocalization in TFSI allows efficient dissociation of LiTFSI within the PEO matrix, resulting in a high fraction of free ions. These can move freely contributing to the conduction process. However, the ratio of *n*(EO)/*n*(Li) plays a significant role for the Li^+ ion conduction: If the ratio of *n*(EO)/*n*(Li) is too low, it can lead to insufficient complexation between the polymer and the lithium ions; if the *n*(EO)/*n*(Li) ratio is too high, the excess of polymer chains may hinder ion mobility.[50] Accordingly, both cases will lead to a reduction of the overall conductivity. According to literature[53],[54], the highest ionic conductivity can be reached, when *n*(EO)/*n*(Li) = 10-25.

It is worth mentioning that the pioneering application of PEO-based SPEs in commercial products in the past was initiated by the Canadian company Avestor. They introduced these electrolytes in power back-up batteries for telecom systems. However, unfortunate incidents involving battery fires led to the closure of the company in 2006.[55],[56] After improving the technology, the French company Bolloré launched its “Bluecar” electric vehicle in 2011, which uses PEO-based SPE in combination with a Li-metal anode and an LFP cathode. In addition to PEO, Bolloré uses LiTFSI as a conducting salt[57] and poly(vinylidene fluoride) (PVDF)[58] to enhance the mechanical properties of the SPE. Meanwhile, Bolloré’s technology is also used by Daimler in its eCitaro electric buses. However, recent fire incidents[59],[60] occurring at bus depots have drawn attention to potential safety concerns related to PEO-based SSBs.

To go beyond PEO, a significant number of polymer hosts were investigated such as polycarbonates, polyesters, polynitriles, polyalcohols and polyamines.[48],[61] These exhibit fundamentally different properties to those of polyethers, and might even be able to overcome the limitations of PEO. For instance, in a recent study by Chen *et al.*[62] a hybrid polymer/oligomer cell design is presented. Thereby, a fluid caprolactone oligomer with high ionic conductivity acts as the catholyte, while a scaffold-supported, cross-linked poly(caprolactone) electrolyte is used as separator. Accordingly, this example illustrates the "all-solid" approach is not necessarily the most rewarding strategy; rather, "almost-solid" may be the most viable strategy.[63]

2.1.2 Electrode Materials

While the SPEs were discussed in the last chapter, the focus of this chapter is on the electrode materials. The subsequent section is structured into two main parts: the first part addresses the anode, the second part the cathode active materials. It should be emphasized that the electrode materials presented below can generally be used not only in LIBs but also in SSBs.

i) Anode materials

The anode, often referred to as the negative electrode, is responsible for the storage and release of lithium ions during the charging and discharging processes of a battery. Key properties of anode materials include low working/delithiation potentials *vs.* Li^+/Li, high capacities in volumetric and gravimetric terms, excellent cycling stability, cost-effectiveness and high levels of safety. When considering the mechanism of lithium storage, existing anode materials can be divided into three main groups: intercalation compounds, alloy compounds and conversion compounds.[64]

In intercalation-type anodes, lithium ions are inserted and extracted from the host structure, enabling the lithiation and delithiation processes, respectively. One prominent example of intercalation anodes are carbon-based materials, particularly graphite, which has established itself as commercially available anode material. In graphite, the intercalation of Li ions is based on the layered structure with half-filled p_z orbitals positioned perpendicular to the graphene planes that can interact with the Li 2s orbitals.[65] However, due to the fact that only one Li ion can be intercalated per six carbon atoms, resulting in the formation of LiC_6[66], the gravimetric capacity of graphite is limited (372 mAh g^{-1}). Furthermore, it is important to note that during initial LIB operation, a solid electrolyte interphase (SEI) is formed on the graphite surface due to side reactions of the electrolyte solvent and salt.[67] While the presence of the SEI is essential for long-term performance of LIBs due to its passivating properties, the continuous growth of the SEI contributes to capacity fading. Significantly higher capacities offer anode materials such as silicon ($Li_{4.4}Si$, 4200 mAh g^{-1}) and tin ($Li_{4.4}Sn$, 994 mAh g^{-1}), that store lithium through alloy/dealloying mechanisms.[64] During lithiation, these materials react with lithium to form lithium-based alloys, during delithiation the reverse reaction occurs. However, this causes an enormous volume expansion, which leads to cracks and pulverization of materials and consequently to fast capacity fading. Nevertheless, it is worth to mention that commercially available LIBs are now beginning to include small fractions (e.g., 2-10 wt.%) of silicon oxide in the negative electrode.[66] Readers interested in silicon as anode in SSBs are referred to a previously published review[68]. In conversion-type anodes, such as transition metal oxides, lithium is stored through a conversion reaction mechanism. While they provide high capacities, these materials also experience volume changes, similar to alloy compounds leading to poor cycle life.[69]

Among these anode compounds, pure lithium metal anodes exhibit the highest specific capacity (3860 mAh g^{-1}) and the lowest potential (−3.04 V *vs.* SHE).[68] As a result, only a 20 µm thick lithium layer is required to replace the much thicker standard graphite anode of a common 18650 LIB cell.[7] However, their use in liquid electrolytes is hindered by a few

significant issues. One primary challenge is the occurrence of side reactions between the reactive lithium metal and the liquid electrolyte. These undesired side reactions can lead to the formation of an unstable SEI layer on the surface of the lithium metal.[70] The unstable SEI layer can lead to continuous consumption of lithium ions and an increase in cell resistance, ultimately resulting in significant capacity fading. Furthermore, the presence of a liquid electrolyte in contact with lithium metal can promote the growth of lithium dendrites, which can eventually lead to shortening of the battery cell. However, the use of a solid separator offers a potential solution to overcome these issues. A remarkable example of this potential is demonstrated by Krauskopf *et al.*[71], who showed that interfacial resistance between LLZO-based SE and lithium metal can be reduced to practically 0 Ω cm^2 by applying an external pressure of several 100 MPa. In addition, PEO-based SPEs are also expected to exhibit comparatively acceptable interfacial stability toward lithium metal.[19],[23]-[26] This will be described in more detail in chapter 2.2.1. The stability of other SEs with lithium such as thiophosphate- and halide-based SEs is limited.

ii) Cathode materials

In comparison, the cathode, often referred to as the positive electrode, is also responsible for the storage and release of lithium ions during the charging and discharging. Therefore, the CAM is delithiated and lithiated. Since graphite shows only a slightly higher redox potential than lithium metal[67], the voltage difference between cathode and anode is mainly influenced by the working potential of the CAM, which can vary from 2 V to 5 V *vs.* Li^+/Li. Additionally, it should be noted, that the cathode represents a significant portion, approximately 51% (referred to NCM cathode), of the total cost of a LIB cell.[72] The cathode materials used in LIBs can be categorized into two groups: low-voltage cathode materials and high-voltage cathode materials. This differentiation is based on the voltage range at which these materials operate in the battery system.

Low-voltage cathode materials operate at lower voltages, typically below 4 V, and include materials such as lithium iron phosphate ($LiFePO_4$, LFP) or lithium manganese oxide ($LiMn_2O_4$, LMO). The olivine-structured LFP, which was firstly reported by Padhi *et al.*[73] in 1997, has relatively low electronic conductivity (~10^{-9} S cm^{-1} at RT) caused by the slow 1D migration of Li ions limited by close-packed hexagonal oxygen atoms.[74] Thus, LFP particles are typically covered with a nm-thick carbon layer. LFP is well known for its cycle stability and safety. In comparison, due to the property of fast 3D diffusion of Li ions in the spinel structure, LMO provides a higher rate capability.[75] However, one drawback of this material is its susceptibility to Mn^{2+} dissolution in liquid electrolytes, limiting the cycle life. This may be mitigated by the utilization of SEs. While low-voltage materials, particularly LFP, offer inherent advantages, their lower cell voltage leads to a limitation on energy density.

As a result, high-voltage cathode materials operating above 4 V have gained significant interest, especially for EV applications. Among these materials, layered oxides have emerged as promising candidates, which were first proposed as intercalation compound for rechargeable batteries by Mizushima *et al*.[76] in 1980. They crystallize in a hexagonal layered structure, commonly known as the α-$NaFeO_2$-type structure. Within this structure, the unit cell structure consists of three slabs of CoO_6 octahedra, where the transition metal atoms are

arranged in an edge sharing configuration.[77] In case of $LiCoO_2$ (LCO), which was first commercially introduced CAM, 50% of lithium ions can be reversibly removed, while Co^{3+} is oxidized to Co^{4+}. When more lithium is extracted, the crystal structure undergoes a phase transition from its initial hexagonal to a monoclinic structure. Due to this intrinsic structural instability the experimental electrochemical capacity is limited to 140 mAh g^{-1} (theoretical capacity 280 mAh g^{-1}).[74] To overcome this low practical capacity and the relatively high cost of cobalt in LCO, cobalt was substituted by other transition metals such as nickel and manganese. Accordingly, in the state-of-the-art LIBs for EV applications $LiNi_xCo_yNi_{1-x-y}O_2$ (NCM) materials are mainly used. It is important to note that the capacity and thermal stability of NCM strongly depend on its composition, especially on the Ni content. Higher Ni content in NCM leads to higher capacity, but also to lower structural and thermal stability. For instance, $LiNi_{1/3}Mn_{1/3}Co_{1/3}O_2$ has a relatively high thermal stability, but delivers only a specific capacity of 150-160 mAh g^{-1}, whereas Ni-rich NCM, such as $LiNi_{0.8}Co_{0.1}Mn_{0.1}O_2$ deliver 200 mAh g^{-1} but exhibit worse thermal stability and cycle life.[78] The thermal instability is associated with the highly delithiated NCM, which reacts with the electrolyte and can cause a thermal runaway. Other detrimental processes limiting the cycle life are particle cracking and phase transition of NCM, which are linked to the operation voltage of the battery. It is worth to mention that Tesla already adopted Ni-rich NCM811 ($LiNi_{0.8}Co0_{0.1}Ni_{0.1}O_2$) cathode materials in their LIB systems.[79] Accordingly, since Ni-rich materials are believed to be the benchmark for high energy density applications, these materials were combined with PEO-based SPE in this dissertation. However, this leads to interfacial instabilities, which will be discussed in the next chapter.

2.2 Interfacial Stability in PEO-based Solid-State Batteries

Although the working principle of a Li-ion battery seems to be simple, detailed processes during charging/discharging, especially on the electrode/electrolyte interface are highly complex and not well understood in literature. The following summary provides an overview of the existing knowledge regarding the Li/PEO- and Cathode/PEO-based SPE interface.

2.2.1 Stability Issues: Li/SPE Interface

This chapter focuses on the interfacial stability issues between PEO-based SPE and the lithium metal anode. In this regard, two main phenomena at this interface are discussed in literature:

i) Lithium dendrite formation and dendrite growth

In general, lithium dendrites are metallic microstructures that form on the anode side during the charging process and can further grow during subsequent cycles. As a consequence, their growth leads to fast capacity fading and to serious safety issues, especially the risk of thermal runaways and fires. The growth of lithium dendrites was not only observed in battery cells with liquid electrolytes, but also in cells with solid electrolytes. In this regard, the

critical current density (CCD) was defined as the highest current density at which a lithium metal cell can be cycled without causing severe lithium dendrite growth, leading to a short circuit.[80] Therefore, traditional testing procedures commonly involve constant current cycling tests using symmetrical lithium cells with stepwise increases in current density. Sudden voltage drops or voltage noise during the cell operation indicate a short circuit by one or multiple dendrites, which electronically connect the electrodes, identifying the CCD value. For Li/PEO-LiTFSI/Li cells these values spread from 0.5 mA cm^{-2}[81] to 0.02 mA cm^{-2}[82] in literature. However, it should be mentioned that the CCD value is neither intrinsic to the cell nor to the material but rather depends on various extrinsic factors, such as current profile, transferred charge, pressure, resting intervals and interface chemistry, as it is commented by Fuchs *et al*.[83] in detail. Besides traditional electrochemical testing, further methods are introduced to reveal lithium dendrite growth such as optical microscopy[84], SEM[85] or ^{7}Li nuclear magnetic resonance (NMR)[86]. Furthermore, it should be mentioned that PEO-based SSBs with NCM can experience voltage noise during charging due to dendrite formation[34], although this has also been associated with oxidation of PEO-based SPEs[35],[36] in the literature (see chapter 2.2.2).

The sensitivity of PEO-based SPEs to lithium dendrite growth has been addressed using various strategies, including the incorporation of inorganic fillers[27],[28], modifications of the polymer structure[87],[33], and the utilization of a spacer[88].

ii) The (electro)chemical instability of PEO-LiTFSI towards lithium

Although many authors believe that PEO-based SPE is sufficiently stable against lithium metal, several authors highlight a significant instability of this interface. In early studies[89],[90] the presence of a resistive SEI on lithium metal in a PEO-based system was confirmed by electrochemical impedance measurements. Static ageing of the SPE/lithium interface under storage conditions shows a parabolic growth of the SEI with growth rates of 1.2 $\Omega\ cm^2\ h^{-0.5}$.[91]

Subsequent XPS investigations[92],[93] confirmed that the inner layer of the SEI contains Li_2O, while the outer layer is formed of ROLi species, LiF and hydrocarbons. In contrast, FTIR studies[94] demonstrated that the formation of Li_2O and also LiOH is not a result of the SPE being unstable towards lithium, but rather stems from the reaction with residual water present in the SPE. A comprehensive degradation mechanism was provided by Ushakova *et al*.[95], who proposed a reductive cleavage of PEO molecules by lithium atoms. According to their results, the reductive reaction path starts with a single electron transfer (SET) from lithium to the PEO, which breaks the ether-bond and leads to the formation of alkoxide and radical fragments, followed by further reaction steps.

In comparison to these experimental results, theoretical studies with density functional theory (DFT)-based modelling revealed a strong thermodynamic driving force for the formation of Li_2O accompanied by the generation of C_2H_4 and H_2 gas, when gaseous PEO oligomers are in contact with a Li(100) surface.[96] In this context, all steps in the decomposition process are exothermic. Interestingly, in the absence of metallic lithium when dealing with a fully oxidized Li_2O (111) surface, the decomposition of PEO should become an endothermic process. However, it is worth noting that even in gloveboxes with low degree of contaminations, lithium metal exhibits a passivation layer composed of mainly Li_2CO_3,

LiOH and Li_2O, as shown by Otto *et al.*[97] This could be one significant factor contributing to the inconsistent results on the stability of PEO-based SPE with lithium metal in literature.

Finally, it should be noted that it is not publicly known how Bolloré manufactures their lithium anodes or whether they use an additional interlayer between the anode and the PEO-based separator.

2.2.2 Stability Issues: Cathode/SPE Interface

This chapter addresses the interfacial stability issues between PEO-based SPEs and cathode active materials. Since the main focus of this dissertation is on the interface with high-voltage CAM, the interfacial stability of PEO-based SPE with LFP is not discussed in detail. However, detrimental processes in the operation window of LFP (<3.6 V) are included, as it can be seen below.

In case of PEO-based SPEs with high-voltage cathodes such as LCO and NCM, various degradation and failure mechanisms have been proposed in the literature, so far. In the following, the main drivers contributing to the interfacial instability of PEO-based SPEs with high-voltage cathodes are presented and discussed. In particular, these are:

i) The instability of the conducting salt

According to the results Ma *et al.*[98], the compatibility between PEO-LiDFOB (lithium difluorooxalatoborate) and an LCO cathode is mainly determined by the stability of the Li salt LiDFOB instead of the PEO-polymer. By FTIR analysis, they suggested a ring-opening reaction of the DFOB anion. Moreover, they attributed the peak splitting observed between 1200 cm^{-1} and 1000 cm^{-1} to the decomposition of the LiDFOB salt. XP spectra supported these findings.[98]

Also, other authors such as Nie *et al.*[99] and Seidl *et al.*[32] confirm that the conducting salt plays a crucial role in the degradation of the SPE. In their studies, they proposed the formation of bis(trifluoromethanesulfonyl)imide acid (HTFSI), which is an extremely strong acid (see below). In order to form HTFSI, the oxidation of the PEO-polymer seems to proceed first[99] or simultaneously[32]. For this reason, this is described in more detail in the following section.

ii) The instability of the PEO polymer

Nie et *al.*[99] performed differential electrochemical mass spectrometry (DEMS) measurements, when PEO-LiTFSI was cycled with LCO. As shown in Figure 3, the onset voltage for obvious gas release (mainly H_2) was observed at 4.2 V *vs.* Li^+/Li. Interestingly, this voltage was lower compared to an active material-free electrode cell, where the onset voltage was 4.5 V. From theoretical calculations Nie *et al.*[99] suggested a surface catalytic effect of $LiCoO_2$ regarding the SPE degradation at high voltages, which was also observed by other authors[25]. Moreover, using the computational calculations of Faglioni *et al.*[100], Nie *et al*. predicted that in the first step of the SPE degradation, one electron is removed from PEO polymer, leading to a proton transfer from PEO to LiTFSI. Consequently, HTFSI is

formed, a highly acidic acid. In the next step, HTFSI could attack PEO, leading to chain scissions. According to Faglioni *et al.* and Nie *et al.*, the generation of H_2 gas is likely a result of the chemical crosstalk of HTFSI reacting with Li metal.

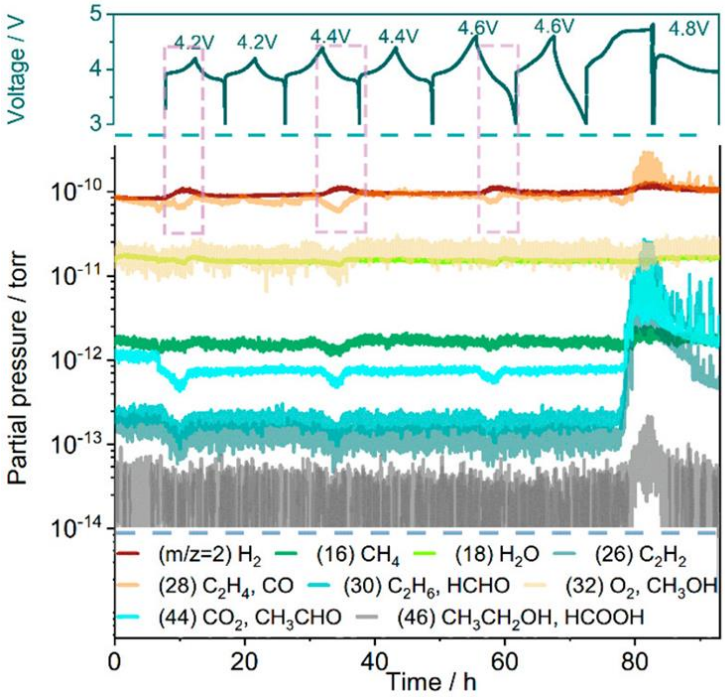

Figure 3: Voltage profile of PEO-based SSB with LCO and corresponding *in situ* DEMS results of different mass signals. The data reveal an H_2 gas release of PEO-based SPE at around 4.2 V. The release of other gases cannot be observed below 4.6 V. The pressure drops of other gases are caused by the increase in H_2 partial pressure. The authors suggest that HTFSI is formed at the cathode, but migrates to the anode side, where it reacts with metallic lithium, generating H_2. Reprinted with permission from ACS Energy Lett. 2020 American Chemical Society.[99]

The presence of HTFSI was experimentally proven by Seidl *et al.*[32]. Based on FTIR measurements they suggest that the onset of PEO oxidation on stainless steel electrodes (no CAM material involved) already occurs at 3.2 V *vs.* Li^+/Li. At this voltage, the alcohol terminal group of PEO is deprotonated and forms HTFSI. Then HTFSI reacts with the ether chain resulting the formation of methanol and 2-methoxyethanol. At higher voltages around 3.6 V, the ether chain is chain is oxidized, accelerating the HTFSI formation, as reported by Seidl *et al.* These findings are partly consistent with the results by Yang *et al.*[33], who also demonstrated that the terminal –OH group is first oxidized when the voltage is higher than 4.05 V. Replacing the reactive –OH group with more stable $–OCH_3$ would extend the electrochemical stability window to 4.3 V. Accordingly, they reported that the ether chain (–C–O–C–) is stable up to 4.3 V, which strongly deviates from the degradation onset suggested by of Seidl *et al.*.

It is worth noting that Seidl *et al.*[32] also studied the gas evolution of PEO-LiTFSI cells with lithium metal as counter and stainless steel as working electrode (no CAM material involved). Interestingly, in their study the release of H_2 gas was already detected under OCV conditions. However, its intensity remained unchanged, when the potential was increased to 5 V *vs.* Li^+/Li.[32] Accordingly, this seems not to be consistent with the study by Nie *et*

al., presented in Figure 3. In this context, other authors write that only traces of gas can be detected before 4.4 V, indicating a negligible decomposition of PEO.[101] This highlights the inconsistency of results regarding the degradation of PEO-based SPEs in the literature.

A further approach was carried out by Kaboli *et al.*[85], who studied the degradation of PEO-LiTFSI with NCM using *in situ* scanning electron microscopy. They found that the thickness of the PEO-based SPE decreased as a function of cycling time, which was associated with the degradation of the PEO-based SPE at high voltages. This was not the case, when PEO-based SPE was cycled with LFP. Moreover, volcano-like features were observed as an indication for the degassing of the SPE due to electrochemical degradation.

Moreover, in some publications a "voltage noise" behavior was observed during charge of PEO-based batteries with high-voltage cathodes. Some authors[35],[36] attributed this phenomenon as indication for oxidation of PEO-based SPE. However, other authors[34] attributed this to dendrite formation.

Finally, one recent work by Homann *et al.*[34] should be mentioned, who determined the onset of the main oxidation of PEO-based SPE via overcharge of the working electrode. Using different electrodes such as NCM, LFP and conductive carbon, they claim that the main oxidation onset of PEO-based SPE could be assigned to 4.6 V *vs.* Li^+/Li. This is independent of the molecular weight of PEO, i.e. the amount of the terminal –OH groups. Additionally, the oxidation onset is independent of the amount of LiTFSI in the SPE. These results are in contrast to some previous studies (see above) that attributed the oxidation onset to lower potentials and emphasized the influence of terminal –OH groups on the electrochemical stability window. In addition, as shown in Figure 3, it seems to be possible to charge PEO-based SSBs to higher potentials than 4.6 V. It should be mentioned, however, that Homann *et al.*[34] do not exclude potential oxidative degradation processes of PEO-based SPEs below 4.6 V.

iii) The intrinsic instability of the cathode active material

Although nickel-rich NCM layered oxides are currently the benchmark for conventional LIBs due to their high specific capacity, their longevity is limited due to various stability issues. These were attributed to particle cracking[102], phase transition[103] and oxygen evolution[104] during cycling. Consequently, the poor performance of PEO-based SSBs with high-voltage CAM was not attributed to the instability of the SPE by many authors, but to the instability of the CAM at higher voltages.

In the study of Qiu *et al.*[25], PEO-based SSBs were paired with $LiMn_{0.7}Fe_{0.3}PO_4$ cathodes, which demonstrate a significantly higher capacity retention compared to cells with LCO, noteworthy with the same cut-off voltage (4.2 V *vs.* Li^+/Li). Moreover, since the interfacial resistance in cells without active material (Super-P as positive electrode) charged to 4.2 V barely changed while the interfacial resistance in cells with active material increased rapidly after cycling to 4.2 V, they concluded that the structural phase transformation of the LCO is the Achilles' heel in PEO-based SSBs. In this regard, they confirmed the presence of CoO rock-salt and Co_3O_4 spinel on the LCO using different methods such as transmission electron microscopy (TEM), X-ray absorption spectroscopy (XAS) and Raman spectroscopy.[25]

Further, Li *et al.*[101] confirm that at the upper cutoff voltage of 4.2 V, the poor electrochemical performance mainly originates from the structure collapse of $LiCoO_2$ at the surface instead of the decomposition of the SPE. According to their study, intensive electrochemical degradation of PEO-based SPEs occurs only at voltages above 4.5 V, which could be the reason for further capacity degradation.

In contrast to these findings, Liang *et al.*[29] conducted Co K-edge XAS measurements of cycled and uncycled LCO materials. Thereby, they were not able to detect any differences between the samples in either the TEY (total electron yield) or FLY (fluorescence yield) modes suggesting LCO is relatively stable during cycling. Furthermore, they demonstrate that SPE degradation mainly occur on the carbon surface and not on the surface of LCO.

Overall, this literature screening highlights the complex and incompletely understood nature of degradation mechanisms in PEO-based SSBs utilizing high-voltage cathodes. The existing body of literature exhibits inconsistencies and gaps in knowledge, further highlighting the need for continued research in this area. As a result, the aim of the dissertation is to delve more deeply into this topic and clarify the inconsistencies.

Nevertheless, a predominant view on the degradation of PEO-based SPEs with high-voltage cathodes can be distilled from the reports in literature, which is presented in a condensed form in Figure 4. It should be noted, however, that this is a simplified illustration that does not consider all reported findings.

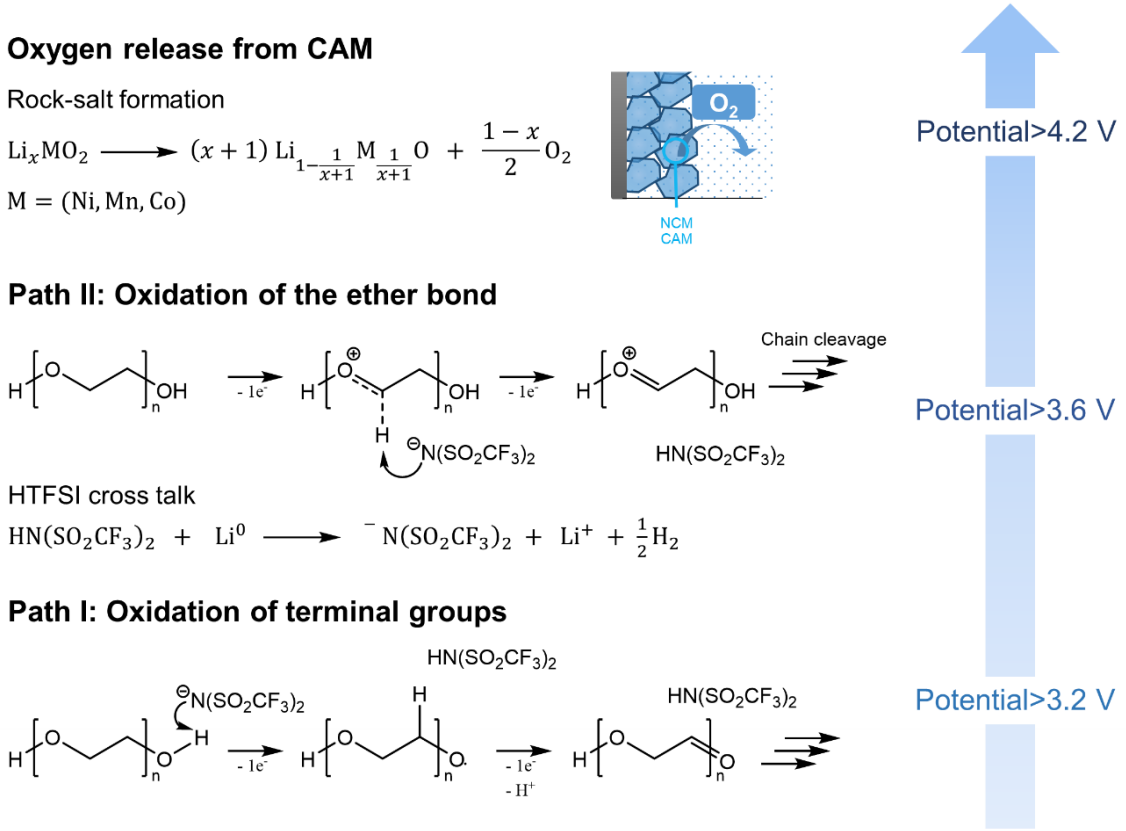

Figure 4: Scheme of the common belief about the degradation in PEO-based SSBs with high-voltage cathodes. Path I and Path II reveal the oxidation of the terminal groups and the

ether bonds, respectively. Both pathways may lead to the formation of HTFSI, which can migrate towards the lithium anode, where it reacts with lithium metal, resulting in the release of H_2. Further, the presence of NCM may catalyze these reactions, releasing oxygen. Please note the given potentials are not exactly defined in the literature and may vary significantly.

Based on this comprehensive overview of the understanding of interfacial processes in PEO-based SSBs with high-voltage cathodes, several open questions can be identified:

(1) What is the underlying cause of "voltage noise" behavior in PEO-based SSBs with high-voltage cathodes?
(2) Is the capacity fading of PEO-based SPEs with high-voltage cathodes determined by resistive processes at the anode side or the cathode side?
(3) Is the capacity fading affected by the structure of PEO-based SPE or entirely by the CAM degradation at high voltages?
(4) In addition to existing knowledge available in the literature, what are the underlying mechanisms responsible for the degradation of PEO-based SPE at high voltages? What is the kinetics of these degradation processes?
(5) What factors may contribute to the varying conclusions found in the literature regarding the interfacial degradation of PEO-based SPE?

In light of these questions, this dissertation aims to address and elucidate the issues outlined in (1)-(5).

2.3 Analytical Challenges

In this chapter, the main analytical challenges related to the interfacial degradation analysis of PEO-based SPEs with high-voltage cathodes in this dissertation are presented. In general, the analysis of these systems is highly complex and not straightforward due to the following reasons:

i) Overlap of impedance contributions

Electrochemical impedance spectroscopy (EIS) is a well-established technique in battery research. It serves as a non-destructive method to monitor the effects of degradation processes on the internal cell resistance within a battery. An electrochemical impedance spectrum of a full cell contains impedance contributions from all parts of the cell. These are the electrolyte bulk resistance, the resistances between the SPE membrane and the electrodes or between the electrodes and the current collectors.[105] Nyquist plots are commonly used to visualize the data, where the imaginary part is plotted against the real part of the impedance as function of the frequency. In accordance to Wurster *et al.*[105], for a SPE-based battery, the serial resistance is seen as the x-interception at high frequencies ($f > 10^5$ Hz), which represents the ionic resistance of the SPE layer. The semicircles in the high and middle frequency region ($10^5 - 10$ Hz) can be assigned to interfacial resistances, which are resistances for electron and ion transfer. The low frequency region ($f < 10$ Hz) is related to diffusion processes in the cathode.[90],[105] In this context, the characteristic frequency

f_{max} defines to which extent different features can be distinguished in the impedance spectrum. It can be expressed as function of the capacitance C and the resistance R:

$$f_{max} = \frac{1}{2\pi RC} \tag{1}$$

However, in full cells, it is almost inevitable that various time constants will overlap. Accordingly, a specific cell configuration is required to separate the impedance contributions from anode and cathode side. One approach is to measure impedance in symmetrical cells. However, for the impedance testing at different SOCs, two anodes or two cathodes from identical cells needs to be reassembled into symmetrical cells, presenting limitations in practicality. To overcome this, cells with a reference electrode (RE) are well-suited to separate the impedance contribution from the anode and cathode sides. Thereby, the RE has to fulfill several requirements:[106] (a) its potential has to be stable during the measurement duration; (b) it has to be located centrally between anode and cathode, where the electric field is homogenous; and (c) its cross-sectional dimensions have to be small compared to the distance between electrodes to minimize the potential gradient across the diameter of the RE. This can be achieved with so called micro-reference electrodes (µ-RE), which is small compared to the size of the electrodes and the distance between them. These have found already broad application in liquid cells[106],[107]. In this dissertation, a gold wire with a polyester coating was burned at the tip in order to obtain a point-like reference electrode. This electrode was placed between two PEO membranes and *in situ* lithiated to obtain a Li_xAu alloy (see Figure 5a). However, it should be mentioned that in case of a high-impedance µ-RE[108] artifacts can dominate the high frequency region of the impedance spectrum. These artifacts often emerge as inductive loops (see Figure 5b).

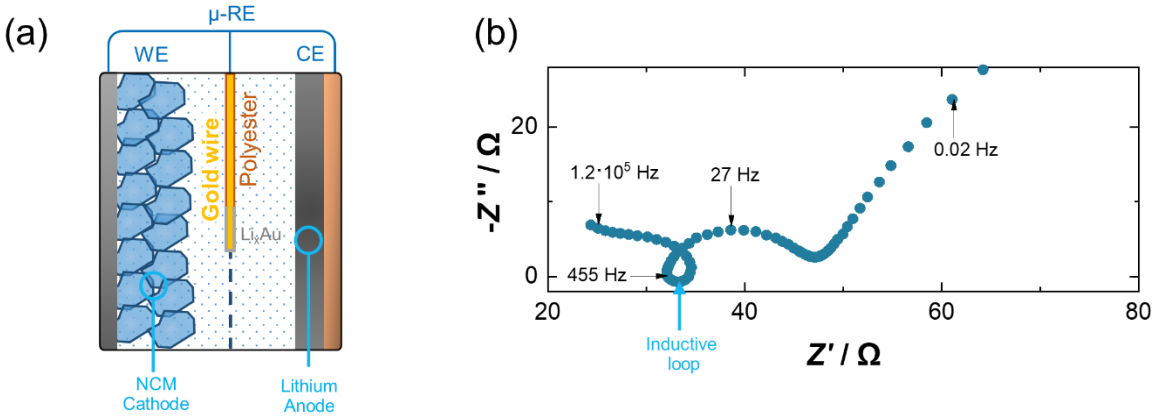

Figure 5: (a) Schematic illustration of a three-electrode setup including a polyester coated gold wire reference electrode to distinguish between the anode and cathode impedance contributions. (b) Impedance spectrum of the cathode at 4.2 V. The inductive loop demonstrates an artifact of the measurement.

ii) Poor accessibility of the SPE/CAM interface

The *post mortem* analysis is conducted after a battery cell completed its operational lifetime to investigate degradation products in PEO-based SSBs with high-voltage cathodes. Therefore, bulk analysis methods such as NMR, X-ray diffraction (XRD) or Raman spectroscopy

may not be suitable because the concentration of the CEI products can be below the detection limits of these methods. Additionally, these methods are not surface sensitive, making it impossible to attribute the degradation products to specific interfaces in PEO-based SSBs. Accordingly, surface sensitive techniques such as XPS, SEM or time-of-flight secondary ion mass spectrometry (ToF-SIMS) are required for a reliable interfacial analysis. However, the access to the electrode/electrolyte interfaces has proven to be extremely difficult due to the sticky nature of PEO, which hinders the disassembly of cells after electrochemical cycling. To still access this interface, some authors[25] apply solvents such as acetonitrile, which, however, can dissolve not only the SPE, but also the CEI components. Another possible way to access these interfaces is to prepare cross-sections of the cell components. Therefore, the cells can be cut with scalpel or scissors. However, this has the consequence that the sticky PEO will be smeared across the interfaces, leading to a coverage of the CEI products on the one hand and to a high surface roughness on the other hand. These phenomena are in general detrimental for the application of surface sensitive techniques. Accordingly, a polishing step is subsequently required, which can be performed mechanically or by ion polishing. Alternatively, a cross section can be prepared with a focused ion beam scanning electron microscope (FIB-SEM). However, both ion beam polishing as well as ion beam cutting can lead to ion-induced degradation of the SPE (see below), making it extremely difficult to distinguish between the degradation products caused by sample preparation or electrochemical cycling. For this reason, a specific workflow was developed in this dissertation to access the PEO/NCM interface and thereby to reduce the impact of preparation-related effects on the analysis. Inspired by the research work of Walther *et al.*, the idea was to remove the current collector of the cathode and thus make the surface accessible. However, this was achievable only if the cathodes were not calendered before. To facilitate removal of the current collector, the cells were cooled to –80 °C. This process aimed to reduce the adhesive characteristics of PEO by increasing its crystallinity. The process is illustrated in Figure 6.

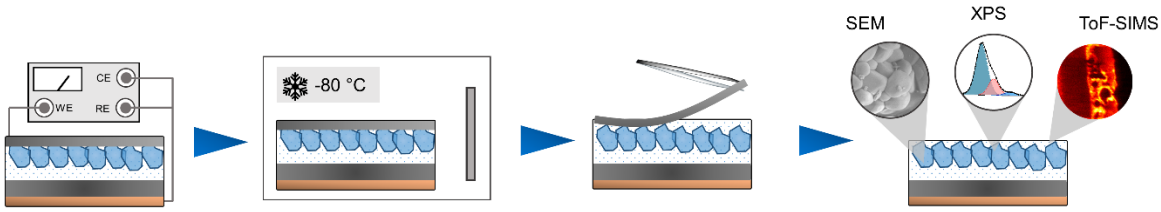

Figure 6: Workflow employed to analytically access the PEO/NCM interface. First, the cells were characterized electrochemically by impedance and cycling tests. Subsequently, the cells were stored at -80 °C to facilitate the removal of the current collector from the uncalendered cathode by simply using tweezers. This enabled the investigation of the PEO/NCM interface with SEM, XPS and ToF-SIMS.

In general, analyzing the interface towards the current collector, as illustrated in Figure 6, enables the detection of CEI products. However, in PEO-based SSBs these can be covered by native polymer. Furthermore, considering that the CEI is nm thick and contains multiple degradation products, surface sensitive techniques can easily reach a detection limit in this context, which is in detail described by F. Walther[109]. Furthermore, since the PEO polymer

is composed of carbon, hydrogen, and oxygen atoms, the data obtained are strongly influenced by a native impurity layer present on any sample surface, even when the samples are stored under UHV conditions.

iii) Radiation damages during analysis

Since the interfaces in SSBs are often buried, milling with focused ion beams (FIBs) to expose them is becoming increasingly popular in the SSB community. In comparison to sputter depth profiling, which suffers from differential sputtering, especially in organic-inorganic hybrid systems, FIB milling enables the fabrication of sample cross-sections for subsequent chemical analysis. For instance, Walther *et al.*[18] used this approach to prepare 45 °FIB crater sidewalls in thiophosphate-based NCM composite cathodes for their interfacial degradation analysis with ToF-SIMS. Their results are outstanding but possible chemical degradation and beam heating effects caused by the FIB hinder direct application of this approach to organic-based samples, which are known to be very beam-sensitive.[110] Thus, extensive "clean-up" processes by sputtering with an argon gas cluster ion source are required to remove the FIB-induced damages. However, sputtering with Ar^+ (and likely to a lesser extent with argon gas clusters) leads to the degradation of LiTFSI to LiF, which was shown in detail by Yu *et al.*[111]

Interfacial analysis without sputtering is not always possible in PEO-based SSBs, as the interfaces can be buried. It should be mentioned that beam-damages of the SPE can also occur during surface analysis. For instance, although X-ray photoelectron spectroscopy (XPS) is one of the common techniques to analyze interfacial degradation in PEO-based SSBs, the X-ray radiation during the measurements leads to photo-induced degradation.[112] This is described in detail in the third publication of this dissertation. As shown in chapter 3.3, the X-ray induced damages can be significantly reduced by shortening the measurement time or by measuring under cryogenic conditions. Consequently, when analyzing PEO-based SPEs with LiTFSI as the conducting salt, researchers must be aware of sputtering and radiation-induced damages in their SPEs to avoid pitfalls in the interpretation of the data.

Overall, this chapter emphasizes the complexity of analyzing PEO-based SPEs with high-voltage cathodes and highlights the need for innovative approaches to overcome challenges such as overlapping impedance contributions, access to interfaces, and mitigation of radiation-induced damages during analysis. Furthermore, this chapter provides insights into, how these challenges were addressed in this dissertation.

3 Results

At the beginning of this dissertation in 2020, the stability of PEO-based SPEs with high-voltage cathodes such as NCM was very contradictory understood in literature, as the oxidation onset of the SPE was assigned to be 3.2 V, 4.0 V or even 4.6 V *vs.* Li^+/Li. Accordingly, the knowledge on the capacity fading of PEO-based SSBs with NCM was limited. In addition, some authors observed a "noisy voltage" related cell failure, which was attributed either to oxidation processes of the PEO at the cathode or to short-circuit behavior due to the penetration of lithium dendrites through the SPE. To clarify the apparent inconsistences in the literature regarding cell failure and capacity decay of PEO-based SSBs, the compatibility and reactivity of PEO-LiTFSI with high-voltage CAM was reinvestigated.

Therefore, the "noisy voltage" related cell failure was evaluated and effectively addressed (publication I)[37]. After enabling stable electrochemical cycling, the stability of PEO-LiTFSI/NCM interface was extensively analyzed (publication II)[38]. In the course of this analysis, potential pitfalls, particularly photodecomposition of conducting salts during XPS analysis, were observed and further examined (publication III).

In addition, detrimental processes at LPSCl/NCM interface were addressed by a surface coating (publication IV)[39]. In this regard, an advanced impedance analysis approach was considered and evaluated (publication V).

It should be noted that although publications I, II and III are the main focus of this dissertation (first authorship), publications IV and V are important contributions (joint first authorship)

3.1 Publication I

Evaluation and Improvement of the Stability of Poly(ethylene oxide)-based Solid-state Batteries with High-Voltage Cathodes

In the first publication[37], the cycle stability in PEO-based SSBs with high-voltage cathodes was evaluated. In particular, the origin of "voltage noise" related cell failure was attributed to the penetration of lithium dendrites through the SPE and not to the oxidation of PEO. Therefore, reaction products of lithium dendrites were visualized using an LATP separator. To overcome this failure and to enable a reasonable cycling performance, an SPE with higher molecular weight was applied, which exhibits higher mechanical rigidity compared to low molecular weight PEO. In addition, it was shown that cell leakage, which can be easily overlooked, can lead to incorrect conclusions about the PEO degradation. But also, in properly closed cells, the XPS results confirmed the presence of oxidative degradation products at the SPE/NCM interface.

Overall, the results of this study support the critical evaluation of the stability of PEO-based SSBs with high-voltage cathodes. However, a more detailed investigation of the interfacial degradation mechanisms is required (see publication II).

The experiments for this work were designed and performed by the first author under the supervision of A. Henss and J. Janek. E. Trevisanello assisted during the material synthesis.

R. Ruess supported in data analysis. A. Mayer, D. Bresser and S. Passerini supported in the validation of the data. All authors contributed to the scientific discussion. The manuscript was written by the first author and edited by all other authors.

Reprinted with permission from Y. Yusim, E. Trevisanello, R. Ruess, F. H. Richter, A. Mayer, D. Bresser, S. Passerini, J. Janek, A. Henss, *Angew Chem Int Ed Engl* **2023**, *62*, e202218316. DOI: 10.1002/anie.202218316.

GDCh Research Articles Angewandte International Edition Chemie www.angewandte.org

Solid-State Batteries

How to cite:
International Edition: doi.org/10.1002/anie.202218316
German Edition: doi.org/10.1002/ange.202218316

Evaluation and Improvement of the Stability of Poly(ethylene oxide)-based Solid-state Batteries with High-Voltage Cathodes

Yuriy Yusim, Enrico Trevisanello, Raffael Ruess, Felix H. Richter, Alexander Mayer, Dominic Bresser, Stefano Passerini, Jürgen Janek, and Anja Henss**

Abstract: Solid-state batteries (SSBs) with high-voltage cathode active materials (CAMs) such as $LiNi_{1-x-y}Co_xMn_yO_2$ (NCM) and poly(ethylene oxide) (PEO) suffer from "noisy voltage" related cell failure. Moreover, reports on their long-term cycling performance with high-voltage CAMs are not consistent. In this work, we verified that the penetration of lithium dendrites through the solid polymer electrolyte (SPE) indeed causes such "noisy voltage cell failure". This problem can be overcome by a simple modification of the SPE using higher molecular weight PEO, resulting in an improved cycling stability compared to lower molecular weight PEO. Furthermore, X-ray photoelectron spectroscopy analysis confirms the formation of oxidative degradation products after cycling with NCM, for what Fourier transform infrared spectroscopy is not suitable as an analytical technique due to its limited surface sensitivity. Overall, our results help to critically evaluate and improve the stability of PEO-based SSBs.

Introduction

State-of-the-art lithium-ion batteries (LIBs) are expected to soon reach their physicochemical limits in terms of energy density.[1] Solid-state batteries (SSBs) are currently one of the most promising concepts to surpass the limitations of LIBs and could be another step towards a society that is less dependent on fossil fuels.[1–3] By replacing flammable liquid electrolytes in LIBs with solid electrolytes (SEs), not only safety is expected to be improved, but also higher energy densities might be achieved by introducing a lithium metal anode.[1,4] A large variety of SEs are currently under intensive investigation. Polymer-,[5] oxide-,[6] halide-[7] and thiophosphate-based[8] SEs show satisfactory properties with different material-specific advantages and disadvantages for practical applications. Among all SEs, solid polymer electrolytes (SPEs) based on poly(ethylene oxide) (PEO) and lithium bis(trifluoromethanesulfonyl)imide (LiTFSI) as conducting salt have been successfully commercialized by Blue Solutions (Bolloré Group) and are currently utilized by Daimler in the electric bus "eCitaro" with $LiFePO_4$ (LFP) as cathode active material (CAM).[9] The practical use of PEO-based SPEs is particularly attractive because they have numerous advantages, including low cost and high flexibility, thereby allowing good interfacial contact to the electrode active materials, the capability of solvating lithium salts and moderate ionic conductivity at elevated temperatures ($\approx 1\,mS\,cm^{-1}$ at 80 °C).[10–14] Despite these characteristics, PEO-based SSBs still face several challenges on the way to large-scale high-energy density applications. Substituting LFP with high-voltage CAMs, such as $LiCoO_2$ (LCO) and nickel-rich $LiNi_{1-x-y}Co_xMn_yO_2$ (NCM) or $LiNi_{1-x-y}Co_xAl_yO_2$ (NCA), would allow a significant increase in energy density.[15–17] In this context, the oxidative stability of the SPE has often been questioned and investigated in the literature. The findings are very contradictory, with the oxidation onset of the SPE being reported to be 3.2 V,[18] 4.0 V[19,20] or even 4.6 V vs. Li^+/Li.[21] As recently discussed by Hernández et al.,[22] the different values of the oxidation onset are highly dependent on the electrochemical measurement methodology. In addition, PEO-based SSBs in combination with high-voltage cathodes experience sudden cell failure related to "voltage noise" during charging. This has often been attributed to oxidation processes of the PEO-based SPE at the cathode.[23] In contrast, in their recent work, Homann et al.[21,24] attributed this cell failure to the formation of lithium dendrites at the anode. Increasing the thickness of the SPE membrane resulted in "voltage noise-free" operation, suggesting that indeed dendrites are the origin of "voltage noise" and cell failure. Nevertheless, direct evidence for the formation of lithium dendrites has not yet been provided. Furthermore, the long-term cycling

[*] Y. Yusim, E. Trevisanello, Dr. R. Ruess, Dr. F. H. Richter, Prof. Dr. Dr. h.c. J. Janek, Dr. A. Henss
Institute of Physical Chemistry, Justus Liebig University Giessen
Heinrich-Buff-Ring 17, 35392 Giessen (Germany)
and
Center for Materials Research (ZfM/LaMa), Justus Liebig University Giessen
Heinrich-Buff-Ring 16, 35392 Giessen (Germany)
E-mail: juergen.janek@phys.chemie.uni-giessen.de
anja.henss@phys.chemie.uni-giessen.de
Dr. A. Mayer, Dr. D. Bresser, Prof. Dr. S. Passerini
Helmholtz Institute Ulm (HIU)
Helmholtzstraße 11, 89081 Ulm (Germany)
and
Karlsruhe Institute of Technology (KIT)
P.O. Box 3640, 76021 Karlsruhe (Germany)

performance with high-voltage cathodes such as LCO in PEO-based cells without cell failure also varies strongly in the literature. While data from Qiu et al. show a discharge capacity of less than 10 mAh g^{-1} after 5 cycles,[10] data from Wang et al. show a discharge capacity of over 100 mAh g^{-1} after 50 cycles.[25] Based on the contradictory results on cell failure and capacity decay of PEO-based SSBs published in the literature, we reinvestigated the compatibility and reactivity of PEO-LiTFSI with high-voltage cathode active materials, such as LCO and NCM. By separating the anode and cathode half cells with a LATP ($Li_{1.4}Al_{0.4}Ti_{1.6}(PO_4)_3$) ceramic solid electrolyte we unequivocally confirm that the "voltage noise" failure is indeed caused by dendrite formation at the anode and not by oxidative processes at the cathode. To overcome this limitation, we increased the mechanical rigidity of the SPE by using PEO with a higher molecular weight, which effectively eliminates the "voltage noise" related cell failure, enabling stable cycling operation. Moreover, we also confirm with XPS the formation of carbonyl groups as oxidative degradation products at the cathode/SPE interface, for what Fourier transform infrared spectroscopy is not suitable due to its limited surface sensitivity.

Results and Discussion

Due to the contradictory results and conclusions on PEO-based SSBs with high-voltage cathodes found in the literature, we first addressed the question of whether the noisy voltage is caused by dendrites or by oxidative processes at the cathode. Thereby, we investigated the origin of this behavior in comparison to the previous results in literature and propose a simple modification of the SPE in order to overcome the "voltage noise" failure, extending former work by Homann et al..[24] In the second part, we look at the stability of the composite cathode. We investigate the cathode side by demonstrating the influence of cell leakage on the cycling performance and SPE decomposition mechanisms.

Evaluation and elimination of "noisy voltage" related cell failure

A Li|PEO-LiTFSI|$LiNi_{0.83}Co_{0.11}Mn_{0.06}O_2$/PVDF/Super P cell was constructed using a PEO-based SPE with a molecular weight $M_w = 300000$ g mol^{-1} as separator and cycled between 3.0 V and 4.3 V against a lithium metal anode at 0.1 C (1 C = 200 mA g^{-1}) and 60 °C. The charge and discharge voltage profiles of the first cycle are shown in Figure 1. As demonstrated in Figure 1, the galvanostatic cycling of the PEO-based SSB shows a "voltage noise" behavior in the initial two charge curves, in good agreement with the report by Homann et al., who also observe such a behavior already at around 3.75 V[21,24] In this context, the authors suggested that the formation of lithium metal dendrites is responsible for this failure, since increasing the thickness of the SPE separator and/or replacing the lithium metal with a graphite anode eliminated this failure.[21] In contrast, this failure was attributed by Simonetti et al.[23] as a clear indication for oxidation processes of the PEO electrolyte. Besides, a possible corrosion of the aluminum current collector should be considered, since LiTFSI-containing electrolytes are known to corrode at high voltages (>3.8 V vs. Li^+/Li) and lead to characteristic pitting.[26,27] To exclude the possibility that this process affects the "voltage noise" behavior and cycling stability of PEO-based SSBs with high voltage cathodes, the aluminum current collector was examined with SEM before and after electrochemical cycling (4 cycles with "voltage noise"). As shown in Figure S1, no difference in the morphology of the aluminum current collector can be seen. Hence, we exclude corrosion of Al-foil of LiTFSI containing SPE as a potential cause of the "voltage noise" behavior.

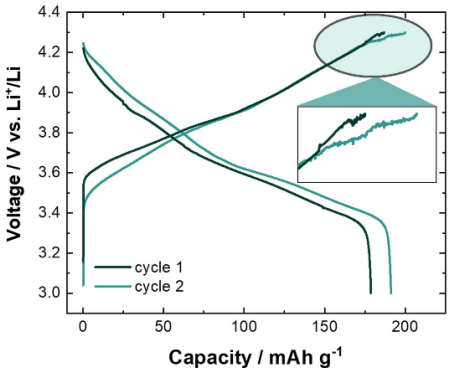

Figure 1. Galvanostatic cycling data of a Li|PEO-LiTFSI|$LiNi_{0.83}Co_{0.11}Mn_{0.06}O_2$/PVDF/Super P cell within a voltage range of 3.0–4.3 V vs. Li^+/Li at 0.1 C and 60 °C using PEO with $M_w = 300000$ g mol^{-1}. Charge and discharge curves of a cell. Magnified view of "voltage noise" behavior.

To evaluate, whether the oxidative degradation of PEO-based SPEs at the cathode or dendrite formation at the anode lead to observed "noisy voltage" cell failure, a LATP pellet was placed between the anode and cathode, as demonstrated in Figure 2a. In this case, the LATP pellet acts as a mechanically rigid separator that prevents the penetration of lithium dendrites through the SPE. Since the SPE is still in physical contact with the NCM cathode, the setup enables possible oxidative processes to occur at the NCM|SPE interface, but precludes lithium dendrite penetration. In addition, the LATP pellet acts as a "white screen" for lithium dendrites. In the case of Li dendrite penetration through the SPE, lithium metal hits the LATP on its way from the anode to the cathode, leading to an immediate reduction of Ti^{4+} to Ti^{3+} of LATP, which is a widely known problem at the interfaces of LATP with Li metal.[28,29] The presence of reduction products can be detected by color changes on the LATP pellet, which is white in its pristine state (Figure 2c).[30] In contrast to Gupta et al.,[31] who visualized the penetration of Li-dendrites in symmetric cells with operando SEM, our approach is much simpler and easier to adopt. Based on this idea, we constructed the Li|PEO-LiTFSI|LATP|PEO-LiTFSI|$LiNi_{0.83}Co_{0.11}Mn_{0.06}O_2$/

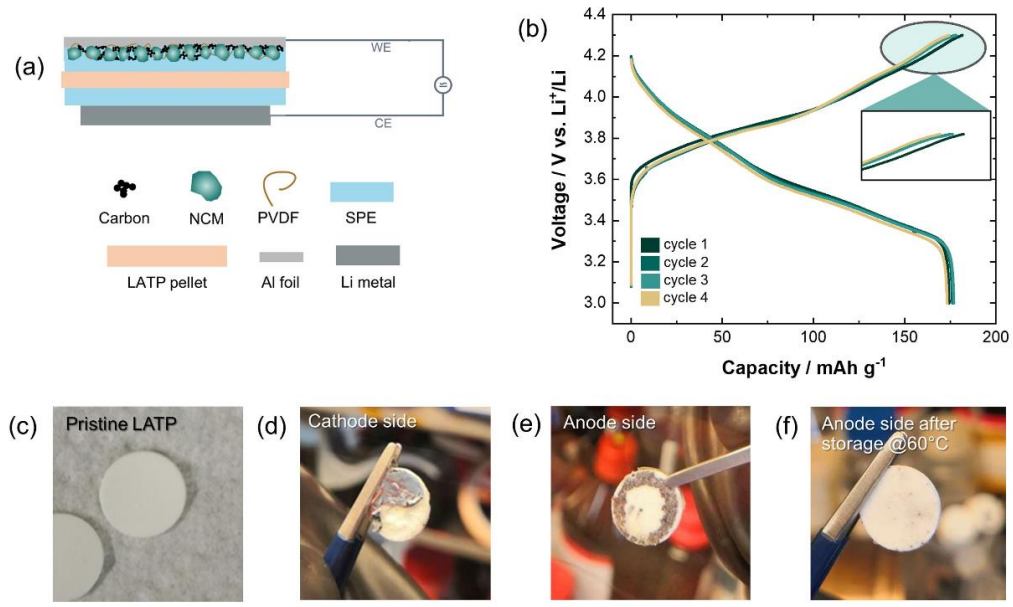

Figure 2. Results from experiments to verify potential dendrite penetration as cause for "voltage noise" failure. (a) Experimental Scheme of the Li | PEO-LiTFSI | LATP | PEO-LiTFSI | $LiNi_{0.83}Co_{0.11}Mn_{0.06}O_2$/PVDF/Super P cell using PEO with $M_w = 300\,000\ g\,mol^{-1}$. (b) Galvanostatic cycling data within a voltage range of 3.0–4.3 V vs. Li^+/Li at 0.1 C and 60 °C. (c) Pristine LATP-pellet. (d) LATP after electrochemical cycling after cathode and SPE removal (cathode side). (e) LATP after electrochemical cycling and after lithium and SPE removal (anode side). (f) LATP after storage at 60 °C without cell cycling and after lithium and SPE removal (anode side).

PVDF/Super P cell and cycled it between 3.0 and 4.3 V vs. Li^+/Li at 0.1 C and 60 °C for 4 cycles. The cycling data are shown in Figure 2b. It should be noted that the LATP pellet leads to an increase in cell impedance and, thus, to a high overpotential which eventually results in a lower initial capacity. Nevertheless, no "voltage noise" behavior was detected. This confirms that the "voltage noise" failure is obviously not a result of PEO oxidation, proving that the reason is definitely not located at the cathode side, but may be caused by the poor mechanical properties of the low molecular weight PEO that allows dendrites to penetrate through the SPE, as proposed by Homann et al.[21,24] To confirm this, after cell disassembly the anode, the cathode and the SPE from both sides were carefully removed. It should be noted that the separation of the sticky PEO based SPE membrane from the LATP is challenging (a common issue of post-mortem analysis of PEO-based solid state batteries[10,21]). As shown in Figure 2d, no color changes on the LATP on the cathode side were observed (the aluminum current collector with the cathode could not be completely removed). This indicates that no lithium dendrites have penetrated through the LATP. However, a grey colored ring of "flake"-like structures can be seen on the LATP pellet on the anode side in Figure 2e. This indicates that lithium dendrites penetrated into the SPE membrane and caused a reaction of the LATP that resulted in a color change. Interestingly, complete coverage of the reduction products on the LATP is not achieved, suggesting that the lithium dendrites mainly penetrate along the edges, which could be the path of least resistance/most external force and most detrimental shrinkage of the SPE when the viscosity of the SPE decreases due to the elevated temperature. In addition, no color changes of the SPE were observed after peeling off the SPE at the anode and cathode side. To exclude the possibility that this behavior is caused by direct contact between the anode and LATP due to shrinkage of the SPE at elevated temperature and applied pressure rather than dendrite formation and growth, we stored a cell at 60 °C at OCV (open-circuit voltage) for about 4 days. As described above, anode and the SPE were removed, obtaining a white LATP pellet without color changes (Figure 2f). This confirms unequivocally that indeed the penetration of dendrites through the SPE is the cause of the "voltage noise" cell failure. In addition, direct contact between the anode and cathode would result in a voltage drop to 0, which was not observed (see Figure 1). Overall, based on the observed color changes on the LATP due to the lithium dendrites, we conclude that lithium dendrites penetrate through the SPE membrane, causing the "voltage noise" behavior and eventually leading to cell failure, which is in good agreement with the results by Homann et al.[21]

To prevent lithium dendrite penetration in a more practical way than increasing the separator thickness[21] or using a spacer[32] and as an alternative to a crosslinked PEO-based SPE,[24] the mechanical strength of the SPE can also be increased by using PEO with a higher molecular weight (here: $M_w = 8\,000\,000\ g\,mol^{-1}$). This is in good agreement with investigations by Wang et al.,[33] who measured the

dependence of tensile strength on the molecular weight of PEO and reported higher tensile strength for higher molecular weights. We observed that at 60 °C PEO-LITFSI with $M_W = 300000\ g\,mol^{-1}$ seems to thermally deform, while PEO-LITFSI with $M_W = 8000000\ g\,mol^{-1}$ keeps its shape. The poor mechanical properties of low molecular weight PEO at 60 °C are shown in the report of Homann et al.[24] As reported by Devaux et al.,[34] the conductivity reaches a plateau above a molecular weight of $10^4\ g\,mol^{-1}$, which means that no significant conductivity losses are expected when further increasing M_w. Thus, a conductivity of about 1 mS cm^{-1} at 80 °C (see Figure S2) can be achieved with PEO-based SPEs with $M_w = 8000000\ g\,mol^{-1}$, which is sufficient to reach full initial cell discharge capacity (> 200 mAh g^{-1} for Ni-rich NCM) (Figure 3). Furthermore, PEO with higher molecular weight enables noise-free charge/discharge cycling in SSBs with NCM, as shown in Figure 3 (no LATP separator was used), in contrast to low molecular weight PEO. To support this, the experiment shown in Figure 2 was repeated, however, using PEO-based SPE with $M_w = 8000000\ g\,mol^{-1}$ at 80 °C. After disassembling the cell and removing PEO and lithium from the anode side, an intact LATP pellet without any color changes was obtained (see Figure 3). This confirms that PEO with higher molecular weight effectively suppresses the penetration of lithium dendrites through the SPE, whereas for lower molecular weight PEO, failure occurs in the first cycle (Figure 1).

In conclusion, we confirm that the "noisy voltage" failure is caused by lithium dendrite formation on the anode side due to the low mechanical strength of low molecular weight PEO-based SPEs rather than by PEO oxidation at the cathode. Indeed, lithium dendrite penetration can be considered as one cell failure mode, which can lead to serious safety concerns. In addition, we demonstrate that the use of PEO with a high molecular weight ($M_w = 8000000\ g\,mol^{-1}$) is a practical and simple way to prevent such cell failure and to enable long-term cyclability of high-voltage PEO-based SSBs compared to lower molecular weight PEO. To the best of our knowledge this modification of the SPE has not been presented so far to overcome the "noisy voltage" failure in PEO-based SSBs. Furthermore, this modification enables to achieve high initial discharge capacities (> 200 mAh g^{-1}) with Ni-rich NCM, which have not been achieved in previous studies.[21,24,32] The dependence of the "voltage noise" failure on the utilized CAM and applied voltage is part of future studies.

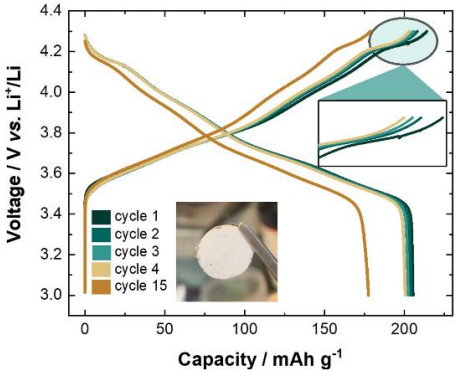

Figure 3. Galvanostatic cycling data of a Li | PEO-LiTFSI | $LiNi_{0.83}Co_{0.11}Mn_{0.06}O_2$/PVDF/Super P cell within a voltage range of 3.0–4.3 V vs. Li^+/Li at 0.1 C and 80 °C using PEO with $M_w = 8000000\ g\,mol^{-1}$. Magnified view without "voltage noise" behavior.

Evaluation of long-term stability and electrolyte oxidation

After evaluating and improving the anode side, we subsequently investigated the long-term cycling behavior of PEO-based SSBs considering the electrolyte oxidation with focus on the cathode side. For this purpose, Li | PEO-LiTFSI | $LiCoO_2$/PEO-LiTFSI/PVDF/Super P cells were prepared and cycled for 40 cycles between 3.0 V and 4.2 V vs. Li^+/Li at 0.1 C and 60 °C using the PEO-based SPE with a molecular weight of $M_w = 8000000\ g\,mol^{-1}$. The corresponding discharge capacities and Coulomb efficiency as a function of cycle number are shown in Figure 4a. As described above, the penetration of lithium dendrites leading to "voltage noise" behavior was effectively avoided by using the SPE with a higher molecular weight. The discharge capacity decreases from to 110 mAh g^{-1} to 97 mAh g^{-1} after 40 cycles (capacity retention of 89 %). This

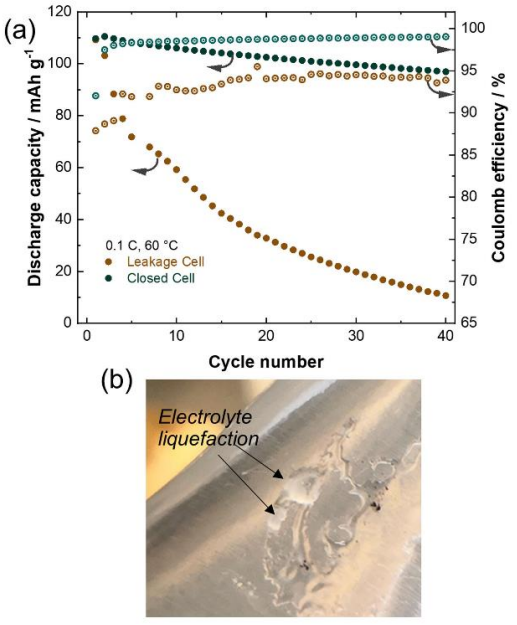

Figure 4. (a) Discharge capacity and Coulomb efficiency as function cycle number of "closed" and "leakage" Li | PEO-LiTFSI | $LiCoO_2$/PEO-LiTFSI/PVDF/Super P cells within a voltage range of 3.0–4.2 V vs. Li^+/Li at 0.1 C and 60 °C using PEO with $M_w = 8000000\ g\,mol^{-1}$. (b) Residues of liquefied electrolyte on the pouch bag walls obtained from cells with leakage after electrochemical cycling.

capacity fading is in good agreement with the data presented by Wang et al.[25] using similar cycling parameters. In contrast, the data of Qiu et al.[10] show a discharge capacity of less than 5 mAh g^{-1} after 10 cycles (capacity retention of 5 %), which is significantly different from the data demonstrated in this study and by Wang et al..[25] One reason for this large difference in capacity fading can be failures in the experimental setup, which can be easily overlooked. We have found that, for example, unexpected leakage in the cell during cell operation significantly affects electrochemical cycle performance. So, we built cells that were intentionally not properly sealed leading to constant exposure to air and moisture during cell operation. In the following, the properly closed cell is denoted as "closed cell" and the other with intentional leakage as "leakage cell". In Figure 4a, the discharge capacity of the leakage cell after 40 cycles is 11.3 mAh g^{-1} (capacity retention of 10 %), which is significantly worse than that of the closed cell. Of course, this is to be expected, since the lithium metal anode is sensitive to air and moisture.[35] Interestingly, the cycle performance of the leakage cell correspond well to the data by Qiu et al.[10] Hence, the reason for the significant differences in cycle performance cannot be fully clarified. However, these results highlight that easily overlooked inaccuracies in the experimental setup can affect the cycling performance and lead to misinterpretation of data. In addition, after disassembling the leakage cells after cycling of PEO with M_w = 8000000 g mol^{-1} in air, we found a liquid-like polymer film inside the pouch bag as shown in Figure 4b. These liquid-like polymer residues were never obtained in closed cells after cycling. Thus, we assume a swelling process of the SPE due to moisture in the atmosphere. Interestingly, such liquid phase has already been observed in literature by Nie et al.[20] reporting the presence of liquid residues after cycling to high voltages, but not relating this to potential cell leakage.

However, because Nie et al. charged their cells to 4.6 V vs. Li$^+$/Li, which significantly extends the electrochemical stability window of LCO,[36,37] a direct comparison with our study is difficult (cells were only cycled to 4.2 V vs. Li$^+$/Li in our study). We examined the liquid-like polymer residues by nuclear magnetic resonance (NMR) spectroscopy. The spectrum obtained is shown in S3 and reveals degradation products that we attribute to the decomposition of SPE by caused by cell leakage and entrance of atmospheric gas. The degradation mechanism in cells with leakage is beyond the scope of this work, but is an interesting issue as the consequences for cell failure may be severe.

Overall, we suggest that the observation of liquid phases of the SPE may indicate cell leakage or residual moisture in the cell. We further note that SPE liquefaction due to leakage in the cell will further accelerate the short-circuit behavior and failure of the cell (c.f. above).

To investigate possible degradation of PEO-based SPEs in high-voltage cathode composites, post mortem Fourier transform infrared (FTIR) spectroscopy was carried out, which is commonly used in this context in literature.[38,10,18] We like to note that FTIR is not spatially resolving, so any information is averaged over the cathode composite. Spatially resolved information was additionally observed by XPS, see below. For the FTIR analysis, samples of the SPE were collected after electrochemical cycling. To ensure reliability and reproducibility of the data, three different spots were measured, obtaining consistent results. Special care was taken to examine electrolyte residues from the vicinity of the cathode/SPE interface, since oxidative processes are to be expected there according to literature.[38,18,10,16] In Figure 5a, FTIR spectra of the pristine PEO-based SPE and the SPE after 40 cycles with LCO are shown. The spectra agree very well, suggesting that no decomposition products were formed by electrochemical cycling of PEO-based SPEs with high-voltage cathodes we formed. In contrast, according to Qiu et al.[10] two additional peaks after electrochemical cycling would be expected in the spectral region between 1750 cm^{-1} and 1600 cm^{-1} which correspond to the C=O stretching mode assigned to the carbonyl functional groups of aldehyde, ketone or ester species, indicating oxidative decomposition processes of the SPE.[39] However, these oxidative decomposition products are absent in our study, as shown in Figure 5b. This is in good agreement with the observations of Seidl et al.[18] and Ma et al.,[38] who also did not report the presence of carbonyl groups after cycling the SPE with NCM or LCO. The latter one was cycled even to higher voltage (4.5 V vs. Li$^+$/Li). Interestingly, after analysis of the cells with leakage (see above) we indeed found these C=O functional groups, as presented in Figure 5b. This indicates that cell leakage can lead to undesirable oxidative decomposition reactions that can easily be mistakenly associated with high-voltage degradation. A formation mechanism for these oxidized species under the influence of moisture and air in the atmosphere is beyond the scope of this work. However, according to our FTIR data, they do not form in appropriately assembled and closed PEO-based cells after electrochemical cycling to higher voltages. Therefore, utmost care must be taken during preparation of cells to avoid any residual moisture or leakage that would cause such rapid degradation.

In addition, post-mortem FTIR analysis was performed with PEO-based SPE which was cycled with NCM for 25 cycles between 3.0–4.3 V vs. Li$^+$/Li at 60 °C and 0.1 C. Consistent with previous results, no C=O functional groups were obtained (see Figure S4). The FTIR spectra of the pristine PEO-based SPE and cycled SPE are presented in Figure 5c. Upon closer inspection, some changes in the entire FTIR spectrum were observed after electrochemical cycling, some of which are comparable to the results of Seidl et al.[18] and Ma et al..[38] According to Seidl et al.[18] and Ma et al.,[38] these changes were attributed to the decomposition of the SPE, in particular to chemical changes of the conducting salt.[38,18] In this context, we prepared an additional sample of the pristine SPE and measured a FTIR spectrum after heating to 70 °C, which is shown in red in Figure 5c. Interestingly, the FTIR spectrum of the pristine SPE after heating to 70 °C corresponds very well with the cycled sample. This suggests that mentioned position shifts and intensity differences are not caused by electrochemical cycling to higher voltage but by heat treatment. In the spectral range of 1200–1000 cm^{-1} the crystalline phase is

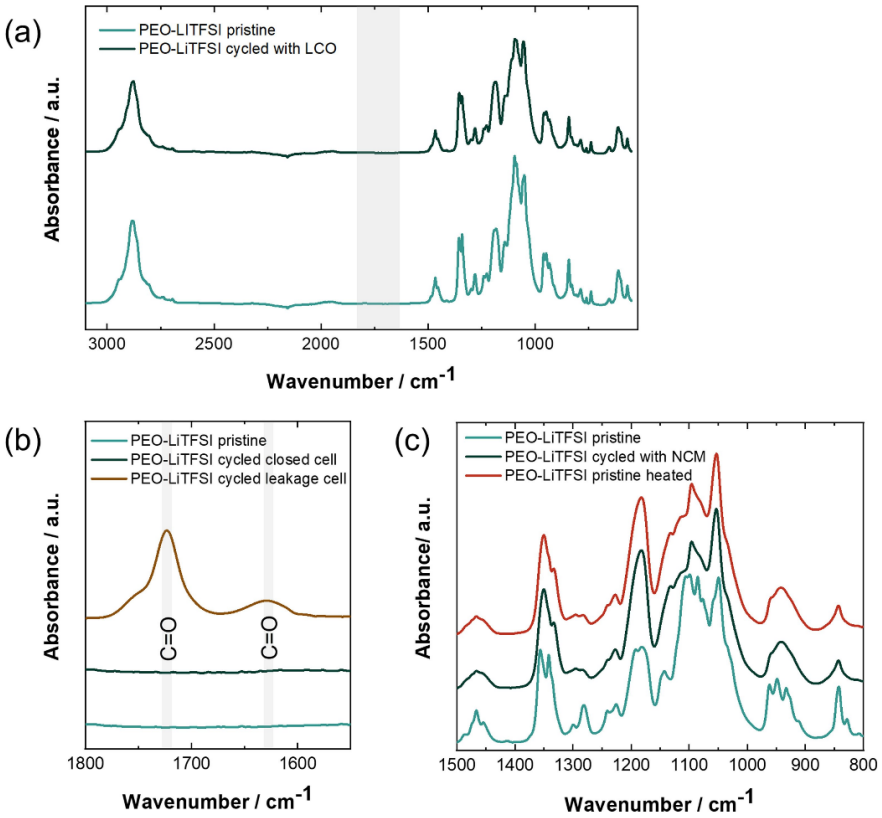

Figure 5. FTIR spectra of PEO-based SPE before and after electrochemical cycling. (a), (b) Cells were cycled with LCO within a voltage range of 3.0–4.2 V vs. Li^+/Li at 0.1 C and 60 °C for 40 cycles using PEO with $M_w = 8\,000\,000\ g\,mol^{-1}$. (c) Cells were cycled with NCM within a voltage range of 3.0–4.3 V vs. Li^+/Li at 0.1 C and 80 °C for 25 cycles using PEO with $M_w = 300\,000\ g\,mol^{-1}$. A spacer for stable cycling operation was used.

featured by the characteristic peaks at 1142, 1091 and 1053 cm^{-1} that mainly correspond to symmetric and asymmetric C–O–C stretching vibrational modes of PEO, which is well documented in literature.[40–42] If PEO is now heated to 70 °C, the fraction of crystalline phase is reduced and the amorphous fraction increases. Interestingly, the corresponding temperature-dependent spectra of pure PEO in the range between 1400 and 800 cm^{-1} as shown by Dissanayake et al.[43] are fully consistent with our SPE data before and after heating. Therefore, the observed changes in FTIR are not caused by any cycling-induced degradation of the PEO, but rather an effect of temperature. We further note that these changes were not seen in the FTIR spectrum in Figure 5a, since a SPE based on higher molecular weight was used, which has a higher tendency for crystallization (c.f. above).

Since FTIR is not a surface-sensitive technique[44] and only offers spatially average information, we also investigated the NCM/SPE interface with X-ray photoelectron spectroscopy (XPS) to identify possible decomposition products near the interface. Therefore, the PEO-based SSBs were assembled and charged to 4.1 V or 4.3 V vs. Li^+/Li. After these potentials were hold for 45 h, the cells were discharged, the aluminum current collector was carefully removed. Accordingly, XP spectra were collected at the surface oriented towards the aluminum current collector. In Figure 6 the peaks at 532.7 eV and 528.7 eV in the O 1s spectra can be assigned to the C–O bonds of PEO[18] and the lattice oxygen in NCM,[45] according to literature. While no changes in the O 1s spectra of the OCV and 4.1 V cell can be seen, a new signal at 531.1 eV, corresponding to the C=O group, is detected in the spectrum of the 4.3 V cell. This is in good agreement with previous XPS investigations.[46,47] In addition, in the C 1s spectra the peaks at 286.6 eV and 284.8 eV can be assigned to C–O and C–C/C–H bonds, respectively. In agreement with the O 1s spectra, the formation of the C=O bond at 288.4 eV is seen in the C 1s spectra of the 4.3 V cell.

Overall, these data show that there is indeed oxidative degradation of PEO at the interface to the active material that cannot be detected by FTIR. This means that the interfacial instability at the cathode side needs to be considered, and we believe that these oxidative degradation products might indeed lead to fast capacity fading in PEO-based SSBs with high voltage cathodes (Figure 3).

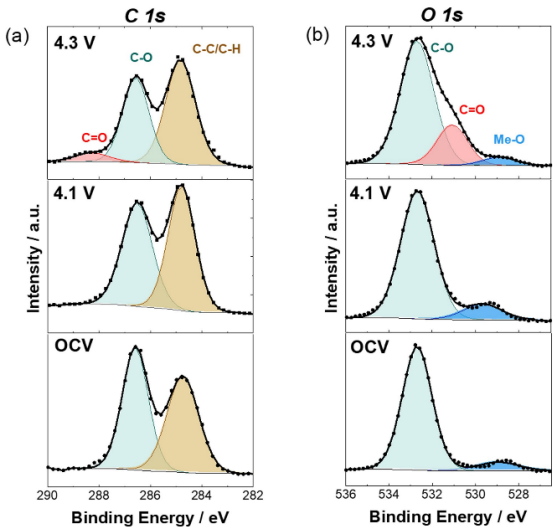

Figure 6. Post-mortem XPS analysis of the SPE/NCM interface using PEO with $M_w = 8\,000\,000\ g\,mol^{-1}$. (a) C 1s spectra and (b) O 1s spectra are shown. The cells were hold at OCV, at 4.1 V or 4.3 V vs. Li^+/Li for 45 h. Surface oriented towards the aluminum current collector was examined with XPS.

Nevertheless, the results obtained to this point suggest that the failure of the SPE cell is an interplay of dendrite growth on the anode side and additional oxidative degradation on the cathode side. However, the effects of oxidative degradation at the interface with the cathode active material do not appear to be as severe as previously reported in the literature. Still, further studies on the PEO/NCM interface for a deeper understanding are needed.

Conclusion

In this study, the compatibility of PEO-based SSBs in combination with high-voltage cathodes is critically evaluated and improved. The hypothesis of the formation of lithium dendrites associated with the failure of high-voltage cells, indicated by "voltage noise" behavior during galvanostatic charging, is confirmed by detection of reaction products of lithium dendrites with LATP. To overcome this failure, an SPE with a higher molecular weight PEO was used, which improved the mechanical rigidity of the SPE and enabled reasonable cycling performance with NCM compared to low molecular weight PEO. Furthermore, we show that often overlooked effects, such as cell leakage and elevated temperatures during cycling, can easily lead to incorrect conclusions about the oxidative degradation of the PEO, when FTIR is used as an analytical technique. Using a more surface sensitive technique like XPS, we demonstrate the formation of oxidative degradation products at the SPE/NCM interface unequivocally. The detailed investigation of this interface degradation and its influence on cell performance, depending on the specific cathode active material and cell voltage will be elucidated in further studies.

Acknowledgements

The authors would like to acknowledge the financial support from the Federal Ministry of Education and Research (BMBF) within the FestBatt II project (03XP0433D and 03XP0429B). D.B. and S.P. would like to thank moreover the Helmholtz Association for the basic funding. A.H. would like to thank the "Professorinnenprogramm III" funded by BMBF. Open Access funding enabled and organized by Projekt DEAL.

Conflict of Interest

The authors declare no conflict of interest.

Data Availability Statement

The data that support the findings of this study are available from the corresponding author upon reasonable request.

Keywords: Cell Failure · High Voltage Cathodes · Interface Stability · Poly(ethylene Oxide) · Solid-State Batteries

[1] J. Janek, W. G. Zeier, *Nat. Energy* **2016**, *1*, 16141.
[2] Y. Kato, S. Hori, T. Saito, K. Suzuki, M. Hirayama, A. Mitsui, M. Yonemura, H. Iba, R. Kanno, *Nat. Energy* **2016**, *1*, 16030.
[3] G. E. Blomgren, *J. Electrochem. Soc.* **2017**, *164*, A5019–A5025.
[4] T. Krauskopf, F. H. Richter, W. G. Zeier, J. Janek, *Chem. Rev.* **2020**, *120*, 7745.
[5] P. Yao, H. Yu, Z. Ding, Y. Liu, J. Lu, M. Lavorgna, J. Wu, X. Liu, *Front. Chem.* **2019**, *7*, 522.
[6] A. Kim, S. Woo, M. Kang, H. Park, B. Kang, *Front. Chem.* **2020**, *8*, 468.
[7] D. Park, H. Park, Y. Lee, S.-O. Kim, H.-G. Jung, K. Yoon Chung, J. Hyung Shim, S. Yu, *ACS Appl. Mater. Interfaces* **2020**, *12*, 34806.
[8] S. S. Berbano, M. Mirsaneh, M. T. Lanagan, C. A. Randall, *Int. J. Appl. Glass Sci.* **2013**, *4*, 414.
[9] A. Varzi, R. Raccichini, S. Passerini, B. Scrosati, *J. Mater. Chem. A* **2016**, *4*, 17251.
[10] J. Qiu, X. Liu, R. Chen, Q. Li, Y. Wang, P. Chen, L. Gan, S. -J Lee, D. Nordlund, Y. Liu, X. Yu, X. Bai, H. Li, L. Chen, *Adv. Funct. Mater.* **2020**, *30*, 1909392.
[11] R. Chen, Q. Li, X. Yu, L. Chen, H. Li, *Chem. Rev.* **2020**, *120*, 6820.
[12] Z. Xue, D. He, X. Xie, *J. Mater. Chem. A* **2015**, *3*, 19218.
[13] J. Ravi Nair, L. Imholt, G. Brunklaus, M. Winter, *Electrochem. Soc. Interface* **2019**, *28*, 55.
[14] A. Maurel, M. Armand, S. Grugeon, B. Fleutot, C. Davoisne, H. Tortajada, M. Courty, S. Panier, L. Dupont, *J. Electrochem. Soc.* **2020**, *167*, 070536.
[15] T. Kobayashi, Y. Kobayashi, M. Tabuchi, K. Shono, Y. Ohno, Y. Mita, H. Miyashiro, *ACS Appl. Mater. Interfaces* **2013**, *5*, 12387.

[16] J. Liang, Y. Sun, Y. Zhao, Q. Sun, J. Luo, F. Zhao, X. Lin, X. Li, R. Li, L. Zhang, S. Lu, H. Huang, X. Sun, *J. Mater. Chem. A* **2020**, *8*, 2769.
[17] Z. Chen, G.-T. Kim, Z. Wang, D. Bresser, B. Qin, D. Geiger, U. Kaiser, X. Wang, Z. Xiang Shen, S. Passerini, *Nano Energy* **2019**, *64*, 103986.
[18] L. Seidl, R. Grissa, L. Zhang, S. Trabesinger, C. Battaglia, *Adv. Mater. Interfaces* **2022**, *9*, 2100704.
[19] Y. Xia, T. Fujieda, K. Tatsumi, P. Paolo Prosini, T. Sakai, *J. Power Sources* **2001**, *92*, 234.
[20] K. Nie, X. Wang, J. Qiu, Y. Wang, Q. Yang, J. Xu, X. Yu, H. Li, X. Huang, L. Chen, *ACS Energy Lett.* **2020**, *5*, 826.
[21] G. Homann, L. Stolz, J. Nair, I. Cekic Laskovic, M. Winter, J. Kasnatscheew, *Sci. Rep.* **2020**, *10*, 4390.
[22] G. Hernández, I. L. Johansson, A. Mathew, C. Sångeland, D. Brandell, J. Mindemark, *J. Electrochem. Soc.* **2021**, *168*, 100523.
[23] E. Simonetti, M. Carewska, M. Di Carli, M. Moreno, M. de Francesco, G. B. Appetecchi, *Electrochim. Acta* **2017**, *235*, 323.
[24] G. Homann, L. Stolz, K. Neuhaus, M. Winter, J. Kasnatscheew, *Adv. Funct. Mater.* **2020**, *30*, 2006289.
[25] C. Wang, T. Wang, L. Wang, Z. Hu, Z. Cui, J. Li, S. Dong, X. Zhou, G. Cui, *Adv. Sci.* **2019**, *6*, 1901036.
[26] K. Matsumoto, K. Inoue, K. Nakahara, R. Yuge, T. Noguchi, K. Utsugi, *J. Power Sources* **2013**, *231*, 234.
[27] M. Nakayama, S. Wada, S. Kuroki, M. Nogami, *Energy Environ. Sci.* **2010**, *3*, 1995.
[28] H.-K. Tian, R. Jalem, B. Gao, Y. Yamamoto, S. Muto, M. Sakakura, Y. Iriyama, Y. Tateyama, *ACS Appl. Mater. Interfaces* **2020**, *12*, 54752.
[29] Y. Zhu, X. He, Y. Mo, *ACS Appl. Mater. Interfaces* **2015**, *7*, 23685.
[30] Q. Cheng, A. Li, N. Li, S. Li, A. Zangiabadi, T.-D. Li, W. Huang, A. Ceng Li, T. Jin, Q. Song, W. Xu, N. Ni, H. Zhai, M. Dontigny, K. Zaghib, X. Chuan, D. Su, K. Yan, Y. Yang, *Joule* **2019**, *3*, 1510.
[31] A. Gupta, E. Kazyak, N. Craig, J. Christensen, N. P. Dasgupta, J. Sakamoto, *J. Electrochem. Soc.* **2018**, *165*, A2801–A2806.
[32] L. Stolz, G. Homann, M. Winter, J. Kasnatscheew, *Mater. Adv.* **2021**, *2*, 3251.
[33] C. Wang, Y. Yang, X. Liu, H. Zhong, H. Xu, Z. Xu, H. Shao, F. Ding, *ACS Appl. Mater. Interfaces* **2017**, *9*, 13694.
[34] D. Devaux, R. Bouchet, D. Glé, R. Denoyel, *Solid State Ionics* **2012**, *227*, 119.
[35] M. H. Cho, J. Trottier, C. Gagnon, P. Hovington, D. Clément, A. Vijh, C.-S. Kim, A. Guerfi, R. Black, L. Nazar, K. Zaghib, *J. Power Sources* **2014**, *268*, 565.
[36] L. Wang, B. Chen, J. Ma, G. Cui, L. Chen, *Chem. Soc. Rev.* **2018**, *47*, 6505.
[37] S. Song, X. Peng, K. Huang, H. Zhang, F. Wu, Y. Xiang, X. Zhang, *Nanoscale Res. Lett.* **2020**, *15*, 110.
[38] J. Ma, Z. Liu, B. Chen, L. Wang, L. Yue, H. Liu, J. Zhang, Z. Liu, G. Cui, *J. Electrochem. Soc.* **2017**, *164*, A3454–A3461.
[39] D. J. Lyman, R. Benck, S. Dell, S. Merle, J. Murray-Wijelath, *J. Agric. Food Chem.* **2003**, *51*, 3268.
[40] L. H. Sim, S. N. Gan, C. H. Chan, R. Yahya, *Spectrochim. Acta Part A* **2010**, *76*, 287.
[41] K. K. Kumar, M. Ravi, Y. Pavani, S. Bhavani, A. K. Sharma, V. V. R. N. Rao, *J. Non-Cryst. Solids* **2012**, *358*, 3205.
[42] H. T. Ahmed, O. Gh Abdullah, *Polymers* **2019**, *11*, 853.
[43] M. A. K. L. Dissanayake, R. Frech, *Macromolecules* **1995**, *28*, 5312.
[44] L.-L. I. Fockaert, D. Ganzinga-Jurg, J. Versluis, B. Boelen, H. J. Bakker, H. Terryn, J. M. C. Mol, *J. Phys. Chem. C* **2020**, *124*, 7127.
[45] R. Li, Y. Ming, W. Xiang, C. Xu, G. Feng, Y. Li, Y. Chen, Z. Wu, B. Zhong, X. Guo, *RSC Adv.* **2019**, *9*, 36849.
[46] J. Li, Y. Ji, H. Song, S. Chen, S. Ding, B. Zhang, L. Yang, Y. Song, F. Pan, *Nano-Micro Lett.* **2022**, *14*, 191.
[47] J. Liang, D. Chen, K. Adair, Q. Sun, N. Graham Holmes, Y. Zhao, Y. Sun, J. Luo, R. Li, L. Zhang, S. Zhao, S. Lu, H. Huang, X. Zhang, C. Veer Singh, X. Sun, *Adv. Energy Mater.* **2021**, *11*, 2002455.

Manuscript received: December 13, 2022
Accepted manuscript online: January 10, 2023
Version of record online: ■■, ■■

3.2 Publication II

Investigation of the Stability of the Poly(ethylene oxide)|$LiNi_{1-x-y}Co_xMn_yO_2$ Interface in Solid-State Batteries

In the second publication[38], the interface between PEO-LiTFSI and NCM was investigated in detail. In order to unambiguously assess the resistance contribution of the PEO-LiTFSI/NCM interface, EIS measurements were conducted in a three-electrode setup. The results confirmed that the NCM/PEO interface is strongly degrading at high voltages. In this regard, the interfacial stability on the cathode side depends not only on the applied potential, but also on the molecular weight of PEO. Both aspects are significantly affecting the cell performance. In addition, SEM images demonstrate that the pores of the cathode are filled by the SPE after cycling to high potentials. Accordingly, this indicates that the electrochemical degradation of the SPE is accompanied by the mechanical degradation, leading to a decrease in viscosity of the SPE.

Overall, the results provide new insights into the detrimental processes occurring in PEO-based SSBs in combination with high-voltage cathodes. Additionally, it is important to note that the results unequivocally demonstrate that the PEO-based SPE is degrading with high-voltage cathodes.

The experiments for this work were designed and performed by the first author under the supervision of A. Henss and J. Janek. D. F. Hunstock assisted with the experimental work. A. Mayer, D. Bresser and S. Passerini supported in the validation of the data. All authors contributed to the scientific discussion. The manuscript was written by the first author and edited by all other authors.

Reprinted from Y. Yusim, D. F. Hunstock, A. Mayer, D. Bresser, S. Passerini, J. Janek, A. Henss, *Adv. Mater. Interfaces* **2023**, 2300532. DOI: 10.1002/admi.202300532.

RESEARCH ARTICLE

ADVANCED MATERIALS INTERFACES Open Access

www.advmatinterfaces.de

Investigation of the Stability of the Poly(ethylene oxide)|$LiNi_{1-x-y}Co_xMn_yO_2$ Interface in Solid-State Batteries

Yuriy Yusim, Dirk F. Hunstock, Alexander Mayer, Dominic Bresser, Stefano Passerini, Jürgen Janek, and Anja Henss**

While solid-state batteries (SSBs) comprising poly(ethylene oxide) (PEO) based electrolytes are successfully commercialized already for operation at elevated temperature, the selection of the cathode active material (CAM) has so far been limited to $LiFePO_4$. When using high-voltage CAMs such as $LiNi_{1-x-y}Co_xMn_yO_2$ (NCM), the cells experience fast capacity fading – the cause of which is not consistently understood in literature. In this study, electrochemical impedance spectroscopy measurements in a three-electrode setup are applied to confirm that the NCM|PEO interface is indeed the Achilles' heel in PEO-based SSBs at high voltages. In this regard, the interfacial stability on the cathode side depends not only on the upper cut-off voltage, but also on the molecular weight of PEO, strongly affecting the cell performance. Scanning electron microscopy images of the cathodes after cycling suggest that at high voltages interfacial degradation leads to fragmentation of the polymer backbone and to a decrease in viscosity of the solid polymer electrolyte. Overall, the results help to understand the detrimental processes occurring in PEO-based SSBs in combination with high-voltage cathodes.

1. Introduction

Conventional state-of-the-art lithium-ion batteries (LIBs) with a liquid electrolyte are expected to reach their limits in terms of energy density.[1] However, the demand for batteries with even higher energy densities is increasing, mainly driven by the electrification of the transportation sector. To meet these demands, solid-state batteries (SSBs) have been regarded as one of the most promising next-generation energy storage devices.[1–3] The replacement of liquid electrolytes in LIBs by solid electrolytes (SEs) is, amongst others, motivated by the transition to high-capacity lithium-metal anodes, eventually leading to higher energy densities.[1] A large variety of SEs is currently investigated for the use in SSBs. Among all classes of SEs, that is, polymer-,[4] oxide-,[5] sulfide-[5] and halide-based[6] SEs, only solid polymer electrolytes (SPEs) based on poly(ethylene oxide) (PEO) with lithium bis(trifluoromethanesulfonyl)imide (LiTFSI) as conducting salt were successfully commercialized so far, which has been achieved by Blue Solutions (Bolloré Group) in 2012 using $LiFePO_4$ (LFP) as the cathode active material (CAM).[7] In addition to their moderate ionic conductivity at elevated temperatures (≈1 mS cm^{-1} at 80 °C),[8] further advantages of PEO-based-SPEs for their application in SSBs include low cost and their malleable nature, which allows good interfacial contact to the electrode active materials.[9]

Nevertheless, there are remaining challenges on the way to higher performance that must be addressed such as substituting the currently utilized low-voltage LFP by high-voltage CAMs such as (Ni-rich) $LiNi_{1-x-y}Co_xMn_yO_2$ (NCM) to achieve significantly higher energy densities, which results in rapid capacity fading. The processes occurring at the interface between the PEO-based

Y. Yusim, D. F. Hunstock, J. Janek, A. Henss
Institute of Physical Chemistry
Justus Liebig University Giessen
Heinrich-Buff-Ring 17, 35392 Giessen, Germany
E-mail: juergen.janek@phys.chemie.uni-giessen.de;
anja.henss@phys.chemie.uni-giessen.de

The ORCID identification number(s) for the author(s) of this article can be found under https://doi.org/10.1002/admi.202300532

DOI: 10.1002/admi.202300532

Y. Yusim, D. F. Hunstock, J. Janek, A. Henss
Center for Materials Research (ZfM/LaMa)
Justus Liebig University Giessen
Heinrich-Buff-Ring 16, 35392 Giessen, Germany

A. Mayer, D. Bresser, S. Passerini
Helmholtz Institute Ulm (HIU)
Helmholtzstraße 11, 89081 Ulm, Germany

A. Mayer, D. Bresser, S. Passerini
Karlsruhe Institute of Technology (KIT)
P.O. Box 3640, 76021 Karlsruhe, Germany

S. Passerini
Department of Chemistry
Sapienza University of Rome
P. Aldo Moro 5, Rome 00185, Italy

ADVANCED SCIENCE NEWS
www.advancedsciencenews.com

ADVANCED MATERIALS INTERFACES
Open Access
www.advmatinterfaces.de

SE and NCM, however, are not yet well understood.[10] Different decomposition and failure mechanisms with high-voltage cathodes (NCM, $LiCoO_2$) have been discussed in literature so far, which are briefly outlined in the following: Some studies found that oxidative electrolyte degradation is the main mechanism for battery failure, as concluded from a gradual thinning of the SPE layer and gas generation during cycling.[11,12] Other studies emphasized the crucial role of the conducting salt, suggesting the generation of bis(trifluoromethanesulfonyl)imide acid (HTFSI), which in turn chemically decomposes PEO.[12–14] Additional studies revealed that oxygen release from the CAMs also acts as further ingredient for PEO decomposition.[15,16] In contrast, other studies suggested that the primary oxidation onset of PEO-LiTFSI occurs only above 4.6 V versus Li^+/Li, irrespective of the CAM's structure and chemical composition, or the molecular weight of the PEO used.[17,18] To address the obvious inconsistencies in literature regarding the capacity decay of PEO-based SSBs and gain a deeper understanding of the degradation mechanism(s), it is crucial to conduct additional studies on the stability of the PEO-LiTFSI|NCM interface. In fact, in order to enable the commercialization of PEO-based SSBs with Ni-rich cathodes, it is essential to overcome these challenges by developing a full understanding of the degradation mechanisms and developing mitigation strategies.

In this study, we conducted a comprehensive EIS investigation in a three-electrode setup to unequivocally separate the impedance contributions from the cathode and anode side. This allowed us to study the interfacial degradation kinetics and to identify the interface at the cathode side as bottleneck for PEO-based SSBs at high voltages. The results demonstrate that the interfacial stability between NCM and PEO-LiTFSI is influenced by both the applied potential and the molecular weight of the PEO-based SPE. SEM images reveal that the morphology and mechanical properties of PEO change due to the degradation at high potentials, leading to a reduction in viscosity for high molecular weight PEO due to polymer chain cleavage.

2. Results and Discussion

The results section of this work is divided into two parts. First, we focus on the electrochemical characterization of the degradation of PEO-based SPEs at various cut-off voltages. In the second part, we shift our attention to the morphological changes of the SPE occurring in the cathode during cycling to different cut-offs.

2.1. Electrochemical Investigation of the PEO-LiTFSI|NCM Interface

Electrochemical imedance spectroscopy (EIS) is a non-destructive method to monitor the effects of degradation processes occurring in a battery cell.[19] However, the assignment of features in the impedance spectra to single battery cell components can be difficult, since the impedance processes at the anode overlap with the impedance processes at the cathode in PEO-based SSBs, as they occur at similar time constants, as shown by Wurster et al.[20] To separate the contributions of the cathode and the anode, we prepared a cell with a μ-reference

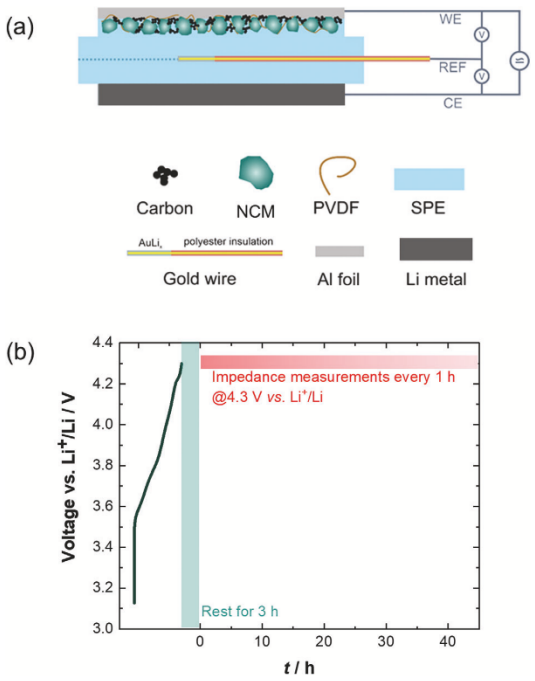

Figure 1. a) Schematic of the three-electrode setup to distinguish between the anode and cathode impedance contributions. b) The utilized testing procedure including an initial charge step prior to the constant potential step along with the continuous impedance measurements.

electrode (three-electrode setup (3P)), as shown in **Figure 1**a. The point-like reference electrode was placed centrally between two PEO separators (M_w = 8 000 000 g mol^{-1})[21] and was lithiated in situ in the fully assembled cell. After the cell was charged to 4.3 V versus Li^+/Li with a dis-/charge rate of 0.15 C, impedance spectra were collected continuously every hour while holding the potential at 4.3 V versus Li^+/Li to monitor the impedance growth during the operation and/or storage of batteries in high-voltage conditions (charged state). Figure 1b shows a scheme of the measuring procedure used in this study, which is similar to that presented by Kumakura[22] from Umicore N.V. at the International Battery Association (IBA) conference in 2022, where the current was measured at different elevated potentials. Nevertheless, to the best of our knowledge the 3P-setup has never been applied to study the impedance in PEO-based SSBs with high-voltage cathodes. The three-electrode cell offers a distinct advantage by allowing the acquisition of not only the whole cell impedance, as achievable with a two-electrode cell, but also enabling the examination of impedance spectra for the individual anode and cathode half-cells.

Figure 2 illustrates the impedance spectra acquired from the three-electrode cell, showcasing a more comprehensive understanding of the full cell's impedance characteristics. Thereby, the separated cathode and anode half-cell impedance spectra are compared with the spectrum of the full cell after 1 h (Figure 2a) and 45 h (Figure 2b) at 4.3 V. Interestingly, the cathode and the

ADVANCED SCIENCE NEWS
www.advancedsciencenews.com

ADVANCED MATERIALS INTERFACES Open Access
www.advmatinterfaces.de

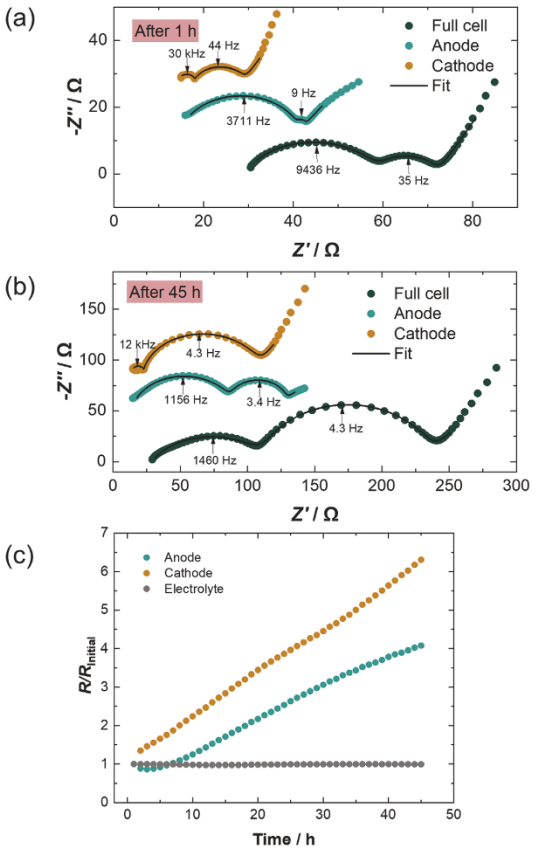

Figure 2. Impedance measurements of a 3P-PEO-based SSB with NCM. Impedance spectra of full cell, cathode half-cell, and anode half-cell a) after 1 h and b) after 45 h at 4.3 V versus Li^+/Li. c) Anode and cathode interface resistance as well as the electrolyte resistance as function of time. Resistances were normalized to their initial values for better comparison. The equivalent circuit is shown in Figure S2 (Supporting Information).

anode half-cell impedance data, as well as the impedance data of the full cell, after 1 h and after 45 h each exhibit two semicircles (the detailed assignment of impedance features to specific physical/electrochemical processes is given below). The analysis of the Distribution of Relaxation Times (DRT) confirms the presence of two main impedance contributions at low and high frequencies (see Figure S1, Supporting Information).

Since the different impedance contributions of anode and cathode have quite close time constants, the differentiation of features from the anode and cathode side from the impedance spectra of cells with only two electrodes is not reliable. Accordingly, a setup with three electrodes is essential and necessary to study the impedance evolution and to understand the reactivity and the degradation kinetics of the individual electrodes. For a quantitative comparison of the impedance contributions, the spectra were fitted using the equivalent circuit shown in Figure S2 (Supporting Information). Subsequently, the total resistance at the cathode and anode side was determined (sum of the two semicircles) and normalized to the initial impedance after 1 h for better comparability of the impedance evolution. In Figure 2c, we find that the resistance values in the anode and cathode half-cells increase significantly during constant voltage holding, which indicates the occurrence of reactions at the Li|PEO-LiTFSI anode and PEO-LiTFSI|NCM cathode interface. The growth rate of the resistance is significantly higher for the PEO-LiTFSI|NCM interface, which confirms that at high potentials the growth of the cathode impedance is dominating. We note that the increase in impedance at the Li|PEO-LiTFSI interface might also (in part) be related to so-called "cross-talk" phenomena,[12] but this is beyond the scope of this study, which focuses on the reactions occurring at the PEO-LiTFSI|NCM interface. However, we refer to extensive work on the Li metal anode interface with PEO electrolytes, in which it was reported, that the middle to high-frequency domain (10^5–10^2 Hz)[23] in the impedance spectra can be attributed to the solid electrolyte interphase (SEI) formed between lithium metal and the SPE, and a lower frequency domain (10^2–0.1 Hz) corresponds to the charge transfer resistance.[24] Both impedance contributions are present in this study. Under static conditions in symmetric Li|SPE|Li cells, a parabolic growth of the SEI between Li and PEO is expected during ageing,[24] which is not clearly observed in this study (see Figure 2c). This may be due to the fact of lithium plating (dynamic conditions) before the EIS measurement, as the cells were initially charged to 4.3 V. Accordingly, fresh lithium without native passivation layer[25] is deposited on the lithium anode, which is expected to be highly reactive. In this context, it should be noted that the literature on the Li|PEO-LiTFSI interface is often very contradictory. Several authors[26,24,27,28] highlighted the instability of this interface. Their results[29,30] show that the degradation of the SPE at the lithium anode leads to the formation Li-O-R and LiF compounds. Other studies[31] demonstrated that this interfacial degradation is dominated by the reaction of the residual water in the SPE, which leads to the formation of LiOH and Li_2O. We will follow these interesting anode observations in a forthcoming study applying advanced analytical techniques.

The obtained impedance data confirm that more resistive processes occur at the PEO-LiTFSI|NCM interface. Moreover, the data demonstrate no significant change of the total electrolyte resistance, which was also reported by Li et al.[32] (50 cycles with $LiCoO_2$ as CAM). The obtained values of the bulk resistance correspond approximately to the expected conductivity of PEO-based SPE at 80 °C.

As mentioned above, the impedance spectrum displayed in Figure 2 shows two semicircles for the cathode impedance. According to Illig et al.[33] the semicircle at higher frequencies can be assigned to contact resistances between the electrode coating and the current collector, which does not increase significantly after 45 h. However, the low-frequency semicircle, which corresponds to the charge transfer resistance R_{CT} including the resistance of the cathode electrolyte interphase (CEI)[20] is significantly increasing over time *t*. In **Figure 3**, the resistance values for R_{CT} are plotted over time. The gradual impedance growth confirms that interfacial reactions occur at the PEO-LiTFSI|NCM interface. Interestingly, the growth of the CEI does not follow the Wagner model for diffusion-controlled reactions ($R_{CT} \sim \sqrt{t}$), which was observed, for example, at the interface between sulfide-based SEs and CAMs.[34]

ADVANCED SCIENCE NEWS
www.advancedsciencenews.com

ADVANCED MATERIALS INTERFACES
Open Access
www.advmatinterfaces.de

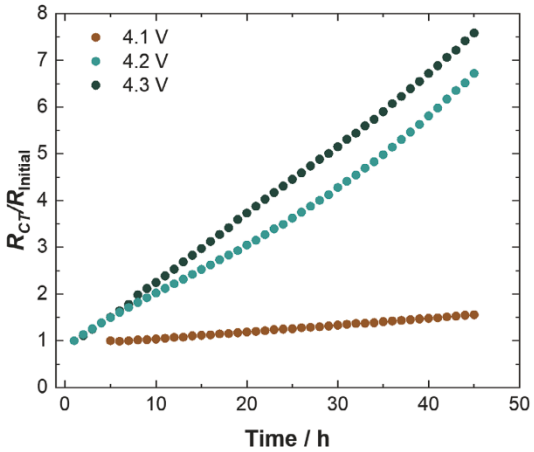

Figure 3. Time-dependent changes of the charge transfer resistance R_{CT} during the constant potential step at 4.1, 4.2, and 4.3 V versus Li^+/Li. The resistances were normalized to their initial values for the sake of comparability.

This rather indicates rate control by the interface reaction itself ($R_{CT} \sim t$).[35]

Subsequently, the experiment shown in Figure 1b was repeated applying different cut-off voltages, that is, the PEO-based cells were charged to 4.1 V and to 4.2 V versus Li^+/Li. The corresponding cathode impedance spectra are presented in Figures S3 and S4 (Supporting Information), respectively. The fitted data displayed in Figure 3 show that the impedance growth depends strongly on the cut-off voltage. In fact, the highest increase in resistance after 45 h is observed for the cell charged to 4.3 V cell (by a factor of 7.6) and the lowest for the cell charged to 4.1 V (by a factor of 1.6), indicating a faster and more pronounced growth of the interphase at elevated potentials. Moreover, there is a significant difference between 4.1 and 4.2 V, which indicates some kind of threshold value in this potential range.

To investigate the impact of the interphase growth on the cathode side, as indicated by the EIS data, on the eventual cycling performance, PEO-comprising full cells in a two-electrode setup were subjected to galvanostatic cycling with different upper cut-off voltages (PEO, $M_w = 8\,000\,000$ g mol^{-1}). **Figure 4**a displays the charge–discharge curves of the first cycle. No "voltage noise" failure associated with dendrite formation can be seen due to use of higher molecular weight PEO, as shown in our previous study.[36]

Please note, that after every charge and discharge step an open-circuit voltage (OCV) step of 2 h was included. The corresponding charge and discharge profiles as function of the cut-off voltage are shown in Figure S5 (Supporting Information). The cells exhibit voltage-dependent charge capacities of 168 mAh g^{-1} (4.1 V), 190 mAh g^{-1} (4.2 V), and 216 mAh g^{-1} (4.3 V). After discharge to 3.0 V, the three cells deliver (reversible) discharge capacities of 158, 181, and 205 mAh g^{-1}. The higher specific capacity indicates that more lithium can be extracted/intercalated, which depends on the cut-off voltage.

The comparison of the cycling stability (Figure 4b) reveals that the cycling stability is inversely proportional to the applied cut-off voltage, especially when increasing it to 4.3 V, which is in line with the larger increase of the charge-transfer resistance. In addition, the average voltages during the discharge process were determined (average voltage = total accumulated voltage in a dataset/number of data points). In good agreement with the cycling stability results, the evolution of the overpotential shows a stronger increase for higher cut-off voltages (Figure 4c).

Consequently, the impedance data in a three-electrode setup and the cycling data confirm that the rate of degradation of PEO-based SEs with NCM cathodes is SOC-dependent, suggesting that the electric potential difference between NCM and PEO-LiTFSI at the cathode side is the driving force for the degradation reaction. To investigate the impact of the SPE properties on the stability of PEO-LiTFSI|NCM interface, PEO-based SPEs with different molecular weights were prepared and the same measuring procedure as shown in Figure 1 was conducted. It should be noted that PEO with M_W of 8 000 000 g mol^{-1} was used as a protective layer for the lithium metal anode in all cells, to prevent dendrite penetration through PEO-based SPE with lower molecular weight that is as shown in previous studies.[36] Accordingly, the molecular weight of the SPE was varied only at the cathode side. The corresponding impedance spectra are shown in Figures S6 and S7 (Supporting Information). The corresponding capacities of the interface at the cathode side are illustrated in Figure S8 (Supporting Information) and are in the order of magnitude of literature values.[37]

The data in Figure 4d confirm that the growth of the charge transfer resistance is inversely correlated with the molecular weight of PEO-based SPE. As a result, the capacity retention significantly improves with an increase in the molecular weight of PEO during galvanostatic cycling, as illustrated in Figure S9 (Supporting Information). This can be explained by the different concentration of terminal hydroxide groups of PEO-based SPE, which are the limiting factor in the electrochemical stability of PEO-based SPEs according to Yang et al.[38] By replacing the —OH group with a more stable —OCH_3 they observed a significant improvement in cycle performance and an extension of the electrochemical stability window from 4.05 to 4.3 V versus Li^+/Li. Accordingly, the concentration of terminal groups is crucial for the growth of charge transfer resistance indicating the growth of a resistive CEI layer. Interestingly, the interfacial degradation kinetics seems to be faster and increasing parabolically, thta is, self-accelerating, for lower molecular weight PEO. A parabolic increase of the cathode charge transfer resistance was already observed by Strehle et al.[39] with liquid-based electrolytes and NCM. Apparently, the degradation reaction is somehow self-catalyzing, which is of course highly critical. While we consider this observation as highly interesting, the detailed mechanism of this kinetics is beyond the scope of this study and will be subject of future studies. In addition, the conducting salt seems to play a role in the oxidative degradation of the SPE. To ensure comparability to other studies, we focused on a fixed concentration of LiTFSI, which is often used in PEO-based SPEs.[18,20,24] However, we intend to vary this parameter systematically in future studies.

Overall, the comprehensive electrochemical investigations provide compelling evidence that the degradation rate of the PEO-LiTFSI|NCM interface is directly influenced by the applied voltage. Notably, within this context, the chemical structure of PEO-based SPEs, especially the concentration of terminal

ADVANCED SCIENCE NEWS
www.advancedsciencenews.com

ADVANCED MATERIALS INTERFACES Open Access
www.advmatinterfaces.de

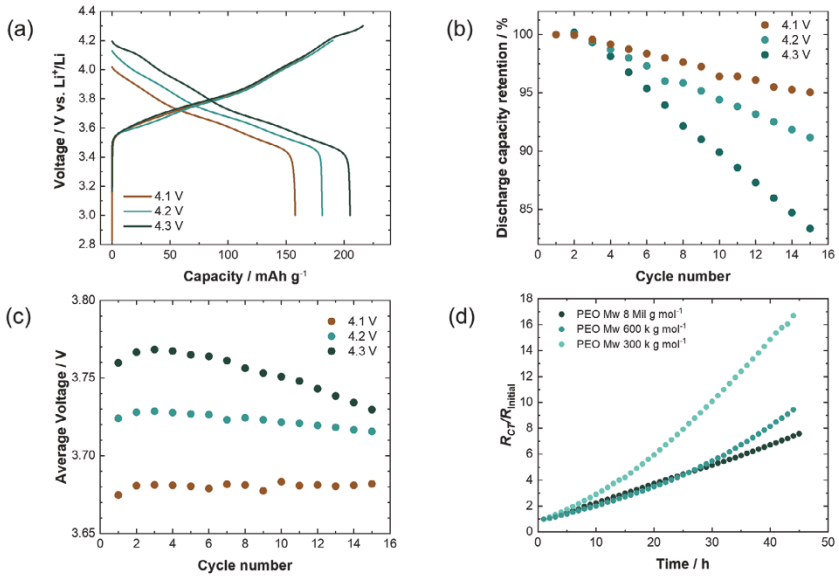

Figure 4. Galvanostatic cycling of Li|PEO-LiTFSI|NCM cells applying different upper cut-off voltages: a) charge and discharge curves of the 1st cycle, b) comparison of the capacity retention over 15 cycles, and c) calculated average discharge voltage over 15 cycles. d) Time-dependent changes of the charge transfer resistance R_{CT} during hold of the potential at 4.3 V of PEO-based SPEs with different molecular weights.

hydroxide groups, seems to be crucial for the interfacial stability and long-term cycle performance with high-voltage cathodes.

2.2. Morphological Investigation of the PEO-LiTFSI|NCM Interface

In addition to the electrochemical investigation, the influence of the applied voltage on the cathode morphology related to the oxidative degradation of PEO-based SPEs was examined using scanning electron microscopy (SEM). For this purpose, SEM measurements were conducted after the PEO-based SSBs were cycled with NCM to different cut-off voltages (4 cycles) and compared to open circuit voltage (OCV) conditions, where the cells were stored at the operation temperature (80 °C) but were not cycled. It is important to note that all cells have the same temperature history (storage at 80 °C for 3 days). As demonstrated in **Figure 5**a,b the cathode morphology of PEO-based SSBs stored at OCV and cycled to 3.6 V versus Li^+/Li are similar. The cathode components seem to be homogenously distributed, however, large pores are present, since the cathodes were not pressed. In contrast, some of these pores seem to be filled by the SPE after cycling to 4.1 V (Figure 5c) and 4.3 V versus Li^+/Li (Figure 5d). Further SEM images are shown in Figure S10 (Supporting Information). The difference between 4.1 and 4.3 V seem to be not significant. The SEM images indicate that the oxidative degradation of PEO-based SPE during electrochemical cycling to high potentials leads to chain cleavage of the polymer chain. Consequently, shorter polymer chains exhibit lower viscosity, which in our case enables the complete infiltration of the cathode pores with the SPE. With regard to the impedance data in Figure 3 and the galvanostatic cycling data in Figure 4, it seems that the decrease in viscosity that already occurs at 4.1 versus Li^+/Li does not result in a high impedance increase. We conclude that other resistive processes occur at 4.3 V versus Li^+/Li in addition to the mere decrease in SPE viscosity. We like to add that according to the time-of-flight secondary ion mass spectrometry (ToF-SIMS) surface spectra in Figure S11 (Supporting Information), the SNO^- and C_2HO^- signals, representing the SPE, are present in all samples at the surface (surface oriented toward the current collector). Accordingly, this indicates that the PEO-based SPE at OCV conditions/cycled to 3.6 V has a sufficiently low viscosity, enabling small amounts of the SPE to infiltrate into the cathode. However, the signal intensity is higher for the cathodes charged to 4.1 and 4.3 V, as shown in Figure S11 (Supporting Information) suggesting a higher fraction of SPE or degraded SPE is present at the surface after cycling to higher potentials, which is consistent with the results from SEM-images. In the corresponding ToF-SIMS spectra, signal intensity of a fragment (y-axis) is presented as a function of its mass-to-charge ratio (x-axis).

In addition, focused ion beam (FIB)-SEM measurements under cryogenic conditions were conducted to investigate the cross-section of the cathodes after cycling. For this experiment thicker electrodes were fabricated and pressed before use. As shown in Figure S12 (Supporting Information), while the cathode before cycling shows empty pores, these are filled after cycling to 4.3 V versus Li^+/Li (4 cycles). Overall, these results indicate that electrochemical degradation of the SPE is accompanied by mechanical degradation, leading to a decrease in viscosity. This decrease in viscosity may explain the observed gradual thinning of the SPE during cycling with high voltage cathodes, as degraded PEO with lower viscosity just exits the cell due to the applied

ADVANCED SCIENCE NEWS
www.advancedsciencenews.com

ADVANCED MATERIALS INTERFACES
Open Access
www.advmatinterfaces.de

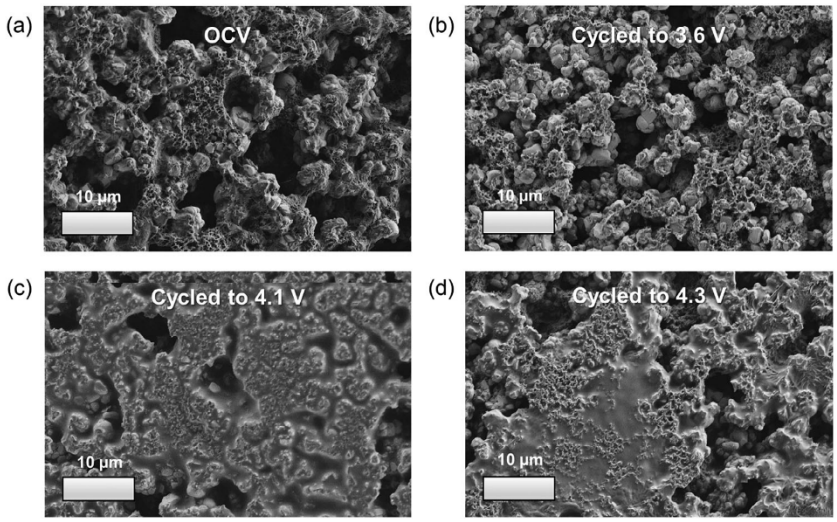

Figure 5. SEM images of cathode surfaces oriented toward the current collector after a) OCV conditions and after cycling to b) 3.6 V, c) 4.1 V, and d) 4.3 V versus Li^+/Li.

pressure and/or fills the pores in the cathode, as reported by Kaboli et al.[11] The results also support previous studies that have extensively described the chemical degradation mechanism of PEO at high voltages,[12,13] attributing the chain cleavage phenomenon to the attack of bis(trifluoromethanesulfonyl)imide acid (HTFSI) on PEO-based SPE. Furthermore, X-ray photoelectron spectroscopy (XPS) has confirmed the formation of ester groups, indicative of oxidized species, in PEO-based SPE after exposure to higher voltages.[32,40,36] Based on our findings and the insights presented in existing literature, we believe that the chain cleavage of PEO-SPE stands as a clear marker for the degradation of the SPE. This degradation process is likely a complete decomposition of the polyether structure leading to novel reaction byproducts. Consequently, these can contribute to a notable reduction in ionic conductivity and an increase in charge transfer resistance. This decline is unlikely to be counter-balanced solely by an increase in contact area. As a side note, although the operation temperature (80 °C in this study) is higher than the melting temperature of the SPE (≈65 °C), the infiltration of the cathode is determined by the viscosity of the SPE, which is comparably high for PEO with high molecular weight. Further, we like to mention that the contact resistance between the electrode coating and the current collector is apparently not influenced by the infiltration of the SPE into the pores, as the SPE exhibits a negligible electronic conductivity. Accordingly, the size of the semicircle at high frequency in Figure 2 is not changing significantly over time.

While the above summarized results expand our knowledge on the kinetics of PEO degradation at high potentials, there are still many relevant questions that could serve as focal points for future studies. First, the mechanism for the continuous growth of the cathodic charge transfer resistance needs to be further investigated. As suggested above, linear kinetics is typically explained by rate control through an interface reaction. Second, the degradation mechanism of PEO-based SPEs, in particular the chain cleavage, needs to be confirmed by chemical characterization techniques. Third, since chemical high voltage degradation leads to mechanical degradation of the SPE, the influence of a potential cross-talk (e.g., promoted dendrite formation at the anode side) needs to be clarified by future studies. Based on these investigations, effective protection strategies may be derived as a next step.

3. Conclusion

In this study, the interface stability between PEO-based SPE and NCM was re-evaluated, aiming to address inconsistencies in the literature. EIS measurements in a three-electrode setup confirmed that the resistance increase on the cathode side is faster than on the anode side, showing that the PEO/NCM interface is indeed the Achilles' heel in PEO-based SSBs at high voltages. We like to note that also the anode showed a substantial resistance increase, probably related to the reaction between the PEO-SPE and freshly deposited lithium. Moreover, the interfacial stability at the cathode is found to be influenced not only by the cut-off potential but also by the molecular weight of PEO, confirming the crucial role of PEO's terminal groups in the oxidative degradation process of PEO with NCM. These impedance results were supported by galvanostatic cycling data, while SEM images of the cathodes revealed interfacial degradation and polymer chain fragmentation, potentially leading to reduced viscosity. Overall, our findings enhance the understanding of the degradation mechanism involved in PEO-based SSBs with high-voltage cathodes. Future applied research needs to focus on proper protecting coatings on high-voltage cathode materials, like in the case of sulfide-based solid electrolyte. In parallel, improved analytical approaches are needed to acquire true mechanistic information on the PEO|CAM interface reactions.

ADVANCED SCIENCE NEWS
www.advancedsciencenews.com

ADVANCED MATERIALS INTERFACES Open Access
www.advmatinterfaces.de

4. Experimental Section

Materials: Poly(ethylene oxide) (PEO, M_w = 8 000 000 g mol^{-1}, M_w = 600 000 g mol^{-1}, and M_w = 300 000 g mol^{-1}) and 1-methyl-2-pyrrolidone (NMP, anhydrous, 99.5%) were purchased from Sigma–Aldrich. Lithium bis(trifluoromethanesulfonyl)imide (LiTFSI, 99.9%) and polyvinylidene difluoride (PVDF, Solef 5130) were purchased from Solvay, the conductive carbon (Super P) from Imerys and single crystalline $LiNi_{0.83}Co_{0.11}Mn_{0.06}O_2$ were purchased from MSE Supplies. Lithium metal (thickness: 60 µm, Honjo, Japan) was used as counter electrode. The siliconized polyester foil (thickness: 100 µm) was purchased from Valentia Industries LTD, Ireland, and pouch bag foil from Showa Denko, Japan. All chemicals and cell components were dried under vacuum before use. Material storage, cell assembly, and disassembly for the post-mortem analysis were carried out in an argon-filled glovebox ($p(H_2O, O_2)/p < 0.1$ ppm).

PEO Membrane Preparation: Free-standing PEO-LiTFSI membranes (M_w = 300 000 g mol^{-1}, M_w = 600 000 g mol^{-1} and M_w = 8 000 000 g mol^{-1}) were prepared by a solvent-free technique to exclude any solvent-related influence.[41] Therefore, 1000 mg of PEO and 650 mg of LiTFSI (EO/Li ratio 10:1) were intensively mixed until the powders formed a sticky composite. The EO/Li ratio of 10:1 is often used in literature[20,24,18] because it enables high ionic conductivity (at elevated temperatures) and appropriate mechanical properties of the SPE. The composite was placed between two siliconized polyester foils, transferred into an aluminum-laminated pouch bag, vacuum sealed (Sealervac) and annealed for 24 h at 90 °C. Subsequently, the pouch bag containing the polymer electrolyte was hot-pressed (Atlas Series Autotouch) between two metal plates at 90 °C and 294 MPa for 15 s. Thus, membranes with a thickness of ≈200–400 µm were obtained. Finally, the membranes were punched into disks of 12 mm diameter.

Electrode Preparation and Cell Assembly: The NCM-based cathodes used in this study consisted of 94 wt.% NCM, 3 wt.% SuperP and 3 wt.% PVDF. Therefore, Super P was homogenized manually in an agate mortar for 5 min and added to a solution of PVDF in NMP. The suspension was mixed for 15 min in a speed mixer (Hauschild DAC 150.1) using ZrO_2 balls. After adding NCM, the suspension was mixed for another 5 min. The slurries were cast on aluminum foil in argon atmosphere using a doctor blade with a gap of 60 µm, if not specified otherwise. The casting process was followed by drying at 100 °C for 6 h under argon and at 120 °C for 12 h under vacuum. The cathodes were punched into disks of 10 mm diameter and were pressed with 20 kN cm^{-2}, if not specified otherwise. A cathode thickness of ≈40 µm (including the thickness of the Al sheet, ≈17 µm) and a porosity of ≈40% were obtained. Pouch bag cells were assembled by subsequently stacking the cathode, one membrane of PEO-LiTFSI (unless otherwise specified) and the lithium metal anode with diameter of 10 mm and were then vacuum sealed (Sealervac). The electrochemical tests were performed at 80 °C using a VMP-300 Biologic potentiostat. The NCM cells were cycled with a dis-/charge rate of 0.15C (1C = 200 mA g^{-1}).

EIS (Electrochemical Impedance Spectroscopy): For the three-electrode setup, a gold wire with a polyester coating (50 µm, GoodFellow) was used, following the approach described by Simon et al.[42] To obtain point-like reference electrodes, the polyester was burned at the tip. The obtained micro-reference electrodes were placed in the center of the interface between the two PEO membranes.[21] The reference electrodes were lithiated in the fully assembled cell with a constant current of −0.5 µA for 12 h at 80 °C (note that the lithiation was only carried out from the lithium side). Using this in situ lithiation process a lithium-gold alloy with a stable potential of 0.30 V versus Li$^+$/Li[21,43] was formed. The cells with the reference electrodes were charged to different potentials versus Li$^+$/Li using a dis-/charge rate of 0.15 C. The potential was kept constant for 3 h to reach equilibrium prior to the electrochemical impedance spectroscopy (EIS) measurements. This step is necessary to ensure comparability between the samples, since the impedance values of layered cathode oxide materials strongly depend on the lithium content (state of charge) in the cathode.[44] The EIS measurements were carried out at 80°C in a frequency range from 1 to 10 MHz, applying a 20 mV amplitude. The evaluation of the EIS data was performed with the software RelaxIS 3.0.17 (rhd instruments).

SEM and FIB-SEM: The morphological characterization was conducted by scanning electron microscopy (SEM) using a Merlin high-resolution scanning electron microscope (Carl Zeiss AG). For the *post mortem* SEM investigation, four types of samples were examined: a cathode from an uncycled cell (after storage at 80 °C) and cathodes from cells, which were cycled with an upper cut-off voltage of 3.6 V, 4.1 and 4.3 V versus Li$^+$/Li (4 cycles in each case). Due to the sticky properties of the SPE, disassembly of PEO-based cells was experimentally very difficult. Therefore, the cathodes were not pressed/calendared before cell assembly in order to enable the removal of the aluminum current collector after cycling. This allowed to analytically access the PEO/NCM interface. These cathodes had a thickness of ≈45 µm (including the thickness of the Al sheet, ≈17 µm) and exhibited a comparably high porosity of ≈50%, in contrast to cathodes, that were pressed (porosity of ≈40%). To ensure comparability, all samples were prepared in the same way having the same temperature history. After the samples were attached to a sample holder using insulating double-sided tape, the samples were transferred from the glovebox to the SEM using an argon-filled LEICA EM VCT500 shuttle (Leica Microsystems) to avoid any contact with the ambient atmosphere.

A focused ion beam (Tescan XEIA3) was used to prepare cross-sections of the pristine and cycled cathodes. For these experiments, thicker cathodes with a wet film thickness of 120 µm were prepared and pressed. The cross-sections were milled with a 2.5 µA Xe-beam under cryo conditions (≈−130 °C). The images were taken using an acceleration voltage of 5 kV.

ToF-SIMS: Time-of-flight secondary ion mass spectrometry (ToF-SIMS) was performed using an M6 Hybrid SIMS (IONTOF GmbH), which was equipped with a 30 kV Bi-cluster primary ion gun for analysis. The samples were attached to the sample holder using an insulating double-side tape and were transferred under argon atmosphere from the glovebox to the ToF-SIMS instrument with a LEICA EM VCT500 shuttle (Leica Microsystems). For the surface analysis, the instrument was operated in the spectrometry mode (bunched mode) using Bi_3^+ ions, which provided high mass resolution (full width at half maximum (FWHM) $m/\Delta m > 8000$ @ m/z = 61.97 (SNO^-)). The analysis area was set to 75 × 75 µm^2, which was rasterized with 64 × 64 pixels and a primary ion dose of 2.00 × 10^{12} ions cm^{-2}. All measurements were carried out in negative ion mode to ensure comparability of the results. The evaluation of the ToF-SIMS data was performed with the software SurfaceLab 7.2 (IONTOF GmbH).

Supporting Information

Supporting Information is available from the Wiley Online Library or from the author.

Acknowledgements

The authors would like to acknowledge the financial support from the Federal Ministry of Education and Research (BMBF) within the FestBatt project (03XP0433D and 03XP0429B). D.B. and S.P. would like to thank moreover the Helmholtz Association for the basic funding. A.H. would like to thank the "Professorinnenprogramm III" funded by BMBF, A.H. and J.J. thank the DFG for funding of the Hybrid-SIMS (M6 Hybrid SIMS, IONTOF GmbH, Muenster, Germany) under grant number INST 162/544-1 FUGG.

Open access funding enabled and organized by Projekt DEAL.

Conflict of Interest

The authors declare no conflict of interest.

Data Availability Statement

The data that support the findings of this study are available from the corresponding author upon reasonable request.

ADVANCED SCIENCE NEWS
www.advancedsciencenews.com

ADVANCED MATERIALS INTERFACES
Open Access
www.advmatinterfaces.de

Keywords

high-voltage cathode active materials, interface stability, poly(ethylene oxide) (PEO), solid polymer electrolytes, solid-state batteries

Received: June 21, 2023
Revised: October 15, 2023
Published online:

[1] J. Janek, W. G. Zeier, *Nat. Energy* **2016**, *1*, 16141.
[2] Y.-K. Sun, *ACS Energy Lett.* **2020**, *5*, 3221.
[3] Z. Gao, H. Sun, L. Fu, F. Ye, Y. Zhang, W. Luo, Y. Huang, *Adv. Mater.* **2018**, *30*, 1870122.
[4] R. C. Agrawal, G. P. Pandey, *J. Phys. D: Appl. Phys.* **2008**, *41*, 223001.
[5] M. Shoji, E. J. Cheng, T. Kimura, K. Kanamura, *J. Phys. D: Appl. Phys.* **2019**, *52*, 103001.
[6] J. Liang, X. Li, S. Wang, K. R. Adair, W. Li, Y. Zhao, C. Wang, Y. Hu, L. Zhang, S. Zhao, S. Lu, H. Huang, R. Li, Y. Mo, X. Sun, *J. Am. Chem. Soc.* **2020**, *142*, 7012.
[7] G. B. Appetecchi, F. Alessandrini, R. G. Duan, A. Arzu, S. Passerini, *J. Power Sources* **2001**, *101*, 42.
[8] A. Gupta, J. Sakamoto, *Electrochem. Soc. Interface* **2019**, *28*, 63.
[9] L. Xu, J. Li, W. Deng, L. Li, G. Zou, H. Hou, L. Huang, X. Ji, *Mater. Chem. Front.* **2021**, *5*, 1315.
[10] J. Liang, Y. Sun, Y. Zhao, Q. Sun, J. Luo, F. Zhao, X. Lin, X. Li, R. Li, L. Zhang, S. Lu, H. Huang, X. Sun, *J. Mater. Chem. A* **2020**, *8*, 2769.
[11] S. Kaboli, H. Demers, A. Paolella, A. Darwiche, M. Dontigny, D. Clément, A. Guerfi, M. L. Trudeau, J. B. Goodenough, K. Zaghib, *Nano Lett.* **2020**, *20*, 1607.
[12] K. Nie, X. Wang, J. Qiu, Y. Wang, Q. Yang, J. Xu, X. Yu, H. Li, X. Huang, L. Chen, *ACS Energy Lett.* **2020**, *5*, 826.
[13] L. Seidl, R. Grissa, L. Zhang, S. Trabesinger, C. Battaglia, *Adv. Mater. Interfaces* **2022**, *9*, 2100704.
[14] J. Ma, Z. Liu, B. Chen, L. Wang, L. Yue, H. Liu, J. Zhang, Z. Liu, G. Cui, *J. Electrochem. Soc.* **2017**, *164*, A3454.
[15] J. Qiu, X. Liu, R. Chen, Q. Li, Y. Wang, P. Chen, L. Gan, S.-J. Lee, D. Nordlund, Y. Liu, X. Yu, X. Bai, H. Li, L. Chen, *Adv. Funct. Mater.* **2020**, *30*, 1909392.
[16] J. Liang, S. Hwang, S. Li, J. Luo, Y. Sun, Y. Zhao, Q. Sun, W. Li, M. Li, M. N. Banis, X. Li, R. Li, L. Zhang, S. Zhao, S. Lu, H. Huang, D. Su, X. Sun, *Nano Energy* **2020**, *78*, 105107.
[17] G. Homann, L. Stolz, J. Nair, I. C. Laskovic, M. Winter, J. Kasnatscheew, *Sci. Rep.* **2020**, *10*, 4390.
[18] G. Homann, L. Stolz, K. Neuhaus, M. Winter, J. Kasnatscheew, *Adv. Funct. Mater.* **2020**, *30*, 2006289.
[19] L. A. Middlemiss, A. J. R. Rennie, R. Sayers, A. R. West, *Energy Rep.* **2020**, *6*, 232.
[20] V. Wurster, C. Engel, H. Graebe, T. Ferber, W. Jaegermann, R. Hausbrand, *J. Electrochem. Soc.* **2019**, *166*, A5410.
[21] J. Landesfeind, D. Pritzl, H. A. Gasteiger, *J. Electrochem. Soc.* **2017**, *164*, A1773.
[22] S. Kumakura from Umicore, "Strategy to Optimize Nmc Materials for All-Solid State Batteries", Presentation at International Battery Association October 4, 2022 Bled, Slovenia.
[23] R. Bouchet, S. Lascaud, M. Rosso, *J. Electrochem. Soc.* **2003**, *150*, A1385.
[24] F. J. Simon, M. Hanauer, F. H. Richter, J. Janek, *ACS Appl. Mater. Interfaces* **2020**, *12*, 11713.
[25] S.-K. Otto, Y. Moryson, T. Krauskopf, K. Peppler, J. Sann, J. Janek, A. Henss, *Chem. Mater.* **2021**, *33*, 859.
[26] H. Liang, S. Wang, Q. Ye, C. Zeng, Z. Tong, Y. Ma, H. Li, *Chem. Commun.* **2022**, *58*, 10821.
[27] E. E. Ushakova, A. Frolov, A. A. Reveguk, D. Y. Usachov, D. M. Itkis, L. V. Yashina, *Appl. Surf. Sci.* **2022**, *589*, 153014.
[28] O. Sheng, J. Zheng, Z. Ju, C. Jin, Y. Wang, M. Chen, J. Nai, T. Liu, W. Zhang, Y. Liu, X. Tao, *Adv. Mater.* **2020**, *32*, 2000223.
[29] M. Le Granvalet-Mancini, *Solid State Ionics* **2000**, *135*, 283.
[30] E. K. W. Andersson, C. Sångeland, E. Berggren, F. O. L. Johansson, D. Kühn, A. Lindblad, J. Mindemark, M. Hahlin, *J. Mater. Chem. A* **2021**, *9*, 22462.
[31] H. Cheng, C. B. Zhu, M. Lu, Y. Yang, *J. Power Sources* **2007**, *174*, 1027.
[32] J. Li, Y. Ji, H. Song, S. Chen, S. Ding, B. Zhang, L. Yang, Y. Song, F. Pan, *Nano-Micro Lett.* **2022**, *14*, 191.
[33] J. Illig, J. P. Schmidt, M. Weiss, A. Weber, E. Ivers-Tiffée, *J. Power Sources* **2013**, *239*, 670.
[34] T.-T. Zuo, R. Rueß, R. Pan, F. Walther, M. Rohnke, S. Hori, R. Kanno, D. Schröder, J. Janek, *Nat. Commun.* **2021**, *12*, 6669.
[35] H. Schmalzried, *Chemical Kinetics of Solids*, Wiley-VCH, Weinheim **1995**.
[36] Y. Yusim, E. Trevisanello, R. Ruess, F. H. Richter, A. Mayer, D. Bresser, S. Passerini, J. Janek, A. Henss, *Angew. Chem., Int. Ed.* **2023**, *62*, e202218316.
[37] E. Trevisanello, R. Ruess, G. Conforto, F. H. Richter, J. Janek, *Adv. Energy Mater.* **2021**, *11*, 2003400.
[38] X. Yang, M. Jiang, X. Gao, D. Bao, Q. Sun, N. Holmes, H. Duan, S. Mukherjee, K. Adair, C. Zhao, J. Liang, W. Li, J. Li, Y. Liu, H. Huang, L. Zhang, S. Lu, Q. Lu, R. Li, C. V. Singh, X. Sun, *Energy Environ. Sci.* **2020**, *13*, 1318.
[39] B. Strehle, F. Friedrich, H. A. Gasteiger, *J. Electrochem. Soc.* **2021**, *168*, 050512.
[40] J. Liang, D. Chen, K. Adair, Q. Sun, N. G. Holmes, Y. Zhao, Y. Sun, J. Luo, R. Li, L. Zhang, S. Zhao, S. Lu, H. Huang, X. Zhang, C. V. Singh, X. Sun, *Adv. Energy Mater.* **2021**, *11*, 2002455.
[41] G. B. Appetecchi, M. Carewska, F. Alessandrini, P. P. Prosini, S. Passerini, *J. Electrochem. Soc.* **2000**, *147*, 451.
[42] F. J. Simon, L. Blume, M. Hanauer, U. Sauter, J. Janek, *J. Electrochem. Soc.* **2018**, *165*, A1363.
[43] S. Solchenbach, D. Pritzl, E. J. Y. Kong, J. Landesfeind, H. A. Gasteiger, *J. Electrochem. Soc.* **2016**, *163*, A2265.
[44] <number>[44]<number>R. S. Negi, P. Minnmann, R. Pan, S. Ahmed, M. J. Herzog, K. Volz, R. Takata, F. Schmidt, J. Janek, M. T. Elm, *Chem. Mater.* **2021**, *33*, 6713.

3.3 Publication III

Challenges in XPS Analysis of PEO-LiTFSI Batteries (Electrolytes): Interpreting X-ray Photodecomposition

The third publication (in preparation) investigates the X-ray photodecomposition of PEO-based SPEs during the XPS analysis. Although the X-Ray photodecomposition of conducting salts has been reported previously, it can be easily overlooked and misinterpreted, especially when analyzing interfacial degradation in PEO-based SSBs. The results of the study provide additional insights in the photodecomposition process and clarify if PEO-LiTFSI degrades to LiF with NCM before and after cycling. In addition, it was shown that the photodecomposition process is more pronounced, when LiTFSI is dissolved in a PEO matrix compared to pure reference material. Further, the photodecomposition can be significantly reduced, when measuring under cryogenic conditions.

Overall, the findings of this study extend the understanding of X-ray photodecomposition of PEO-based SPEs and demonstrate pitfalls in their XPS analysis.

The experiments for this work were designed and performed by the first author under the supervision of A. Henss and J. Sann. Y. Moryson assisted in performing the XPS measurements. K. Seipp supported in the validation of the data. All authors contributed to the scientific discussion. The manuscript was written by the first author and edited by all other authors.

Challenges in XPS Analysis of PEO-LiTFSI Batteries (Electrolytes): Interpreting X-ray Photodecomposition

Yuriy Yusim[a,b], Yannik Moryson[a,b], Kevin Seipp[c], Joachim Sann[a,b*] and Anja Henss[a,b]

[a]*Institute of Physical Chemistry, Justus Liebig University Giessen, Heinrich-Buff-Ring 17, 35392 Giessen, Germany*

[b]*Center for Materials Research (ZfM/LaMa), Justus Liebig University Giessen, Heinrich-Buff-Ring 16, 35392 Giessen, Germany*

[c]*Department of Chemistry, Johannes Gutenberg University, Duesbergweg 10–14, 55128 Mainz, Germany*

Corresponding Author

*Email:

Joachim.Sann@phys.chemie.uni-giessen.de (J. Sann)

Anja.Henss@phys.chemie.uni-giessen.de (A. Henss)

Keywords: XPS, Cryogenic conditions, Solid polymer electrolytes, Poly(ethylene oxide) (PEO), Conducting salts, Interface stability

Abstract

The cycle life of poly(ethylene oxide) (PEO)-batteries with lithium bis(trifluoromethanesulfonyl)imide (LiTFSI) is limited by interfacial degradation, which is commonly characterized by X-ray photoelectron spectroscopy (XPS). While the X-ray photodecomposition of conducting salts has been reported previously, our study emphasizes the potential for misinterpretation of this phenomenon as chemical degradation, particularly when analyzing PEO-LiTFSI and PEO-LiTFSI with NCM. Additional insights into the photodecomposition process are demonstrated, which is more pronounced, when LiTFSI is dissolved compared to pure material. Furthermore, the decomposition can be significantly reduced under cryogenic conditions. Overall, these findings deepen the understanding of photodecomposition, demonstrating pitfalls in XPS analysis.

Main part

Due to its high energy and power density lithium-ion batteries (LIBs) play a crucial role, when it comes to electrochemical energy storage in consumer goods and electric vehicles. Although the energy density has been strongly increased since the LIB commercialization by Sony in 1991,[1] LIBs with a liquid electrolyte will soon approach a limit in terms of energy density.[2,3] Thus, potential follow-up systems are under intensive research, such as solid-state batteries (SSBs) with a solid electrolyte (SE).[4] In this context, solid polymer electrolytes (SPEs) based on poly(ethylene oxide) with lithium bis(trifluoromethanesulfonyl)imide (LiTFSI) as conducting salt were successfully commercialized by Blue Solutions (Bolloré Group).[5-7] Furthermore, tremendous research efforts have been spent to use PEO-LiTFSI in combination with other SEs in hybrid cell concepts, leading to a layered-like concept[8,9] or even a three-dimensional mixing[10,11] to improve the mechanical properties, to increase the lithium-ion conductivity or to lower the interfacial resistance. In this context, various techniques such as Fourier-transform infrared spectroscopy, Raman spectroscopy and X-ray photoelectron spectroscopy (XPS) were employed to characterize interfacial processes and elucidate electrochemical phenomena. Among these valuable techniques, XPS stood out as notably advantageous, due to its high surface sensitivity and quantitative nature. However, during XPS measurements, X-ray radiation and ion beam sputtering can trigger various decomposition processes, especially when measuring radiation-sensitive samples such as polymer electrolytes. As shown by Shterenberg et al.,[12] the magnesium and lithium salts based on TFSI, FSI and PF_6 anions undergo a significant photodegradation during XPS measurements leading to the formation of new peaks at lower binding energy (BE) in fluorine and sulfur XP spectra. In this context, the signal arising in the XP spectrum of F 1s at approximately 685 eV[13,14] can be attributed to the formation of LiF species. These results are supported by Yu et al.[15] who emphasize that during XPS analysis any residual salt in the electrode sample is likely to produce LiF, regardless of battery operation. In addition, high-energy Ar^+ sputtering, which is commonly employed for depth profiling of thick SEI-layers, strongly promotes the LiF formation.[16,15] Nevertheless, the decomposition of lithium salts during XPS analysis can be easily overlooked. According to Hobold et al.[17], quantitative titration experiments revealed that the amount of LiF content in the solid electrolyte interphase (SEI) of lithium metal tends to be overestimated when analyzed by XPS, which may be related to possible photodegradation of the lithium salt during XPS measurements. Considering this photodecomposition effects, we carefully analyzed PEO-based SPE systems with XPS within this study.

We initially focused on analyzing the PEO-LiTFSI|NCM interface using XPS. Therefore, we prepared a Li|PEO-LiTFSI|$LiNi_{0.83}Mn_{0.06}Co_{0.11}O_2$/PVDF/Super P cell and stored it at 80 °C allowing partial infiltration of the cathode with PEO-LiTFSI. Subsequently, the aluminum current collector was removed from the cathode, and the surface facing the current collector was examined using XPS. Thereby, it is important to note that the XPS measurement standards were followed according to the literature (including measuring procedure and measuring time). In Figure 1a, the F 1s spectrum is shown, containing the -CF_3 group of LiTFSI and -CF_2 of PVDF at 688.7 eV. The LiF signal is often associated with a decomposition product of LiTFSI in the existing literature.[13] Previous studies have reported the formation of a LiF-containing reaction layer when depositing PEO-LiTFSI (M_W = 2.000 g mol^{-1}) on LCO thin films.[18] Other researchers[19] have also suggested that the degradation of PEO-LiTFSI may occur at a very low potential, close the open circuit potential of NCM against Li[20]. Taken together, these reports provide a plausible explanation for our observation of the LiF signal in the XP spectrum when PEO-LiTFSI is in contact with NCM. Additionally, we conducted XPS measurements on pristine PEO-LiTFSI as a reference material as depicted in Figure 1b. Notably, the LiF signal is present to a similar extent in both the PEO-LiTFSI case and the NCM cathode with PEO-LiTFSI. In a previous study by Simon et al.[10], the presence of LiF in "pristine" PEO-LiTFSI in the XP spectra was also demonstrated.

Interestingly, when we repeatedly measured the same position of PEO-LiTFSI increasing the X-ray exposure time (an X-ray exposure of 13 min leads to an energy dose of $1.2 \cdot 10^7$ J cm^{-2}), we observed an increasing amount of LiF in the PEO-LiTFSI accompanied by a corresponding decrease in the amount of -CF_3, as illustrated in Figure 1c. A similar trend was observed for PEO-LiFSI (see Figure S2). To quantify these changes, we plotted the relative fraction of LiF from the total F 1s spectrum, derived from the fitting of the XP spectra, against the X-ray exposure time in Figure 1d. It can be seen that the LiF fraction increases linearly at the beginning until it reaches a plateau at a relative amount of 80-90% LiF fraction for PEO-LiTFSI and PEO-LiFSI, respectively. These findings strongly indicate that the duration of X-ray radiation significantly impacts the detected amount of LiF, aligning well with the results presented by Shterenberg et al.[12] and Högström et al.[21,22] Consequently, it becomes evident that the LiF signal is highly susceptible to X-ray photodecomposition. In this regard, it is important to note that the energy which is the sample is exposed to (1486.6 eV = $1.4 \cdot 10^6$ kJ mol^{-1}), is sufficient to break chemical bonds, as the bond energy of C-F is about $3.9 \cdot 10^3$ kJ mol^{-1}.[23] Moreover, we can exclude that the degradation of the conducting salt is caused by the high vacuum in the chamber, since we repeated the same experiment after long pumping times (12h) obtaining same results.

We performed further experiments by measuring XPS detail spectra in different orders. In particular, we examined the comparison between recording the F 1s spectrum of PEO-LiTFSI (refer to Figure 1b) initially versus recording it after analyzing all the other regions (survey, C, O, Li, S, and N). As depicted in Figure S1, the LiF content is notably reduced when capturing the F 1s detailed spectrum initially (with a LiF fraction of 5%) compared to post-analysis of the other elements (resulting in a LiF fraction of 53%). This finding further corroborates our observation concerning the photodecomposition of LiTFSI during XPS analysis. These experiments demonstrate the importance of estimating the sensitivity of the battery sample to radiation damage and determining the rate of change in order to establish a consistent and accurate measurement protocol. These experiments also emphasize the need to keep the analysis time and measurement procedure consistent when comparing different samples to ensure a similar X-ray exposure time. This approach was recommended by Philippe et al.[21] in their study.

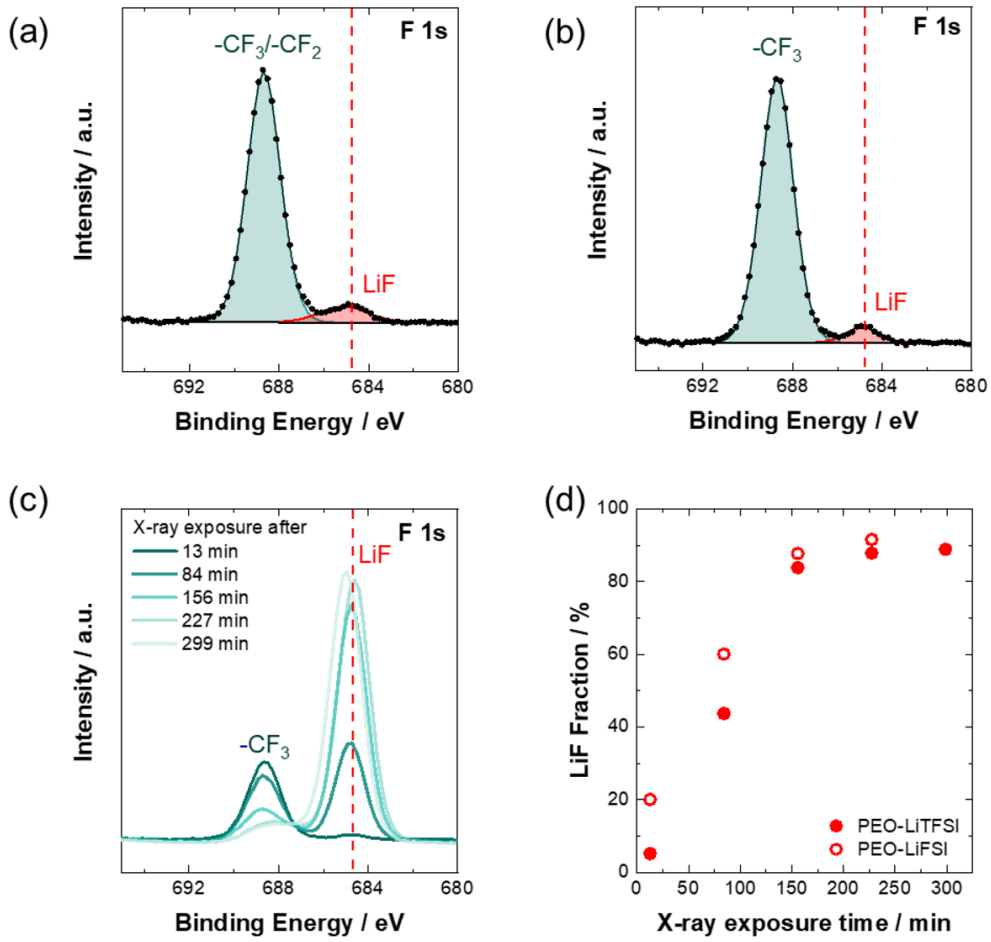

Figure 1. F 1s XP spectra of (a) PEO-LiTFSI in contact with NCM cathode and (b) pure PEO-LITFSI. (c) PEO-LiTFSI after different X-ray exposure times. (d) LiF fraction as function of the X-ray exposure time for PEO-LiTFSI and PEO-LiFSI.

Considering the observed instability of PEO-LiTFSI samples under X-ray radiation, it can be hypothesized that the LiF signal found in the XP-spectra of both PEO-LiTFSI and PEO-LiTFSI in contact with NCM is primarily attributed to X-ray photodegradation during the XPS measurement rather than chemical degradation. To mitigate the effect of X-ray photodecomposition of LiTFSI in the PEO-matrix, we minimized the number of scans for the XP spectrum acquisition.[24] Instead of the 35 scans used in Figure 1, we performed a measurement with a single scan. It is important to note, that while the signal quality improves with increasing number of scans, the radiation damage becomes more pronounced. Using a single scan, no LiF-signal can be detected at 685 eV for PEO-LiTFSI (Figure 2a) and for PEO-LiTFSI in contact with NCM (Figure 2b) indicating the absence of LiTFSI decomposition into LiF in either sample. Same

results were obtained, when the cell was cycled to 4.3 V *vs.* Li^+/Li. To enhance the signal-to-noise ratio, XP spectra were collected at 48 different points on the surface of PEO-LiTFSI with one scan each (analysis areas do not overlap), and subsequently summed, confirming the absence of LiF (see Figure 2c). Overall, it can be concluded that the LiF signal in pristine PEO-LITFSI and PEO-LiTFSI in contact with NCM is a consequence of X-ray radiation damage and not chemical degradation. Notably, there was no observed increase in chamber pressure, and no gas release was detected by mass spectrometry, thereby excluding the formation of gaseous products during the photodegradation, as opposed to the findings of Shterenberg et al.[12] However, it is important to note that, we do not completely rule out the possibility that PEO-LiTFSI undergoing several degradation reactions when in contact with NCM. Furthermore, our results are only partially comparable to the data of Ferber et al.[18], who observed the degradation of PEO-LiTFSI in contact with LCO. In contrast to our study, they utilized LCO instead of NCM as the cathode material. In addition, it's worth mentioning, that our NCM materials are coated, similar to many commercially available cathode active materials. It is well known that coatings can help mitigate degradation at the interface between cathode material and SPE.

Furthermore, we collected an XP surface spectrum of pure LiTFSI and compared it to the PEO-LiTFSI using the same measurement procedure (summed 35 scans). As shown in Figure 2d, only a small fraction of LiF (<1.2%) can be detected on the surface of pure LiTFSI. Moreover, the observed X-ray decomposition over time shows differences between pure LiTFSI and PEO-LiTFSI (see Figure 2d). Corresponding to the surface spectra in Figure 2c, it appears that X-ray degradation is more pronounced, when LiTFSI is dissolved in the PEO-matrix, compared to pure LiTFSI, as demonstrated in Figure 2e. To ensure the reliability of our findings, we repeated this trend with LiFSI and PEO-LiFSI (see Figure S3). These data indicate that the X-ray photodecomposition of conducting salts differs whether they are ionically bonded in the pure solid state or dissolved. Considering the structure of LiTFSI, a possible explanation for this behavior may lie in the increased mobility of the lithium cation when LiTFSI is dissolved, potentially bringing it into closer proximity with the $-CF_3$ group (see Figure 2f). Consequently, the likelihood of collision between $-CF_3$ group and Li cation, leading to the formation of LiF, is enhanced.

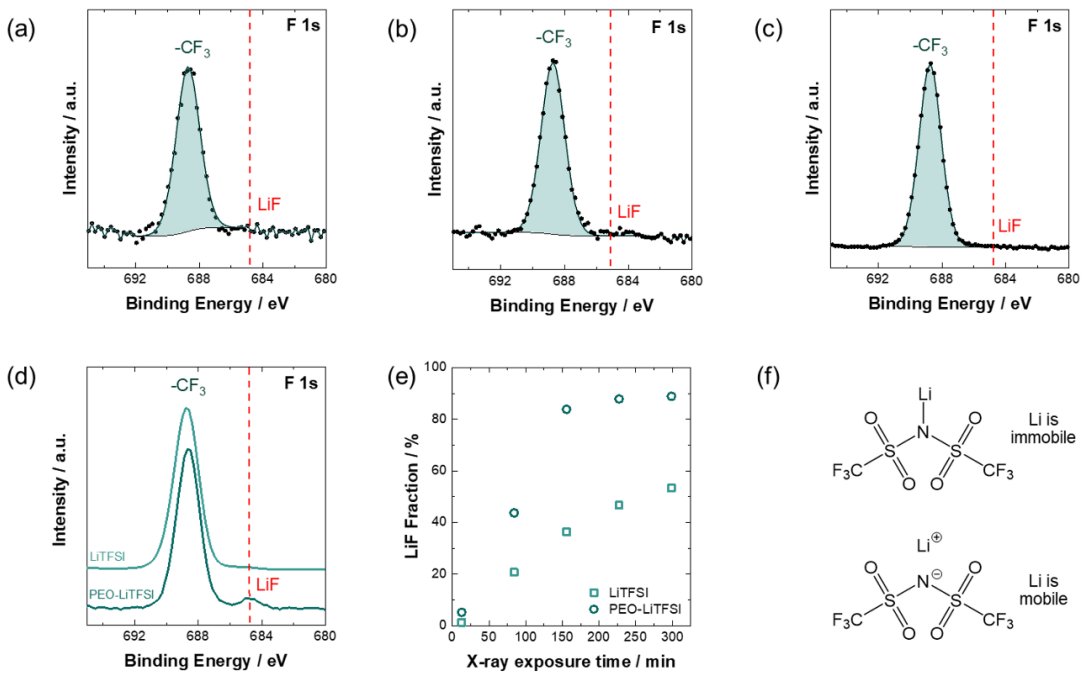

Figure 2. XP F 1s spectra using one scan of (a) PEO-LiTFSI and (b) PEO-LiTFSI in contact with NCM cathode. (c) Summed F 1s XP spectra using one scan from 48 different surface points of PEO-LiTFSI (d) Comparison of XP spectra of PEO-LiTFSI and pure LiTFSI powder. (e) LiF fraction as function of the X-ray exposure time for PEO-LiTFSI and LiTFSI. (f) Schematic comparison of the structure of pure LiTFSI and LiTFSI dissolved in PEO.

Since it seems that the photodegradation rate of LiTFSI to LiF during XP exposure depends on the mobility of lithium cations (see above), we conducted XPS measurements of PEO-LiTFSI under cryogenic conditions in order to slow down the kinetics of the X-ray induced degradation reaction. In contrast to PEO-LiTFSI measured at room temperature in Figure 1b, no LiF-signal can be seen, when the XP spectra are collected at −130 °C (see Figure 3). This suggests that the X-ray induced decomposition of LiTFSI to LiF can be overcome when measuring at low temperatures. To ensure the reliability of our findings, we conducted the same experiment with PEO-LiFSI, and obtained similar results (see Figure S4). This further confirms that no degradation occurred between PEO and LiTFSI and supports the validity of our conclusion. Overall, the enhanced photodecomposition process observed in dissolved LiTFSI, particularly at elevated temperatures, implies that the pivotal reaction step is governed by transport phenomena. We hypothesize that due to the photoelectronic effect, one electron of the nitrogen of the LiTFSI/LiFSI may be removed in an oxidative process, potentially leading to an intermolecular or intramolecular reduction in the CF_3 group in subsequent steps (see Figure S5). The latter process may be similar to the CF_4 gas phase reaction mechanisms, as reported by Zhang et al.[25],

who investigated plasma-surface reactions in fluorocarbon plasmas and simulated potential CF_4 gas phase reaction mechanism.

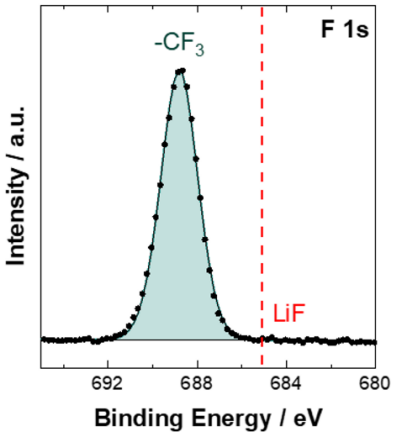

Figure 3. F 1s XP spectrum of PEO-LiTFSI measured under cryogenic conditions (−130 °C).

This study aimed to investigate the decomposition of Li conducting salts in solid polymer electrolytes during XPS analysis. Through the collection of XP surface spectra of PEO-LiTFSI and PEO-LiTFSI in contact with NCM, we observed that the LiF content significantly increases with X-ray exposure time, confirming the X-ray photodecomposition of LiTFSI during XPS analysis. However, it can be easily misinterpreted as chemical degradation. In this regard, no LiF-containing degradation products were detected in the PEO-LiTFSI membrane and PEO-LiTFSI in contact with NCM before and after cycling. This emphasizes the need for fast XPS measurements to minimize beam damage and to ensure accurate surface analysis. Moreover, we demonstrated that cryogenic conditions can significantly slow down the photodegradation rate of lithium salts forming LiF during X-ray exposure. These observations provide new insights in the photodecomposition process, whose pivotal reaction step is likely controlled by transport phenomena. Overall, our work expands the understanding of X-ray photodecomposition and suggest strategies for achieving reliable XPS analysis.

Supporting Information

Experimental section; F 1s XP spectrum of PEO-LITFSI after other elements were measured; PEO-LiFSI after different X-ray exposure times; LiF fraction as function of X-ray exposure

time for PEO-LiFSI and LiFSI; F 1s XP spectrum of PEO-LiFSI at RT and cryogenic conditions; Suggested mechanism of X-ray photodecomposition.

ORCID

Yuriy Yusim: 0000-0002-7690-0844

Anja Henss: 0000-0001-5009-6512

Joachim Sann: 0000-0003-4663-2671

Author contributions

Y.Y., A.H. and J.S. conceived the idea. A.H. and J.S. supervised all aspects of the research. Y.Y. carried out the XPS measurements including the sample preparation. Y.M. and K.S. supported in the interpretation and analysis of measured data. Y.Y. wrote the first draft of the manuscript. All authors revised and approved the manuscript.

Notes

The authors declare no competing financial interest.

Acknowledgments

The authors would like to acknowledge the financial support from the Federal Ministry of Education and Research (BMBF) within the FestBatt project (03XP0433D). A.H. would like to thank the “Professorinnenprogramm III” funded by BMBF.

References

1 Reddy, M. V.; Mauger, A.; Julien, C. M.; Paolella, A.; Zaghib, K. Brief History of Early Lithium-Battery Development. *Materials* **2020**, *13*, 1884. DOI: 10.3390/ma13081884

2 Janek, J. and Zeier, W. G. A solid future for battery development. *Nat. Energy* **2016**, *1*, 16141. DOI: 10.1038/nenergy.2016.141

3 Janek, J. and Zeier, W. G. Challenges in speeding up solid-state battery development. *Nat. Energy* **2023**, *8*, 230–240. DOI: 10.1038/s41560-023-01208-9

4 Negi, R. S.; Yusim, Y.; Pan, R.; Ahmed, S.; Volz, K.; Takata, R.; Schmidt, F.; Henss, A.; Elm, M. T. A Dry-Processed Al 2 O 3 /LiAlO 2 Coating for Stabilizing the Cathode/Electrolyte Interface in High-Ni NCM-Based All-Solid-State Batteries. *Adv. Mater. Interfaces* **2022**, *9*, 2270039. DOI: 10.1002/admi.202270039

5 Yusim, Y.; Trevisanello, E.; Ruess, R.; Richter, F. H.; Mayer, A.; Bresser, D.; Passerini, S.; Janek, J.; Henss, A. Evaluation and Improvement of the Stability of Poly(ethylene oxide)-based Solid-state Batteries with High-Voltage Cathodes. *Angew. Chem. Int. Ed.* **2023**, *62*, e202218316. DOI: 10.1002/anie.202218316

6 Varzi, A.; Raccichini, R.; Passerini, S.; Scrosati, B. Challenges and prospects of the role of solid electrolytes in the revitalization of lithium metal batteries. *J. Mater. Chem. A* **2016**, *4*, 17251–17259. DOI: 10.1039/C6TA07384K

7 Huo, H.; Jiang, M.; Mogwitz, B.; Sann, J.; Yusim, Y.; Zuo, T.-T.; Moryson, Y.; Minnmann, P.; Richter, F. H.; Veer Singh, C.; Janek, J. Interface Design Enabling Stable Polymer/Thiophosphate Electrolyte Separators for Dendrite-Free Lithium Metal Batteries. *Angew. Chem. Int. Ed.* **2023**, *62*, e202218044. DOI: 10.1002/ange.202218044

8 Simon, F. J.; Hanauer, M.; Henss, A.; Richter, F. H.; Janek, J. Properties of the Interphase Formed between Argyrodite-Type Li6PS5Cl and Polymer-Based PEO10:LiTFSI. *ACS Appl. Mater. Interfaces* **2019**, *11*, 42186–42196. DOI: 10.1021/acsami.9b14506

9 Chi, S.-S.; Liu, Y.; Zhao, N.; Guo, X.; Nan, C.-W.; Fan, L.-Z. Solid polymer electrolyte soft interface layer with 3D lithium anode for all-solid-state lithium batteries. *Energy Stor. Mater.* **2019**, *17*, 309–316. DOI: 10.1016/j.ensm.2018.07.004

10 Simon, F. J.; Hanauer, M.; Richter, F. H.; Janek, J. Interphase Formation of PEO20:LiTFSI-Li6PS5Cl Composite Electrolytes with Lithium Metal. *ACS Appl. Mater. Interfaces* **2020**, *12*, 11713–11723. DOI: 10.1021/acsami.9b22968

11 Zhao, Y.; Huang, Z.; Chen, S.; Chen, B.; Yang, J.; Zhang, Q.; Ding, F.; Chen, Y.; Xu, X. A promising PEO/LAGP hybrid electrolyte prepared by a simple method for all-solid-state lithium batteries. *Solid State Ion.* **2016**, *295*, 65–71. DOI: 10.1016/j.ssi.2016.07.013

12 Shterenberg, I.; Salama, M.; Gofer, Y.; Aurbach, D. X-ray Photodecomposition of Bis(trifluoromethanesulfonyl)imide, Bis(fluorosulfonyl)imide, and Hexafluorophosphate. *J. Phys. Chem. C* **2017**, *121*, 3744–3751. DOI: 10.1021/acs.jpcc.6b11524

13 Busche, M. R.; Drossel, T.; Leichtweiss, T.; Weber, D. A.; Falk, M.; Schneider, M.; Reich, M.-L.; Sommer, H.; Adelhelm, P.; Janek, J. Dynamic formation of a solid-liquid electrolyte interphase and its consequences for hybrid-battery concepts. *Nat. Chem.* **2016**, *8*, 426–434. DOI: 10.1038/nchem.2470

14 Huang, Z.; Meng, J.; Xie, M.; Shen, Y.; Huang, Y. A pretreatment method to form high-quality LiF-enriched solid-electrolyte interfaces for Li anode protection in Li–O 2 batteries. *J. Mater. Chem. A* **2020**, *8*, 14198–14204. DOI: 10.1039/D0TA05147K

15 Yu, W.; Yu, Z.; Cui, Y.; Bao, Z. Degradation and Speciation of Li Salts during XPS Analysis for Battery Research. *ACS Energy Lett.* **2022**, *7*, 3270–3275. DOI: 10.1021/acsenergylett.2c01587

16 Ota, H.; Sakata, Y.; Wang, X.; Sasahara, J.; Yasukawa, E. Characterization of Lithium Electrode in Lithium Imides/Ethylene Carbonate and Cyclic Ether Electrolytes. *J. Electrochem. Soc.* **2004**, *151*, A437. DOI: 10.1149/1.1644137

17 Hobold, G. M. and Gallant, B. M. Quantifying Capacity Loss Mechanisms of Li Metal Anodes beyond Inactive Li 0. *ACS Energy Lett.* **2022**, *7*, 3458–3466. DOI: 10.1021/acsenergylett.2c01845

18 Ferber, T. H.; Cangaz, Ş.; Jaegermann, W.; Hausbrand, R. Interface reactivity of in-situ formed LiCoO2 - PEO solid-state interfaces investigated by X-ray photoelectron spectroscopy: Reaction products, energy level offsets and double layer formation. *Appl. Surf. Sci.* **2022**, *571*, 151218. DOI: 10.1016/j.apsusc.2021.151218

19 Seidl, L.; Grissa, R.; Zhang, L.; Trabesinger, S.; Battaglia, C. Unraveling the Voltage-Dependent Oxidation Mechanisms of Poly(Ethylene Oxide)-Based Solid Electrolytes for Solid-State Batteries. *Adv. Mater. Interfaces* **2022**, *9*, 2100704. DOI: 10.1002/admi.202100704

20 Schmalstieg, J.; Rahe, C.; Ecker, M.; Sauer, D. Uwe Full Cell Parameterization of a High-Power Lithium-Ion Battery for a Physico-Chemical Model: Part I. Physical and Electrochemical Parameters. *J. Electrochem. Soc.* **2018**, *165*, A3799-A3810. DOI: 10.1149/2.0321816jes

21 Philippe, B.; Hahlin, M.; Edström, K.; Gustafsson, T.; Siegbahn, H.; Rensmo, H. Photoelectron Spectroscopy for Lithium Battery Interface Studies. *J. Electrochem. Soc.* **2016**, *163*, A178-A191. DOI: 10.1149/2.0051602jes

22 K. C. Högström. *Doctroral thesis* **2014**, Uppsala University

23 Huggins, M. L. Bond Energies and Polarities 1. *J. Am. Chem. Soc.* **1953**, *75*, 4123–4126. DOI: 10.1021/ja01113a001

24 Malmgren, S.; Ciosek, K.; Lindblad, R.; Plogmaker, S.; Kühn, J.; Rensmo, H.; Edström, K.; Hahlin, M. Consequences of air exposure on the lithiated graphite SEI. *Electrochim. Acta* **2013**, *105*, 83–91. DOI: 10.1016/j.electacta.2013.04.118

25 Da Zhang and Kushner, M. J. Mechanisms for CF2 radical generation and loss on surfaces in fluorocarbon plasmas. *J. Vac. Sci. Technol. A* **2000**, *18*, 2661–2668. DOI: 10.1116/1.1319816

3.4 Meaningful Contributions (shared first authorship)

3.4.1 Publication IV

A Dry-Processed $Al_2O_3/LiAlO_2$ Coating for Stabilizing the Cathode/Electrolyte Interface in High-Ni NCM-Based All-Solid-State Batteries

In the fourth publication[39], an $Al_2O_3/LiAlO_2$ surface coating was introduced on Ni-rich NCM to reduce interfacial degradation between thiophosphate-based SE and NCM. Therefore, the coating was obtained by a dry coating process followed by post-annealing at 600 °C. Various structural characterization methods confirmed the formation of a dense $Al_2O_3/LiAlO_2$ coating layer. Electrochemical evaluation experiments demonstrated that annealing-induced changes of the coating have beneficial effects on the SSBs. Cells containing $Al_2O_3/LiAlO_2$-coated NCM exhibit significantly improve the rate capability and the long-term cycling performance compared to cells assembled from uncoated or Al_2O_3-coated CAM. This is supported by EIS measurements showing lower cell resistance after cycling with $Al_2O_3/LiAlO_2$-coated NCM compared to pristine NCM.

Overall, the results of this study present an effective dry coating method that is suitable for large-scale processing of cathodes for next-generation SSBs, excluding solvent-related influences and costs.

The experiments for this work were designed and performed by R. S. Negi under the supervision of R. Takata, F. Schmidt and M. T. Elm. Y. Yusim and A. Henss supported in the validation of the data and conducted the impedance analysis. S. Ahmed and K. Volz performed the TEM measurements. The manuscript was written by Y. Yusim and edited by all other authors. The first authorship of this work was shared between R. S. Negi and Y. Yusim.

RESEARCH ARTICLE

ADVANCED MATERIALS INTERFACES
www.advmatinterfaces.de

A Dry-Processed $Al_2O_3/LiAlO_2$ Coating for Stabilizing the Cathode/Electrolyte Interface in High-Ni NCM-Based All-Solid-State Batteries

Rajendra S. Negi, Yuriy Yusim, Ruijun Pan, Shamail Ahmed, Kerstin Volz, Ryo Takata, Franz Schmidt, Anja Henss,* and Matthias T. Elm**

Due to their high theoretical energy densities and superior safety, thiophosphate-based all-solid-state batteries (ASSBs) are considered as promising power source for electric vehicles. However, for large-scale industrial applications, interfacial degradation between high-voltage cathode active materials (CAMs) and solid-state electrolytes (SSEs) needs to be overcome with a simple, cost-effective solution. Surface coatings, which prevent the direct physical contact between CAM and SSE and in turn stabilize the interface, are considered as promising approach to solve this issue. In this work, an $Al_2O_3/LiAlO_2$ coating for $Li(Ni_{0.70}Co_{0.15}Mn_{0.15})O_2$ (NCM) is tested for ASSBs. The coating is obtained from a recently developed dry coating process followed by post-annealing at 600 °C. Structural characterization reveals that the heat treatment results in the formation of a dense $Al_2O_3/LiAlO_2$ coating layer. Electrochemical evaluations confirm that the annealing-induced structural changes are beneficial for ASSB. Cells containing $Al_2O_3/LiAlO_2$-coated NCM show a significant improvement of the rate capability and long-term cycling performance compared to those assembled from Al_2O_3-coated and uncoated cathodes. Moreover, electrochemical impedance spectroscopy analysis shows a decreased cell impedance after cycling indicating a reduced interfacial degradation for the $Al_2O_3/LiAlO_2$-coated electrode. The results highlight a promising low-cost and scalable CAM coating process, enabling large-scale cathode coating for next-generation ASSBs.

1. Introduction

All-solid-state batteries (ASSBs) are one of the most promising approaches to achieve electrical energy storage and transport electrification goals.[1–3] In comparison to state-of-the-art lithium-ion batteries (LIBs) containing liquid electrolyte, ASSBs provide an improved safety due to the non-flammability of the solid-state electrolytes (SSEs) along with the possibility to achieve higher capacity when using a lithium metal anode.[4] So far, several SSEs with high ionic conductivity have been discovered for ASSBs.[4,5] Among them, oxide-based SSEs including garnet ceramics (e.g., $Li_7La_3Zr_2O_{12}$),[6] perovskites (e.g., $Li_{1+x}Al_xTi_{2-x}(PO_4)_3$),[7] and thiophosphate-based SSEs (TSSEs)[8] including $Li_{10}GeP_2S_{12}$ are considered as promising candidates for practical applications.[9] Oxide-based SSEs require high-temperature sintering (>700 °C) to achieve sufficient interfacial contact between SSEs and cathode active materials (CAMs) due to their hard mechanical properties. Unfortunately, the heat treatment causes irreversible

R. S. Negi, R. Pan, A. Henss, M. T. Elm
Center for Materials Research (LaMa)
Justus Liebig University Giessen
Heinrich-Buff-Ring 16, 35392 Giessen, Germany

Y. Yusim, R. Pan, A. Henss, M. T. Elm
Institute of Physical Chemistry
Justus Liebig University Giessen
Heinrich-Buff-Ring 17, 35392 Giessen, Germany
E-mail: Ruijun.Pan@phys.chemie.uni-giessen.de;
Anja.Henss@phys.chemie.uni-giessen.de;
Matthias.Elm@phys.chemie.uni-giessen.de

The ORCID identification number(s) for the author(s) of this article can be found under https://doi.org/10.1002/admi.202101428.

DOI: 10.1002/admi.202101428

R. Pan
Materials Science and Engineering Program and Texas Materials Institute
University of Texas at Austin
Austin, TX 78712, USA

S. Ahmed, K. Volz
Materials Science Centre and Faculty of Physics
Philipps University Marburg
Hans-Meerwein-Strasse 6, 35043 Marburg, Germany

R. Takata, F. Schmidt
Evonik Operations GmbH
Rodenbacher Chaussee 4, 63457 Hanau, Germany

M. T. Elm
Institute of Experimental Physics I
Justus Liebig University Giessen
Heinrich-Buff-Ring 16, 35392 Giessen, Germany

ADVANCED SCIENCE NEWS
www.advancedsciencenews.com

ADVANCED MATERIALS INTERFACES
www.advmatinterfaces.de

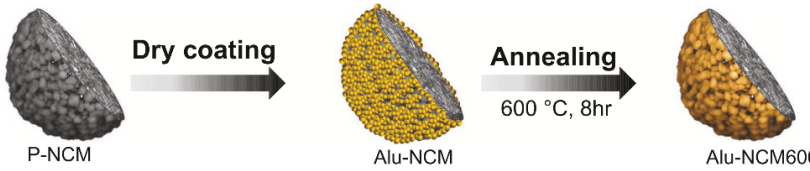

Figure 1. Schematic illustration of the $Al_2O_3/LiAlO_2$ dry coating process and the additional post-annealing process of Ni-rich NCM for ASSBs.

degradation reactions at the electrolyte–electrode interface resulting in increased interfacial resistances.[10–12] In contrast, thiophosphate-based SSEs are rather soft and, thus, provide good interfacial contact to CAMs. Furthermore, they exhibit high ionic conductivities of above 20 mS cm^{-1} at room temperature[3,13] making them more attractive for applications in ASSBs.[14]

Despite numerous advantages of TSSEs, several remaining challenges have to be addressed on the way to large-scale industrial application of ASSBs, such as interfacial stability issues[15,16] between high voltage CAMs and TSSEs. Ni-rich $LiNi_{1-x-y}Co_xMn_yO_2$ (NCM) CAMs are commonly accepted as the state-of-the-art high energy density CAMs for ASSBs with high specific capacities and high working voltages combined with mature industrial-scale production.[17,18] However, inside the cell, NCMs and TSSEs form a cathode–electrolyte interphase (CEI) consisting of degradation products of both.[19] Various studies suggest that the formed CEI layer between CAM and SSE is responsible for long-term capacity fading and limited operational life.[15,20,21] Therefore, research efforts are dedicated to improve the interfacial stability between CAMs and TSSEs.

Surface coating is a well-established strategy to enhance the interfacial stability between CAM and SSE by preventing direct physical contact.[22] For NCM-CAM, oxide-based coatings such as $LiNbO_3$,[23–25] $Li_4Ti_5O_{12}$,[24] Li_2O-ZrO_2,[26] HfO_2,[27] and $Li_3B_{11}O_{18}$[28] have been reported to improve the electrochemical performance of ASSBs, as they effectively prevent or reduce detrimental side reactions at the NCM/SSE interface. In conventional LIBs, Al_2O_3-based coatings have been considered as promising coatings due to their effectiveness against side reactions and low synthesis cost.[29–32] However, they are not well explored in ASSBs yet.[33–36] Although Al_2O_3-based coatings enhance the interfacial stability, the rate capability could not be improved significantly, primarily due to the ionically and electronically insulating nature of the coating.[37] In contrast, $LiAlO_2$ provides good lithium-ion transport properties due to partially occupied Li sites.[38] This means that $LiAlO_2$ or mixed $Al_2O_3/LiAlO_2$ coating layers stabilize the CAM/SSE interface effectively without significantly increasing the interfacial resistance.[39,40] Thus, $LiAlO_2$-based coatings could be promising candidates to improve the overall performance of ASSBs.

Surface coatings on cathode materials using wet-chemical approaches,[41] atomic layer deposition (ALD),[42] or spray coating procedures[24,43] are already successfully established in thiophosphate-based ASSBs.[44] However, wet-chemical approaches require additional drying steps that increase the energy costs and manufacturing time.[45] While the ALD technology provides thin coating layers with excellent conformity, it often requires toxic precursors and shows slow deposition rates.[34,46,47] With spray coating procedures, the manufacturing time can be reduced, but an expensive piece of instrument is needed.[44]

In order to reduce ecological and economic costs, a new dry coating procedure on CAM was recently introduced by Herzog et al.[34] It has been shown that by using a high energy mixer, fumed nanostructured Al_2O_3 physically absorb on the surface of NCM particles and form a porous Al_2O_3-coating layer, which significantly improves the electrochemical rate performance and capacity retention in liquid-electrolyte-based LIBs.[34]

In the study presented here, we modified the dry coating procedure by using an additional annealing step in order to make it more suitable for thiophosphate-based ASSBs and to achieve a dry-processed $Al_2O_3/LiAlO_2$ coating for $Li(Ni_{0.70}Co_{0.15}Mn_{0.15})O_2$ (NCM701515) CAM. The high-temperature treatment is found to improve various aspects of the coating (such as better interface formation, reduced porosity, and thickness), which altogether significantly improve the electrochemical performance of the NCM-based ASSBs in terms of the C-rate and long-term cycling performance. The full cells with coated NCM cathodes show a decreased interfacial impedance, which indicates a better interfacial stability between CAM and TSSE. Our results highlight that the low-cost and simple dry coating process without any detrimental environmental solvents is a highly promising approach for large-scale industrial production of coated cathode active material for next-generation ASSBs.

2. Results and Discussion

2.1. Characterization of the Al_2O_3- and $Al_2O_3/LiAlO_2$-Coated NCM

Figure 1 shows a schematic illustration of the dry coating process used to coat NCM secondary particles with $Al_2O_3/LiAlO_2$. As described in the Experimental Section, the Al_2O_3 powder was mixed with the NCM powder in a high-energy mixer to achieve an Al_2O_3 coating on the surface of the NCM secondary particles (denoted as Alu-NCM) in the first step. In a second step, the Alu-NCM was divided into two batches. One of the batches was annealed at 600 °C for 8 h, resulting in the conversion of Al_2O_3 to $Al_2O_3/LiAlO_2$ (denoted as Alu-NCM600). The formation of $Al_2O_3/LiAlO_2$ is confirmed by X-ray photoelectron spectroscopy (XPS) as will be discussed later. The principle of the dry coating process is described in detail by Herzog et al.[34] In brief, during high energy mixing, nanostructured fumed Al_2O_3 powder produced from flame hydrolysis is deagglomerated into smaller aggregates with a high specific surface area. This ensures a good adhesion capability of the aggregates at the CAM surface, which

ADVANCED SCIENCE NEWS
www.advancedsciencenews.com

ADVANCED MATERIALS INTERFACES
www.advmatinterfaces.de

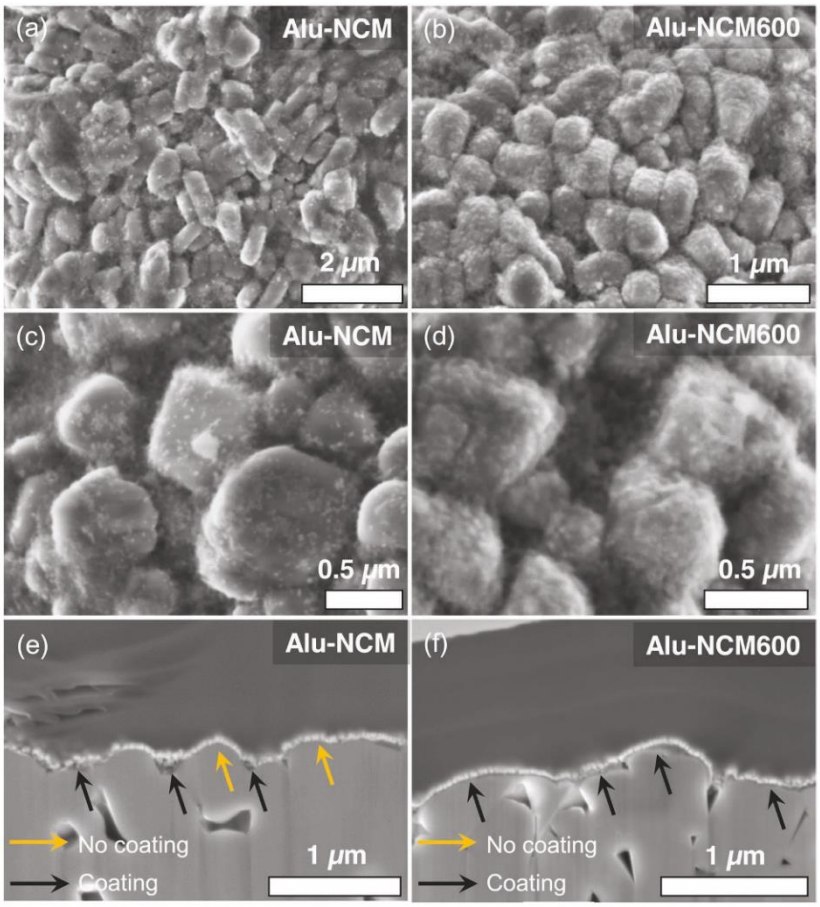

Figure 2. SEM images of the coated NCM powder: a,c) Alu-NCM and b,d) Alu-NCM600. SEM cross-section images of coated NCM secondary particles: e) Alu-NCM and f) Alu-NCM600. For Alu-NCM the coating is only observable between the NCM grains as particles (black arrow), f) while for Alu-NCM600 a homogeneous coating is detectable as a dark line between NCM and the deposited Pt layer (white layer).

is decisive for the formation of a complete and strongly adherent coating layer.[34] Due to the short processing time, easy application, and solvent-free nature, the dry coating process is a promising method for large-scale production at low costs.

The NCM-based CAM with an Al_2O_3 and $Al_2O_3/LiAlO_2$ coating layer was investigated by scanning electron microscopy (SEM). As shown in Figure S1 in the Supporting Information, the secondary particles of the uncoated NCM are spherical in shape with a diameter of 5–15 µm and are composed of nano-sized primary particles. The SEM images in **Figure 2**a–d show a comparison between Alu-NCM and Alu-NCM600. It can be seen that in both cases, the coated NCM reveals a narrow size distribution of the primary particles, which agrees well with those of the uncoated NCM primary particles (see Figure S1, Supporting Information). This indicates that the mixing intensity is strong enough to break the fumed Al_2O_3 agglomerates and to coat the secondary NCM particles while maintaining their structural integrity during the dry coating process.

However, the surface of non-annealed Alu-NCM shows significant differences compared to that of Alu-NCM600. After the coating process, the Al_2O_3 looks inhomogeneously distributed with incomplete coverage of the NCM surface. In contrast, the coating seems to be fused after the annealing step, resulting in a very homogeneous and complete coverage of the NCM surface. Focused-ion beam (FIB)-SEM analysis was carried out to compare the cross-section of the NCM particles after coating and annealing. In Figure 2e, the coating without annealing looks rough and is mainly accumulated in the gaps between neighboring primary NCM particles. However, as shown in Figure 2f, the coating after annealing is much smoother and completely distributed over the surface with slight variations of the thickness (see also Figure S2, Supporting Information). In addition, SEM images of Alu-NCM and Alu-NCM600 with higher magnification are shown in Figure S3a,b in the Supporting Information. SEM-energy dispersive spectroscopy (EDS) mapping confirms the homogeneous distribution of Al

ADVANCED SCIENCE NEWS
www.advancedsciencenews.com

ADVANCED MATERIALS INTERFACES
www.advmatinterfaces.de

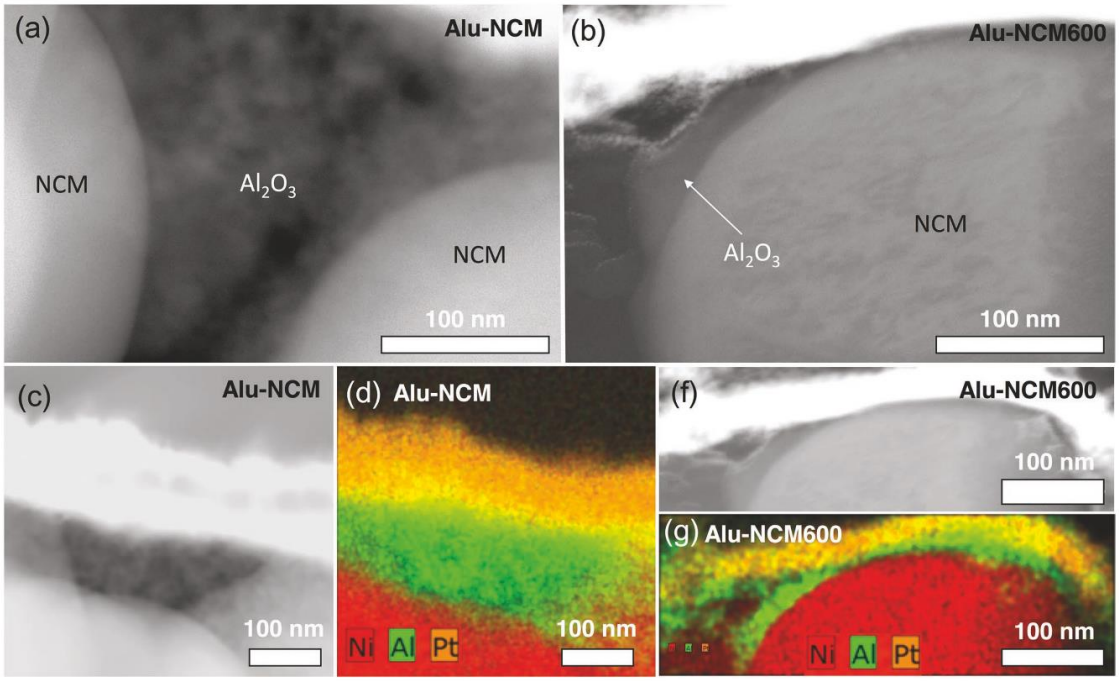

Figure 3. STEM-HAADF images of a cross-section of coated NCM701515: a,c) Alu-NCM and b,f) Alu-NCM600. STEM-EDS analysis of a cross-section of coated NCM701515 showing a three-color superposition image of Ni, Al, and Pt: d) Alu-NCM and g) Alu-NCM600.

on Alu-NCM600 as shown in Figure S3c in the Supporting Information.

For a more detailed surface analysis, the microstructure of the coating layer was characterized by transmission electron microscopy (TEM) in combination with EDS.[48] As shown in **Figure 3**a,c, for Alu-NCM, the coating layer is highly porous as observed by Herzog et al.[34] Figure 3a shows that the gaps between the primary NCM particles are completely filled with Al_2O_3, leaving the surface uncovered. On the other hand, in the case of Alu-NCM600 (Figure 3b,f), the coating layer is less porous and much thinner after the annealing step. No structural changes of the NCM particles are observable. Only the structural properties of the coating are affected by the additional annealing step. EDS analysis confirms the drastic change of the coating thickness and porosity after annealing (Figure 3d,g). There are no hints for the diffusion of aluminum into the NCM bulk phase observable for the non-annealed Alu-NCM sample. This is expected as no high-temperature step is involved in the coating process and aluminum diffusion is unlikely to occur at room temperature.[34] However, in case of Alu-NCM600 (Figure 3g) the possibility of interdiffusion of a small Al amount into the NCM bulk structure during annealing cannot be excluded.[49] As reported in literature, the interdiffusion of Al between the CAM and the coating layer may enhance the overall stability of the CAM and lead to improved cycling performance.[50] However, a detailed discussion of aluminum diffusion into the NCM bulk is beyond the scope of this study.

The porosity of the CAM particles after the coating process was investigated by N_2 adsorption. The measurements were evaluated using the Brunauer–Emmett–Teller (BET) model. As shown in **Figure 4**a, the uncoated NCM has a very low BET surface of 0.40 $m^2\ g^{-1}$. After coating with fumed Al_2O_3, the BET surface area increases drastically to 0.70 $m^2\ g^{-1}$ (Alu-NCM sample), which is well expected due to the high porosity of the coating as observed by TEM measurements (Figure 3c). After the annealing step (Alu-NCM600 sample), the BET area is significantly decreased (0.50 $m^2\ g^{-1}$). This confirms that the annealing step leads to a densification of the coating layer and a lower surface area.

Powder X-ray diffraction (XRD) measurements were carried out on P-NCM, Alu-NCM and Alu-NCM600 samples to investigate the potential influence of the coating process on the crystal structure of NCM. As shown in Figure 4b, the XRD patterns confirm that all NCM samples exhibit the same crystal structure of $LiCoO_2$ (space group *R-3m*). No peak shifts are observed, confirming that no significant bulk crystallographic defects are generated in the NCM structure during coating or the annealing step. In addition, both coated samples show no additional peaks belonging to Al_2O_3 due to the low amount of coating material, as observed in our previous study.[39]

XPS measurements were carried out to investigate the coating composition and the effect of annealing on the structural properties of the coating layer. The NCM XPS analysis delivers quantitative element and compound-specific information with a detection limit of about 1 at%.[51] The survey

ADVANCED SCIENCE NEWS
www.advancedsciencenews.com

ADVANCED MATERIALS INTERFACES
www.advmatinterfaces.de

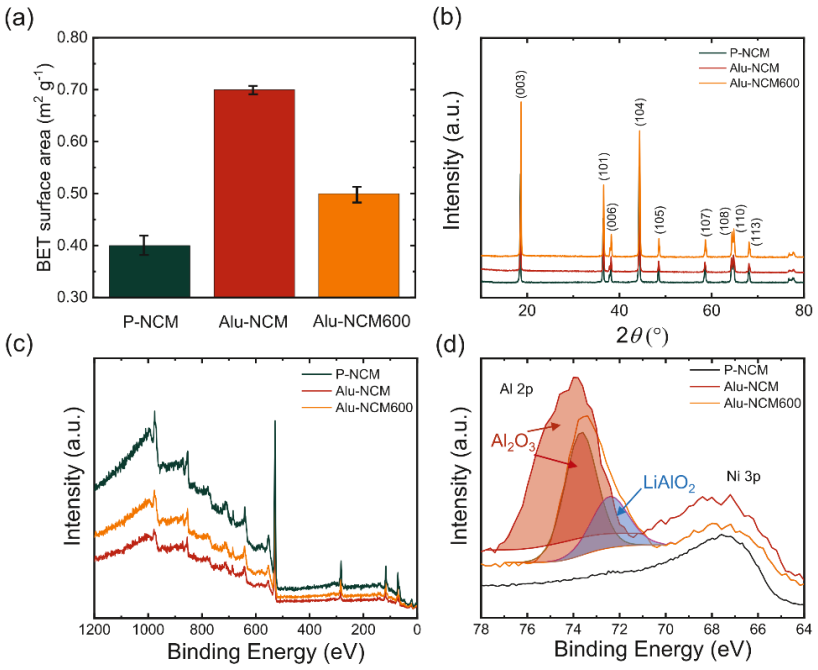

Figure 4. Comparison of a) Brunauer–Emmett–Teller (BET) measurements, b) X-ray diffraction pattern, c) survey XP spectra, and d) detailed XP spectra of P-NCM, Alu-NCM, and Alu-NCM600.

spectrum of P-NCM shown in Figure 4c confirms the presence of Ni, Co, Mn, and O without any additional elements apart from the carbon contaminations at the NCM surface, which is commonly used as a calibration reference for X-ray photoelectron (XP) spectra.[52] In addition, the characteristic peak of Al 2p is detected on the surface of Alu-NCM and Alu-NCM600, which proves the existence of Al species on the surface of the coated NCM with Al_2O_3 (Figure 4d). A detailed spectrum in the region between 78 and 64 eV is shown in Figure 4d. It includes the Al 2p core levels and the Ni 3p peak. No peak shift is observed for the Ni 3p peak for all samples, which additionally confirms the structural stability of NCM during the coating and annealing processes. However, the presence of Ni implies that the coating is not completely covering the NCM surface or, alternatively, thinner than the typical probing depth of XPS of about 3–7 nm,[53] as already indicated by the TEM measurements shown in Figure 3f,g. Deconvolution of the Al 2p peak (Figure 4d) reveals that Alu-NCM shows only one peak at a binding energy of 73.9 eV, which is distinctive for Al atoms in an oxygen environment, such as Al_2O_3 or $Al(OH)_3$.[35] However, after annealing a significant peak shift of Al 2p to a lower binding energy is observed. The deconvolution confirms that the signal comprises two different peaks. One at a binding energy of 73.9 eV (corresponding to Al_2O_3 or $Al(OH)_3$)[53] and a second one at 72.8 eV, which is attributed to $LiAlO_2$ as observed by Tang et al.[54] The results confirm the conversion of an insulating Al_2O_3 coating into an ion conducting $Al_2O_3/LiAlO_2$ coating during heat treatment, as discussed in detail in previous studies.[39,40] The diffusion of Li^+ from NCM into the Al_2O_3 layer during the heat treatment is expected to result in the formation of conductive pathways for the Li^+ ions and thus an improvement of the ionic conductivity of the $Al_2O_3/LiAlO_2$ coating.[39]

The results reveal the tremendous effect of the annealing step on the structural properties of the coating layer, which are illustrated in **Figure 5**. The recently developed dry coating process enables the successful deposition of an Al_2O_3 coating on the surface of NCM particles. The coating is rather thick, porous, and inhomogeneously distributed on the surface of NCM. After annealing at 600 °C, various aspects of the coating morphology are improved. The coating becomes more homogenous (SEM, FIB-SEM), thinner (SEM, TEM), and exhibits a lower porosity, i.e., lower surface area as confirmed by TEM and BET. In addition, the diffusion of Li^+ into the coating results in the conversion from an insulating Al_2O_3 coating layer to $Al_2O_3/LiAlO_2$, which is known to exhibit an improved Li^+ conductivity. All these changes are expected to affect the electrochemical performance of NCM, as will be discussed in detail in the next section.

2.2. Electrochemical Characterization

To elucidate the impact of the obtained microstructural and compositional differences of the two different coatings on the cell performance, we assembled and cycled ASSB cells at different C-rates. The C-rate was varied between 0.1 and 2 C,

ADVANCED SCIENCE NEWS
www.advancedsciencenews.com

ADVANCED MATERIALS INTERFACES
www.advmatinterfaces.de

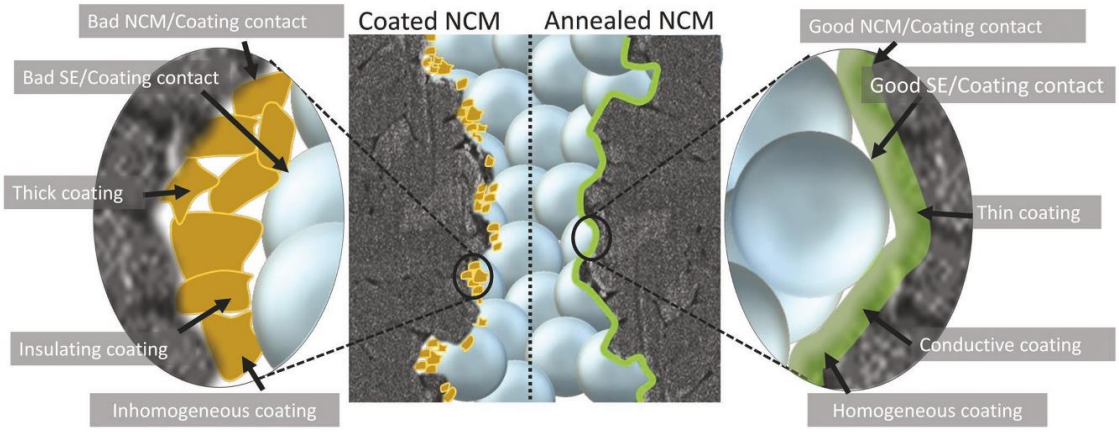

Figure 5. Schematic illustration comparing the differences in coating properties before and after annealing.

within the voltage window of 2.0–3.7 V (vs In/InLi), exceeding the electrochemical stability window of thiophosphate-based SSEs (1.7–2.3 V vs Li^+/Li).[55] The rate capability tests and the long-term cycling stability were investigated for two independent cells in all three cases to ensure reproducibility of the results.

Figure 6a shows the rate capability performance of the coated CAMs in comparison with the performance of the uncoated ones. For a better comparison, Figure 6b also shows the normalized discharge capacity, i.e., the specific discharge capacity of each cell was normalized to the CAM mass and related to the initial specific discharge capacity. The initial specific discharge capacity of the P-NCM cells (136 mAh g^{-1}) is found significantly lower compared to cells with liquid electrolytes (≈ 180 mAh g^{-1})[34,39] indicating a higher interfacial degradation of the SSE than for cells with liquid electrolytes (as the achievable theoretical capacity of NCM is ≈ 180 mAh g^{-1}) as reviewed by Jena et al.[56] The Alu-coated NCM material shows a slightly lower initial specific capacity (130 mAh g^{-1}) than the P-CAM. This indicates that the insulating nature of the Al_2O_3 coating along with its structural properties (such as porosity, insufficient contact area, and interfacial degradation) limits the initial discharge capacity. In contrast, Alu-NCM600 shows a significantly higher initial specific discharge capacity (154 mAh g^{-1}). This is attributed to a lower interfacial resistance, either due to the higher Li^+ conductivity of the Al_2O_3/$LiAlO_2$ coating layer, an increased contact area, or improved interfacial stability (as discussed in the previous section). Furthermore, with increasing C-rate, the discharge capacity of Alu-NCM tends to be slightly superior to P-NCM, revealing the protective effect of the Al_2O_3 coating. However, at a C-rate of 2 C, both the P-NCM and the Alu-NCM samples exhibit no capacity, probably caused by a high internal cell resistance. However, a significant improvement of the C-rate performance in our ASSBs is observed for the Alu-NCM600 samples for all C-rates. In particular, Alu-NCM600 shows a discharge capacity of ≈20 mAh g^{-1} even at 2 C. These results indicate that at high C-rates, a sufficient lithium-ion conductivity still persists in the Al_2O_3/$LiAlO_2$ coating layer, while in the case of the uncoated NCM, the formation of an insulating CEI caused by electrolyte degradation impedes lithium-ion exchange between electrode and electrolyte. Thus, the less porous and more conductive Al_2O_3/$LiAlO_2$ coating material in Alu-NCM600 enables a superior rate capability as compared to Al_2O_3-coated Alu-NCM samples. It is worth noting that the Al_2O_3-dry coating is very effective in improving the electrochemical performance of liquid electrolyte-based cells, as recently shown by Herzog et al.[34] One main reason is that the liquid electrolyte can penetrate into the highly porous Al_2O_3 coating, which facilitates the transport of lithium ions through the surface layer. In contrast, the solid electrolyte used in ASSBs is not able to reach the interior of the pores of the coating (Alu-NCM), i.e., the porous coating impedes lithium-ion transport between active material and electrolyte due to its insulating properties and the reduced contact area. Thus, the results highlight that effective coatings for ASSBs need to fulfill other demands regarding their structural properties than coatings used for liquid-electrolyte-based LIBs.

After the C-rate capability tests, the long-term cycling performance was investigated. Figure 6c compares the discharge capacity and the coulombic efficiency (CE) of pristine NCM, Alu-NCM, and Alu-NCM600 for 100 cycles at 0.25 C in the voltage range between 2.0 and 3.7 V (vs In/InLi). A significantly improved capacity retention is found for Alu-NCM600, which exhibits a discharge capacity of 75 mAh g^{-1} after 100 cycles implying capacity retention of 54% based on the first cycle capacity. In contrast, for the P-NCM sample, a capacity of only 25 mAh g^{-1}, i.e., capacity retention of 20%, is achieved. Furthermore, the corresponding CE of the Alu-NCM600 is superior compared to that of the uncoated sample. As shown in Figure 6d,e, the increase in overpotential is much higher for P-NCM than for Alu-NCM, indicating a more severe electrolyte degradation at the P-NCM surface. The Alu-NCM sample shows a similar behavior as P-NCM during long-term cycling. Although the Al_2O_3 coating certainly suppresses the electrolyte degradation at the NCM-electrolyte interface, its insulating nature, along with the rather worse coating properties, is responsible for a high interfacial resistance, which explains the poor cycling performance. However, the results confirm that

ADVANCED SCIENCE NEWS
www.advancedsciencenews.com

ADVANCED MATERIALS INTERFACES
www.advmatinterfaces.de

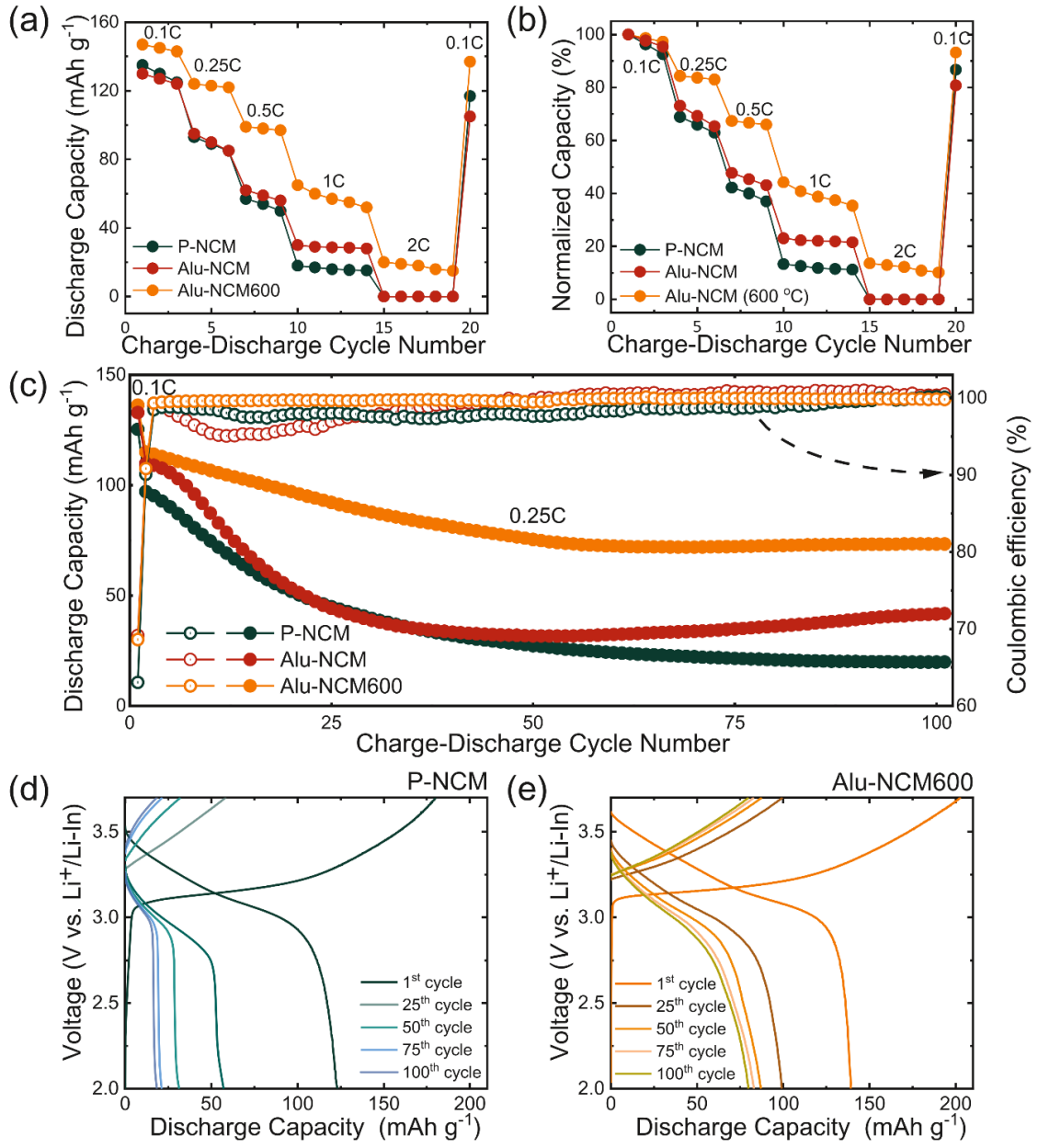

Figure 6. Comparison of a) rate capability and b) corresponding normalized capacity plot of P-NCM, Alu-NCM, and Alu-NCM600. c) Long-term cycling capability at 0.25 C of P-NCM, Alu-NCM, and Alu-NCM600. d,e) Charge–discharge voltage profiles of P-NCM and Alu-NCM600, respectively. The cells were cycled in a voltage window of 2.0 and 3.7 V versus In|InLi, corresponding to 2.6–4.3 V versus Li^+/Li at 25 °C.

the $Al_2O_3/LiAlO_2$ coating significantly improves the long-term cycling stability of NCM in ASSBs. The coating is expected to prevent side reactions between Li_6PS_5Cl (LPS) and NCM, which lead to the formation of a highly resistive CEI consisting of sulfur and phosphorus pentasulfide oxidation products.[19]

To support this assumption, electrochemical impedance spectroscopy (EIS) measurements were carried out on ASSB cells containing P-NCM or Alu-NCM600 as EIS allows to distinguish between different processes in ASSBs and to determine their contribution to the total impedance of the cells.[15,16,57]

ADVANCED SCIENCE NEWS
www.advancedsciencenews.com

ADVANCED MATERIALS INTERFACES
www.advmatinterfaces.de

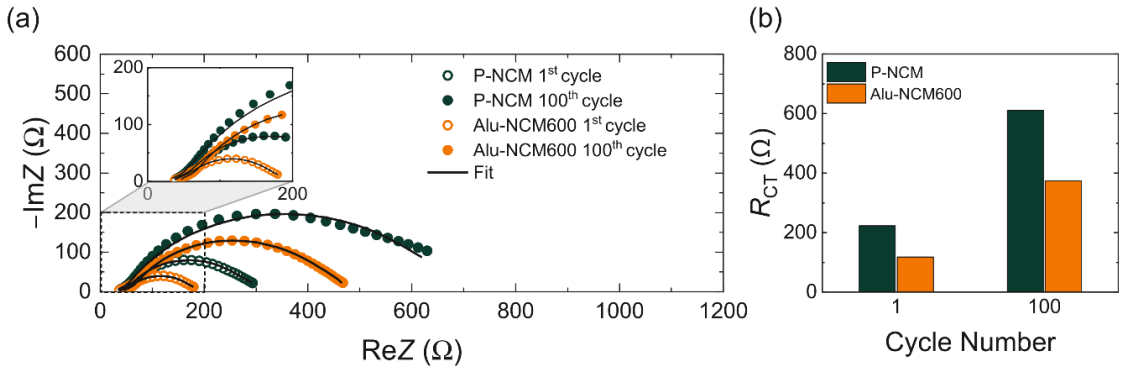

Figure 7. Comparison of a) Nyquist plots of the impedance of full cells containing P-NCM and Alu-NCM600 after the 1st and 100th cycle. b) Corresponding charge transfer resistance R_{CT} measured at an open-circuit voltage of 3.1 V.

As no drastic improvement of the cycling capability is found for the Alu-NCM samples, only P-NCM and Alu-NCM600 are investigated. The EIS measurements were performed at an open-circuit potential of 3.1 V (vs In/InLi) after the 1st cycle and 100th cycle to determine the long-term impedance evolution. A constant potential step was included after constant-current discharge in order to achieve an equilibration of Li within the CAM particles by diffusion processes. This step is necessary to ensure comparability between P-NCM and Alu-NCM600 as the impedance of layered oxide cathode materials depends on the lithium content (state of charge) of the electrode.[58] Comparing the impedance spectra after the 1st and 100th cycle, displayed in **Figure 7**a, a distinct increase of the impedance is observed for the pristine sample indicating a strong degradation reaction at the SSE/CAM interface due to the oxidation of the solid electrolyte.[16,21] The total impedance of the coated NCM cell is significantly lower after the 1st and 100th cycle, corroborating the protection function of the $Al_2O_3/LiAlO_2$ coating. The spectra were fitted using the transmission line model, which describes the impedance of porous electrodes considering SSE-filled pores.[59,60] Due to the presence of nonblocking conditions and negligible electronic conductivity, a Bisquert Open element[61] was used to fit the composite cathode (CC) impedance. The equivalent circuit model, including the Bisquert open element, is described in more detail in Figure S4 in the Supporting Information. The fitting reveals that the differences in the impedance are mainly caused by changes in the charge transfer resistance R_{CT}. The other fitting parameters, such as the anode contribution or the ionic resistance of the electrolyte, do not differ significantly for the different cells (see Table S1, Supporting Information). The determined values of the charge transfer resistance R_{CT} after the 1st and 100th cycles for the pristine and coated samples are shown in Figure 7b. As is evident, the charge transfer resistance of the Alu-NCM600-containing cell is significantly lower not only after the 1st but also after the 100th cycle. Moreover, the comparison with the other impedance values obtained from the fitting (Table S1, Supporting Information) demonstrates that the impedance of the full cell is dominated by the charge transfer resistance of the composite cathode. The comparison of the R_{CT} values confirms that the $Al_2O_3/LiAlO_2$ coating layer significantly improves the interfacial stability by reducing oxidative interfacial decomposition of the SSE on the cathode side.

3. Conclusions

In this study, we present a low-cost, straightforward, and scalable dry coating process to modify the surface of Ni-rich NCM for thiophosphate-based ASSBs. A highly efficient $Al_2O_3/LiAlO_2$ coating is achieved by a high-energy mixing process followed by a high-temperature annealing step. While the Al_2O_3 coating shows a certain porosity after the coating process, the annealing step results in the formation of a dense and thin coating layer as confirmed by TEM and BET measurements. Furthermore, XPS analysis confirms that a mixed $Al_2O_3/LiAlO_2$ layer is formed during the heat treatment, while no significant changes in bulk NCM are observed. Electrochemical characterization demonstrates that the $Al_2O_3/LiAlO_2$ coating significantly improves the electrochemical performance of NCM cathodes in LPS-based ASSBs. As the coating prevents the direct contact between CAM and thiophosphate-based SSE, interfacial degradation reactions responsible for the formation of an insulating CEI are reduced, as demonstrated by EIS analysis. Compared to the porous Al_2O_3 coating, the $Al_2O_3/LiAlO_2$ coating layer provides an improved rate capability and long-term cycling performance, including higher initial cycling capacity. Thus, the results present a highly effective dry coating method, which is suitable for large-scale processing of cathodes for next-generation ASSBs, excluding any solvent-related influences and costs.

4. Experimental Section

Surface Modification of Ni-Rich NCM Using an Al_2O_3-Dry Coating Process: Commercial $Li(Ni_{0.70}Co_{0.15}Mn_{0.15})O_2$ (NCM701515, Linyi Gelon LIB. Co.) was used as CAM and nanostructured fumed Al_2O_3 (AEROXIDE Alu 65, primary particle ≈12 nm, Evonik Operations GmbH) powder was utilized as coating material during the dry-coating process. A lab-scale high-energy Somakon mixer MP-GL (Somakon Verfahrenstechnik UG) was used for mixing. Two different steps were performed for the dry-coating process. Initially, the CAM powder was well mixed with nanostructured Al_2O_3 (1 wt%) at 500 rpm for 1 min.

ADVANCED SCIENCE NEWS
www.advancedsciencenews.com

ADVANCED MATERIALS INTERFACES
www.advmatinterfaces.de

Subsequently, the mixing intensity was raised to 2000 rpm for 6 min to achieve a well-distributed coating on the surface of the CAM. Then, the powder obtained was divided into two batches. The first batch was dried and transferred into the glovebox for further use (denoted as Alu-NCM). The second batch was additionally annealed at 600 °C for 8 h to modify the coating layer. Subsequently, it was dried and transferred to the glovebox for further use (denoted as Alu-NCM600).

During the first step of the dry-coating process, the fumed nanostructured Al_2O_3 deagglomerates into smaller aggregates and interacts with the cathode surface, resulting in smaller Al_2O_3 aggregates with very strong adhesion to the CAM surface. During the second step, at higher mixing rotation, desirable densification and coalescence of Al_2O_3 aggregates is achieved on the surface of the cathode, which results in a highly homogenous coating.

Materials Characterization: The surface morphology and the elemental composition of the pristine and coated NCM were investigated with SEM (Merlin, Zeiss) at an accelerating voltage of 7 kV and a current of 3000 pA. FIB cross-sections of the coated secondary particles were prepared by a dual-beam JEOL JIB-4601 FIB -SEM. First, a thin layer of platinum was deposited on the surfaces of the coated secondary particles via a Leica EM ACE600 sputter coater before loading them to the FIB-SEM. This is done to protect the coated surfaces of the secondary particles coming in direct contact with the electron beam during FIB cross-section preparation. On top of the thin platinum coating, thick carbon and tungsten protective layers were deposited, respectively, using a Ga-ion beam to further protect the surfaces from Ga-ion beam damage during FIB milling. The samples were milled down using a 30 kV Ga-ion beam to roughly about 200 nm and further thinned down using a 5 kV Ga-ion beam to electron transparency. A double Cs-corrected JEOL 2200-FS microscope was used for scanning TEM (STEM) high-angle annular dark-field (HAADF) imaging and EDS. The microscope was operated at 200 kV.

Powder XRD diffractograms of pristine and coated NCM were obtained using an Empyrean XRD (Panalytical) system with Cu Kα radiation. The XPS analysis was performed using a PHI5000 Versa Probe II (Physical Electronics GmbH) with an Al anode. The pass energy of the analyzer was fixed at 93.5 eV and 23.5 eV to obtain the survey and the detailed spectra, respectively. The chamber pressure was maintained below 10^{-7} Pa. Furthermore, Brunauer–Emmett–Teller (BET) analysis was performed on pristine and coated NCM in order to determine the porosity change after coating and heat treatment. Single point BET was performed using a MICROMERITICS TRISTAR 3000 with a nitrogen/helium flow (28.6% N_2). The samples were degassed for 20 min at 150 °C before the measurement.

Composite Cathode: The CC comprise the pristine or coated $Li(Ni_{0.70}Co_{0.15}Mn_{0.15})O_2$ (NCM701515), LPS (NEI Corporation), and vapor-grown carbon fibers (VGCFs, Sigma-Aldrich Inc., iron-free). At first, NCM and LPS powders were mixed in a mass ratio of 70:30 (volume ratio 47:53). Then, 3 wt% of VGCF was additionally added (exact mass ratio 68:29.1:2.9 (NCM: LPS:VGCF)) to the mixture. Finally, the resulting mixture was hand grounded using an agate mortar for 15 min.

Cell Assembly: The composite cathode was prepared fresh before preparing the cells in order to avoid time-dependent side reactions. All the electrochemical tests were performed using an in-house (pellet type) cell casing.[15,16] For cell assembly, one side of the poly(ether-ether-ketone) (PEEK) cylinder (inner diameter: 10 mm) was closed using a stainless-steel stamp. 60 mg of LPS was uniformly put into the PEEK cylinder, followed by a manual hand compression. Subsequently, 12 mg of CC was added to one side of the pressed LPS and distributed uniformly. The whole stack was then pressed uniaxially at 30 kN (380 MPa) for a duration of 3 min, resulting in a pressed pellet with a thickness of 430 µm (400 µm SSE and 30 µm SSE). An indium foil (In, chemPUR GmbH, diameter = 9 mm, thickness = 125 µm) and a lithium foil (Li, Albermarle (Rockwood Lithium GmbH), diameter = 9 mm, thickness = 120 µm) were placed on the other side of the pellet as an anode. Then, the whole stack was closed using another stainless-steel stamp. Finally, the complete cell assembly was fully closed. During electrochemical characterization, an external frame under constant pressure of ≈50 MPa was used around the cell casing.

Electrochemical Characterization: For electrochemical characterization, Maccor inc. potentiostats/galvanostats and VMP-300 potentiostats (Biologic) were used. The cycling tests (i.e., C-rate and long-term cycling tests) were performed on Maccor inc., while the electrochemical impedance spectroscopy (EIS) measurements were performed on VMP-300. The cells were cycled in a voltage window of 2.0 and 3.7 V versus In|InLi, corresponding to 2.6–4.3 V versus Li^+/Li at 25 °C. For the C-rate tests, the cells were cycled up to 2 C, 1 C = 200 mA g^{-1} (three cycles at 0.1 C, three cycles at 0.25 C, three cycles at 0.5 C, five cycles at 1 C) and five cycles at 2 C). For the long-term cycling, the cells were cycled at 0.1 C for one cycle, followed by 100 cycles at 0.25 C. EIS measurements were performed after the 1st and 100th cycle. All EIS measurements were performed in the frequency range between 7 MHz and 50 mHz, applying a 10 mV AC bias. To ensure reproducibility, every electrochemical experiment was performed with two independent cells.

Supporting Information

Supporting Information is available from the Wiley Online Library or from the author.

Acknowledgements

R.S.N. and Y.Y. contributed equally to this work. R.S.N. and M.T.E. thank the German Federal Ministry of Education and Research (BMBF) for the funding of the NanoMatFutur project NiKo (03XP0093). S.A. and K.V. acknowledge the Federal Ministry of Education and Research (BMBF, Germany) within the cluster of competence FESTBATT (project 03XP0176D).

Open access funding enabled and organized by Projekt DEAL.

Conflict of Interest

The authors declare no conflict of interest.

Data Availability Statement

The data that support the findings of this study are available from the corresponding author upon reasonable request.

Keywords

all-solid-state batteries, electrolyte–electrode interface modification, lithium-ion batteries, solid-state electrolytes, surface coatings on cathode materials

Received: August 5, 2021
Revised: August 20, 2021
Published online: November 9, 2021

[1] G. E. Blomgren, *J. Electrochem. Soc.* **2017**, *164*, A5019.
[2] D. Liu, W. Zhu, Z. Feng, A. Guerfi, A. Vijh, K. Zaghib, *Mater. Sci. Eng. B* **2016**, *213*, 169.
[3] Y. Kato, S. Hori, T. Saito, K. Suzuki, M. Hirayama, A. Mitsui, M. Yonemura, H. Iba, R. Kanno, *Nat. Energy* **2016**, *1*, 16030.
[4] J. Janek, W. G. Zeier, *Nat. Energy* **2016**, *1*, 16141.
[5] J. M. Tarascon, M. Armand, *Nature* **2001**, *414*, 359.

ADVANCED SCIENCE NEWS
www.advancedsciencenews.com

ADVANCED MATERIALS INTERFACES
www.advmatinterfaces.de

[6] S. Ramakumar, C. Deviannapoorani, L. Dhivya, L. S. Shankar, R. Murugan, *Prog. Mater. Sci.* **2017**, *88*, 325.
[7] M. Monchak, T. Hupfer, A. Senyshyn, H. Boysen, D. Chernyshov, T. Hansen, K. G. Schell, E. C. Bucharsky, M. J. Hoffmann, H. Ehrenberg, *Inorg. Chem.* **2016**, *55*, 2941.
[8] N. Kamaya, K. Homma, Y. Yamakawa, M. Hirayama, R. Kanno, M. Yonemura, T. Kamiyama, Y. Kato, S. Hama, K. Kawamoto, A. Mitsui, *Nat. Mater.* **2011**, *10*, 682.
[9] T. Krauskopf, F. H. Richter, W. G. Zeier, J. Janek, *Chem. Rev.* **2020**, *120*, 7745.
[10] M. Bertrand, S. Rousselot, D. Aymé-Perrot, M. Dollé, *Mater. Adv.* **2021**, *2*, 2989.
[11] J.-H. Seo, H. Nakaya, Y. Takeuchi, Z. Fan, H. Hikosaka, R. Rajagopalan, E. D. Gomez, M. Iwasaki, C. A. Randall, *J. Eur. Ceram. Soc.* **2020**, *40*, 6241.
[12] A. Kim, S. Woo, M. Kang, H. Park, B. Kang, *Front. Chem.* **2020**, *8*, 468.
[13] S. V. Patel, S. Banerjee, H. Liu, P. Wang, P.-H. Chien, X. Feng, J. Liu, S. P. Ong, Y.-Y. Hu, *Chem. Mater.* **2021**, *33*, 1435.
[14] M. Shoji, E. Jianfeng Cheng, T. Kimura, K. Kanamura, *J. Phys. D: Appl. Phys.* **2019**, *52*, 103001.
[15] W. Zhang, D. A. Weber, H. Weigand, T. Arlt, I. Manke, D. Schröder, R. Koerver, T. Leichtweiss, P. Hartmann, W. G. Zeier, J. Janek, *ACS Appl. Mater. Interfaces* **2017**, *9*, 17835.
[16] R. Koerver, I. Aygün, T. Leichtweiß, C. Dietrich, W. Zhang, J. O. Binder, P. Hartmann, W. G. Zeier, J. Janek, *Chem. Mater.* **2017**, *29*, 5574.
[17] P. Zou, Z. Lin, M. Fan, F. Wang, Y. Liu, X. Xiong, *Appl. Surf. Sci.* **2020**, *504*, 144506.
[18] X. Li, W. Peng, R. Tian, D. Song, Z. Wang, H. Zhang, L. Zhu, L. Zhang, *Electrochim. Acta* **2020**, *363*, 137185.
[19] D. H. S. Tan, E. A. Wu, H. Nguyen, Z. Chen, M. A. T. Marple, J.-M. Doux, X. Wang, H. Yang, A. Banerjee, Y. S. Meng, *ACS Energy Lett.* **2019**, *4*, 2418.
[20] S. Wang, R. Fang, Y. Li, Y. Liu, C. Xin, F. H. Richter, C.-W. Nan, *J. Materiomics* **2021**, *7*, 209.
[21] F. Walther, R. Koerver, T. Fuchs, S. Ohno, J. Sann, M. Rohnke, W. G. Zeier, J. Janek, *Chem. Mater.* **2019**, *31*, 3745.
[22] A. Banerjee, X. Wang, C. Fang, E. A. Wu, Y. S. Meng, *Chem. Rev.* **2020**, *120*, 6878.
[23] J. Zhang, H. Zhong, C. Zheng, Y. Xia, C. Liang, H. Huang, Y. Gan, X. Tao, W. Zhang, *J. Power Sources* **2018**, *391*, 73.
[24] K. Takada, N. Ohta, L. Zhang, K. Fukuda, I. Sakaguchi, R. Ma, M. Osada, T. Sasaki, *Solid State Ionics* **2008**, *179*, 1333.
[25] S. Yubuchi, S. Teragawa, K. Aso, K. Tadanaga, A. Hayashi, M. Tatsumisago, *J. Power Sources* **2015**, *293*, 941.
[26] S. Ito, S. Fujiki, T. Yamada, Y. Aihara, Y. Park, T. Y. Kim, S.-W. Baek, J.-M. Lee, S. Doo, N. Machida, *J. Power Sources* **2014**, *248*, 943.
[27] D. Kitsche, Y. Tang, Y. Ma, D. Goonetilleke, J. Sann, F. Walther, M. Bianchini, J. Janek, T. Brezesinski, *ACS Appl. Energy Mater.* **2021**, *4*, 7338.
[28] Y.-Q. Zhang, Y. Tian, Y. Xiao, L. J. Miara, Y. Aihara, T. Tsujimura, T. Shi, M. C. Scott, G. Ceder, *Adv. Energy Mater.* **2020**, *10*, 1903778.
[29] J. Cho, Y. Jeong Kim, B. Park, *Chem. Mater.* **2000**, *12*, 3788.
[30] J.-Y. Liao, A. Manthiram, *J. Power Sources* **2015**, *282*, 429.
[31] R. S. Negi, S. P. Culver, A. Mazilkin, T. Brezesinski, M. T. Elm, *ACS Appl. Mater. Interfaces* **2020**, *12*, 31392.
[32] R. S. Negi, S. P. Culver, M. Wiche, S. Ahmed, K. Volz, M. T. Elm, *Phys. Chem. Chem. Phys.* **2021**, *23*, 6725.
[33] L. Liu, *Solid State Ionics* **2002**, *152–153*, 341.
[34] M. J. Herzog, N. Gauquelin, D. Esken, J. Verbeeck, J. Janek, *Energy Technol.* **2021**, *9*, 2100028.
[35] W. Zhu, X. Huang, T. Liu, Z. Xie, Y. Wang, K. Tian, L. Bu, H. Wang, L. Gao, J. Zhao, *Coatings* **2019**, *9*, 92.
[36] X. Wen, K. Liang, L. Tian, K. Shi, J. Zheng, *Electrochim. Acta* **2018**, *260*, 549.
[37] X. Li, J. Liu, M. Norouzi Banis, A. Lushington, R. Li, M. Cai, X. Sun, *Energy Environ. Sci.* **2014**, *7*, 768.
[38] A. Garcia, *Solid State Ionics* **1990**, *40*, 13.
[39] R. S. Negi, E. Celik, R. Pan, R. Stäglich, J. Senker, M. T. Elm, *ACS Appl. Energy Mater.* **2021**, *4*, 3369.
[40] B. Han, T. Paulauskas, B. Key, C. Peebles, J. S. Park, R. F. Klie, J. T. Vaughey, F. Dogan, *ACS Appl. Mater. Interfaces* **2017**, *9*, 14769.
[41] G. Oh, M. Hirayama, O. Kwon, K. Suzuki, R. Kanno, *Chem. Mater.* **2016**, *28*, 2634.
[42] J. Ha Woo, J. E. Trevey, A. S. Cavanagh, Y. Seok Choi, S. Cham Kim, S. M. George, K. Hwan Oh, S.-H. Lee, *J. Electrochem. Soc.* **2012**, *159*, A1120.
[43] K. Takada, N. Ohta, L. Zhang, X. Xu, B. Thi Hang, T. Ohnishi, M. Osada, T. Sasaki, *Solid State Ionics* **2012**, *225*, 594.
[44] S. P. Culver, R. Koerver, W. G. Zeier, J. Janek, *Adv. Energy Mater.* **2019**, *9*, 1900626.
[45] W. B. Hawley, J. Li, *J. Energy Storage* **2019**, *25*, 100862.
[46] R. L. Puurunen, *J. Appl. Phys.* **2005**, *97*, 121301.
[47] C. Geng, S. Trussler, M. B. Johnson, N. Zaker, B. Scott, G. Botton, J. R. Dahn, *J. Electrochem. Soc.* **2020**, *167*, 110509.
[48] Y. Moryson, F. Walther, J. Sann, B. Mogwitz, S. Ahmed, S. Burkhardt, L. Chen, P. J. Klar, K. Volz, S. Fearn, M. Rohnke, J. Janek, *ACS Appl. Energy Mater.* **2021**, *4*, 7168.
[49] B. Han, B. Key, S. H. Lapidus, J. C. Garcia, H. Iddir, J. T. Vaughey, F. Dogan, *ACS Appl. Mater. Interfaces* **2017**, *9*, 41291.
[50] T. Teranishi, Y. Yoshikawa, M. Yoneda, A. Kishimoto, J. Halpin, S. O'Brien, M. Modreanu, I. M. Povey, *ACS Appl. Energy Mater.* **2018**, *1*, 3277.
[51] S.-K. Otto, Y. Moryson, T. Krauskopf, K. Peppler, J. Sann, J. Janek, A. Henss, *Chem. Mater.* **2021**, *33*, 859.
[52] F. He, d. Fang, J. Xie, L. Xue, *J. Wuhan Univ. Technol. Mater. Sci. Ed.* **2020**, *35*, 711.
[53] H. Hemmelmann, J. K. Dinter, M. T. Elm, *Adv. Mater. Interfaces* **2021**, *8*, 2002074.
[54] W. Tang, Z. Chen, F. Xiong, F. Chen, C. Huang, Q. Gao, T. Wang, Z. Yang, W. Zhang, *J. Power Sources* **2019**, *412*, 246.
[55] Y. Zhu, X. He, Y. Mo, *ACS Appl. Mater. Interfaces* **2015**, *7*, 23685.
[56] A. Jena, Y. Meesala, S.-F. Hu, H. Chang, R.-S. Liu, *ACS Energy Lett.* **2018**, *3*, 2775.
[57] R. S. Negi, P. Minnmann, R. Pan, S. Ahmed, M. Herzog, K. Volz, R. Takata, F. Schmidt, J. Janek, M. T. Elm, *Chem. Mater.* **2021**, *33*, 6713.
[58] R. Pan, D. Rau, Y. Moryson, J. Sann, J. Janek, *ACS Appl. Energy Mater.* **2020**, *3*, 6065.
[59] J. Moškon, M. Gaberšček, *J. Power Sources Advances* **2021**, *7*, 100047.
[60] N. Ogihara, S. Kawauchi, C. Okuda, Y. Itou, Y. Takeuchi, Y. Ukyo, *J. Electrochem. Soc.* **2012**, *159*, A1034.
[61] J. Bisquert, *Phys. Chem. Chem. Phys.* **2000**, *2*, 4185.

3.4.2 Publication V

State of Charge Dependent Impedance Spectroscopy as a Helpful Tool to Identify Reasons for Fast Capacity Fading in All-Solid-State Batteries

In the fifth publication (submitted), the influence of the charge transfer resistance on the galvanostatic cycling performance of SSBs was investigated. In many reports, the capacity fading of thiophosphate-based SSBs is attributed to an increase of the charge transfer resistance in the composite cathode caused by interface degradation and/or chemo-mechanical failure. However, in this work large differences in the long-term cycling performance were observed, with comparable charge transfer resistance on the cathode side. Accordingly, the charge transfer resistance of the cathode is not necessarily responsible for capacity fading. Other processes, such as resistive processes on the anode side, can also play an important role. Since these processes usually depend on the SOC, they may not appear in the impedance spectra of fully charged cells. Thus, analyzing the impedance spectra of charged cells only is insufficient for the identification of major resistive processes in SSBs.

Overall, the results of this study recommend to measure impedance spectra at different SOCs, which can gain a better understanding of the different degradation phenomena, responsible for capacity fading in SSBs.

The experiments for this work were designed and performed by M. Wiche under the supervision of M. T. Elm. Y. Yusim and A. Henss performed supporting ToF-SIMS measurements, assisted in validation of the data and conducted in-depth impedance analysis. K. Vettori performed the FIB-SEM measurements. R. Ruess assisted with data interpretation. The manuscript was written by Y. Yusim and edited by all other authors. The first authorship of this work was shared between M. Wiche and Y. Yusim.

State of Charge Dependent Impedance Spectroscopy as a Helpful Tool to Identify Reasons for Fast Capacity Fading in All-Solid-State Batteries

Miguel Wiche[a,b,c=], Yuriy Yusim[a,b=], Kilian Vettori[a,b], Raffael Ruess[a,b], Anja Henss[a,b*] and Matthias T. Elm[a,b,c*]

[a]*Center for Materials Research (LaMa), Justus Liebig University Giessen, Heinrich-Buff-Ring 16, 35392 Giessen, Germany*

[b]*Institute of Physical Chemistry, Justus Liebig University Giessen, Heinrich-Buff-Ring 17, 35392 Giessen, Germany*

[c]*Institute of Experimental Physics I, Justus Liebig University Giessen, Heinrich-Buff-Ring 16, 35392 Giessen, Germany*

=*These authors contributed equally to this work*

Abstract

Thiophosphate-based all-solid-state batteries (ASSBs) are considered as most promising candidate for the next generation of energy storage systems. However, thiophosphate-based ASSBs suffer from fast capacity fading with Nickel-rich cathode materials. In many reports, this capacity fading is attributed to an increase of the charge transfer resistance of the composite cathode caused by interface degradation and/or chemo-mechanical failure. The change of the charge transfer resistance is typically determined using impedance spectroscopy after charging the cells. In this work, we demonstrate that large differences in the long-term cycling performance also arise in cells, which exhibit a comparable charge transfer resistance at cathode side. Our results confirm that the charge transfer resistance of the cathode is not necessarily responsible for capacity fading. Other processes, such as resistive processes on the anode side, can also play a major role. Since these processes usually depend on the state of charge (SOC), they may not appear in the impedance spectra of fully charged cells, i.e., analyzing the impedance spectra of charged cells only is insufficient for the identification of major resistive processes. Thus, we recommend to measure the impedance at different potentials to get a complete understanding of the reasons for capacity fading in ASSBs.

1. Introduction

All-solid-state batteries (ASSBs) are expected to be one of the most promising candidates for the future generation of batteries.[1,2] Compared to state-of-the-art lithium-ion batteries (LIBs) with a liquid electrolyte, ASSBs with a solid-state electrolyte (SSE) could offer higher energy density when using a lithium metal anode.[3–5] Among different classes of SSEs, thiophosphate-based SSEs are currently highly attractive for applications in ASSBs. In addition to their high ionic conductivity values, which in some cases can be higher than 20 mS cm^{-1} at room temperature,[5] another advantage is their malleable nature, which enables good interfacial contact between electrolyte and electrode in ASSBs.[6] Thiophosphate-based ASSBs exhibit a strong capacity fading with Ni-rich $LiNi_{1-x-y}Co_xMn_yO_2$ (NCM), which is commonly accepted as state-of-the-art high energy density cathode active material with high specific capacities.[7] According to many reports in literature[8–15] this strong capacity fading is attributed to the increase of the charge transfer resistance in the composite cathode caused by interfacial degradation[16–23] as well as chemo-mechanical effects such as contact loss.[13,15] The change of the charge transfer resistance is monitored using electrochemical impedance spectroscopy (EIS). The EIS measurements are mostly performed only after fully charging the cells[10,12–14,24] and there are only a few reports, where the evolution of the impedance is measured in more detail for varying state of charge (SOC).[11,25–27] Beside degradation effects at the composite cathode, there are other SOC-dependent processes which can result in a higher resistance of the cells. For example, the results of Santhosha et al.[28] show that an inappropriate In/Li ratio in the In/InLi anode may also affect the electrochemical cycle causing a rapid increase of the anode interface resistance.

In this study, the electrochemical performance of Li_6PS_5Cl -based ASSBs was characterized in detail using Al_2O_3-coated $Li(Ni_{0.70}Co_{0.15}Mn_{0.15})O_2$ as cathode active material (CAM) and In/InLi as metal anode. We confirm that a rapid decrease of the capacity of the thiophosphate-based ASSBs does not necessarily indicate a degradation of the interface between composite cathode and electrolyte. Although the cells show large differences in their long-term cycling performance, they exhibit a comparable increase of the charge transfer resistance at the cathode side during cycling. Only the analysis of the electrochemical impedance at low state of charge (3.1 V) indicates that the rapid capacity fading of the worse performing cell is caused by a significantly increased resistance contribution at the anode side. The results emphasize the necessity of performing impedance measurements at different state of charge in order to

elucidate different degradation mechanisms, which affect the electrochemical behavior and the long-term cycling performance of ASSBs.

2. Experimental

Surface modification of NCM

$Li(Ni_{0.70}Co_{0.15}Mn_{0.15})O_2$ (Gelon LIB) was coated by a wet chemical coating approach to improve the surface stability of NCM in contact with the solid-state electrolyte as recently discussed in detail in our previous work.[29,30] In brief, 0.279 mL of Trimethylaluminum-solution (2 M in toluene, Sigma Aldrich) was added to 15 mL of dried toluene (Sigma Aldrich) and stirred for 1 h. After adding 2 g of $Li(Ni_{0.70}Co_{0.15}Mn_{0.15})O_2$, the suspension was stirred for 12 h, filtered, washed with 20 mL of toluene and dried at 200 °C. The obtained powder was divided into two batches. The first batch (Al_2O_3 coating) was transferred into the glovebox for further use (denoted as Alu-NCM). The second batch ($Al_2O_3/LiAlO_2$ coating) was additionally annealed at 600 °C for 8 h to modify the coating layer properties (denoted as Alu-NCM600). The beneficial effects of the additional annealing step on the cycle performance are well known and are discussed in previous reports.[12,31,32]

Electrode preparation and cell assembly

All cell tests were performed in a pellet-type cell casing. At first, 60 mg of Li_6PS_5Cl (LPSCl, NEI Corporation) were pressed into a pellet within a peek cylinder (10 mm diameter). For the preparation of the composite cathode, 35 mg of coated NCM, 15 mg of LPSCl and additional 1.5 mg of vapor-grown carbon fibers (VGCF, Sigma Aldrich) were mixed in an agate mortar for 15 minutes, which is the common procedure for the preparation of cathodes according to literature.[11,13,33] Then, 12 mg of the cathode composite were pressed with 380 MPa on one side of the electrolyte. On the other side of the electrolyte first indium (9 mm diameter, 100 µm thickness, chemPur GmbH), and then lithium (6 mm diameter, 30 µm thickness, Honjo) were placed as anode. The In : Li atomic ratio was 6.2 : 1, indicating a low Li-content.[28] After closing of the cells, they were analyzed under external pressure (~50 MPa) using an aluminum framework (no additional springs). All materials for cell assembly were dried in a vacuum oven (Büchi) before use and stored in an argon-filled glovebox (< 0.1 ppm of O_2, < 0.1 ppm of H_2O). In this study, the results of three representative cells are presented: One cell with Alu-NCM (denoted as Alu-NCM) as CAM and two identically assembled cells with Alu-NCM600 (denoted as Alu-NCM600a and Alu-NCM600b). The results of three additional cells (Alu-NCM600c, Alu-NCM600d, and AluNCM600e) are presented in Figure S1 of the SI.

Electrochemical characterization

Cell cycling was performed using a MACCOR battery cycler. The cells were cycled between 2.0 V and 3.7 V *vs.* In/InLi (corresponding to 2.62 and 4.32 V *vs.* Li^+/Li) with 0.25 C (1 C = 200 mAh g^{-1}) for 100 cycles at 25 °C. After the 100th cycle electrochemical impedance spectroscopy (EIS) measurements were performed using VMP-300 potentiostat (Biologic). To measure impedance data for different state of charge (SOC), the ASSB cells were charged to defined potentials. The potentials were kept constant for maximum 24 h with a current limit of 5 µA in order to reach equilibrium before the EIS measurement was started. The potential was also kept constant during the EIS measurements. The measurements were carried out at 25 °C in a frequency range from 7 Hz to 10 mHz, applying an amplitude of 10 mV. The evaluation of the EIS data was performed with the software RelaxIS 3.0.17 (Rhd instruments).

FIB-SEM measurements

Cross-section images of the cycled cathodes were taken using a FIB-SEM instrument (Tescan XEIA3). FIB-craters were milled with a 2.5 µA Xe-beam. The images were taken using an acceleration voltage of 5 kV.

3. Results and discussion

The prepared pellet-type In/InLi|LPSCl|$LiNi_{0.7}Co_{0.15}Mn_{0.15}O_2$/LPSCl/VGCF ASSBs were assembled and cycled between 2.0 V and 3.7 V *vs.* In/InLi (corresponds to 2.6 and 4.3 V *vs.* Li^+/Li) with 0.25 C for 100 cycles, where Alu-NCM and Alu-NCM600 were used as cathode active material. Figure 1 shows the corresponding charge and discharge profiles of one cell with Alu-NCM (Figure 1 (a)) and two cells with Alu-NCM600 (denoted as Alu-NCM600a and Alu-NCM600b (Figure 1 (b) and (c)). A comparison of the battery discharge capacity of the three cells is shown in Figure 1 (d) as function of the cycle number. A significantly improved capacity retention is demonstrated for Alu-NCM600a, which has a discharge capacity of 77.2 mAh g^{-1} after 100 cycles. In contrast, the Alu-NCM cell exhibits a capacity of only 13.3 mAh g^{-1} after 100 cycles. The difference in the long-term cycling performance can be associated with the improved coating properties of Alu-NCM600 compared to Alu-NCM, as discussed in detail by Negi et al. for thiophosphate-based ASSBs.[31] In short, the additional annealing step results in the formation of an $Al_2O_3/LiAlO_2$ coating, which exhibits mainly an improved conductivity compared to the Al_2O_3 coating of Alu-NCM.[31,32]

However, when the experiment was repeated with the same batch of Alu-NCM600, a significantly worse electrochemical long-term performance was observed (Figure 1 (c)). The second Alu-NCM600b cell achieves only a capacity of 32.9 mAh g^{-1} after 100 cycles, as shown in Figure 1 (d), which is still higher compared to Alu-NCM. Differences in the long-term cycling behavior are also observed for the three cells Alu-NCM600c, Alu-NCM600d and Alu-NCM600e as shown in Figure S1. In the following we will restrict the discussion to the two representative cells Alu-NCM600a and Alu-NCM600b, which exhibit the best and worse cycling behavior, respectively. Interestingly, the discharge capacity curves of the two cells Alu-NCM600a and Alu-NCM600b are also completely different. While the capacity of the Alu-NCM600a gradually decreases at a relatively constant rate with increasing cycle number (when first cycles are not considered), the capacity fading of Alu-NCM600b is very rapid between the 10^{th} and 30^{th} cycle. Shi et al. attributed such a rapid capacity decay to mechanical degradation due to the loss of mechanical contact in the composite cathode.[34] However, since the same pressure (~50 MPa) was applied to all cells during cycling, this cannot be the reason for the significant difference in capacity decay between the Alu-NCM600a and Alu-NCM600b cells. The average potential during charge was determined for Alu-NCM, Alu-NCM600a and Alu-NCM600b (see Figure S2). These data give an indication for the overpotential, which is highest for Alu-NCM, followed by Alu-NCM600b, and Alu-NCM600a. The absolute values and the trend of the data (plateau after 50 cycles) is in good agreement with the capacity behavior shown in Figure 1 (d).

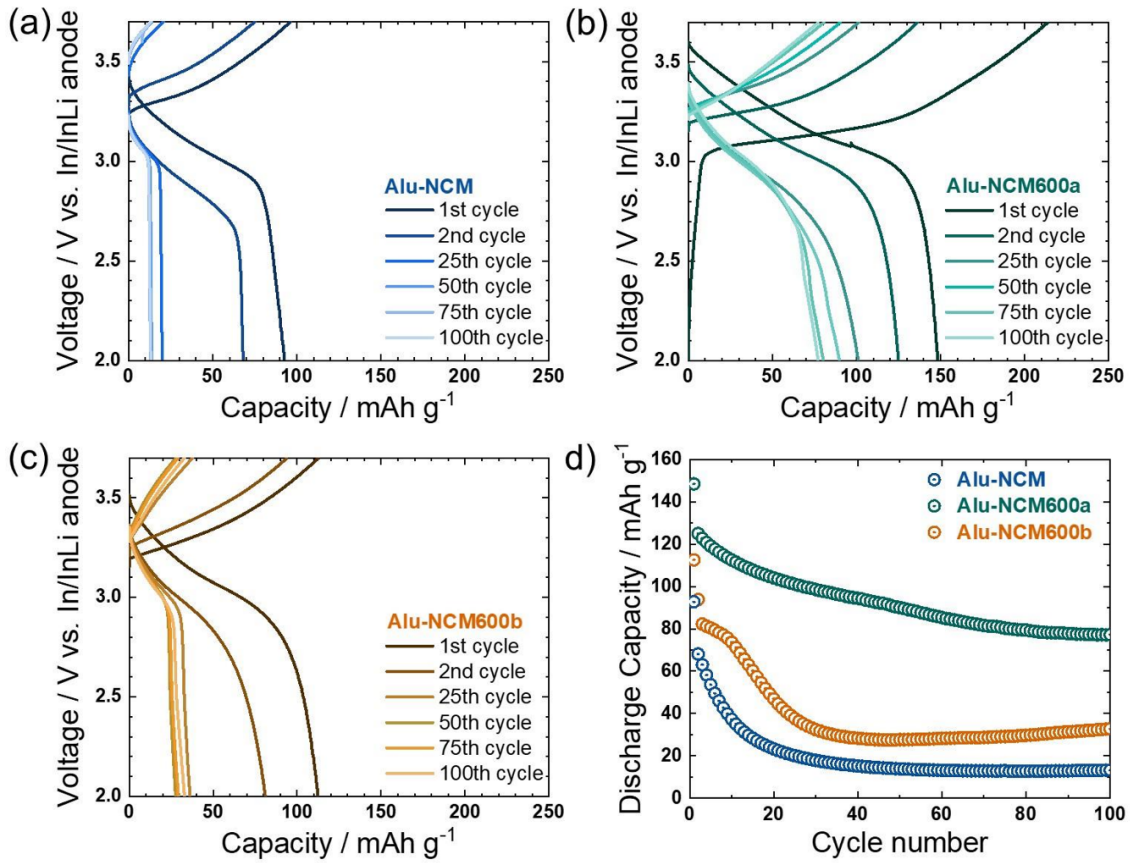

Figure 1. Charge and discharge profiles of In/InLi|LPSCl|$LiNi_{0.7}Co_{0.15}Mn_{0.15}O_2$/LPSCl/VGCF cells with (a) Alu-NCM, (b) Alu-NCM600a, and (c) Alu-NCM600b as CAM cycled with 0.25 C between 2.0 V and 3.7 V *vs.* In/InLi anode for 100 cycles. (d) Comparison of the discharge capacity of Alu-NCM, Alu-NCM600a, and Alu-NCM600b with increasing cycle number.

To investigate the origin of the significant difference in the cycling performance of the ASSBs with coated NCM, electrochemical impedance spectroscopy (EIS) measurements were carried out after 100 cycles. The impedance spectra were collected for different state of charge between 3.1 V and 3.7 V *vs.* In/InLi. A constant potential step was included in order to achieve equilibration of Li concentration within the CAM particles.[26] This step is necessary to ensure comparability between the samples since the impedance values of layered oxide cathode materials strongly depend on the lithium content (state of charge) in the composite electrode.[11,25]

In Figure 2 potential-dependent impedance spectra of Alu-NCM (Figure 2 (a)), Alu-NCM600a (Figure 2 (b)) and Alu-NCM600b (Figure 2 (c)) cells after cycling are shown. Comparing the impedance spectra of the Alu-NCM cell and the Alu-NCM600a cell, a significant difference in the total impedance is observed. While the total impedance of the Alu-NCM cell is around 1.9 kΩ at 3.7 V *vs.* In/InLi, the resistance of the Alu-NCM600a cell is around 1 kΩ. This is in

good agreement with the electrochemical performance data shown in Figure 1 (d), as the Alu-NCM cell with the higher impedance has a poorer cycling performance compared to the Alu-NCM600a cell. The higher impedance of the Alu-NCM cell reveals a higher charge transfer resistance R_{CT} at the cathode-electrolyte interface due to the inferior coating properties. However, also the Alu-NCM600b cell shows a comparable impedance as the Alu-NCM600a cell of less than 1 kΩ at 3.7 V *vs.* In/InLi and, thus, a comparable R_{CT} at the cathode side, despite their worse electrochemical performance. For a quantitative comparison of the charge transfer resistance R_{CT} at the cathode side, the spectra were fitted using a transmission line model, which describes the impedance behavior of porous electrodes considering SSE filled pores. The equivalent circuit is described in more detail in Figure S3. To fit the data at higher potentials, the relaxation time of the anode contribution at low frequencies was kept constant (0.01-0.1 s). Thereby, a negligible impedance from the anode side is observed. The impedance contribution of the cathode arises at higher frequencies.[35] It is important to note that physically meaningful parameters can be extracted since the ionic resistance (R_{ion}) of the composite cathode is lower than the charge transfer resistance (R_{CT}) (No typical Gerischer-type behavior).[35,36] The fitting values of R_{CT} in Figure 2 (d) show a typical U-shape behavior:[11,26,27] At first, R_{CT} slightly decreases with increasing voltage and then increases for voltages above 3.4 V (data at 3.1 V *vs.* In/InLi cannot be reliably analyzed due to the large impedance contribution of the anode side (see below)). It can be seen that R_{CT} of the Alu-NCM600a cell is significantly lower than for the Alu-NCM cell due to the improved coating properties after annealing, in excellent agreement with previous reports.[12,31] Accordingly, the difference of R_{CT} on the cathode side can be correlated with the different long-term cycling performance for Alu-NCM and Alu-NCM600a cells presented in Figure 1. However, R_{CT} on the cathode side is very similar for both Alu-NCM600a and Alu-NCM600b cells independent of the SOC (Figure 2 (d)). No significant difference can be observed in the impedance spectra of Alu-NCM600a and Alu-NCM600b (Figure 2) at higher potentials (3.3 - 3.7 V *vs.* In/InLi), which confirms a comparable charge transfer resistance for both cells. This is somewhat surprising, since a cell with a poor performance is expected to exhibit a higher charge transfer resistance at the cathode side.

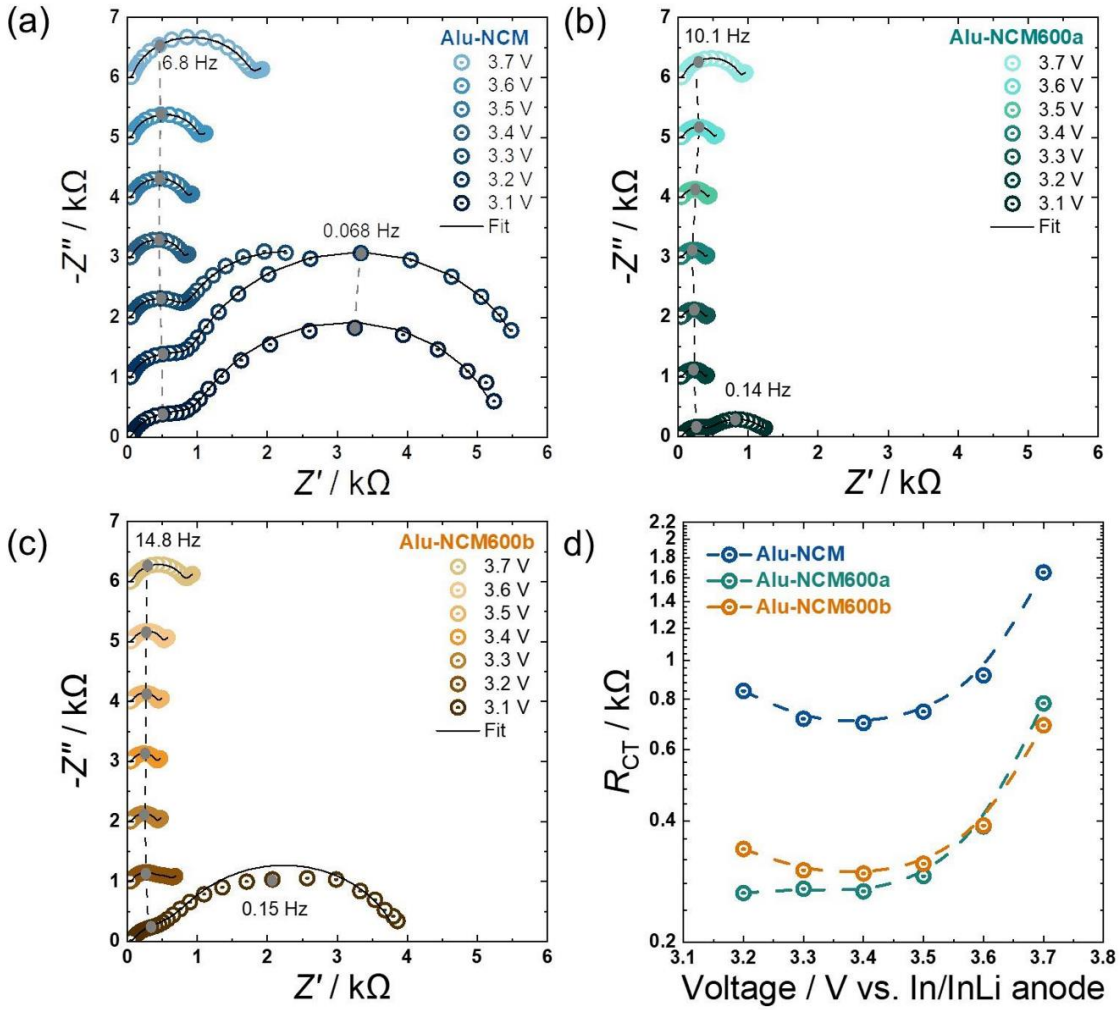

Figure 2. EIS measurements during charging after 100 cycles for the cells with (a) Alu-NCM, (b) Alu-NCM600a and (c) Alu-NCM600b as cathode active material. (d) Potential-dependent charge transfer resistance of the cathode side for Alu-NCM, Alu-NCM600a, and Alu-NCM600b after 100 cycles.

However, an additional second semicircle can be identified at 0.15 Hz at 3.1 V *vs.* In/InLi. According to previous reports[8,13,15,37] this low frequency impedance contribution can be assigned to the anode with the In/InLi|Li_6PS_5Cl interface. The corresponding resistance R_{Anode} is almost a factor of four higher for the Alu-NCM600b than for the Alu-NCM600a cell (see fit values in Figure 3). It is worth noting that this huge additional second semicircle in the Alu-NCM600b cell was not observed during the first charge cycle (see Figure S4), indicating that the formation of this semicircle is caused by long-term cycling. Accordingly, our data suggest that the discharge capacity of the Alu-NCM600b cell is limited by the resistance R_{Anode} of the anode side and not by R_{CT} on the cathode side. The data presented in this study, of course, do not exclude that a large R_{CT} of the composite cathodes is responsible for a strong capacity fading of ASSBs as shown in many previous reports in literature. However, it is important to note that

the anode and the In/InLi|Li_6PS_5Cl interface can also have a significant impact on the cell performance. Most important, the results reveal that impedance measurements at different SOC are needed in order to identify the underlying degradation processes responsible for the capacity fading. To ensure reliability of our data, we analyzed the impedance of the Alu-NCM600c, Alu-NCM600d, and Alu-NCM600e cells. As can be seen in Figure S1, all cells show a comparable charge transfer resistance on the cathode side as the Alu-NCM600a and Alu-NCM600b cells (consistent with the results shown above). The anode resistance R_{Anode} of all cells (Figure S1 (f)) is higher than for Alu-NCM600b and can be correlated with the differences in the capacity retention after 100 cycles.

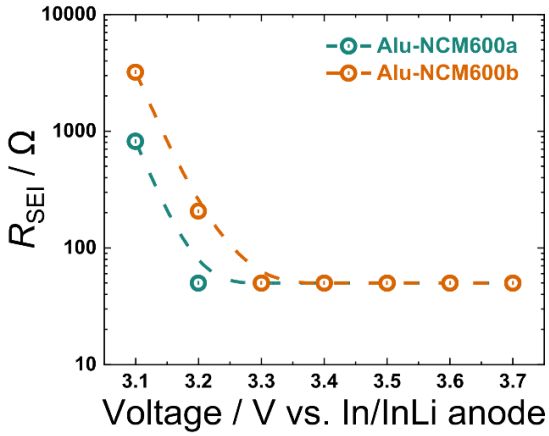

Figure 3. Resistance R_{Anode} of the anode after 100 cycles for Alu-NCM600a and Alu-NCM600b at different potentials.

One possible reason for the high R_{Anode} at the anode side of the worse performing cells is an insufficient amount of lithium present in the In/InLi anode. This can be due to the thin Li foil (only 30 µm), due to side reactions between lithium and the SSE, and/or a lithium concentration gradient during discharge. Accordingly, dead lithium is formed during cycling (lithium depletion), which is a well-known problem in anode-free lithium metal batteries.[38,39] Consequently, only a small amount of lithium can be extracted from the anode during discharging, limiting the discharge capacity of the cell. Nevertheless, at higher potentials, the impedance on the anode side decreases because the anode is partially lithiated again. Additionally, volume expansion of the In/InLi anode[40] may also lead to an improved interfacial contact decreasing the impedance on the anode side. In this regard, the strong variation of R_{Anode} of the different cells may be attributed to the insufficient amount of lithium in the anode, as small changes of the interfacial degradation involving Li loss can have a significant effect. It should be noted that a high R_{Anode} on the anode side is also observed for the Alu-NCM cell

(Figure 2 (a), 3.1 V), whose value is similar to the Alu-NCM600 cells (Figure S1 (f)). Since the Alu-NCM600 cells perform better than Alu-NCM (Figure S1 (a)), this can be attributed to the higher charge transfer resistance R_{CT} of Alu-NCM compared to the Alu-NCM600 cells (Figure S4 (d)).

The structural properties of the composite cathodes were investigated after cycling using FIB-SEM in order to verify differences in interfacial degradation as indicated by the impedance analysis (see Figure S5, S6, and S7). It should be noted that the solid electrolyte separator is visible at the bottom part of the images (darker areas). The NCM secondary particles of the composite cathodes of Alu-NCM, Alu-NCM600a and Alu-NCM600b are spherical and have a diameter of 5-20 µm, consisting of nanosized primary particles. The particle size distribution is comparable for all composites. However, the Alu-NCM particles (Figure S5) potentially show more cracks and exhibit a larger contact loss area between NCM and the SSE compared to Alu-NCM600a and Alu-NCM600b. This can be related to the poor coating properties of Alu-NCM and explains the higher interfacial resistance of the Alu-NCM cell, which is, together with R_{Anode}, responsible for the observed capacity loss.[13] The mechanism of how the coatings affect particle cracking is not completely understood in the literature and is beyond the scope of this study. However, no significant difference in morphology of the cathodes of Alu-NCM600a (Figure S6) and Alu-NCM600b (Figure S7) is found. The contact area between NCM and SSE as well as the particle cracking seems to be comparable for both composite cathodes, which explains why both Alu-NCM600 cells show a comparable R_{CT}. It is worth noting that the different contrast of LPSCl in the FIB-SEM images is due to artifacts during the measurement and not due to degradation. Overall, the FIB-SEM images support that both composite cathodes in Alu-NCM600a and Alu-NCM600b cells show comparable degree of degradation of the composite cathode.

4. Conclusions

In this study, the influence of the charge transfer resistance on the galvanostatic cycling performance of ASSBs was investigated in detail. Our results demonstrate that a poor cycling performance does not necessarily indicate degradation on the cathode side, which is typically identified by analyzing the impedance spectra of charged cells (high SOC). Other processes, e.g. at the In/InLi|Li_6PS_5Cl interface, may also play a major role. Referring to our data, the impact of the In/InLi|Li_6PS_5Cl interface is particularly evident when performing electrochemical impedance spectroscopy at a low SOC state, while its impact on the impedance spectra is negligible for a high SOC. However, it needs to be clarified in future studies how

resistive contributions from the anode side or other detrimental effects affect the long-term cycling performance of ASSBs. Nevertheless, we recommend to measure impedance spectra at different states of charge. This will help to gain a better understanding of the different degradation mechanisms, which are responsible for a rapid capacity fading in ASSBs.

Supporting Information

Discharge capacity curve, impedance spectra and impedance fitting parameter for Alu-NCM600c, Alu-NCM600d, and Alu-NCM600e; Average charge voltage of Alu-NCM, Alu-NCM600a, and Alu-NCM600b; Impedance fitting model including fitting results; EIS measurements for Alu-NCM, Alu-NCM600b, and Alu-NCM600e before cycling; FIB-SEM images of Alu-NCM, Alu-NCM600a and Alu-NCM600b after 100 cycles at different magnifications.

AUTHOR INFORMATION

=These authors contributed equally to this work

Corresponding Authors

*Email:
Matthias.elm@phys.chemie.uni-giessen.de (M. T. Elm)
Anja.Henss@phys.chemie.uni-giessen.de (A. Henss)

Notes

The authors declare no competing financial interests.

Acknowledgments

M.T.E. acknowledges financial support by the Heisenberg Program (project number 498993886, grant no. EL 863/6-1) from the German Research Foundation (DFG).

5. References

(1) Miao, X.; Guan, S.; Ma, C.; Li, L.; Nan, W.; Miao, X.; Guan, S.; Li, L.; Nan, C.-W.; Ma, C. Role of Interfaces in Solid-State Batteries. *Adv. Mater.* **2023**, 2206402. https://doi.org/10.1002/ADMA.202206402.

(2) Gao, Z.; Sun, H.; Fu, L.; Ye, F.; Zhang, Y.; Luo, W.; Huang, Y. Promises, Challenges, and Recent Progress of Inorganic Solid-State Electrolytes for All-Solid-State Lithium Batteries. *Adv. Mater.* **2018**, *30* (17), 1705702. https://doi.org/10.1002/ADMA.201705702.

(3) Sun, Y. K. Promising All-Solid-State Batteries for Future Electric Vehicles. *ACS Energy Lett.* **2020**, *5* (10), 3221–3223. https://doi.org/10.1021/ACSENERGYLETT.0C01977/ASSET/IMAGES/LARGE/NZ0C01977_0001.JPEG.

(4) Janek, J.; Zeier, W. G. A Solid Future for Battery Development. *Nat. Energy* **2016**, *1* (9), 16141. https://doi.org/10.1038/nenergy.2016.141.

(5) Kato, Y.; Hori, S.; Saito, T.; Suzuki, K.; Hirayama, M.; Mitsui, A.; Yonemura, M.; Iba, H.; Kanno, R. High-Power All-Solid-State Batteries Using Sulfide Superionic Conductors. *Nat. Energy* **2016**, *1* (4), 16030. https://doi.org/10.1038/nenergy.2016.30.

(6) Kato, A.; Yamamoto, M.; Sakuda, A.; Hayashi, A.; Tatsumisago, M. Mechanical Properties of Li2S-P2S5 Glasses with Lithium Halides and Application in All-Solid-State Batteries. *ACS Appl. Energy Mater.* **2018**, *1* (3), 1002–1007. https://doi.org/10.1021/ACSAEM.7B00140/ASSET/IMAGES/LARGE/AE-2017-00140R_0005.JPEG.

(7) Zhengwei Xu, C.; Wang, Z.; Tan, X.; Song, J.; Zhu, L.; Li, Y.; -, al; Zhuang, D.; Bazant, M. Z.; Li, J.; Zhong, W.; Deng, Q.; Zhang, Q.; Yang, C. Recent Progress in Synthesis and Surface Modification of Nickel-Rich Layered Oxide Cathode Materials for Lithium-Ion Batteries. *Int. J. Extreme Manuf.* **2022**, *4* (4), 042004. https://doi.org/10.1088/2631-7990/AC92EF.

(8) Minnmann, P.; Quillman, L.; Burkhardt, S.; Richter, F. H.; Janek, J. Editors' Choice—Quantifying the Impact of Charge Transport Bottlenecks in Composite Cathodes of All-Solid-State Batteries. *J. Electrochem. Soc.* **2021**, *168* (4), 040537. https://doi.org/10.1149/1945-7111/ABF8D7.

(9) Gellert, M.; Gries, K. I.; Sann, J.; Pfeifer, E.; Volz, K.; Roling, B. Impedance Spectroscopic Study of the Charge Transfer Resistance at the Interface between a $LiNi_{0.5}Mn_{1.5}O_4$ High-Voltage Cathode Film and a $LiNbO_3$ Coating Film. *Solid State Ionics* **2016**, *287*, 8–12. https://doi.org/10.1016/J.SSI.2016.01.031.

(10) MacHida, N.; Kashiwagi, J.; Naito, M.; Shigematsu, T. Electrochemical Properties of All-Solid-State Batteries with ZrO_2-Coated $LiNi_{1/3}Mn_{1/3}Co_{1/3}O_2$ as Cathode Materials. *Solid State Ionics* **2012**, *225*, 354–358. https://doi.org/10.1016/J.SSI.2011.11.026.

(11) Negi, R. S.; Minnmann, P.; Pan, R.; Ahmed, S.; J. Herzog, M.; Volz, K.; Takata, R.; Schmidt, F.; Janek, J.; Elm, M. T. Stabilizing the Cathode/Electrolyte Interface Using a Dry-Processed Lithium Titanate Coating for All-Solid-State Batteries. *Chem. Mater.* **2021**, *33* (17), 6713–6723. https://doi.org/10.1021/acs.chemmater.1c01123.

(12) Negi, R. S.; Yusim, Y.; Pan, R.; Ahmed, S.; Volz, K.; Takata, R.; Schmidt, F.; Henss, A.; Elm, M. T. A Dry-Processed $Al_2O_3/LiAlO_2$ Coating for Stabilizing the Cathode/Electrolyte Interface in High-Ni NCM-Based All-Solid-State Batteries. *Adv. Mater. Interfaces* **2022**, *9* (8), 2101428. https://doi.org/https://doi.org/10.1002/admi.202101428.

(13) Koerver, R.; Aygün, I.; Leichtweiß, T.; Dietrich, C.; Zhang, W.; Binder, J. O.; Hartmann, P.; Zeier, W. G.; Janek, J. Capacity Fade in Solid-State Batteries: Interphase Formation and

Chemomechanical Processes in Nickel-Rich Layered Oxide Cathodes and Lithium Thiophosphate Solid Electrolytes. *Chem. Mater.* **2017**, *29* (13), 5574–5582. https://doi.org/10.1021/acs.chemmater.7b00931.

(14) Morino, Y. Impact of Surface Coating on the Low Temperature Performance of a Sulfide-Based All-Solid-State Battery Cathode. *Electrochemistry* **2022**, *90* (2), 027001–027001. https://doi.org/10.5796/ELECTROCHEMISTRY.21-00126.

(15) Zuo, T. T.; Rueß, R.; Pan, R.; Walther, F.; Rohnke, M.; Hori, S.; Kanno, R.; Schröder, D.; Janek, J. A Mechanistic Investigation of the $Li_{10}GeP_2S_{12}|LiNi_{1-x-y}Co_xMn_yO2$ Interface Stability in All-Solid-State Lithium Batteries. *Nat. Comm.* .**2021**, *12* (1), 1–10. https://doi.org/10.1038/s41467-021-26895-4.

(16) Walther, F.; Koerver, R.; Fuchs, T.; Ohno, S.; Sann, J.; Rohnke, M.; Zeier, W. G.; Janek, J. Visualization of the Interfacial Decomposition of Composite Cathodes in Argyrodite-Based All-Solid-State Batteries Using Time-of-Flight Secondary-Ion Mass Spectrometry. *Chem. Mater.* **2019**, *31* (10), 3745–3755. https://doi.org/10.1021/acs.chemmater.9b00770.

(17) Richards, W. D.; Miara, L. J.; Wang, Y.; Kim, J. C.; Ceder, G. Interface Stability in Solid-State Batteries. *Chem. Mater.* **2016**, *28* (1), 266–273. https://doi.org/10.1021/acs.chemmater.5b04082.

(18) Zhu, Y.; He, X.; Mo, Y. First Principles Study on Electrochemical and Chemical Stability of Solid Electrolyte–Electrode Interfaces in All-Solid-State Li-Ion Batteries. *J. Mater. Chem. A* **2016**, *4* (9), 3253–3266. https://doi.org/10.1039/C5TA08574H.

(19) Morino, Y.; Kanada, S. Electrochemical and Material Analyses for Sulfide-Based Solid Electrolyte–Cathode Interface under High Voltage. *J. Power Sources* **2021**, *509*, 230376. https://doi.org/10.1016/J.JPOWSOUR.2021.230376.

(20) Vinado, C.; Wang, S.; He, Y.; Xiao, X.; Li, Y.; Wang, C.; Yang, J. Electrochemical and Interfacial Behavior of All Solid State Batteries Using $Li_{10}SnP_2S_{12}$ Solid Electrolyte. *J. Power Sources* **2018**, *396*, 824–830. https://doi.org/10.1016/J.JPOWSOUR.2018.06.038.

(21) Yu, R.; Wang, C.; Duan, H.; Jiang, M.; Zhang, A.; Fraser, A.; Zuo, J.; Wu, Y.; Sun, Y.; Zhao, Y.; Liang, J.; Fu, J.; Deng, S.; Ren, Z.; Li, G.; Huang, H.; Li, R.; Chen, N.; Wang, J.; Li, X.; Singh, C. V.; Sun, X.; Yu, R.; Wang, C.; Duan, H.; Fraser, A.; Sun, Y.; Zhao, Y.; Liang, J.; Fu, J.; Deng, S.; Li, R.; Sun, X.; Huang, H.; Wang, J.; Jiang, M.; Zhang, A.; Wu, Y.; Ren, Z.; Li, G.; Zuo, J.; Li, X.; Chen, N.; Singh, C. V. Manipulating Charge-Transfer Kinetics of Lithium-Rich Layered Oxide Cathodes in Halide All-Solid-State Batteries. *Adv. Mater.* **2023**, *35* (5), 2207234. https://doi.org/10.1002/ADMA.202207234.

(22) Zhang, Z.; Yao, J.; Yu, C.; Xu, R.; Ma, J.; Wei, C.; Peng, L.; Zhang, L.; Cheng, S.; Xie, J. Failure Analysis of the Ge-Substituted Li_6PS_5I with Bare $LiNi_{0.8}Co_{0.1}Mn_{0.1}O_2$ and Performance Improvement via Li_2ZrO_3 Coating. *J. Mater. Chem. A* **2022**, *10* (41), 22155–22165. https://doi.org/10.1039/D2TA03168J.

(23) Quemin, E.; Dugas, R.; Koç, T.; Hennequart, B.; Chometon, R.; Tarascon, J. M. Decoupling Parasitic Reactions at the Positive Electrode Interfaces in Argyrodite-Based Systems. *ACS Appl. Mater. Interfaces* **2022**, *14* (43), 49284–49294. https://doi.org/10.1021/ACSAMI.2C13150/ASSET/IMAGES/LARGE/AM2C13150_0011.JPEG.

(24) Kitsche, D.; Tang, Y.; Ma, Y.; Goonetilleke, D.; Sann, J.; Walther, F.; Bianchini, M.; Janek, J.; Brezesinski, T. High Performance All-Solid-State Batteries with a Ni-Rich NCM Cathode Coated by Atomic Layer Deposition and Lithium Thiophosphate Solid Electrolyte. *ACS Appl. Energy Mater.* **2021**, *4* (7), 7338–7345. https://doi.org/10.1021/acsaem.1c01487.

(25) Jang, J.; Chen, Y. T.; Deysher, G.; Cheng, D.; Ham, S. Y.; Cronk, A.; Ridley, P.; Yang, H.; Sayahpour, B.; Han, B.; Li, W.; Yao, W.; Wu, E. A.; Doux, J. M.; Nguyen, L. H. B.; Oh, J. A. S.; Tan, D. H. S.; Meng, Y. S. Enabling a Co-Free, High-Voltage $LiNi_{0.5}Mn_{1.5}O_4$ Cathode in All-Solid-State Batteries with a Halide Electrolyte. *ACS Energy Lett.* **2022**, *7* (8), 2531–2539. https://doi.org/10.1021/ACSENERGYLETT.2C01397/ASSET/IMAGES/LARGE/NZ2C01397_0006.JPEG.

(26) Ruess, R.; Schweidler, S.; Hemmelmann, H.; Conforto, G.; Bielefeld, A.; Weber, D. A.; Sann, J.; Elm, M. T.; Janek, J. Influence of NCM Particle Cracking on Kinetics of Lithium-Ion Batteries with Liquid or Solid Electrolyte. *J. Electrochem. Soc.* **2020**, *167* (10), 100532. https://doi.org/10.1149/1945-7111/ab9a2c.

(27) Zahiri, B.; Patra, A.; Kiggins, C.; Yong, A. X. Bin; Ertekin, E.; Cook, J. B.; Braun, P. V. Revealing the Role of the Cathode–Electrolyte Interface on Solid-State Batteries. *Nat. Mater.* **2021**, *20* (10), 1392–1400. https://doi.org/10.1038/s41563-021-01016-0.

(28) Santhosha, A. L.; Medenbach, L.; Buchheim, J. R.; Adelhelm, P. The Indium−Lithium Electrode in Solid-State Lithium-Ion Batteries: Phase Formation, Redox Potentials, and Interface Stability. *Batter. Supercaps* **2019**, *2* (6), 524–529. https://doi.org/10.1002/BATT.201800149.

(29) Negi, R. S.; Culver, S. P.; Mazilkin, A.; Brezesinski, T.; Elm, M. T. Enhancing the Electrochemical Performance of $LiNi_{0.70}Co_{0.15}Mn_{0.15}O_2$ Cathodes Using a Practical Solution-Based Al_2O_3 Coating. *ACS Appl. Mater. Interfaces* **2020**, *12* (28), 31392–31400. https://doi.org/10.1021/acsami.0c06484.

(30) Negi, R. S.; Elm, M. T. Reproducible Long-Term Cycling Data of Al2O3 Coated $LiNi_{0.70}Co_{0.15}Mn_{0.15}O_2$ Cathodes for Lithium-Ion Batteries. *Sci. Data* **2022**, *9* (1), 127. https://doi.org/10.1038/s41597-022-01217-5.

(31) Negi, R. S.; Celik, E.; Pan, R.; Stäglich, R.; Senker, J.; Elm, M. T. Insights into the Positive Effect of Post-Annealing on the Electrochemical Performance of Al_2O_3-Coated Ni-Rich NCM Cathodes for Lithium-Ion Batteries. *ACS Appl. Energy Mater.* **2021**, *4* (4), 3369–3380. https://doi.org/10.1021/acsaem.0c03135.

(32) Han, B.; Paulauskas, T.; Key, B.; Peebles, C.; Park, J. S.; Klie, R. F.; Vaughey, J. T.; Dogan, F. Understanding the Role of Temperature and Cathode Composition on Interface and Bulk: Optimizing Aluminum Oxide Coatings for Li-Ion Cathodes. *ACS Appl. Mater. Interfaces* **2017**, *9* (17), 14769–14778. https://doi.org/10.1021/acsami.7b00595.

(33) Randau, S.; Weber, D. A.; Kötz, O.; Koerver, R.; Braun, P.; Weber, A.; Ivers-Tiffée, E.; Adermann, T.; Kulisch, J.; Zeier, W. G.; Richter, F. H.; Janek, J. Benchmarking the Performance of All-Solid-State Lithium Batteries. *Nat. Energy* **2020**, *5* (3), 259–270. https://doi.org/10.1038/s41560-020-0565-1.

(34) Shi, T.; Zhang, Y. Q.; Tu, Q.; Wang, Y.; Scott, M. C.; Ceder, G. Characterization of Mechanical Degradation in an All-Solid-State Battery Cathode. *J. Mater. Chem. A* **2020**, *8* (34), 17399–17404. https://doi.org/10.1039/D0TA06985J.

(35) Zuo, T. T.; Walther, F.; Teo, J. H.; Rueß, R.; Wang, Y.; Rohnke, M.; Schröder, D.; Nazar, L. F.; Janek, J. Impact of the Chlorination of Lithium Argyrodites on the Electrolyte/Cathode Interface in Solid-State Batteries. *Angew. Chem., Int. Ed.* **2023**, *62* (7), e202213228. https://doi.org/10.1002/ANIE.202213228.

(36) Moškon, J.; Žuntar, J.; Drvarič Talian, S.; Dominko, R.; Gaberšček, M. A Powerful Transmission Line Model for Analysis of Impedance of Insertion Battery Cells: A Case Study on the NMC-Li System. *J. Electrochem. Soc.* **2020**, *167* (14), 140539. https://doi.org/10.1149/1945-7111/abc769.

(37) Hertle, J.; Walther, F.; Mogwitz, B.; Schröder, S.; Wu, X.; Richter, F. H.; Janek, J. Miniaturization of Reference Electrodes for Solid-State Lithium-Ion Batteries. *J. Electrochem. Soc.* **2023**, *170* (4), 040519. https://doi.org/10.1149/1945-7111/ACCB6F.

(38) Huang, C. J.; Hsu, Y. C.; Shitaw, K. N.; Siao, Y. J.; Wu, S. H.; Wang, C. H.; Su, W. N.; Hwang, B. J. Lithium Oxalate as a Lifespan Extender for Anode-Free Lithium Metal Batteries. *ACS Appl. Mater. Interfaces* **2022**, *14* (23), 26724–26732. https://doi.org/10.1021/ACSAMI.2C04693/ASSET/IMAGES/LARGE/AM2C04693_0007.JPEG.

(39) Salvatierra, R. V.; Chen, W.; Tour, J. M. What Can Be Expected from “Anode-Free” Lithium Metal Batteries? *Adv. Energy Sustainability Res.* **2021**, *2* (5), 2000110. https://doi.org/10.1002/AESR.202000110.

(40) Zhang, W.; Schröder, D.; Arlt, T.; Manke, I.; Koerver, R.; Pinedo, R.; Weber, D. A.; Sann, J.; Zeier, W. G.; Janek, J. (Electro)Chemical Expansion during Cycling: Monitoring the Pressure Changes in Operating Solid-State Lithium Batteries. *J. Mater. Chem. A* **2017**, *5* (20), 9929–9936. https://doi.org/10.1039/C7TA02730C.

4 Conclusions and Outlook

In this dissertation, a comprehensive investigation was undertaken to explore the interfacial degradation phenomena in PEO-based SSBs with high-voltage cathodes. These phenomena had not been fully and consistently understood in the existing literature. As a result, this dissertation provides in-depth insights into the underlying failure mechanisms and intricate interfacial processes.

Based on this, it was shown that the "voltage noise" failure, observed in PEO-based SSBs with high-voltage cathodes, is caused by the penetration of lithium dendrites though the SPE and not by the oxidation of the SPE. Therefore, an LATP pellet was introduced between anode and cathode, which could act as a "white screen" to monitor the lithium dendrites growth. Accordingly, to overcome the "voltage noise" behavior, an SPE with higher molecular weight PEO was introduced, which improves the mechanical rigidity of the SPE and enables a reasonable cycling performance. Obtaining discharge capacities of over 200 mAh g^{-1} with PEO-based SPE and Ni-rich NCM is a notable result in comparison to other reports.

Since the cells could be successfully cycled, it became possible to conduct a more in-depth analysis of the interfacial processes. Therefore, EIS measurements in a three-electrode setup were applied to separate the impedance contributions from the anode and cathode side. The results confirmed that the PEO/NCM interface is indeed the Achilles' heel in PEO-based SSBs at high voltages. In this context, it is worth noting that the interfacial stability on the cathode side is influenced by not just the cut-off voltage, but also by the molecular weight of PEO. This observation underscores that the number of terminal hydroxide groups in PEO plays a significant role in the oxidative degradation process of the SPE. Consequently, PEO with M_w=8,000,000 g mol^{-1} has the highest capacity retention compared to PEO with lower molecular weight. Moreover, to provide access to the PEO/NCM interface for *post mortem* analysis, a special workflow was developed in this dissertation to remove the current collector from the cathode. Based on this, XPS analysis demonstrated the presence of oxidative degradation products of the SPE after cycling to high voltages, especially leading the formation of C=O species. Another important key finding emerged from the SEM analysis, when comparing the cathodes before and after cycling to high potentials. Before cycling large empty pores were present in the cathode, which, however, were filled by the SPE after cycling to 4.1 or 4.3 V. Hence, this suggests that the oxidative degradation of the PEO-based SPE results in chain cleavage of the polymer, leading to a lower viscosity that facilitates complete infiltration of the cathode pores with the electrolyte. Consequently, the operation of PEO-based SSBs with high-voltage cathodes results not only in an electrochemical degradation of the SPE, but also in mechanical degradation of the SPE. Altogether, the results unequivocally confirmed that PEO-based SPEs degrade when they are cycled with high-voltage cathodes.

It is worth noting that during the XPS analysis the X-Ray photodecomposition of conducting salts can be easily overlooked and misinterpreted. In this regard, the photodecomposition process is more pronounced when LiTFSI is dissolved in a PEO matrix compared to pure reference material. Further, the photodecomposition process can be significantly reduced, when measuring under cryogenic conditions or reducing the measurement time. As a

consequence, no LiF degradation products were observed in pristine PEO-LiTFSI and PEO-LiTFSI with NCM (before and after cycling).

Overall, this dissertation expands the understanding of the stability of PEO-based SPEs with high-voltage cathodes. In particular, this work shows how interfaces in PEO-based SSBs, which are typically challenging to access, can be effectively approached. The findings are placed within the broader context of the existing literature on the interfacial stability of SPEs. The knowledge gained in this dissertation is crucial to develop effective protection strategies in order to improve the cycle stability of SSBs.

Although the above summarized results expand the knowledge of interfacial degradation in PEO-based SSBs, there are still many relevant questions that could serve as focal points for future studies:

i) Further characterization of the degraded PEO-based SPE

In this work, it was proposed that the electrochemical degradation of PEO-based SPEs is accompanied by mechanical degradation leading to cleavage of the polymer backbone and consequent decrease in viscosity. Although the cleavage of the polymer is proposed in other reports, direct evidence of this phenomenon has not been provided yet. Accordingly, this hypothesis needs to be confirmed in further studies, e.g., by gel permeation chromatography (GPC) measurements that could determine the molecular weight distribution of PEO-based SPE before and after cycling. However, this requires the assembly of larger cells than those used in this work (cell diameter here: 10 mm) to obtain sufficient analytical material. Further, it is not understood, whether the mechanical degradation of the SPE at the cathode side can promote the growth of lithium dendrites at the anode side leading to cell failure, as indicated by "voltage noise". Therefore, *in situ* monitoring of dendrite growth, e.g., using SEM and long-term cycling to different cut-off potentials, could provide further insights.

ii) Further characterization of the Li/PEO-LiTFSI interface

In addition, it was shown in this dissertation that degradation processes on the anode side should not be neglected. Impedance measurements in a three-electrode setup showed a significant increase of the interfacial resistance at the anode side. This could be due to a potential cross-talk from the cathode side or due to other phenomena. Although the interfacial resistance of the anode side is not focus of this dissertation, it is worth to reinvestigate this interface not only during ageing but also after lithium platting stripping (dynamic conditions) in future studies. Since higher molecular weight PEO can mitigate the dendrite formation, it is important to understand if, in addition, the interfacial (electro)chemical stability on the anode is improved.

iii) Development of protection strategies

This dissertation is consistent with the common belief that PEO-based SPEs are not stable at higher voltages. Accordingly, effective protection strategies must be developed on the way to high energy density PEO-based SSBs. Potential strategies may involve substituting the terminal groups of PEO and/or developing protective coatings for high-voltage CAM. According to literature reports, several coatings such as LATP[25],[99] or lithium tantalate[29]

have already demonstrated a significant improvement in the long-term cycle stability of PEO-based SSBs with high-voltage LCO.

Finally, solid-state batteries based on both organic and inorganic solid electrolytes continue to face a number of challenges that must be addressed to facilitate their path to market. Additionally, it seems that the "all-solid" concept may not be the most rewarding target; instead, "almost-solid" may be the most viable strategy.[63] Nevertheless, progress to date is promising and suggests that SSBs (or almost-SSBs) are on the verge of commercial success (see QuantumScape, Factorial Energy, Solid Power etc.). The specific nature of this success, whether it relates to niche applications or the mass market, remains an open question.[6]

"If we knew what it is we were doing, it would not be called research, would it?"
– Albert Einstein (1879 – 1955)

5 References

[1] T.-H. Kim, J.-S. Park, S. Kyun Chang, S. Choi, J. Heon Ryu, H.-K. Song, *Adv. Energy Mater.* **2012**, *2*, 860.

[2] T. Placke, R. Kloepsch, S. Dühnen, M. Winter, *J Solid State Electrochem* **2017**, *21*, 1939.

[3] https://www.grandviewresearch.com/industry-analysis/lithium-ion-battery-market, **27.04.2023**.

[4] https://www.bundesregierung.de/breg-de/themen/klimaschutz/eenergie-und-mobilitaet/nachhaltige-mobilitaet-2044132, **27.04.2023**.

[5] R. F. Service, *Science* **2019**, *366*, 292.

[6] J. Janek, W. G. Zeier, *Nat Energy* **2023**, *8*, 230.

[7] J. Janek, W. G. Zeier, *Nat Energy* **2016**, *1*.

[8] S. Evers, L. F. Nazar, *Acc Chem Res* **2013**, *46*, 1135.

[9] J. Betz, G. Bieker, P. Meister, T. Placke, M. Winter, R. Schmuch, *Adv. Energy Mater.* **2019**, *9*, 1900761.

[10] O. C. Harris, S. E. Lee, C. Lees, M. Tang, *J. Phys. Energy* **2020**, *2*, 32002.

[11] Q. Lv, Y. Jiang, B. Wang, Y. Chen, F. Jin, B. Wu, H. Ren, N. Zhang, R. Xu, Y. Li, T. Zhang, Y. Zhou, D. Wang, H. Liu, S. Dou, *Cell Rep. Phys. Sci.* **2022**, *3*, 100706.

[12] X. Zhang, S. Wang, C. Xue, C. Xin, Y. Lin, Y. Shen, L. Li, C.-W. Nan, *Adv Mater* **2019**, *31*, e1806082.

[13] C. Wang, K. Fu, S. Palakkathodi Kammampata, D. W. McOwen, A. Junio Samson, L. Zhang, G. T. Hitz, A. M. Nolan, E. D. Wachsman, Y. Mo, V. Thangadurai, L. Hu, *Chem Rev* **2020**, *120*, 4257.

[14] Q. Liu, Z. Geng, C. Han, Y. Fu, S. Li, Y. He, F. Kang, B. Li, *J. Power Sources* **2018**, *389*, 120.

[15] X. Li, J. Liang, X. Yang, K. R. Adair, C. Wang, F. Zhao, X. Sun, *Energy Environ. Sci.* **2020**, *13*, 1429.

[16] X. Zhao, Z. Zhao-Karger, M. Fichtner, X. Shen, *Angew Chem Int Ed Engl* **2020**, *59*, 5902.

[17] S. P. Culver, R. Koerver, W. G. Zeier, J. Janek, *Adv. Energy Mater.* **2019**, *9*, 1900626.

[18] F. Walther, S. Randau, Y. Schneider, J. Sann, M. Rohnke, F. H. Richter, W. G. Zeier, J. Janek, *Chem. Mater.* **2020**, *32*, 6123.

[19] Y. Jiang, X. Yan, Z. Ma, P. Mei, W. Xiao, Q. You, Y. Zhang, *Polymers (Basel)* **2018**, *10*.

[20] J.-H. Shin, W. A. Henderson, C. Tizzani, S. Passerini, S.-S. Jeong, K.-W. Kim, *J. Electrochem. Soc.* **2006**, *153*, A1649.

[21] D. E. Fenton, J. M. Parker, P. V. Wright, *Polymer* **1973**, *14*, 589.

[22] M. Armand, J.M. Chabagno, M. Duclot, *Second International Meeting on Solid Electrolytes* **1978**, St. Andrews, Scotland.

[23] H. Zhang, C. Li, M. Piszcz, E. Coya, T. Rojo, L. M. Rodriguez-Martinez, M. Armand, Z. Zhou, *Chem Soc Rev* **2017**, *46*, 797.

[24] Y. Zhu, J. Cao, H. Chen, Q. Yu, B. Li, *J. Mater. Chem. A* **2019**, *7*, 6832.

[25] J. Qiu, X. Liu, R. Chen, Q. Li, Y. Wang, P. Chen, L. Gan, S.-J. Lee, D. Nordlund, Y. Liu, X. Yu, X. Bai, H. Li, L. Chen, *Adv. Funct. Mater.* **2020**, *30*, 1909392.

[26] R. Fang, B. Xu, N. S. Grundish, Y. Xia, Y. Li, C. Lu, Y. Liu, N. Wu, J. B. Goodenough, *Angew. Chem.* **2021**, *133*, 17842.
[27] J. Yin, X. Xu, S. Jiang, H. Wu, L. Wei, Y. Li, J. He, K. Xi, Y. Gao, *J. Chem. Eng.* **2022**, *431*, 133352.
[28] C. Wang, Y. Yang, X. Liu, H. Zhong, H. Xu, Z. Xu, H. Shao, F. Ding, *ACS Appl Mater Interfaces* **2017**, *9*, 13694.
[29] J. Liang, Y. Sun, Y. Zhao, Q. Sun, J. Luo, F. Zhao, X. Lin, X. Li, R. Li, L. Zhang, S. Lu, H. Huang, X. Sun, *J. Mater. Chem. A* **2020**, *8*, 2769.
[30] G.-T. Kim, G. B. Appetecchi, F. Alessandrini, S. Passerini, *J. Power Sources* **2007**, *171*, 861.
[31] Y. Liu, Y. Zhao, W. Lu, L. Sun, L. Lin, M. Zheng, X. Sun, H. Xie, *Nano Energy* **2021**, *88*, 106205.
[32] L. Seidl, R. Grissa, L. Zhang, S. Trabesinger, C. Battaglia, *Adv. Mater. Interfaces* **2022**, *9*, 2100704.
[33] X. Yang, M. Jiang, X. Gao, D. Bao, Q. Sun, N. Holmes, H. Duan, S. Mukherjee, K. Adair, C. Zhao, J. Liang, W. Li, J. Li, Y. Liu, H. Huang, L. Zhang, S. Lu, Q. Lu, R. Li, C. Veer Singh, X. Sun, *Energy Environ. Sci.* **2020**, *13*, 1318.
[34] G. Homann, L. Stolz, J. Nair, I. Cekic Laskovic, M. Winter, J. Kasnatscheew, *Sci Rep* **2020**, *10*, 4390.
[35] E. Simonetti, M. Carewska, M. Di Carli, M. Moreno, M. de Francesco, G. B. Appetecchi, *Electrochim. Acta* **2017**, *235*, 323.
[36] S. Usta, M. Çelik, T. Çetinkaya, *J. Power Sources* **2023**, *580*, 233404.
[37] Y. Yusim, E. Trevisanello, R. Ruess, F. H. Richter, A. Mayer, D. Bresser, S. Passerini, J. Janek, A. Henss, *Angew Chem Int Ed Engl* **2023**, *62*, e202218316.
[38] Y. Yusim, D. F. Hunstock, A. Mayer, D. Bresser, S. Passerini, J. Janek, A. Henss, *Adv. Mater. Interfaces* **2023**, 2300532.
[39] R. S. Negi, Y. Yusim, R. Pan, S. Ahmed, K. Volz, R. Takata, F. Schmidt, A. Henss, M. T. Elm, *Adv. Mater. Interfaces* **2022**, *9*, 2101428.
[40] M. Faraday, *Phil. Trans. R. Soc.* **1833**, *123*, 23.
[41] M. Bertrand, S. Rousselot, D. Aymé-Perrot, M. Dollé, *Mater. Adv.* **2021**, *2*, 2989.
[42] Y. Ren, T. Danner, A. Moy, M. Finsterbusch, T. Hamann, J. Dippell, T. Fuchs, M. Müller, R. Hoft, A. Weber, L. A. Curtiss, P. Zapol, M. Klenk, A. T. Ngo, P. Barai, B. C. Wood, R. Shi, L. F. Wan, T. Wook Heo, M. Engels, J. Nanda, F. H. Richter, A. Latz, V. Srinivasan, J. Janek, J. Sakamoto, E. D. Wachsman, D. Fattakhova-Rohlfing, *Adv. Energy Mater.* **2023**, *13*, 2201939.
[43] L. M. Riegger, R. Schlem, J. Sann, W. G. Zeier, J. Janek, *Angew Chem Int Ed Engl* **2021**, *60*, 6718.
[44] P. Minnmann, L. Quillman, S. Burkhardt, F. H. Richter, J. Janek, *J. Electrochem. Soc.* **2021**, *168*, 40537.
[45] L. M. Riegger, S.-K. Otto, M. Sadowski, S. Jovanovic, O. Kötz, S. Harm, L. G. Balzat, S. Merz, S. Burkhardt, F. H. Richter, J. Sann, R.-A. Eichel, B. V. Lotsch, J. Granwehr, K. Albe, J. Janek, *Chem. Mater.* **2022**, *34*, 3659.
[46] R. Koerver, I. Aygün, T. Leichtweiß, C. Dietrich, W. Zhang, J. O. Binder, P. Hartmann, W. G. Zeier, J. Janek, *Chem. Mater.* **2017**, *29*, 5574.
[47] D. Zhou, D. Shanmukaraj, A. Tkacheva, M. Armand, G. Wang, *Chem* **2019**, *5*, 2326.
[48] J. Ravi Nair, L. Imholt, G. Brunklaus, M. Winter, *Electrochem. Soc. Interface* **2019**, *28*, 55.

[49] C. Dingels, M. Schömer, H. Frey, *Chemie in unserer Zeit* **2011**, *45*, 338.
[50] J. Feng, L. Wang, Y. Chen, P. Wang, H. Zhang, X. He, *Nano Converg* **2021**, *8*, 2.
[51] D. Devaux, R. Bouchet, D. Glé, R. Denoyel, *Solid State Ion.* **2012**, *227*, 119.
[52] M. Marzantowicz, J. R. Dygas, F. Krok, J. L. Nowiński, A. Tomaszewska, Z. Florjańczyk, E. Zygadło-Monikowska, *J. Power Sources* **2006**, *159*, 420.
[53] Q. Ma, X. Qi, B. Tong, Y. Zheng, W. Feng, J. Nie, Y.-S. Hu, H. Li, X. Huang, L. Chen, Z. Zhou, *ACS Appl Mater Interfaces* **2016**, *8*, 29705.
[54] A. Maurel, M. Armand, S. Grugeon, B. Fleutot, C. Davoisne, H. Tortajada, M. Courty, S. Panier, L. Dupont, *J. Electrochem. Soc.* **2020**, *167*, 70536.
[55] https://www.greencarcongress.com/2006/11/avestor_shuts_d.html, **07.06.2023**.
[56] K. Brandt, *Meet. Abstr.* **2021**, *MA2021-02*, 726.
[57] https://www.worldofchemicals.com/media/solvay-gets-bollore-groups-multi-year-contract-to-supply-lithium-salt/3994.html, **07.06.2023**.
[58] A. Mauger, C. M. Julien, *Inorganics* **2022**, *10*, 110.
[59] https://www.tagesschau.de/wirtschaft/technologie/elektrobusse-depotbrand-101.html, **07.06.2023**.
[60] https://www.bw24.de/stuttgart/daimler-ag-stuttgart-busdepot-brand-mercedes-e-bus-citaro-produktion-fehler-akku-mannheim-91061567.html, **07.06.2023**.
[61] J. Mindemark, M. J. Lacey, T. Bowden, D. Brandell, *Prog. Polym. Sci.* **2018**, *81*, 114.
[62] Y.-H. Chen, P. Lennartz, K. Ling Liu, Y.-C. Hsieh, F. Scharf, R. Guerdelli, A. Buchheit, M. Grünebaum, F. Kempe, M. Winter, G. Brunklaus, *Adv. Funct. Mater.* **2023**, *33*.
[63] H. Huo, J. Janek, *Natl Sci Rev* **2023**, *10*, nwad098.
[64] P. Selinis, F. Farmakis, *J. Electrochem. Soc.* **2022**, *169*, 10526.
[65] J. Xie, Y.-C. Lu, *Nat Commun* **2020**, *11*, 2499.
[66] J. T. Frith, M. J. Lacey, U. Ulissi, *Nat Commun* **2023**, *14*, 420.
[67] S. Jin An, J. Li, C. Daniel, D. Mohanty, S. Nagpure, D. L. Wood, *Carbon* **2016**, *105*, 52.
[68] H. Huo, J. Janek, *ACS Energy Lett.* **2022**, *7*, 4005.
[69] M. T. McDowell, S. Xia, T. Zhu, *Extreme Mechanics Letters* **2016**, *9*, 480.
[70] P. Zhai, L. Liu, X. Gu, T. Wang, Y. Gong, *Adv. Energy Mater.* **2020**, *10*, 2001257.
[71] T. Krauskopf, H. Hartmann, W. G. Zeier, J. Janek, *ACS Appl Mater Interfaces* **2019**, *11*, 14463.
[72] https://www.arenaev.com/heres_a_breakdown_of_the_cost_of_an_ev_battery-news-55.php, **19.06.2023**.
[73] A. K. Padhi, K. S. Nanjundaswamy, J. B. Goodenough, *J. Electrochem. Soc.* **1997**, *144*, 1188.
[74] C. Daniel, D. Mohanty, J. Li, D. L. Wood, *AIP Conference Proceedings* **2014**, *1597*, 26.
[75] N. Boaretto, I. Garbayo, S. Valiyaveettil-SobhanRaj, A. Quintela, C. Li, M. Casas-Cabanas, F. Aguesse, *J. Power Sources* **2021**, *502*, 229919.
[76] K. Mizushima, P. C. Jones, P. J. Wiseman, J. B. Goodenough, *Mat. Res. Bull.* **1980**, *15*, 783.
[77] S. Song, Y. Li, K. Yang, Z. Chen, J. Liu, R. Qi, Z. Li, C. Zuo, W. Zhao, N. Yang, M. Zhang, F. Pan, *J. Mater. Chem. A* **2021**, *9*, 5702.
[78] S. Liu, L. Xiong, C. He, *J. Power Sources* **2014**, *261*, 285.

[79] https://insideevs.de/news/598966/tesla-4690zellen-zerlegung-aufbau-ncm811chemie/, **21.06.2023**.
[80] B. Guo, Y. Fu, J. Wang, Y. Gong, Y. Zhao, K. Yang, S. Zhou, L. Liu, S. Yang, X. Liu, F. Pan, *Chem Commun (Camb)* **2022**, *58*, 8182.
[81] A. Gupta, E. Kazyak, N. Craig, J. Christensen, N. P. Dasgupta, J. Sakamoto, *J. Electrochem. Soc.* **2018**, *165*, A2801-A2806.
[82] Y. Ma, J. Wan, Y. Yang, Y. Ye, X. Xiao, D. T. Boyle, W. Burke, Z. Huang, H. Chen, Y. Cui, Z. Yu, S. T. Oyakhire, *Adv. Energy Mater.* **2022**, *12*.
[83] T. Fuchs, C. G. Haslam, F. H. Richter, J. Sakamoto, J. Janek, *Adv. Energy Mater.* **2023**.
[84] X. He, S. Schmohl, H.-D. Wiemhöfer, *ChemElectroChem* **2019**, *6*, 1166.
[85] S. Kaboli, H. Demers, A. Paolella, A. Darwiche, M. Dontigny, D. Clément, A. Guerfi, M. L. Trudeau, J. B. Goodenough, K. Zaghib, *Nano Lett* **2020**, *20*, 1607.
[86] N. Schweikert, A. Hofmann, M. Schulz, M. Scheuermann, S. T. Boles, T. Hanemann, H. Hahn, S. Indris, *J. Power Sources* **2013**, *228*, 237.
[87] G. Homann, L. Stolz, K. Neuhaus, M. Winter, J. Kasnatscheew, *Adv. Funct. Mater.* **2020**, *30*.
[88] L. Stolz, G. Homann, M. Winter, J. Kasnatscheew, *Mater. Adv.* **2021**, *2*, 3251.
[89] E. Peled, D. Golodnitsky, G. Ardel, V. Eshkenazy, *Electrochim. Acta* **1995**, *40*, 2197.
[90] R. Bouchet, S. Lascaud, M. Rosso, *J. Electrochem. Soc.* **2003**, *150*, A1385.
[91] F. J. Simon, M. Hanauer, F. H. Richter, J. Janek, *ACS Appl Mater Interfaces* **2020**, *12*, 11713.
[92] C. Xu, B. Sun, T. Gustafsson, K. Edström, D. Brandell, M. Hahlin, *J. Mater. Chem. A* **2014**, *2*, 7256.
[93] E. K. W. Andersson, C. Sångeland, E. Berggren, F. O. L. Johansson, D. Kühn, A. Lindblad, J. Mindemark, M. Hahlin, *J. Mater. Chem. A* **2021**, *9*, 22462.
[94] H. Cheng, C. B. Zhu, M. Lu, Y. Yang, *J. Power Sources* **2007**, *174*, 1027.
[95] E. E. Ushakova, A. Frolov, A. A. Reveguk, D. Yu. Usachov, D. M. Itkis, L. V. Yashina, *Applied Surface Science* **2022**, *589*, 153014.
[96] A. Mirsakiyeva, M. Ebadi, C. Moyses Araujo, D. Brandell, P. Broqvist, J. Kullgren, *J. Phys. Chem. C* **2019**, *123*, 22851.
[97] S.-K. Otto, T. Fuchs, Y. Moryson, C. Lerch, B. Mogwitz, J. Sann, J. Janek, A. Henss, *ACS Appl. Energy Mater.* **2021**, *4*, 12798.
[98] J. Ma, Z. Liu, B. Chen, L. Wang, L. Yue, H. Liu, J. Zhang, Z. Liu, G. Cui, *J. Electrochem. Soc.* **2017**, *164*, A3454-A3461.
[99] K. Nie, X. Wang, J. Qiu, Y. Wang, Q. Yang, J. Xu, X. Yu, H. Li, X. Huang, L. Chen, *ACS Energy Lett.* **2020**, *5*, 826.
[100] F. Faglioni, B. V. Merinov, W. A. Goddard, B. Kozinsky, *Phys Chem Chem Phys* **2018**, *20*, 26098.
[101] J. Li, Y. Ji, H. Song, S. Chen, S. Ding, B. Zhang, L. Yang, Y. Song, F. Pan, *Nano-micro Lett* **2022**, *14*, 191.
[102] E. Trevisanello, R. Ruess, G. Conforto, F. H. Richter, J. Janek, *Adv. Energy Mater.* **2021**, *11*, 2003400.
[103] L.-Y. Kuo, O. Guillon, P. Kaghazchi, *ACS Sustainable Chem. Eng.* **2021**, *9*, 7437.
[104] J. Li, X. Yang, X. Guan, R. Guo, Y. Che, J. Lan, L. Xing, M. Xu, W. Fan, W. Li, *Electrochim. Acta* **2020**, *354*, 136722.

[105] V. Wurster, C. Engel, H. Graebe, T. Ferber, W. Jaegermann, R. Hausbrand, *J. Electrochem. Soc.* **2019**, *166*, A5410-A5420.
[106] F. Linsenmann, D. Pritzl, H. A. Gasteiger, *J. Electrochem. Soc.* **2019**, *166*, A3668-A3674.
[107] S. Solchenbach, D. Pritzl, E. Jia Yi Kong, J. Landesfeind, H. A. Gasteiger, *J. Electrochem. Soc.* **2016**, *163*, A2265-A2272.
[108] L. Raijmakers, M. Lammers, P. Notten, *Electrochim. Acta* **2018**, *259*, 517.
[109] F. Walther, Dissertation, Gießen, *Interfacial Degradation in Lithium Thiophosphate-Based Composite Cathodes for All-Solid-State Lithium-Ion Batteries,* **2021**.
[110] M. Tiddia, I. Mihara, M. P. Seah, G. Ferraz Trindade, F. Kollmer, C. J. Roberts, R. Hague, G. Mula, I. S. Gilmore, R. Havelund, *ACS Appl Mater Interfaces* **2019**, *11*, 4500.
[111] W. Yu, Z. Yu, Y. Cui, Z. Bao, *ACS Energy Lett.* **2022**, *7*, 3270.
[112] I. Shterenberg, M. Salama, Y. Gofer, D. Aurbach, *J. Phys. Chem. C* **2017**, *121*, 3744.

6 Appendix

6.1 Supporting Information

6.1.1 Publication I

Supporting Information

Evaluation and Improvement of the Stability of Poly(ethylene oxide)-based Solid-state Batteries with High-Voltage Cathodes

Y. Yusim, E. Trevisanello, R. Ruess, F. H. Richter, A. Mayer, D. Bresser, S. Passerini, J. Janek, A. Henss**

WILEY-VCH

SUPPORTING INFORMATION

Table of Contents

Experimental Procedures

Materials. Poly(ethylene oxide) (PEO, M_w = 8,000,000 g mol^{-1} and M_w = 300,000 g mol^{-1}), $LiCoO_2$ (LCO, 99.8%) and 1-methyl-2-pyrrolidone (NMP, anhydrous, 99.5%) were purchased from Sigma-Aldrich. Single crystalline $LiNi_{0.83}Co_{0.11}Mn_{0.06}O_2$ (NCM) and $Li_{1.3}Al_{0.3}Ti_{1.7}(PO_4)_3$ (LATP) were purchased from MSE Supplies. Lithium bis(trifluoromethanesulfonyl)imide (LiTFSI, 99.9%) and polyvinylidene difluoride (PVDF, Solef 5130) were purchased from Solvay and the conductive carbon (Super P) from Timcal. The siliconized polyester foil (thickness: 100 µm) was purchased from Valentia Industries LTD, Ireland and pouch bag foil from Showa Denko, Japan. Lithium metal (thickness: 60 µm, Honjo, Japan) was used as counter electrode. All chemicals were dried under vacuum before use. Material storage, cell assembly and disassembly for post-mortem analysis were carried out in an argon-filled glovebox.

PEO membrane preparation. Free-standing PEO-LiTFSI membranes (M_w = 300,000 g mol^{-1} and M_w = 8,000,000 g mol^{-1}) were prepared by a solvent-free technique to exclude any solvent related influence.[1],[2] Briefly, 1000 mg of PEO and 650 mg of LiTFSI (EO/Li ratio 10:1) were intensively mixed until the powders formed a sticky composite, which was transferred into an aluminum-laminated pouch bag between two siliconized polyester foils, vacuum sealed (Sealervac) and annealed for 24 h at 90 °C. After annealing, the pouch bag containing the polymer electrolyte was hot-pressed (Atlas™ Series Autotouch) between two metal sheets at 90 °C with 294 MPa for 20 s. Thus, membranes with thickness of about 150-300 µm were obtained. The membranes were punched into disks of 12 mm diameter.

Electrode preparation and cell assembly. The LCO composite cathodes consisted of 75 wt% LCO, 10 wt% Super P, 10 wt% PEO-LiTFSI (EO/Li ratio 10:1) and 5 wt% PVDF. After PVDF was dissolved at vigorous agitation in NMP, LCO, Super P, PEO and LiTFSI were added. The suspension was mixed in a speed mixer (Hauschild DAC 150.1) using ZrO_2 balls. NCM cathodes consisted of 94 wt% NCM, 3 wt% SuperP and 3 wt% PVDF were prepared without adding the solid polymer electrolyte. Therefore, Super P was homogenized in an agate mortar for 5 min and was added to the PVDF solution. After the suspension was mixed in a speed mixer, NCM was added and mixed again. The slurries were cast on aluminum foil in argon atmosphere using a doctor blade with a gap of 200 µm for LCO and 60 µm for NCM. The casting process was followed by drying at 100 °C for 6 h under argon and at 120 °C for 12 h under vacuum. The cathodes were punched into disks of 10 mm diameter. While the LCO composite cathodes were not pressed, the NCM were pressed with 20 kN cm^{-2}. For LCO cathodes the mass loading was 1.5 mg cm^{-2} and for NCM cathodes the mass loading was 3.4 mg cm^{-2}. The LCO and NCM cathodes as well as the lithium metal anodes were punched into disks of 10 mm diameter. To prepare a LATP pellet, 200 mg of LATP powder was hand pressed in a 13 mm die and then isostatically pressed at 400 MPa. The subsequent sintering was performed at 1000 °C (100 K/h heating ramp and natural cooling). The obtained pellet with 10.3 mm diameter was dried under vacuum and brought inside an argon filled glovebox before use. Pouch bag cells were assembled by subsequently stacking the cathode, one membrane of PEO-LiTFSI (unless otherwise specified) and the lithium metal anode and were then vacuum sealed (Sealervac). The electrochemical tests were performed at 60 °C using a VMP-300 Biologic potentiostat if not specified otherwise. The LCO cells were cycled in the voltage range of 3.0-4.2 V (*vs*. Li$^+$/Li) with dis-/charge rates of 0.1C (1C = 135 mAh g^{-1}) and the NCM cells were cycled in the voltage range of 3.0-4.3 V (*vs*. Li$^+$/Li) with dis-/charge rates of 0.1C (1C = 200 mAh g^{-1}). After the electrochemical procedures, the cells with LATP (see Figure 2a in the main manuscript) were stored at -80 °C (ProfiLine Pegasus) for 3 h before cell disassembly. In the case of the cells with an intentional leakage (leakage cell)), the pouch bag cells were prepared with a little leakage, so that the cells were constantly exposed to the lab atmosphere (air and moisture) during the cycling. Of course, all other cells (i.e. the majority of cells) were properly closed (no exposure to air and moisture, thus representing the normal standard). Temperature-dependent electrochemical impedance spectroscopy measurements were performed in a climate camber WKL 64 by Weiss in a frequency range from 1 MHz to 10 mHz with an amplitude of 10 mV. Therefore, the SPE membrane was positioned between two cooper electrodes (blocking conditions) with a diameter of 10 mm.

Fourier-transform infrared spectroscopy. For the post-mortem Fourier-transform infrared spectroscopy (FTIR) analysis, electrolyte residues were collected after opening the pouch bag cell and transferred to the spectrometer placed in an argon-filled glovebox. FTIR spectra were collected on Nicolet iS5 in an attenuated total reflectance (ATR) mode in a frequency range from 400 to 4000 cm^{-1}.

Scanning electron microscopy. In order to characterize the morphology of pristine aluminum current collector and aluminum current collector exposed to high voltage after electrochemical cycling, the samples were measured by a Merlin high-resolution scanning electron microscope (Carl Zeiss AG). For this purpose, the aluminum current collector was removed from the cathode and washed twice with NMP solution. The samples were attached to a sample holder using insulating double-sided tape and were transferred from the glovebox to the SEM instrument using an argon-filled LEICA EM VCT500 shuttle (Leica Microsystems) to avoid air contact.

WILEY-VCH

SUPPORTING INFORMATION

X-ray Photoelectron Spectroscopy. X-ray photoelectron spectroscopy (XPS) measurements were performed using a PHI5000 Versa Probe II (Physical Electronics GmbH) with an aluminum anode. The X-ray power, beam voltage and beam diameter were 50 W, 15 kV and 200 µm, respectively. The pass energy of the analyzer was set to 93.90 eV to obtain the survey and 23.50 eV to obtain the detail spectra. For XPS investigations, three different samples were prepared: First cell was held at OCV for 45 h. The second and the third cells were charged with 0.15C to 4.1 V or 4.3 V *vs.* Li^+/Li, respectively, using PEO with M_W = 8,000.000 g mol^{-1} and NCM. These potentials were hold for 45 h. Subsequently, the cells were discharged with 0.15C. To access the NCM/SPE interface, the aluminum current collector was removed carefully. The samples were transferred with an argon-filled transfer module by PREVAC. The chamber pressure was maintained below 10^{-7} Pa. XPS data evaluation was carried out with CasaXPS (Version 2.3.23PR1.0). All spectra were calibrated in relation to the signal of adventitious carbon at 284.8 eV.

Results and Discussion

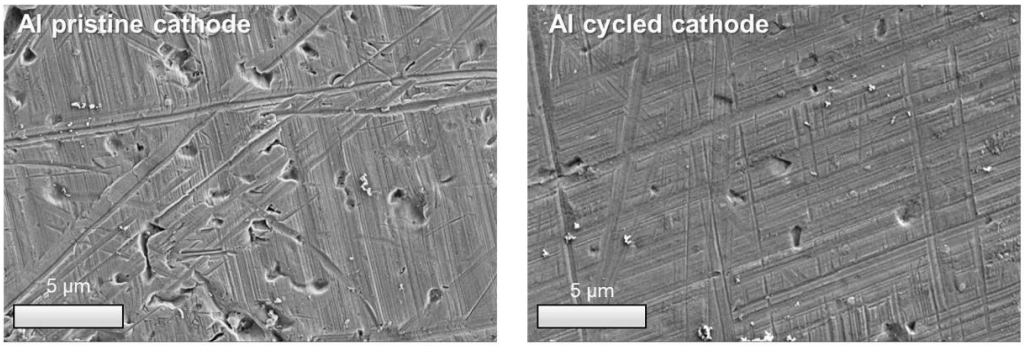

Figure S1. SEM images of the aluminum current collector before and after electrochemical cycling. The surface oriented towards the cathode material was investigated after removal of the cathode material.

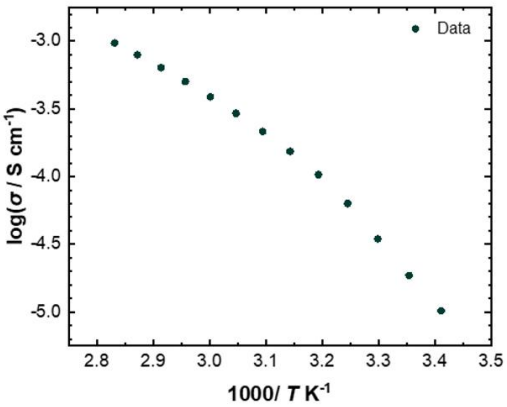

Figure S2. Temperature-dependent conductivities of the PEO-based SPE with M_w = 8,000,000 g mol^{-1}.

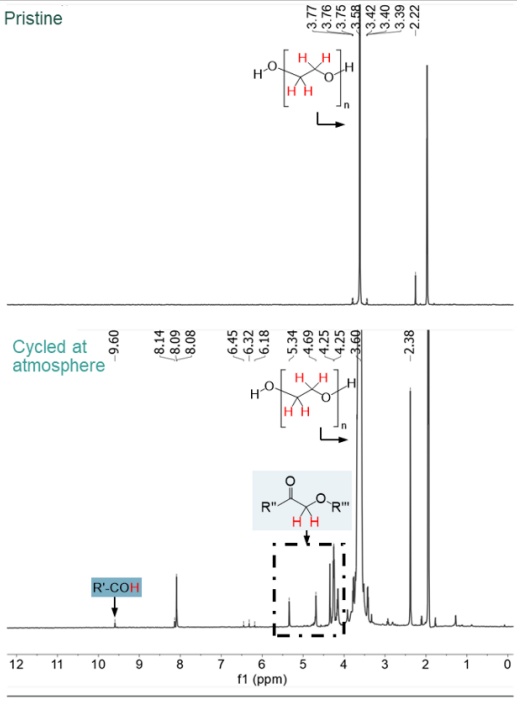

^{1}H NMR spectra (400 MHz, 300 K, CD_3CN)

Figure S3. ^{1}H NMR spectra for PEO-based SPE before (pristine, SPE accordingly dried and stored) and after cycling in cells with leakage. An unambiguous identification of the SPE degradation products is not possible here. Please note the spectra of the cycled cell with leakage were zoomed in for visualization reasons.

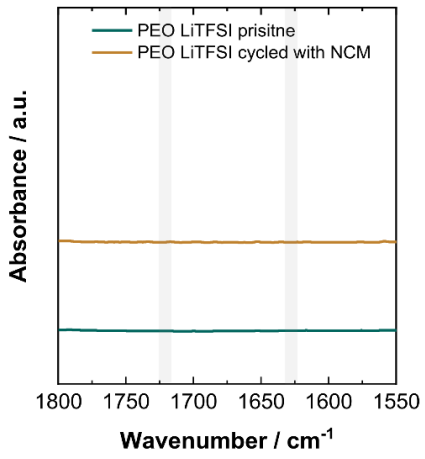

Figure S4. FTIR spectra in the range of 1800-1550 cm^{-1} of PEO-based SPE before and after electrochemical cycling. Cells were cycled with NCM within a voltage range of 3.0-4.3 V vs. Li^+/Li at 0.1C and 80 °C for 25 cycles using PEO with M_w = 8,000,000 g mol^{-1}.

SUPPORTING INFORMATION

References

[1] G. B. Appetecchi, M. Carewska, F. Alessandrini, P. P. Prosini, S. Passerini, *J. Electrochem. Soc.* **2000**, *147*, 451.

[2] F. J. Simon, M. Hanauer, A. Henss, F. H. Richter, J. Janek, *ACS Appl. Mater. Interfaces* **2019**, *11*, 42186.

Author Contributions

Y. Yusim:
data curation (lead)
formal analysis (lead)
investigation (lead)
writing of original draft (lead)

E. Trevisanello:
material synthesis (supporting)
data curation (supporting)
investigation (supporting)

Dr. R. Ruess:
data curation (supporting)
investigation (supporting)
writing of original draft (lead)

Dr. F. H. Richter:
writing of original draft (supporting)

A. Mayer:
investigation (supporting)

Dr. D. Bresser:
validation (supporting)
writing of original draft (supporting)

Prof. Dr. S. Passerini:
validation (supporting)
writing of original draft (supporting)

Prof. Dr. Dr. h.c. J. Janek:
validation (equal)
funding acquisition (supporting)
writing of original draft (supporting)
project administration (equal)

Dr. A. Henss:
validation (equal)
funding acquisition (lead)
project administration (equal)
writing of original draft (supporting)

6.1.2 Publication II

ADVANCED MATERIALS INTERFACES
Open Access

Supporting Information

for *Adv. Mater. Interfaces*, DOI 10.1002/admi.202300532

Investigation of the Stability of the Poly(ethylene oxide)|$LiNi_{1-x-y}Co_xMn_yO_2$ Interface in Solid-State Batteries

Yuriy Yusim, Dirk F. Hunstock, Alexander Mayer, Dominic Bresser, Stefano Passerini, Jürgen Janek and Anja Henss**

Supporting Information

Investigation of the Stability of the Poly(ethylene oxide)|$LiNi_{1-x-y}Co_xMn_yO_2$ Interface in Solid-state Batteries

Yuriy Yusim[a,b], Dirk F. Hunstock[a,b], Alexander Mayer[c,d], Dominic Bresser[c,d], Stefano Passerini[c,d,e], Jürgen Janek[a,b*] and Anja Henss[a,b*]

[a]*Institute of Physical Chemistry, Justus Liebig University Giessen, Heinrich-Buff-Ring 17, 35392 Giessen, Germany*

[b]*Center for Materials Research (ZfM/LaMa), Justus Liebig University Giessen, Heinrich-Buff-Ring 16, 35392 Giessen, Germany*

[c]*Helmholtz Institute Ulm (HIU), Helmholtzstraße 11, 89081 Ulm, Germany*

[d]*Karlsruhe Institute of Technology (KIT), P.O. Box 3640, 76021 Karlsruhe, Germany*

[e]*Department of Chemistry, Sapienza University of Rome, P. Aldo Moro 5, 00185 Rome, Italy*

Corresponding Authors

*Email:

Anja.Henss@phys.chemie.uni-giessen.de (A. Henss)

Juergen.Janek@phys.chemie.uni-giessen.de (J. Janek)

Keywords: Solid-state batteries, Solid polymer electrolytes, Poly(ethylene oxide) (PEO), High voltage cathode active material, Interface stability

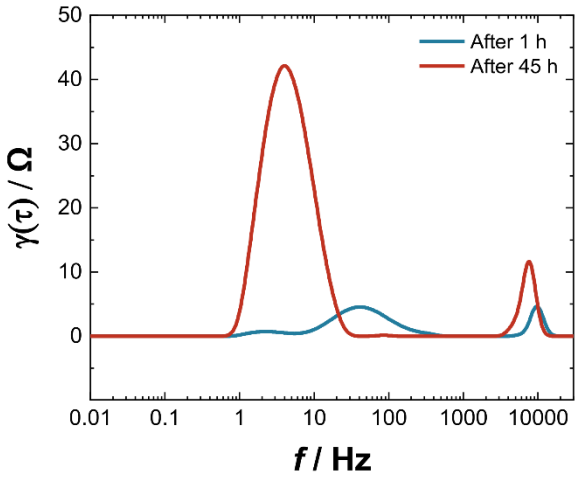

Figure S1: Distribution of Relaxation Times (DRT) analysis of cathode impedance after 1 h and after 45 h at 4.3 vs. Li^+/Li using Lamda: 0.01; Shape factor: 0.5; Extrapolation factor: 10 and Gaussian fit. The low frequency polarization was subtracted. Data indicate two main impedance contributions.

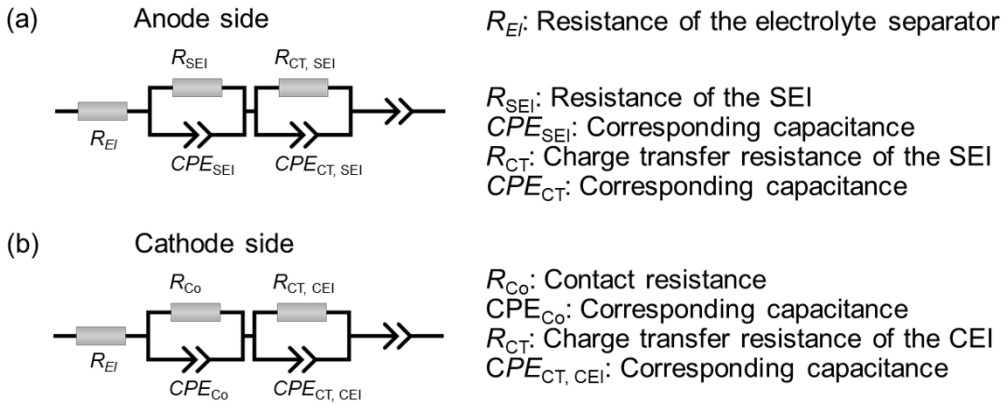

Figure S2: Equivalent circuit used to fit the experimental data for the (a) anode side and (b) cathode side.

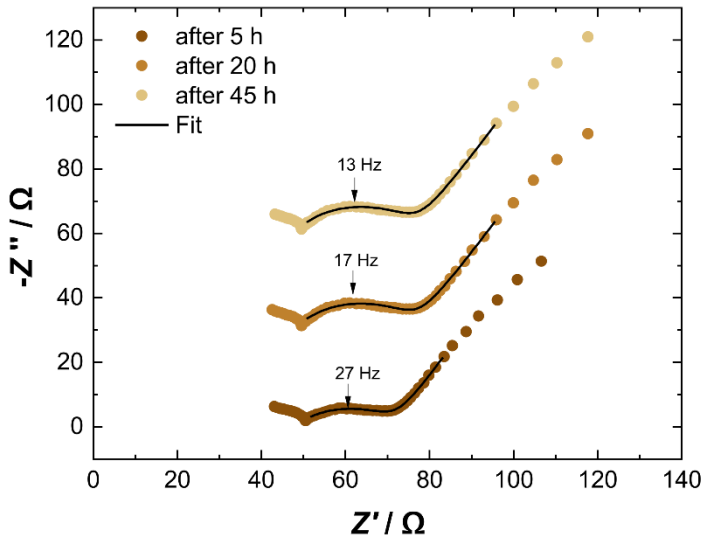

Figure S3: Time-dependent cathode impedance spectra during potential holding at 4.1 V vs. Li^+/Li (PEO, M_W = 8,000,0000 g mol^{-1}).

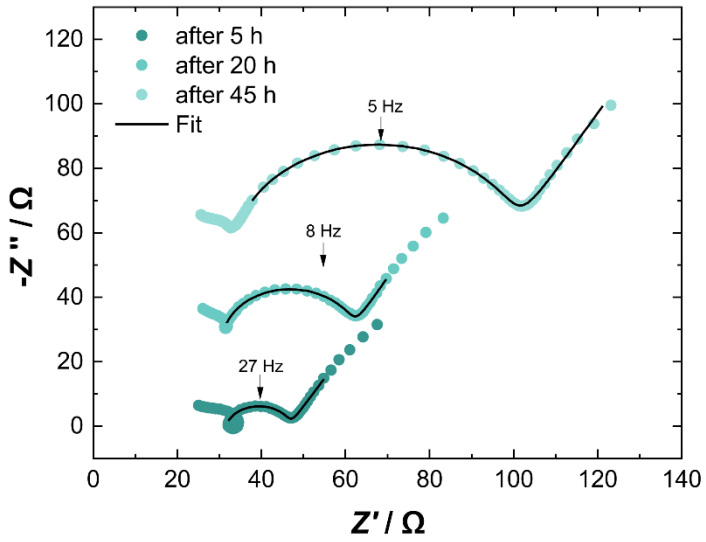

Figure S4: Time-dependent cathode impedance spectra during potential holding at 4.2 V vs. Li^+/Li (PEO, M_W = 8,000,0000 g mol^{-1}).

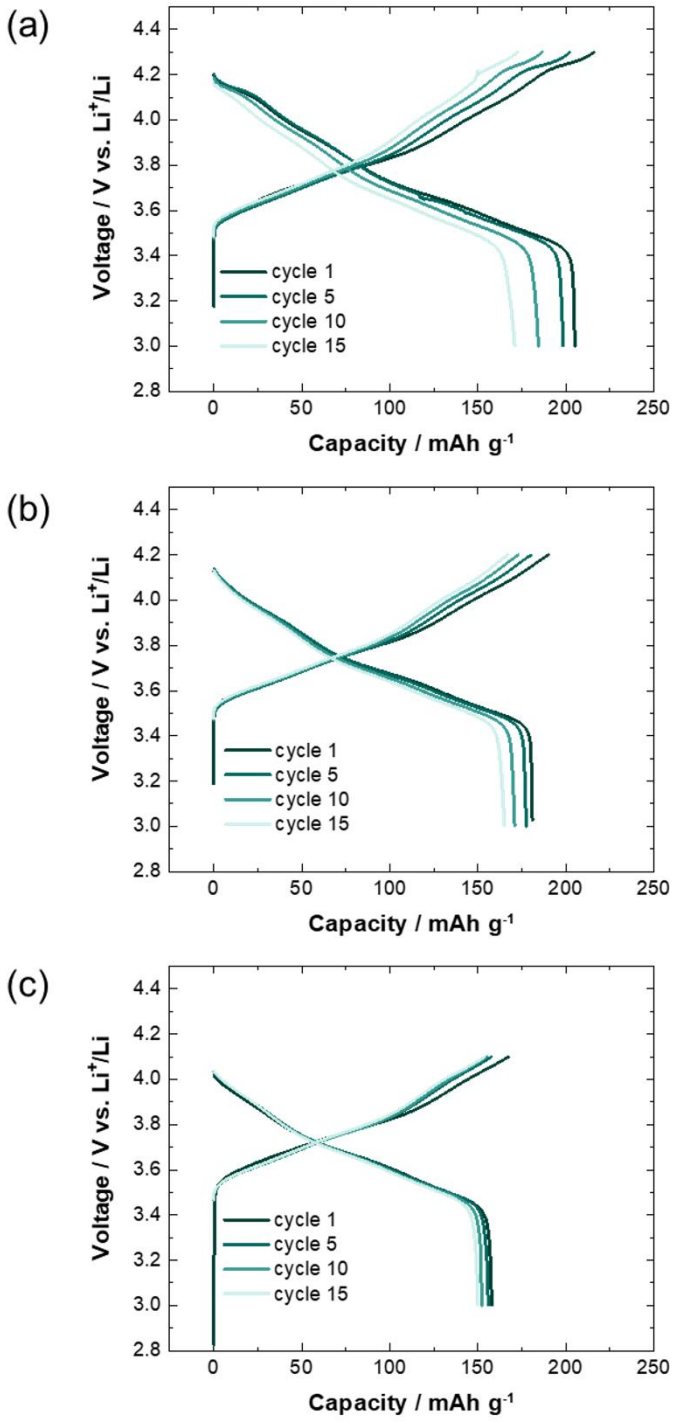

Figure S5: Charge and discharge profiles with cut-off voltages of (a) 4.3 V, (b) 4.2 V, and (c) 4.1 V vs. Li^+/Li (PEO, M_W = 8,000,0000 g mol^{-1}).

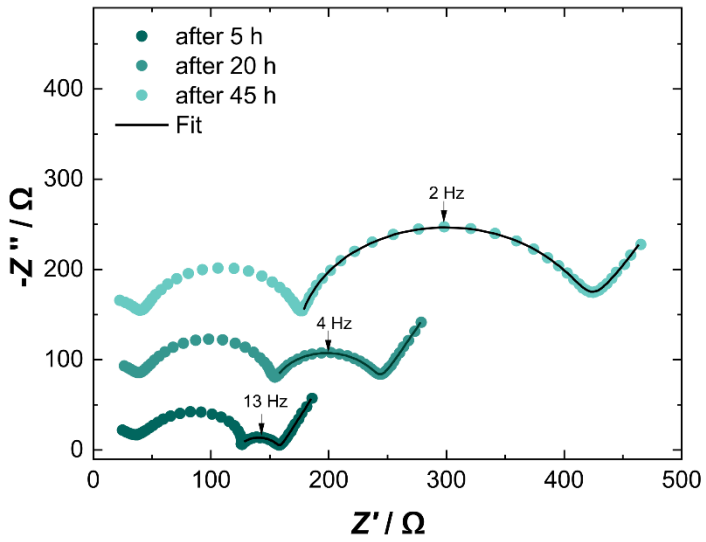

Figure S6: Time-dependent cathode impedance spectra during potential holding at 4.3 V vs. Li^+/Li (PEO, M_W = 600,000 g mol^{-1}).

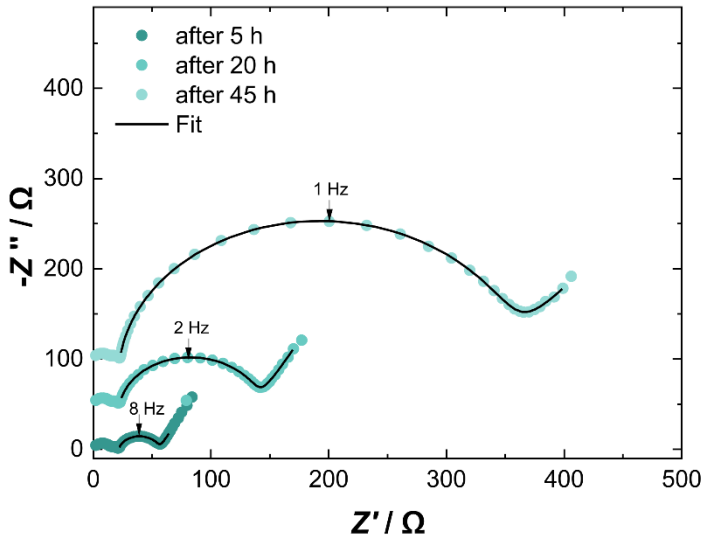

Figure S7: Time-dependent cathode impedance spectra during potential holding at 4.3 V vs. Li^+/Li (PEO, M_W = 300,000 g mol^{-1}).

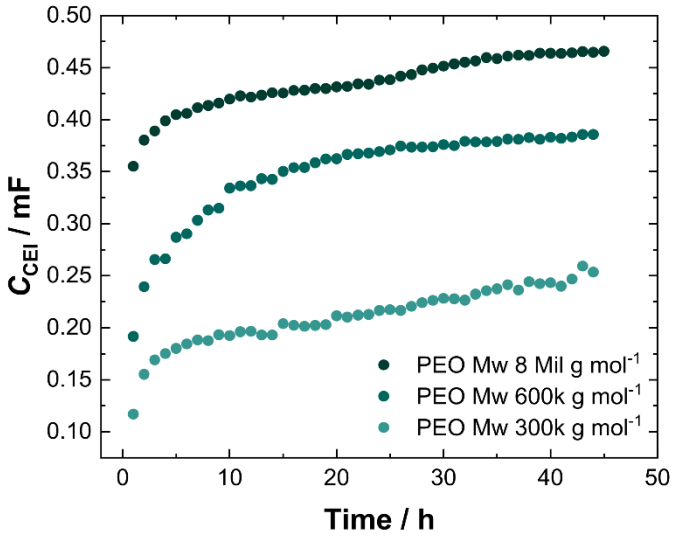

Figure S8: Temporal evolution of the capacity values of the interface between NCM and PEO-based SPE with different at 4.3 V vs. Li^+/Li.

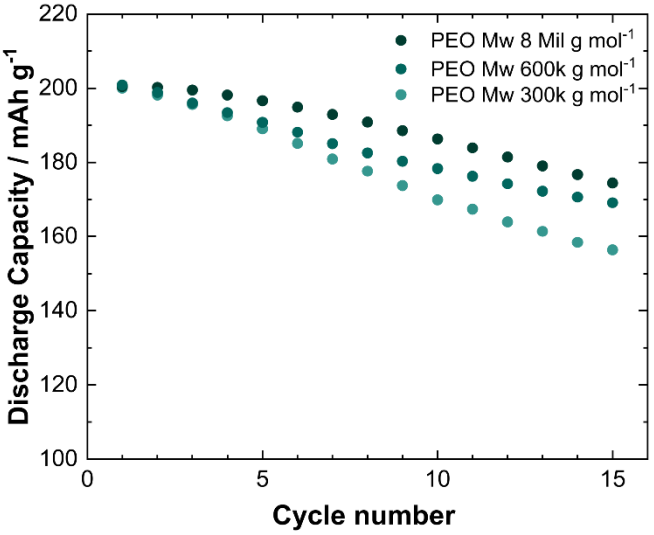

Figure S9: Galvanostatic cycling of PEO-based SPE with M_w of 8,000,000 g mol^{-1}, 600,000 g mol^{-1}, and 300,000 g mol^{-1} within a voltage range of 3.0-4.3 V vs. Li^+/Li at 0.15C.

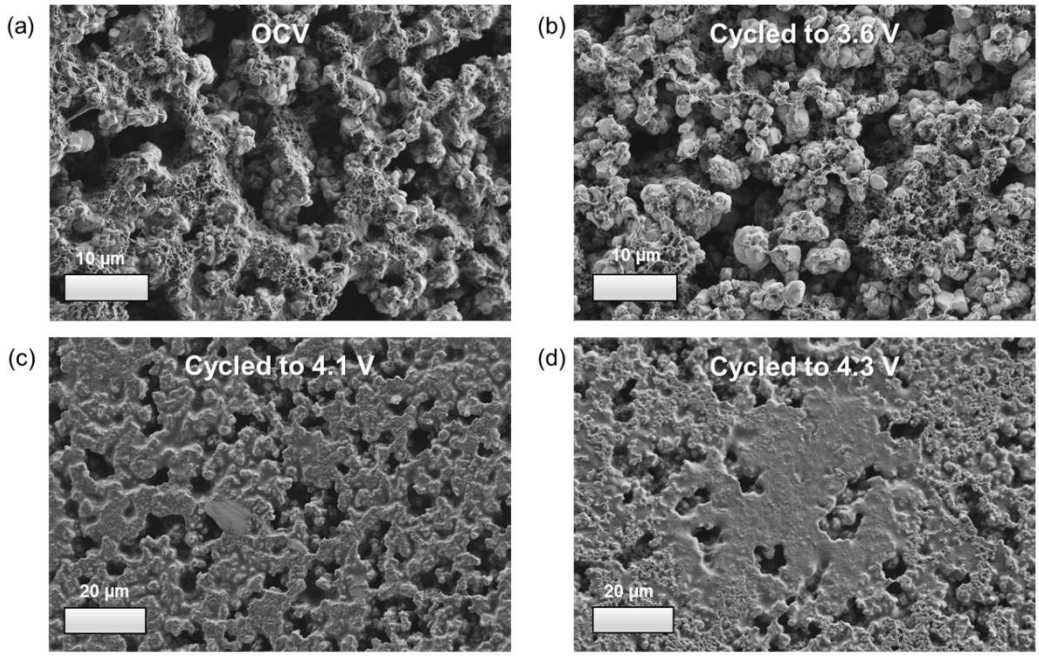

Figure S10: SEM images of cathode surfaces oriented towards the current collector after (a) OCV conditions and after cycling to (b) 3.6 V, (c) 4.1 V, and (d) 4.3 V vs. *Li^+/Li.*

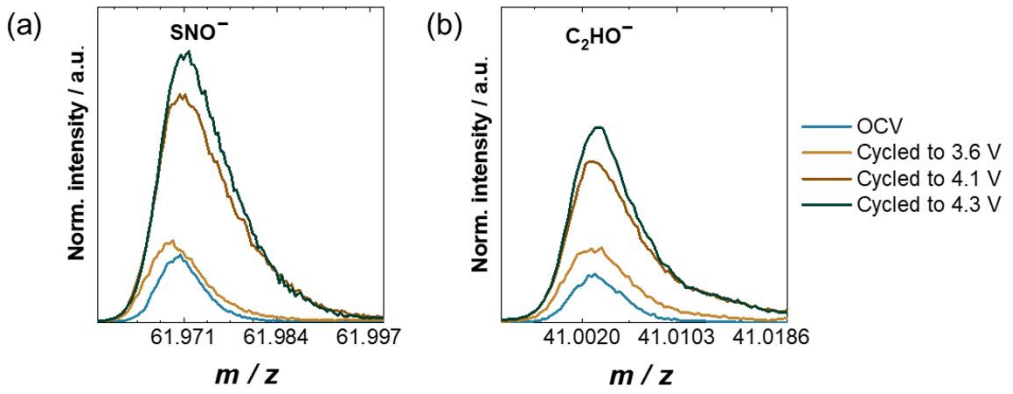

Figure S11: ToF-SIMS surface spectra of (a) SNO^- (representing the LiTFSI salt) and C_2HO^- fragments (representing the SPE) from an analysis area of 75 x 75 µm^2.

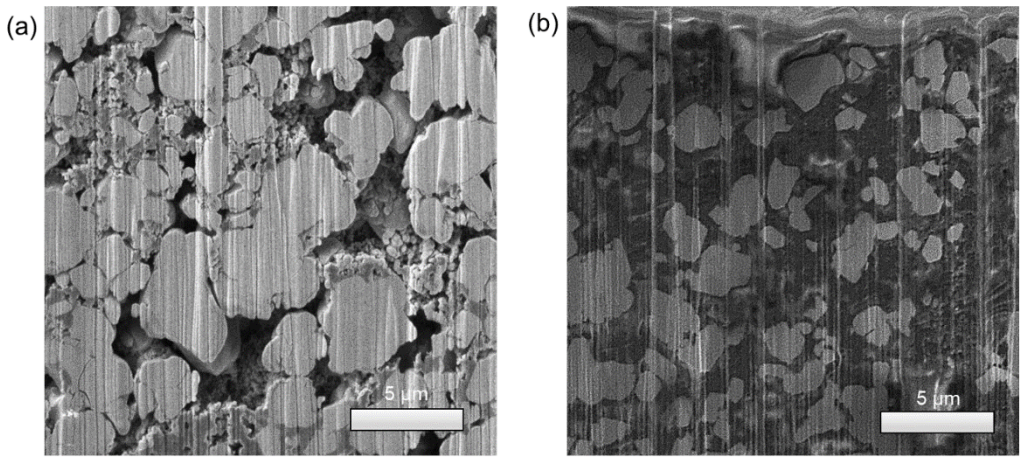

Figure S12: FIB-SEM cross section of (a) pristine cathode and (b) cycled cathode (4 cycles to 4.3 V vs. Li^+/Li). The pristine cathode was obtained from cell disassembly after storage at 80 °C.

6.1.3 Publication III

Supporting Information

Challenges in XPS Analysis of PEO-LiTFSI Batteries (Electrolytes): Interpreting X-ray Photodecomposition

Yuriy Yusim[a,b], Yannik Moryson[a,b], Kevin Seipp[c], Joachim Sann[a,b*] and Anja Henss[a,b]

[a]*Institute of Physical Chemistry, Justus Liebig University Giessen, Heinrich-Buff-Ring 17, 35392 Giessen, Germany*

[b]*Center for Materials Research (ZfM/LaMa), Justus Liebig University Giessen, Heinrich-Buff-Ring 16, 35392 Giessen, Germany*

[c]*Department of Chemistry, Johannes Gutenberg University, Duesbergweg 10–14, 55128 Mainz, Germany*

Corresponding Authors

*Email:
Joachim.Sann@phys.chemie.uni-giessen.de (J. Sann)

Keywords: XPS**,** Cryogenic conditions, Solid polymer electrolytes, Poly(ethylene oxide) (PEO), Conducing salts, Interface stability

Experimental Section

Materials. Poly(ethylene oxide) (PEO, M_w = 8,000,000 g mol^{-1}) and 1-methyl-2-pyrrolidone (NMP, anhydrous, 99.5%) were purchased from Sigma-Aldrich. Lithium bis(trifluoro-methanesulfonyl)imide (LiTFSI, 99.9%), Lithiumbis(fluorosulfonyl)imid (LiFSI, >98.0%) and polyvinylidene difluoride (PVDF, Solef 5130) were purchased from Solvay, the conductive carbon (Super P) from Timcal and single crystalline $LiNi_{0.83}Co_{0.11}Mn_{0.06}O_2$ was purchased from MSE Supplies. Lithium metal (thickness: 60 µm, Honjo, Japan) was used as counter electrode. The siliconized polyester foil (thickness: 100 µm) was purchased from Valentia Industries LTD, Ireland and pouch bag foil from Showa Denko, Japan. All chemicals and cell components were dried under vacuum before use. In particular, PEO was vacuum dried at 50 °C for 72 hours, according to literature[1]. Material storage were carried out in an argon-filled glovebox (<0.1 ppm of O_2, <0.1 ppm of H_2O).

PEO membrane preparation.[2] Free-standing PEO-LiTFSI membranes (M_w = 8,000,000 g mol^{-1}) were prepared by a solvent-free technique in order to exclude any solvent related affect.[3] For this reason, 1000 mg of PEO and 650 mg of LiTFSI (EO/Li ratio 10:1) were mixed until the powders formed a sticky composite, which was placed between two siliconized polyester foils, transferred into an aluminum-laminated pouch bag, vacuum sealed (Sealervac) and annealed for 12 h at 90 °C. Then the pouch bag with the polymer electrolyte was hot-pressed (Atlas™ Series Autotouch) between two metal plates at 90 °C with 294 MPa for 10 s. To prepare the SPE for XPS analysis, the membrane was punched into pieces. For the preparation of PEO-LIFSI, 1000 mg PEO and 419 mg LiFSI were mixed (EO/Li ratio 10:1) and the same procedure was followed, however, the mixture was not pressed, but cut into pieces.

Electrode preparation and cell assembly. Electrode preparation and cell assembly are described in our previous work[2].

XPS measurements. X-ray photoelectron spectroscopy (XPS) measurements were performed using a PHI5000 Versa Probe IV (Physical Electronics GmbH) with an aluminum anode (Al Kα =1486,6 eV). The X-ray power, beam voltage and beam diameter were 50 W, 15 kV and 200 µm, respectively. The pass energy of the analyzer was set to 112 eV to obtain the survey and 27 eV to obtain detailed spectra. The samples were transferred with an argon-filled transfer module. XPS data evaluation was carried out with CasaXPS (Version 2.3.23PR1.0). All spectra were calibrated in relation to the F 1s -CF_3 signal at 688.7 eV.

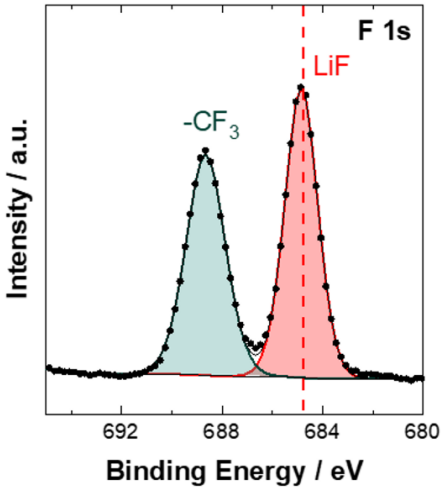

Figure S1: F 1s XP spectrum of PEO-LiTFSI, when F 1 spectrum was measured after survey, C 1s, O 1s, Li 1s, S 2p and N 1s spectra.

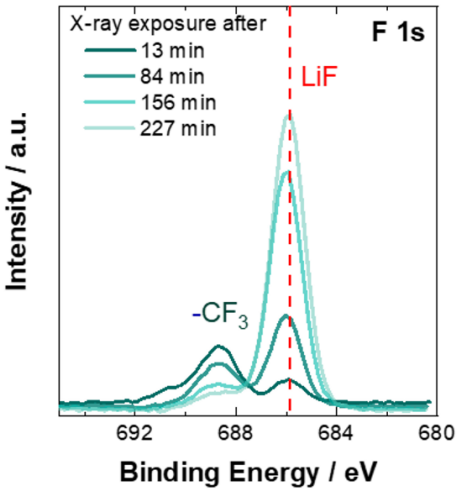

Figure S2: PEO-LiFSI after different X-ray exposure times.

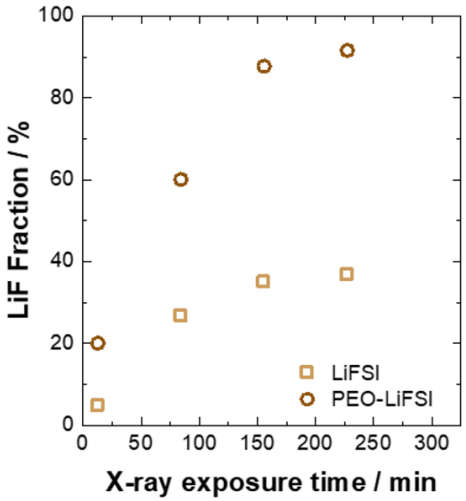

Figure S3: LiF fraction as function of the X-ray exposure time for PEO-LiFSI and LiFSI.

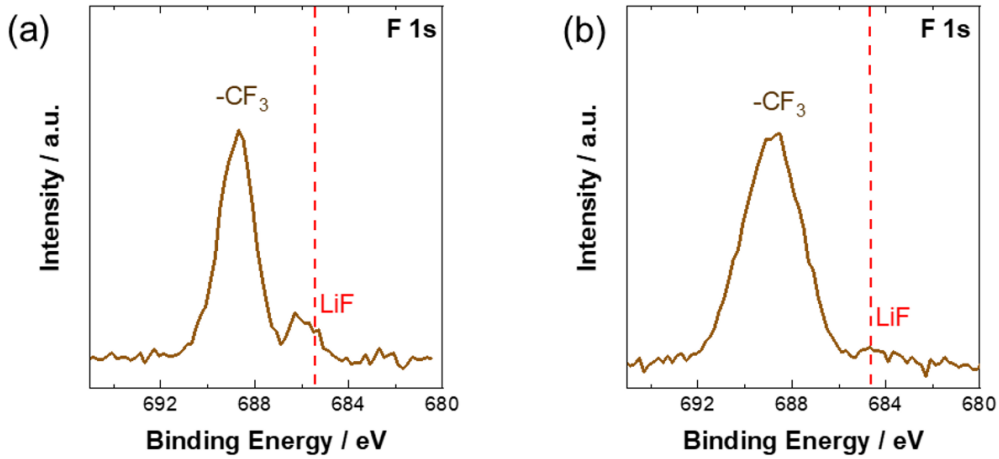

Figure S4: F 1s XP spectrum of PEO-LiFSI measured at (a) RT and (b) cryogenic conditions (−130 °C). X-ray exposure time was same in (a) and (b).

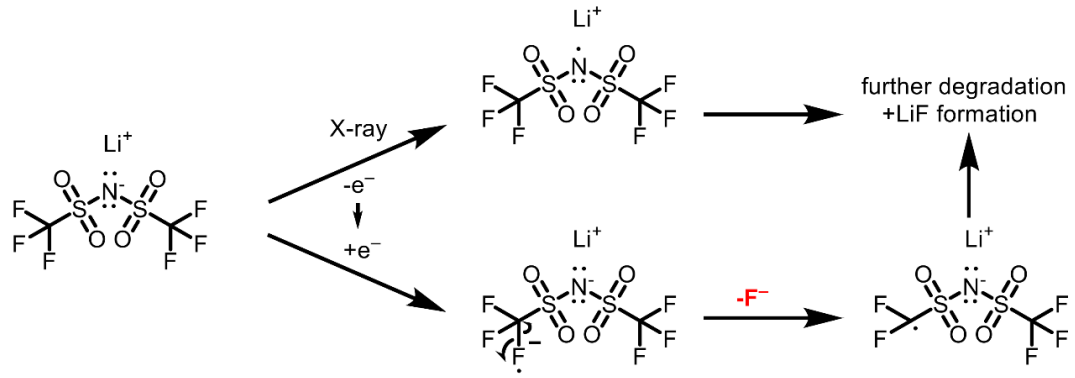

Figure S5: Suggested intermolecular mechanism of X-ray photodecomposition of LiTFSI.

References

1 Simon, F. J.; Hanauer, M.; Henss, A.; Richter, F. H.; Janek, J. Properties of the Interphase Formed between Argyrodite-Type Li6PS5Cl and Polymer-Based PEO10:LiTFSI. *ACS Appl. Mater. Interfaces* **2019**, *11*, 42186–42196. DOI: 10.1021/acsami.9b14506

2 Yusim, Y.; Trevisanello, E.; Ruess, R.; Richter, F. H.; Mayer, A.; Bresser, D.; Passerini, S.; Janek, J.; Henss, A. Evaluation and Improvement of the Stability of Poly(ethylene oxide)-based Solid-state Batteries with High-Voltage Cathodes. *Angew. Chem. Int. Ed. Engl.* **2023**, *62*, e202218316. DOI: 10.1002/anie.202218316

3 Appetecchi, G. B.; Carewska, M.; Alessandrini, F.; Prosini, P. P.; Passerini, S. Characterization of PEO-Based Composite Cathodes. I. Morphological, Thermal, Mechanical, and Electrical Properties. *J. Electrochem. Soc.* **2000**, *147*, 451. DOI: 10.1149/1.1393217

6.1.4 Publication IV

ADVANCED MATERIALS INTERFACES

Supporting Information

for *Adv. Mater. Interfaces,* DOI: 10.1002/admi.202101428

A Dry-Processed Al_2O_3/$LiAlO_2$ Coating for Stabilizing the Cathode/Electrolyte Interface in High-Ni NCM-Based All-Solid-State Batteries

Rajendra S. Negi, Yuriy Yusim, Ruijun Pan, Shamail Ahmed, Kerstin Volz, Ryo Takata, Franz Schmidt, Anja Henss,* and Matthias T. Elm**

Supporting Information

A dry-processed $Al_2O_3/LiAlO_2$ coating for stabilizing the cathode/electrolyte interface in high-Ni NCM-based all-solid-state batteries

Rajendra S. Negi[a,=], Yuriy Yusim[b,=], Ruijun Pan[a,b,c*], Shamail Ahmed[d], Kerstin Volz[d], Ryo Takata[e], Franz Schmidt[e], Anja Henss[a,b*] and Matthias T. Elm[a,b,f*]

[a]*Center for Materials Research (LaMa), Justus Liebig University Giessen, Heinrich-Buff-Ring 16, 35392 Giessen, Germany*

[b]*Institute of Physical Chemistry, Justus Liebig University Giessen, Heinrich-Buff-Ring 17, 35392 Giessen, Germany*

[c]*Materials Science and Engineering Program and Texas Materials Institute, University of Texas at Austin, Austin, TX, 78712 USA*

[d]*Materials Science Centre and Faculty of Physics, Philipps University Marburg, Hans-Meerwein-Strasse 6, 35043 Marburg, Germany*

[e]*Evonik Operations GmbH, Rodenbacher Chaussee 4, 63457 Hanau, Germany*

[f]*Institute of Experimental Physics I, Justus Liebig University Giessen, Heinrich-Buff-Ring 16, 35392 Giessen, Germany*

=These authors contributed equally to this work

Corresponding Authors

*Email:

Matthias.elm@phys.chemie.uni-giessen.de (M. T. Elm)

Anja.Henss@phys.chemie.uni-giessen.de (A. Henss)

Ruijun.Pan@phys.chemie.uni-geissen.de (R. Pan)

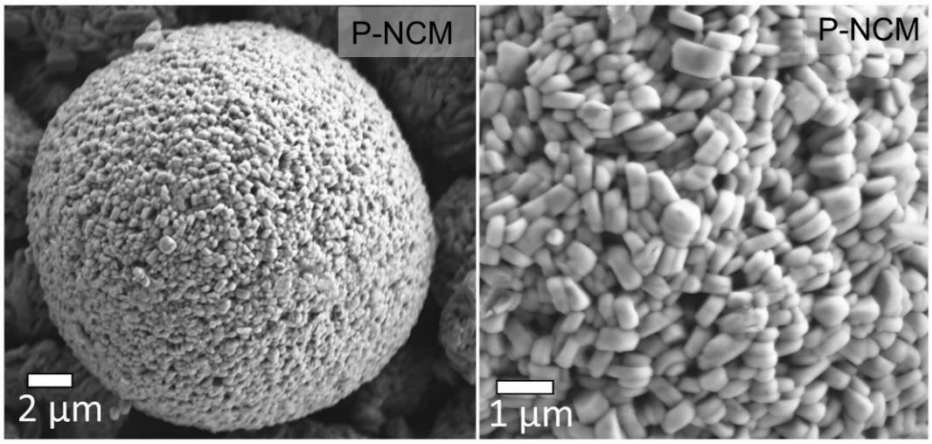

Figure S1: SEM-images of pristine NCM.

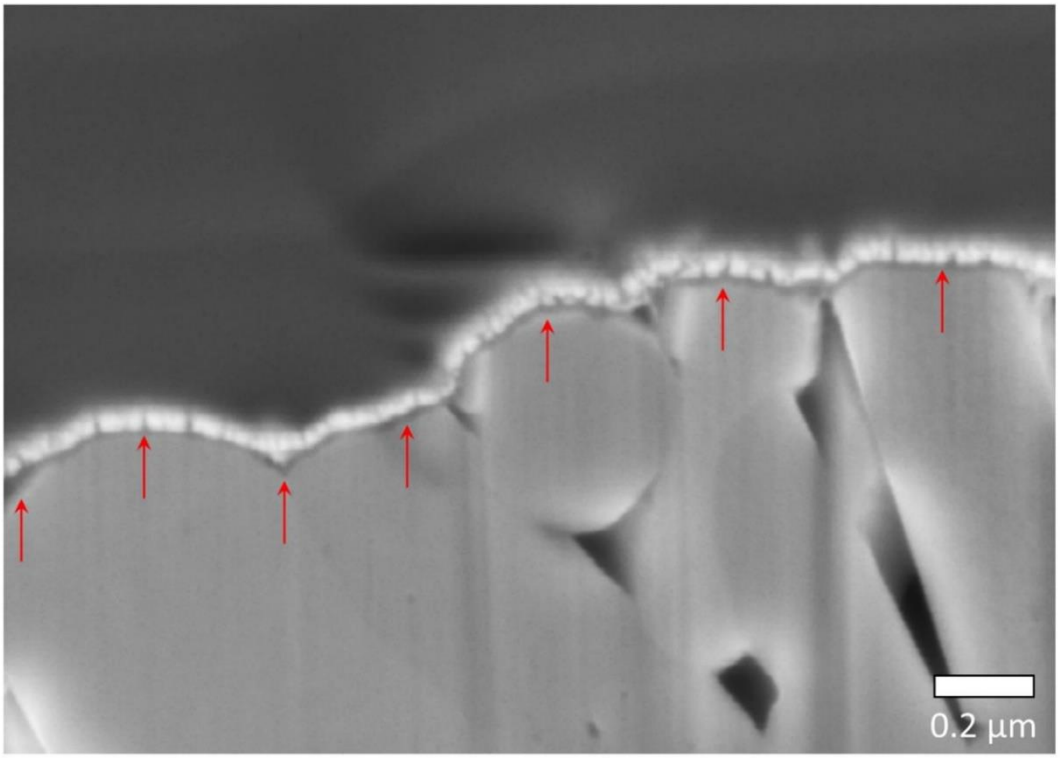

Figure S2: SEM cross-section image of the surface of the secondary particle confirming the homogenous coating for Alu-NCM600.

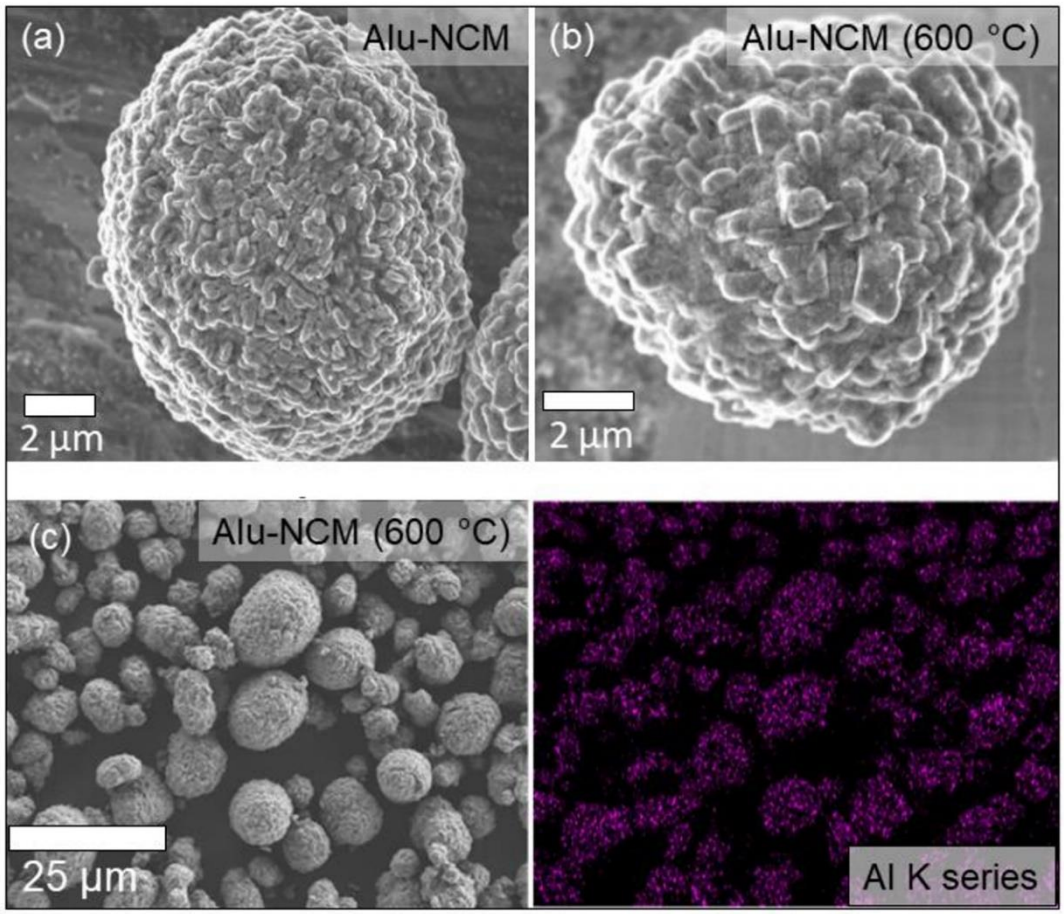

Figure S3: SEM images of the secondary particles of (a) Alu-NCM, (b) Alu-NCM600 and (c) SEM-EDS mapping of the Al signal of Alu-NCM600.

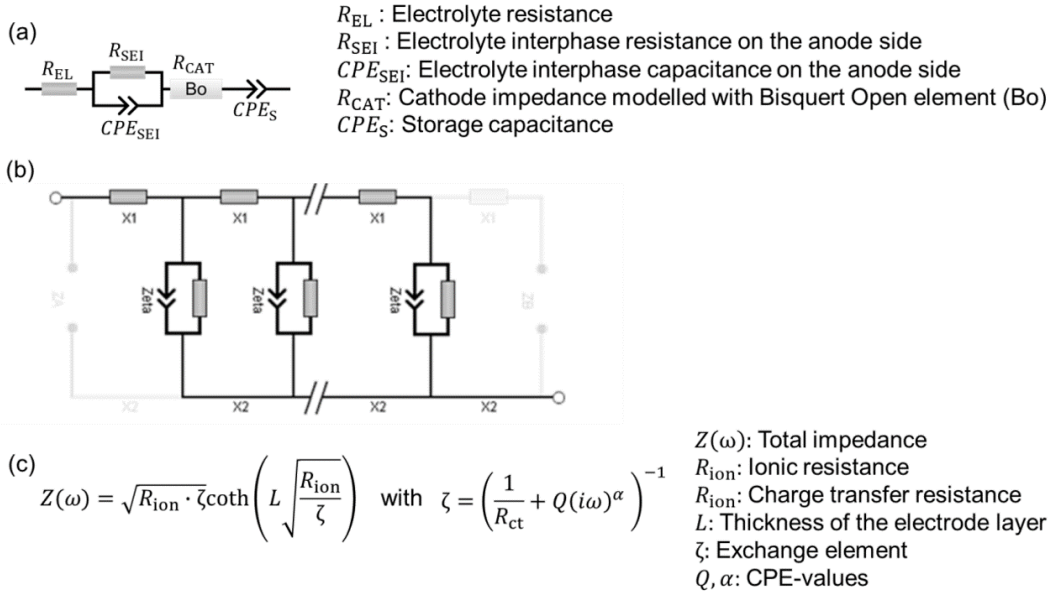

Figure S4: Impedance model used for fitting the full cell impedance spectra: (a) Equivalent circuit model including (b) Bisquert open element, which is based on (c) the Bisquert open-element equation (obtained from Relaxis, RHD instruments).

Impedance spectroscopy on full cells was performed. The resulting data were fitted to an equivalent circuit consisting of a single resistor R_{EL} representing the SSE layer in series to a parallel arrangement of a single resistor R_{SEI} and CPE_{SEI} representing the In/InLi|SSE interface. The time constant as well as feasible resistance values of 10-20 Ω for In/InLi|SSE interface was adopted from P. Minnmann et al.[1] Furthermore, a Bisquert open element[2] shown in Figure S3b was added in series in order to model the porous structure of the composite cathode. The fitting parameters obtained are listed in Table S1.

Table S1: Fitting parameter of impedance spectra after 1st and 100th cycle for P-NCM and Alu-NCM600 full cells.

	Parameter name	P-NCM 1st cycle	P-NCM 100th cycle	Alu-NCM600 1st cycle	Alu-NCM600 100th cycle
Electrolyte	R_{EL} / Ω	31.1	25.4	32.7	40.4
Anode side	R_{SEI} / Ω	10.0	40.0	20.0	41.6
	Q / F/s$^{1-\alpha}$	0.01	0.01	0.02	0.004
	α	1.00	0.92	0.62	0.78
Cathode side	R_{ion} / Ω	75.8	65.0	71.6	67.6
	R_{ct} / Ω	223.4	610.8	118.3	373.9
	L	1	1	1	1
	Q / F/s$^{1-\alpha}$	$8.30 \cdot 10^{-5}$	$6.51 \cdot 10^{-5}$	$1.35 \cdot 10^{-4}$	$4.74 \cdot 10^{-5}$
	α	0.77	0.72	0.72	0.75

References

[1] P. Minnmann, L. Quillman, S. Burkhardt, F. H. Richter, J. Janek, *J. Electrochem Soc.* **2021**, *168*, 040537.

[2] J. Bisquert, *Phys. Chem. Chem. Phys.* **2000**, *2*, 4185.

6.1.5 Publication V

Supporting Information

State of Charge Dependent Impedance Spectroscopy as a Helpful Tool to Identify Reasons for Fast Capacity Fading in All-Solid-State Batteries

Miguel Wiche[a,b,c=], Yuriy Yusim[a,b=], Kilian Vettori[a,b], Raffael Ruess[a,b], Anja Henss[a,b*] and Matthias T. Elm[a,b,c*]

[a]*Center for Materials Research (LaMa), Justus Liebig University Giessen, Heinrich-Buff-Ring 16, 35392 Giessen, Germany*

[b]*Institute of Physical Chemistry, Justus Liebig University Giessen, Heinrich-Buff-Ring 17, 35392 Giessen, Germany*

[c]*Institute of Experimental Physics I, Justus Liebig University Giessen, Heinrich-Buff-Ring 16, 35392 Giessen, Germany*

=These authors contributed equally to this work

Corresponding Authors

*Email:

Matthias.Elm@phys.chemie.uni-giessen.de (M.T. Elm)

Anja.Henss@phys.chemie.uni-giessen.de (A. Henss)

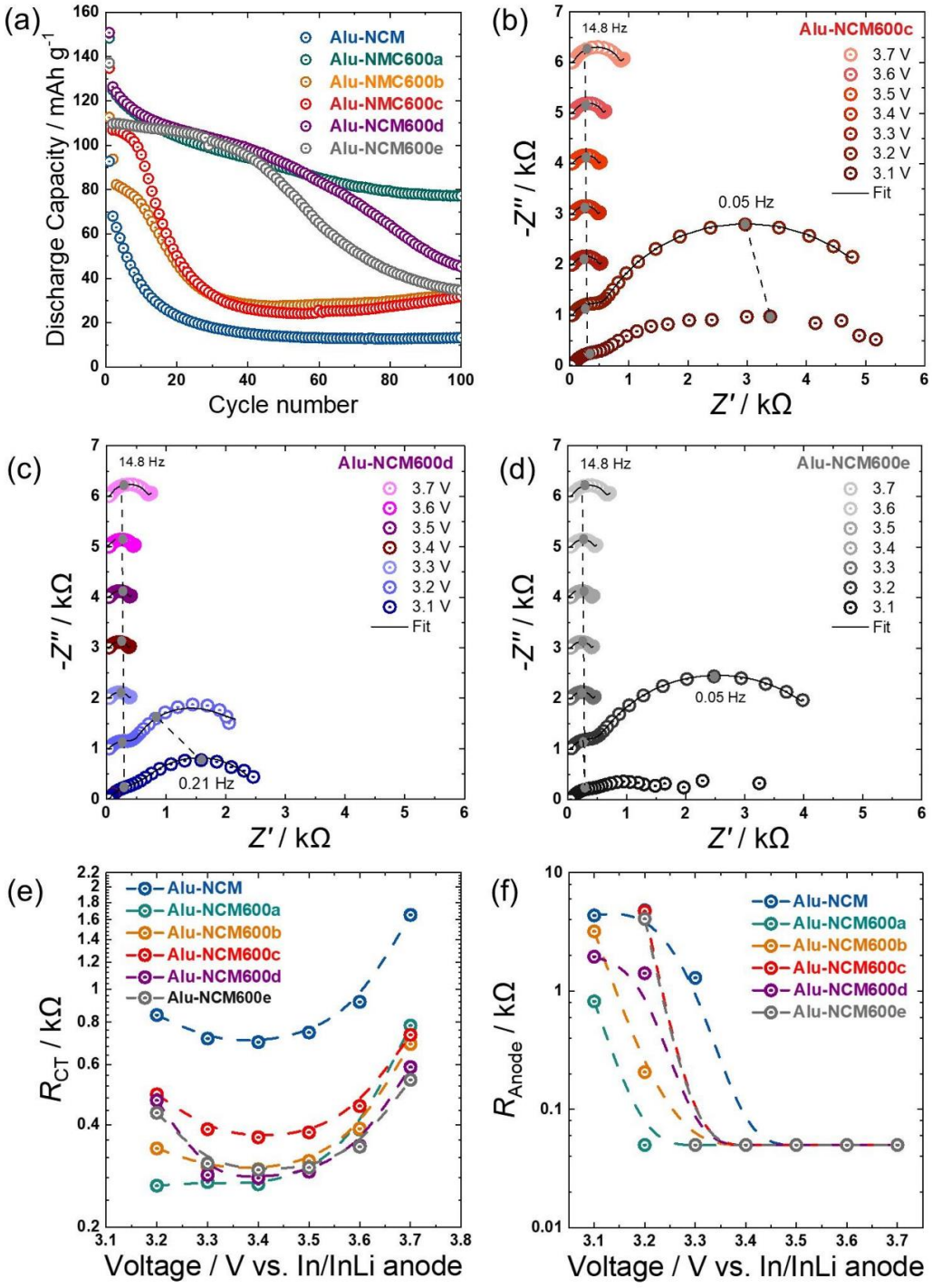

Figure S1:(a) Discharge capacity curves of Alu-NCM, Alu-NCM600a, Alu-NCM600b, Alu-NCM600c, Alu-NCM600d, and Alu-NCM600e. (b) and (c) EIS measurements during charge after 100 cycles for the Alu-NCM600c, Alu-NCM600d, and Alu-NCM600e cell, respectively.

(d) Potential-dependent charge transfer resistance R_{CT} on the cathode side after 100 cycles. (e) Comparison of the anode resistance R_{SEI} of all cells for varying potential after 100 cycles.

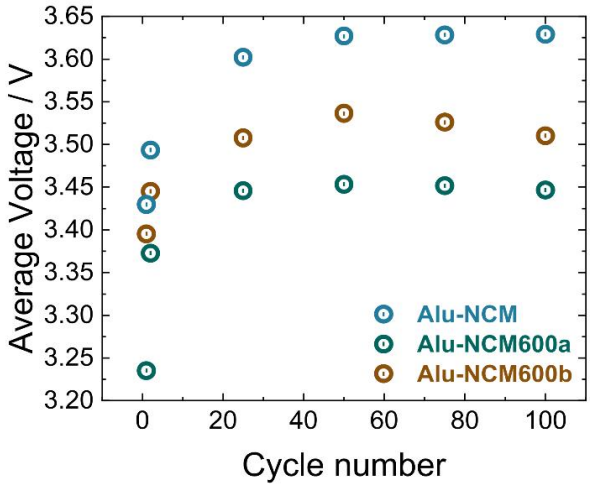

Figure S2: Comparison of the average voltage during charge as function of the cycle number for Alu-NCM, Alu-NCM600a and Alu-NCM-600b. The highest overpotential can be observed for Alu-NCM, followed by Alu-NCM600b, and Alu-NCM600a.

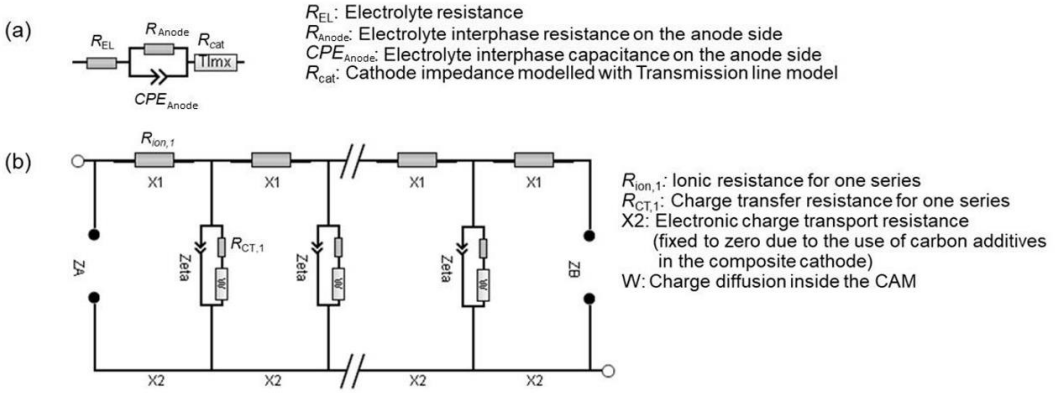

Figure S3: (a) Impedance model used for fitting the full cell impedance spectra (b) including the transmission line model used to describe the composite cathode. R_{ion} and R_{CT} is the sum over all $R_{ion,n}$ and $R_{CT,n}$ values.

Impedance spectroscopy was performed on all full cells. The resulting data were fitted with an equivalent circuit consisting of a single resistor R_{EL} representing the SSE layer in series to a parallel arrangement of a single resistor R_{Anode} and CPE_{Anode} representing the In/InLi anode with the In/InLi|SSE interface. In addition, the transmission line model shown in Figure S1b was added in series to model the impedance contribution of the composite cathode. The relevant fitting parameters are listed in Table S1.

Table S1: Parameters obtained from fitting the impedance spectra measured after 100 cycles for Alu-NCM600a, Alu-NCM600b, Alu-NCM and Alu-NCM600c.

		Alu-NCM600a			Alu-NCM600b		
	Voltage / V	3.2	3.4	3.7	3.2	3.4	3.7
Electrolyte	R_{EL} / Ω	34.59	34.71	34.00	34.03	35.70	35.31
Anode side	R_{Anode} / Ω	50.00	50.00	50.00	206.31	50.00	50.00
	Q / F/s$^{1-\alpha}$	2.18E-03	2.18E-03	2.18E-03	1.74E-03	2.18E-03	2.18E-03
	α	0.71	0.67	0.72	0.74	0.63	0.63
Cathode side	R_{ion} / Ω	111.51	111.51	111.51	111.98	111.98	111.98
	R_{CT} / Ω	264.73	267.22	761.83	340.46	296.09	690.42
	L	1.00	1.00	1.00	1.00	1.00	1.00
	Q / F/s$^{1-\alpha}$	6.86E-05	7.08E-05	7.19E-05	5.90E-05	5.77E-05	0.00
	α	0.87	0.87	0.85	0.85	0.87	0.85
	Warburg coefficient	6.32	7.00	19.31	(20.69)	12.35	30.03

		Alu-NCM			Alu-NCM600c		
	Voltage / V	3.2	3.4	3.7	3.2	3.4	3.7
Electrolyte	R_{EL} / Ω	27.48	30.04	30.26	33.41	34.43	34.63
Anode side	R_{Anode} / Ω	4821	50	50	4713	50	50
	Q / F/s$^{1-\alpha}$	4.42E-4	5.56E-03	5.56E-03	5.81E-4	2.18E-3	2.18E-3
	α	0.91	0.57	0.56	0.82	0.47	0.453
Cathode side	R_{ion}/ Ω	104.07	104.51	104.07	78.84	78.84	78.84
	R_{CT} / Ω	839.7	699.39	1653.20	491.06	367.3	734.5
	L	1	1	1	1	1	1
	Q / F/s$^{1-\alpha}$	5.17E-5	4.66E-5	5.02E-5	5.88E-5	4.64E-4	5.01E-5
	α	0.83	0.87	0.86	0.80	0.88	0.86
	Warburg coefficient	-	14.09	35.19	-	8.10	17.5

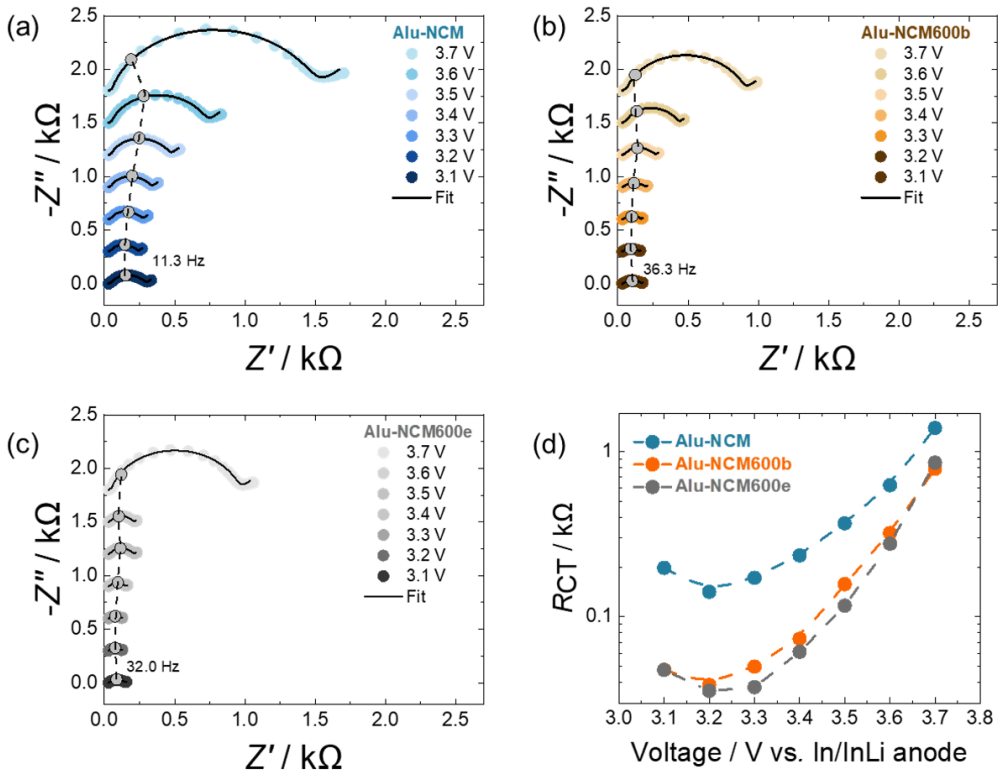

Figure S4: EIS measurements during charge before first cycle for (a) Alu-NCM, (b) Alu-NCM600b, and (c) Alu-NCM600e. (d) Potential-dependent charge transfer resistance R_{CT} on the cathode side before first cycle.

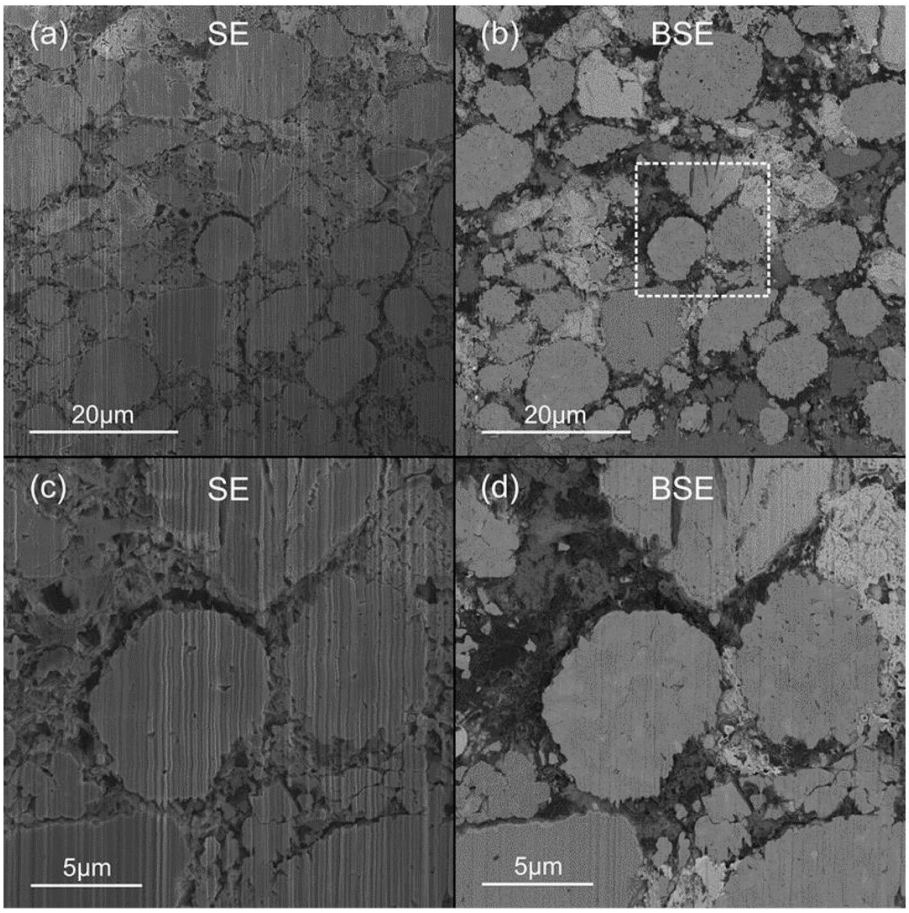

Figure S1: FIB-SEM images of the cathode composite of the Alu-NCM cell after 100 cycles. (a) 60 µm, SE detector, (b) 60 µm, BSE detector, (c) 20 µm, SE detector and (d) 20 µm, BSE detector.

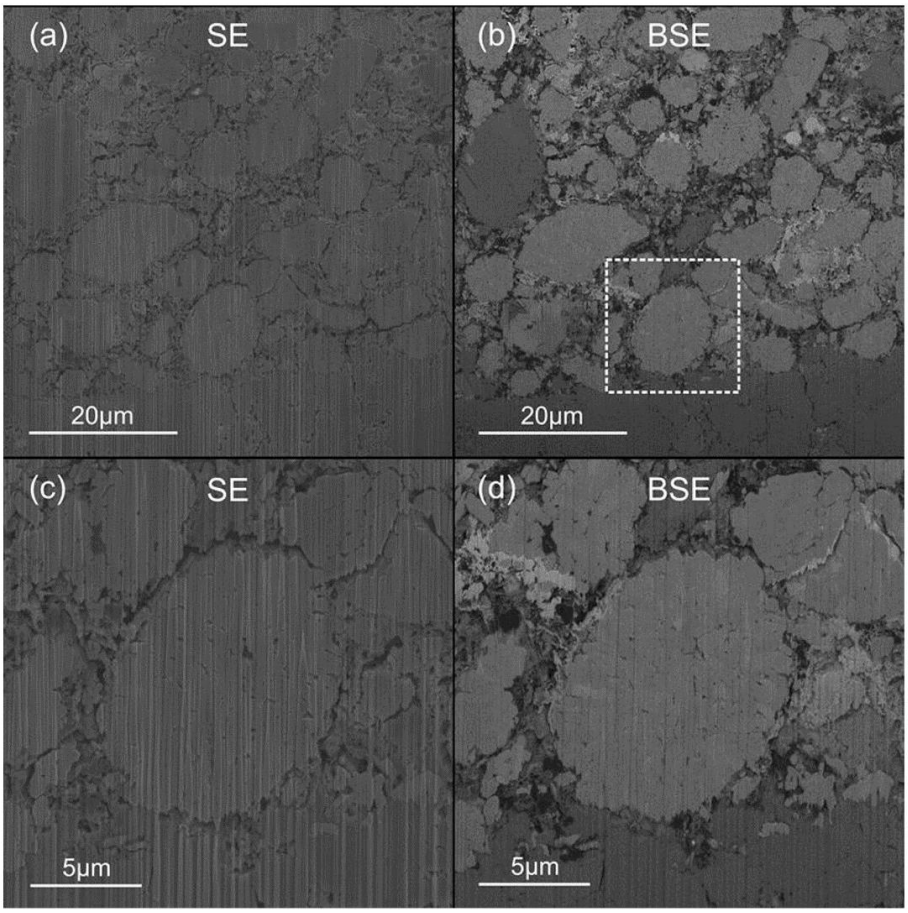

Figure S2: FIB-SEM images of the cathode composite of the Alu-NCM600a cell after 100 cycles. (a) 60 µm, SE detector, (b) 60 µm, BSE detector, (c) 20 µm, SE detector and (d) 20 µm, BSE detector. The dark area at the bottom is the solid electrolyte.

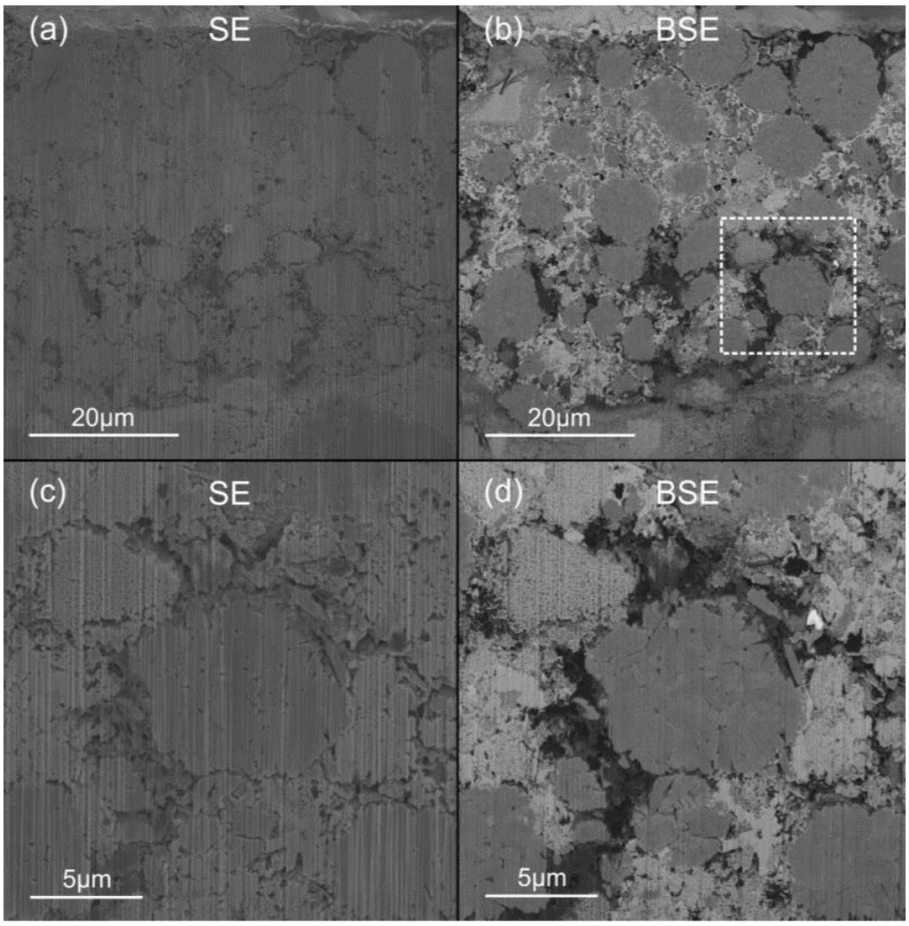

Figure S3: FIB-SEM images of the cathode composite of the Alu-NCM600b cell after 100 cycles. (a) 60 µm, SE detector, (b) 60 µm, BSE detector, (c) 20 µm, SE detector and (d) 20 µm, BSE detector.

6.2 Scientific Contributions

6.2.1 List of Publications

Published online status from 28.11.2023
[1] Indicates shared first authorship

2023

H. Huo, M. Jiang, B. Mogwitz, J. Sann, **Y. Yusim**, T. Zuo, Y. Moryson, P. Minnmann, F. H. Richter, C. V. Singh, J. Janek, *Interface Design Enabling Stable Polymer/Thiophosphate Electrolyte Separators for Dendrite-Free Lithium Metal Batteries*, Angew. Chem. Int. Ed., **2023**, *62*, e202218044.

Y. Yusim, E. Trevisanello, R. Ruess, F. H. Richter, A. Mayer, D. Bresser, S. Passerini, J. Janek, A. Henss, *Evaluation and Improvement of the Stability of Poly(ethylene oxide)-based Solid-state Batteries with High-Voltage Cathodes*, Angew. Chem. Int. Ed., **2023**, *62*, e202218316.

B. Shi, **Y. Yusim**, S. Sen, T. Demuth, R. Ruess, K. Volz, A. Henss, F. H. Richter, *Mitigating contact loss in Li_6PS_5Cl-based solid-state batteries using a thin cationic polymer coating on NCM*, Adv. Energy Mater., **2023**, *13*, 2300310.

Z. Wei, D. K. Singh, K. Helmbrecht, J. Sann, **Y. Yusim**, J. A. Kieser, C. Glaser, M. Rohnke, A. Groß, J. Janek, *In Situ Observation of Room-Temperature Magnesium Metal Deposition on a NASICON/IL Hybrid Solid Electrolyte*, Adv. Energy Mater., **2023**, *13*, 2302525.

Y. Yusim, D. F. Hunstock, A. Mayer, D. Bresser, S. Passerini, J. Janek, A. Henss, *Investigation of the Stability of the Poly(ethylene oxide)|$LiNi_{1-x-y}Co_xMn_yO_2$ Interface in Solid-State Batteries*, Adv. Mater. Interfaces, **2023**, 2300532.

2022

R. S. Negi[1], **Y. Yusim**[1], R. Pan, S. Ahmed, K. Volz, R. Takata, F. Schmidt, A. Henss, M. T. Elm, *A Dry-Processed $Al_2O_3/LiAlO_2$ Coating for Stabilizing the Cathode/Electrolyte Interface in High-Ni NCM-Based All-Solid-State Batteries*, Adv. Mater. Interfaces, **2022**, *9*, 2101428.

2020

W. E. Arter, **Y. Yusim**, Q. Peter, C. G. Taylor, D. Klenerman, U. F. Keyser, T. P. J. Knowles, *Digital Sensing and Molecular Computation by an Enzyme-Free DNA Circuit*, ACS Nano, **2020**, *14*, 5763-5771.

2019

S. Kranz, T. Kranz, T. Graubner, **Y. Yusim**, L. Hellweg, B. Roling, *Influence of the Formation Current Density on the Transport Properties of Galvanostatically Formed Model-Type Solid Electrolyte Interphases*, Batteries & Supercaps, **2019**, *2*, 1026-1036.

6.2.2 List of Conference Contributions

2023 Poster Presentation: **Materials Science Day 2023,** Marburg, Deutschland, (06/2023): *Evaluation and Improvement of the Stability of PEO-based Solid-State Batteries with NCM.*

2023 Oral Presentation: **MRS Spring Meeting 2023,** San Francisco, USA, (04/2023): *Investigations of the Stability of Poly(ethylene oxide)|$LiNi_{1-x-y}Co_xMn_yO_2$ Interface in Solid-State Batteries.*

Oral Presentation**: GIBS 2023**, Ein Gedi, Israel (02/2023): *Evaluation and Improvement of the Stability of Poly(ethylene oxide) Based Solid-State Batteries with NCM.*

Poster Presentation: **Batterieforum Deutschland**, Berlin, Deutschland (01/2023): *Evaluation and Improvement of the Stability of PEO-based Solid-State Batteries with NCM* – **Poster Prize Award**.

2022 Poster Presentation: **IBA 2022**, Bled, Slovenia, (10/2022): *Evaluation and Improvement of the Stability of PEO-based Solid-state Batteries with NCM.*

7 Acknowledgments

This chapter of the dissertation plays a very special role for me, as I want to express my gratitude to all the people, who have supported me over the past three years.

First of all, I would like to thank my supervisor, Dr. Anja Henss, who gave me the opportunity to work, learn, and grow in her research group. Her door was always open to me and her constructive feedback was truly invaluable for my professional and personal development.

Further, I would like to thank Prof. Jürgen Janek for his continuous supervision and support of my work. I am grateful for his interest in my research, for his respect for me as a person, and for his positive attitude.

Special thanks go to Prof. Stefano Passerini and Dr. Dominic Bresser, who advised me on the interpretation and evaluation of my results. It was very fruitful to receive your feedback. Additionally, I would like to thank Prof. Stefano Passerini for his role as the second reviewer of this dissertation. In this context, I would also like to thank Dr. Matthias Elm and Prof. Jörg Sundermeyer for being part of the examination committee for my defense.

Additionally, I express my gratitude to Dr. Joachim Sann for the scientific discussions regarding the XPS measurements and for sharing his knowledge about battery technologies in EVs with me.

"Kisses also go out" to my colleagues, with whom I shared a highly productive and enjoyable working environment. The conference trips and the scientific and personal discussions with Enrico Trevisanello, Dominik Rau, Dr. Till Fuchs, Till Ortmann, Konrad Münch, Maximilian Kissel, Dr. Rajendra Singh Negi, and Bing-Xuan Shi were truly enriching.

In addition, I extend my appreciation to my friends Kevin Dittmann and Kevin Seipp, who have been by my side for many years, providing unwavering friendship and support.

Last but certainly not least, I would like to thank my parents, Mykhaylo and Nataliya Yusim, who have always supported me and who gave me the chance to live in peace in Germany, at the cost of their own professional life. I am doing my best to make the most of this opportunity.

Finally, I would like to mention that this work was not always crowned with success, scientific relevance, publications. There were challenging and hard times, but during those moments, all the people mentioned above stood steadfastly behind me. I am deeply grateful for this.